Cronfa
Swansea University's Research Repository

Towards MRI scanner design: the Proper Generalised Decomposition method in the context of coupled magneto-mechanical problems

by

Guillem Barroso

Submitted to the College of Engineering
in fulfilment of the requirements for the degree of

Doctor of Philosophy

at

Swansea University

1st September 2020

Copyright: The author, Guillem Barroso Gassiot, 2020.

"Sometimes science is more art than science."
Rick Sanchez

Abstract

Latest developments in high-strength Magnetic Resonance Imaging (MRI) scanners, with in-built high resolution, have dramatically enhanced the ability of clinicians to diagnose tumours and rare illnesses. However, their high-strength transient magnetic fields induce unwanted eddy currents in shielding components, which result in high-frequency vibrations, noise, imaging artefacts and, ultimately, heat dissipation and boiling off of the helium used to super-cool the magnets. Optimum MRI scanner design requires the capturing of complex electro-magneto-mechanical interactions with high fidelity computational tools. Moreover, manufacturing new MRI scanners still represents a computational challenge to industry due to the large variability in material parameters and geometrical configurations that need to be tested during the early design phase. This process can be highly optimised through the employment of user-friendly computational metamodels constructed on the basis of Reduced Order Modelling (ROM) techniques, where high-dimensional parametric offline solutions are obtained, stored and assimilated in order to be efficiently queried in real time.

This thesis presents a novel *a priori* Proper Generalised Decomposition (PGD) computational framework for the analysis of the electro-magneto-mechanical interactions in the context of MRI scanner design to address the urgent need for the development of new cost-effective methods, whereby previously performed computations can be assimilated as training solutions of a surrogate digital twin model to allow for real-time simulations. The PGD methodology is derived for coupled electro-magneto-mechanical problems in an axisymmetric Lagrangian setting, including the possibility to vary several material and geometrical parameters (as part of the high-dimensional offline solution), that are relevant for the industrial partner of the project, Siemens Healthineers. A regularised-adaptive strategy and a staggered PGD approach are proposed in order to enhance the accuracy and robustness of the PGD algorithm while preserving its *a priori* nature. The Lagrangian adaptation of the governing equations will allow for a comparison between staggered and monolithic solvers, where the staggered approach will be shown to enhance the robustness and accuracy of the PGD technique. Moreover, geometric changes in the computational domain will be accounted for in the PGD solution by using a PGD-projection technique that will enable the computation of a separable expression even for geometrical variations, preserving thus the efficiency of the online PGD stage. A set of numerical problems will be presented in order to validate the PGD formulation, which will be benchmarked against the full order (reference) model. Moreover, a comparison between two families of ROM methods, the *a priori* PGD and the *a posteriori* Proper Orthogonal Decomposition (POD), will also be performed in order to assess and compare different ROM strategies.

DECLARATION

This work has not previously been accepted in substance for any degree and is not being concurrently submitted in candidature for any degree.

Signed .... [redacted] ....

Date .... 1st September 2020 ....

STATEMENT 1

This thesis is the result of my own investigations, except where otherwise stated. When correction services have been used, the extent and nature of the correction is clearly marked in a footnote(s). Other sources are acknowledged by footnotes giving explicit references. A bibliography is appended.

Signed .... [redacted] ....

Date .... 1st September 2020 ....

STATEMENT 2

I hereby give consent for my thesis, if accepted, to be available for photocopying and for inter-library loan, and for the title and summary to be made available to outside organisations.

Signed .... [redacted] ....

Date .... 1st September 2020 ....

Acknowledgements

This thesis contains the research carried out during my three years as a PhD researcher, mainly based at Swansea University but also working in close collaboration with Universitat Politècnica de Catalunya and Siemens Healthineers. Firstly, I would like to thank Prof. Antonio J. Gil and Dr. Paul D. Ledger for their supervision and advice. I feel grateful to have had the opportunity to work with them and more importantly, to learn from them. Also, I would like to express my gratitude to Prof. Antonio Huerta for his scientific and personal advise. The industry insight brought by Dr. Mike Mallett has been determinant for the progress of my research as a PhD candidate. Thank you to all the supervisory team for transmitting me your passion for research, this thesis would have not been possible without the knowledge I acquired from all of you.

Of course, many people have been essential during these three years. A huge thank you to the entire PhD office in Swansea, your company has been crucial in several difficult moments that every PhD student suffers at some point of this long journey. Also to Rubén, thank you for being a good friend, always there to chat and to release stress while enjoying a good Welsh beer. In addition, I met many amazing people during my stages in Barcelona, specially the AdMoRe group. I really enjoyed all the activities, dinners, conferences, seminars and talks we attended and organised together. It has been amazing to share these years of intense work with you guys.

The support from my family and friends back in Barcelona has been crucial during my entire life and particularly during my PhD. Even after four years of being more than 1000 km away from Barcelona and you are still the most important people in my life. Now I am closing a stage here in Swansea and I am ready to start a new one in Barcelona. Get ready because I am coming back!

Thank you all!

Contents

Abstract iii

Acknowledgements vii

List of Figures xiii

List of Tables xxi

1 Introduction 1
- 1.1 MRI scanners 1
  - 1.1.1 Imaging process 2
  - 1.1.2 The need for computational simulation 3
  - 1.1.3 Design stage bottleneck 7
- 1.2 Coupled magneto-mechanics 8
- 1.3 Reduced Order Modelling 9
  - 1.3.1 *A posteriori* Proper Orthogonal Decomposition method 10
  - 1.3.2 *A priori* Proper Generalised Decomposition method 11
- 1.4 Objectives 12
- 1.5 Thesis structure 13
- 1.6 Scientific contributions 15
  - 1.6.1 Journal publications 15
  - 1.6.2 Conference presentations 15
  - 1.6.3 Research posters 16

2 Full order model 17
- 2.1 Introduction 17
- 2.2 Coupled magneto-mechanical problem 17
- 2.3 Numerical treatment 20
  - 2.3.1 Linearisation approach 20
  - 2.3.2 Time-harmonic formulation 21
- 2.4 Time-harmonic magneto-mechanical problem 22
  - 2.4.1 Non-linear static DC problem 22
  - 2.4.2 Linearised time-harmonic AC problem 22
- 2.5 Axisymmetric time-harmonic problem 23

2.5.1 Monolithic formulation 24
2.5.2 Staggered formulation 26
2.6 Finite element discretisation 27
2.7 Effect of the addition of numerical regularisation 29
2.8 Description of industrially relevant problems 30
2.8.1 Test magnet problem 30
2.8.2 Full magnet problem 36
2.9 Chapter summary 38

3 General PGD formulation 39
3.1 Introduction 39
3.2 Augmented weak formulation 40
3.3 Offline high-dimensional parametric PGD formulation 40
3.4 Non-homogeneous Dirichlet boundary conditions 43
3.5 Modal scaling 44
3.6 Convergence criteria 44
3.6.1 Alternating Direction Scheme (ADS) 45
3.6.2 Greedy algorithm 46
3.7 Online PGD stage 47
3.8 Chapter summary 48

4 Monolithic frequency-based PGD technique 49
4.1 Introduction 49
4.2 Augmented weak formulation 50
4.3 PGD for magneto-mechanical problems 50
4.3.1 Alternating direction scheme 52
4.3.2 Greedy algorithm convergence 52
4.3.3 Finite element discretisation 53
4.4 Monolithic adaptive frequency splitting 55
4.5 Test magnet problem 57
4.5.1 PGD algorithm convergence 59
4.5.2 Modes visualisation 62
4.5.3 Validation of the PGD method 65
4.6 Full magnet problem 65
4.6.1 PGD algorithm convergence 68
4.6.2 Modes visualisation 72
4.6.3 Validation of the PGD method 75
4.7 Chapter summary 77

5 Staggered high-dimensional PGD technique 79
5.1 Introduction 79
5.2 High-dimensional parametric space 80
5.3 Augmented weak formulation 81

5.4 PGD for magneto-mechanical problems 83
5.4.1 PGD formulation for electromagnetics 83
5.4.2 PGD formulation for mechanics 84
5.4.3 Staggered PGD solver 86
5.4.4 Alternating direction scheme 86
5.4.5 Finite element discretisation 91
5.5 Staggered versus monolithic PGD techniques 93
5.5.1 Staggered adaptive frequency splitting 95
5.6 Test magnet problem 96
5.6.1 ROM techniques on the electromagnetic problem 96
5.6.2 Coupled magneto-mechanical problem 99
5.7 Full magnet problem 107
5.7.1 Frequency splitting 109
5.7.2 PGD algorithm convergence 110
5.7.3 Modes visualisation 114
5.7.4 Validation of the PGD method 118
5.7.5 Sensitivity maps 118
5.8 Chapter summary 121

6 Integration of geometric parameters into the PGD methodology 123
6.1 Introduction 123
6.2 Problems of interest 124
6.2.1 Visualisation of the solution for several geometries 125
6.3 Characteristic polynomial 126
6.4 Mesh deformation through linear elasticity 128
6.5 Higher-order PGD-projection technique 132
6.6 Incorporation of h variations into the frequency-based PGD method . 134
6.7 Incorporation of h variations into the high-dimensional PGD method 138
6.8 Chapter summary 142

7 Concluding remarks 145
7.1 Conclusions 145
7.2 Further work 147
7.2.1 Further research developments 147
7.2.2 Transfer to industry developments 149

Appendices 151

A EM-POD methodology 153

B One-dimensional mortar integral treatment 157

C Efficient computation of integrated quantities 159
C.1 Integration of the output power 159
C.1.1 Full order model approach 161
C.1.2 PGD approach 162

D Sensitivity maps 165

E GUI for the online PGD stage and code description 169
E.1 GUI for the online PGD stage 169
E.2 Code description 170
E.2.1 Code structure 171
E.2.2 PGD user-defined parameters 171
E.2.3 Online PGD parameters 173
E.2.4 One-dimensional parametric domains 173
E.2.5 Spatial discretisation 174
E.2.6 Geometry definition 175
E.2.7 Full order model options 176
E.2.8 Code output 177
E.2.9 Online PGD stage 178

References 181

List of Figures

1.1 MRI scanner description; (a) new MRI device model MAGNETOM Altea 1.5 T Open Bore system. (b) Simplified axisymmetric MRI components. Courtesy of Siemens Healthineers. 2
1.2 Presence of ghosting artefacts in MRI scans caused by motion. Courtesy of Siemens Healthineers. 4
1.3 Numerical simulation of a simplified MRI configuration in order to study the eddy current generation in the radiation shields. Courtesy of Siemens Healthineers. 4
1.4 Frequency sweep study displaying mechanical resonance in the vicinity of the natural frequencies of the OVC radiation shield. Right figure shows a zoomed view in the resonance region (red rectangle). . 5
1.5 Helium safety valve for a small animal 1.5 T MRI scanner. Courtesy of Hallmarq Veterinary Imaging. 6
1.6 Shim elements (yellow arrows) mounted in an MRI scanner. Image taken from http://mriquestions.com/passive-shimming.html on 29/11/2019. 7

2.1 Description of a general magneto-mechanic problem; conducting component Ω^C (with magnetic permeability $\mu = \mu_*$ and electrical conductivity $\gamma = \gamma_*$) in a non-conducting three dimensional space $\mathbb{R}^3 \backslash \overline{\Omega^C}$ (with $\mu = \mu_0$ and $\gamma = 0$). Problem excited by a current source $\boldsymbol{J}^S$ acting in a series of coils. 18
2.2 Linearisation process; initial state excited through static current source $\boldsymbol{J}^{DC}$. Solution of static problem is used as the initial state for the transient problem with time-harmonic current source $\boldsymbol{\mathcal{J}}^{AC}$. 21
2.3 Axisymmetric reduction of a real three-dimensional problem. 24
2.4 Axisymmetric $\{r, \phi, z\}$ representation of the problem; a conducting component Ω_p^C in a non-conducting domain Ω_p. 25
2.5 Magneto-mechanical test problem; geometry description and kinetic energy in the conducting mechanical shell. 29
2.6 Magneto-mechanical test problem; values of the kinetic energy $E^k_{\Omega^C}$ in the mechanical shell Ω_p^C for different damping ratios ξ. 30

2.7 Test magnet problem; geometry description. 3D view (left) and 2D axisymmetric view (right) with components names and boundary conditions. 31

2.8 Test magnet problem; value of the dissipated Power $E^k_{\Omega^C_{OVC}}$ in the OVC shield for different frequencies from 1 to 5000 Hz. Right Figure shows a zoomed view in the resonance region (red rectangle). Results shown are for a mesh of 2.9K triangular elements using a polynomial order $p = 4$. 32

2.9 Test magnet problem; h-refinement (left) using a polynomial order $p = 1$ and p-refinement (right) with a mesh of 2.9K elements. 33

2.10 Test magnet problem; comparison between solutions obtained with a mesh with 500K elements with $p = 1$ and a mesh with $p = 6$ with 2.9K elements. 33

2.11 Test magnet problem; study on the number sampling of points in the frequency interval required to accurately capture the solution. 34

2.12 Test magnet problem; visualisation of the magnetic field $|\boldsymbol{\mathcal{B}}_0^{AC}|$ contour lines on the axisymmetric plane and the magnitude of the displacements $|\boldsymbol{\mathcal{U}}|$ in the OVC shield. Plot of the deformed OVC shield for different frequencies. 35

2.13 Full magnet problem; geometry description. 3D view (left) and 2D axisymmetric view (right) with components names and boundary conditions (only the top half of the axisymmetric domain is presented due to symmetry). 36

2.14 Full magnet problem; full order solution of both DC and AC problems for a frequency of 1000 Hz. 37

2.15 Full magnet problem; line plot of both static (DC) and transient (AC) magnetic fields along the $r = 0$ axis for a frequency of 1000 Hz. . . . 38

3.1 Flow chart algorithm; description of the d-dimensional PGD algorithm. 43

3.2 Flow chart algorithm; description of the d-dimensional online PGD stage. 48

4.1 Visualisation of the dirac Delta function, which has a value equal to one in a particular point ω_a and zero everywhere else. 54

4.2 Magneto-mechanical test problem; comparison between the full order model and the PGD approximation obtained considering the entire frequency domain $f \in (0, 5000]$ Hz. 55

4.3 Magneto-mechanical test problem; description of the automatic splitting process performed to locate the resonance frequencies and refine around them. Plot of kinetic energy $E^k_{\Omega^C}$ in the conducting mechanical shell with a damping coefficient $\alpha = 50$. 57

4.4 Test magnet problem; splitting of the frequency domain to increase PGD accuracy. 58

4.5 Test magnet problem; Greedy algorithm convergence for all frequency subdomains. 60
4.6 Test magnet problem; fixed-point alternating direction scheme convergence for all frequency subdomains. 61
4.7 Test magnet problem; first 12 computed electromagnetic spatial modes $F_{\mathcal{A}_\phi}(r, z)$ for the first frequency subdomain $f \in [1, 3331]$ Hz. Same colour scale for all subfigures. 62
4.8 Test magnet problem; first 12 computed mechanical spatial modes $F_{\boldsymbol{\mathcal{U}}}(r, z)$ for the first frequency subdomain $f \in [1, 3331]$ Hz. Same colour scale for all subfigures. 63
4.9 Test magnet problem; parametric modes $G(\omega)$ computed for each frequency subdomain. 64
4.10 Test magnet problem; comparison between PGD approximation and full order model for $f = 4000$ Hz. 66
4.11 Test magnet problem; comparison between PGD approximation and full order model. Plot of dissipated power $P^0_{\Omega^C}$ and kinetic energy $E^k_{\Omega^C}$ in the three conducting shields OVC, 77K and 4K. 67
4.12 Test magnet problem; splitting of the frequency domain to increase PGD accuracy. 68
4.13 Full magnet problem; Greedy algorithm convergence for all frequency subdomains. 70
4.14 Full magnet problem; fixed-point alternating direction scheme convergence for all frequency subdomains. 71
4.15 Full magnet problem; first 8 computed electromagnetic spatial modes $F_{\mathcal{A}_\phi}(r, z)$ for the first frequency subdomain $f \in [1, 167]$ Hz. All modes have been L^2 normalised. Same colour scale for all subfigures. 72
4.16 Full magnet problem; first 8 computed mechanical spatial modes $F_{\boldsymbol{\mathcal{U}}}(r, z)$ for the first frequency subdomain $f \in [1, 167]$ Hz. All modes have been L^2 normalised. Same colour scale for all subfigures. 73
4.17 Full magnet problem; first 8 computed normalised parametric modes $G(\omega)$ for each frequency subdomain. 74
4.18 Full magnet problem; comparison between solution fields obtained using the full order model ($\cdot_{full}$) and the PGD approach ($\cdot_{PGD}$). Visualisation of $|\boldsymbol{\mathcal{B}}_0^{AC}|$ around the gradient coils and $|\boldsymbol{\mathcal{U}}|$ in the conducting shields for a frequency of 100 Hz. 75
4.19 Full magnet problem; comparison between PGD approximation and full order model. Plot of dissipated power $P^0_{\Omega^C}$ and kinetic energy $E^k_{\Omega^C}$ in the three conducting shields OVC, 77K and 4K. 76

5.1 Different parametric domains for electromagnetics and mechanics due to adaptive splitting PGD technique. 81

5.2 Typical axisymmetric MRI scanner geometry; presence of multiple ($N^C = 3$) isolated conducting components Ω_p^C embedded in a truncated non-conducting domain Ω_p. 82

5.3 Flow chart algorithm; description of the staggered PGD nature. The continuous and discrete formulations are detailed in Sections 5.4.4 and 5.4.5. 87

5.4 Test magnet problem; Last mode contribution for electromagnetics e^A and mechanics e^u. Comparison between monolithic PGD e_{mono} and staggered PGD e_{stag} approaches. Both PGD algorithms only depending on space (r, z) and frequency ω with no splitting in the frequency domain. 94

5.5 Test magnet problem; natural frequencies (red) obtained from eigenvalue analysis and frequency subdomains (black) defined through frequency splitting. Right figure shows a zoomed view in the resonance region (red rectangle). Full order model results (blue) shown for a mesh of 2.9K triangular elements using a polynomial order $p = 4$. . . 95

5.6 Test magnet problem; comparison between staggered (black dashed lines) and monolithic (grey dashed lines) frequency splitting algorithms. Full order model results (blue) shown for a mesh of 2.9K triangular elements using a polynomial order $p = 4$. 96

5.7 Electromagnetic test magnet problem; comparison between PGD and EM-POD approximations against the reference full order model. . . . 98

5.8 Test magnet problem; frequency subdomains resulting from staggered frequency splitting algorithm. Plotting the full order model solution (dissipated power) for $B_0 = 7$ T and $\alpha_\gamma = 1.5$. 100

5.9 Test magnet problem; Greedy algorithm convergence for electromagnetics and for the three (mechanical) frequency subdomains. 102

5.10 Test magnet problem; convergence of the fixed-point ADS algorithm for each of the six frequency subdomains of the OVC shield. 103

5.11 Test magnet problem; first 12 computed electromagnetic spatial modes $F_{\mathcal{A}_\phi}(r, z)$. All modes have been L^2 normalised. Same colour scale for all subfigures. 104

5.12 Test magnet problem; visualisation of the one-dimensional parametric electromagnetic modes $G_{\mathcal{A}_\phi}(\omega)$ and $H_{\mathcal{A}_\phi}(\gamma)$ for the entire range of the one-dimensional parametric domains; frequency $f \in [1, 5000]$ Hz and dimensionless conductivity scaling factor $\alpha_\gamma \in [0.5, 2]$. All modes have been L^2 normalised. 105

5.13 Test magnet problem; first 12 computed mechanical spatial modes $F_{\boldsymbol{u}}(r, z)$ for the first frequency subdomain. All modes have been L^2 normalised. Same colour scale for all subfigures. 105

5.14 Test magnet problem; visualisation of the three one-dimensional parametric mechanical modes $G_{\boldsymbol{u}}(\omega)$, $H_{\boldsymbol{u}}(\gamma)$ and $L_{\boldsymbol{u}}(B_0)$ of the OVC shield for the three frequency subdomains. All modes have been L^2 normalised. 106

5.15 Test magnet problem; comparison between PGD solution and full order model. Plot of the dissipated power $P^0_{\Omega^C}$ and kinetic energy $E^k_{\Omega^C}$ in the three conducting shields OVC, 77K and 4K for six different cases. 108

5.16 Test magnet problem; study of the computational time taken by the full order model and both offline and online stages of the PGD technique. 700 frequencies have been sampled for each case of study. . . . 109

5.17 Full magnet problem; frequency subdomains resulting from staggered frequency splitting algorithm. Plotting the full order model solution (dissipated power) for $B_0 = 7$ T and $\alpha_\gamma = 1.5$. 110

5.18 Full magnet problem; electromagnetic Greedy algorithm convergence. 110

5.19 Full magnet problem; mechanical Greedy algorithm convergence for the six frequency subdomains. 111

5.20 Full magnet problem; electromagnetic convergence of the fixed-point ADS algorithm. 112

5.21 Full magnet problem; mechanical convergence of the fixed-point ADS algorithm for each of the six frequency subdomains of the OVC shield. 113

5.22 Full magnet problem; first 8 computed electromagnetic spatial modes $F_{\mathcal{A}_\phi}(r, z)$ for the entire range of the one-dimensional parametric domains; frequency $f \in [1, 2000]$ Hz. All modes have been L^2 normalised. Same colour scale for all subfigures. 114

5.23 Full magnet problem; visualisation of the one-dimensional parametric electromagnetic modes $G_{\mathcal{A}_\phi}(\omega)$ and $H_{\mathcal{A}_\phi}(\gamma)$ for the entire range of the one-dimensional parametric domains; frequency $f \in [1, 2000]$ Hz and dimensionless conductivity scaling factor $\alpha_\gamma \in [0.5, 2]$. All modes have been L^2 normalised. 115

5.24 Full magnet problem; first 8 computed mechanical spatial modes $F_{\boldsymbol{u}}(r, z)$ for the first frequency subdomain. All modes have been L^2 normalised. Same colour scale for all subfigures. 116

5.25 Full magnet problem; visualisation of the three one-dimensional parametric mechanical modes $G_{\boldsymbol{u}}(\omega)$, $H_{\boldsymbol{u}}(\gamma)$ and $L_{\boldsymbol{u}}(B_0)$ of the OVC shield for the six frequency subdomains. All modes have been L^2 normalised. 117

5.26 Full magnet problem; comparison between PGD solution and full order model. Plot of the dissipated power $P^0_{\Omega^C}$ and kinetic energy $E^k_{\Omega^C}$ in the three conducting shields OVC, 77K and 4K for six different cases. 119

5.27 Full magnet problem; study of the computational time taken by the full order model and the staggered PGD approach. 400 frequencies have been sampled for each case of study. 120

5.28 Full magnet problem; Eddy current distribution within the radiation (conducting) shields for different frequencies f, $B_0 = 1.5$ T and $\gamma = 1$. 120

5.29 Full magnet problem; response surfaces of the output power in the OVC shield $P^0_{\Omega^C_{OVC}}$ for different values of f, B_0 and α_γ. 121

6.1 Description of the three MRI configurations considered. Two different Dirichlet boundary conditions are set for the test magnet geometry. . 125

6.2 Frequency sweep for three different MRI configurations computing the dissipated power $P^0_{\Omega^C_{4K}}$ from the precomputed PGD offline solution for five different geometries. 127

6.3 Visualisation of three characteristic polynomials for three different geometries of an illustrative problem. 129

6.4 Test magnet problem; tracking of the three smallest and biggest eigenvalues for five different geometries within the frequency range of interest. 129

6.5 Reference (r_X, z_X) axisymmetric MRI shield that is mapped through $\Psi(\boldsymbol{r}_X)$ to the actual deformed (r, z) domain. 130

6.6 Mesh deformation of the test magnet problem; reference mesh with $h_0 = 3$ mm (left) and deformed mesh with $h = 1$ mm (right). 131

6.7 Mesh deformation of the full magnet problem; process of computing the required Dirichlet boundary conditions to deform mesh using linear elastic solver. 131

6.8 Mesh deformation of the full magnet problem; reference mesh with $h_0 = 3$ mm (left) and deformed mesh with $h = 5$ mm (right). 132

6.9 Test magnet problem; Approximation of the frequency sweep for a new geometry $h = 1.6$ mm using stored PGD solutions (6.17) for N_h sampled geometries with $\alpha_\gamma = 1$ and $B_0 = 1.5$ T. Plotting the L^2 norm of the displacement field $|\boldsymbol{\mathcal{U}}|_{L^2(\Omega^C_{4K})}$ in the 4K shield. 137

6.10 Approximation of the frequency sweep for a new geometry $h = 1.6$ mm, computing the L^2 norm of the displacement field $|\boldsymbol{\mathcal{U}}|_{L^2(\Omega^C_{4K})}$ from the precomputed offline PGD solutions (6.17) for $N_h = 9$ with $\alpha_\gamma = 1$ and $B_0 = 1.5$ T. Displaying two different MRI configurations (test magnet 2 and full magnet). 138

6.11 Test magnet problem; collocation PGD-projection approximation for different values of B_0, α_γ and h benchmarked against the full order model for the same parameter combination. Plotting the dissipated power for the three radiation shields (OVC, 77K and 4K). 141

6.12 Test magnet 2 problem; collocation PGD-projection approximation for different values of B_0, α_γ and h benchmarked against the full order model for the same parameter combination. Plotting the dissipated power for the three radiation shields (OVC, 77K and 4K). 142

6.13 Full magnet problem; collocation PGD-projection approximation for different values of B_0, α_γ and h benchmarked against the full order model for the same parameter combination. Plotting the dissipated power for the three radiation shields (OVC, 77K and 4K). 143

A.1 Flow chart algorithm; description of the EM-POD technique. 155

B.1 Representation of two non-matching one-dimensional meshes. 158

E.1 On-line PGD application for coupled magneto-mechanical problems with application to MRI scanners. Visualisation of the four tabs; Presentation, Loading PGD, Plotting and Frequency sweep. 170
E.2 Definition of the PGD input options. 172
E.3 Specification of the online PGD parameters to evaluate the previously stored offline PGD solution. 173
E.4 Information related to the one-dimensional parametric domains considered in the PGD technique. 174
E.5 Spatial discretisation of the 2D (r, z) domain for both full order and PGD approaches. 175
E.6 Problem file definition in the code. 175
E.7 Problem files included in the code and tested with both full order model and PGD approaches. 176
E.8 Switches (0 or 1 values) to activate certain features regarding the full order model. 177
E.9 Output of the `main.m` script when running the staggered PGD technique. 178
E.10 Switches (0 or 1 values) to activate certain features in `onlinePGDstage.m`.179

List of Tables

4.1 Magneto-mechanical test problem; user-defined parameters for the monolithic frequency-based PGD method. 56

4.2 Test magnet problem; user-defined parameters for the monolithic frequency-based PGD method. 58

4.3 Full magnet problem; user-defined parameters for the monolithic frequency-based PGD method. 68

5.1 Electromagnetic test magnet problem; user-defined parameters for the staggered high-dimensional PGD method. 97

5.2 Electromagnetic test magnet problem; user-defined parameters for the EM-POD method. Quantity $f^{snap} = [f_{min} : \Delta f : f_{max}]$ defined through minimum f_{min} and maximum f_{max} frequencies and spacing Δf. 98

5.3 Test magnet problem; user-defined parameters for the staggered high-dimensional PGD method. 100

5.4 Full magnet problem; user-defined PGD parameters for the staggered high-dimensional PGD method. 109

6.1 Test magnet problem; user-defined parameters for the staggered frequency-based PGD method. 126

6.2 User-defined parameters used to compute the frequency-based PGD solutions for N_h sampled geometries. Three different MRI configurations considered, see Figure 6.1. 135

6.3 User-defined parameters for the PGD-projection algorithm used to separate the high-order tensor coefficients. 135

6.4 Sampled points in Ω_h for different resolutions N_h. Quantity $h^{snap} = [h_{min} : \Delta h : h_{max}]$ defined through minimum h_{min} and maximum h_{max} thicknesses and spacing Δh. 136

6.5 Sampled points in the parametric domains for the generation of the high-order tensor coefficients 139

6.6 User-defined parameters for the PGD-projection algorithm used to separate the high-order tensor coefficients. 140

Chapter 1

Introduction

1.1 MRI scanners

The use of Magnetic Resonance Imaging (MRI) [1] has become standard in the decision process within a medical and/or clinical environment. This imaging method has dramatically enhanced the ability of clinicians to diagnose due to the MRI scanners' high in-built resolution when imaging fractures [2], joints [3] and soft tissues, such as damaged cartilage [2] and tumours [4]. Another exceptional feature of MRI is its non-intrusive nature [5], with no harmful ionising radiation being used. Consequently, this imaging technique has become particularly suitable for patients requiring multiple imaging examinations as it minimises any secondary radiation effects on the patient, which is of great interest to the medical community.

A typical MRI scanner, see Figure 1.1, consists of a cryostat enclosing three main components: main Direct Current (DC) coils, gradient Alternating Current (AC) coils and radiation shields. The main DC coils [6] generate a strong uniform background magnetic field with magnetic strength, in clinical MRI scanners, of up to 7 Tesla (T), with most devices having a strength of 1.5 T and 3 T. Although it is generally accepted that the image quality improves with higher magnetic strength, some image-degrading factors become more dominant for high-strength magnets [7] and they have been found to have an increased discomfort for the patient [8]. In order to achieve such high magnetic strengths, the DC coils (also known as magnets) are superconducting where, under certain conditions, there is no resistance to the flow of electrons and, thus, a minimum of energy is dissipated [7]. To achieve this state, magnets are supercooled with liquid helium within the radiation shield at a temperature of 4 K (-269 °C). In addition, to preserve the helium temperature, another radiation shield is used to enclose liquid nitrogen at 77 K (-196 °C). Note that the radiation shields are closed conducting shells that try to prevent the introduction of the kinetic energy generated by vibrations to the nitrogen and helium vessels and stop radiation from escaping the device.

In contrast, the gradient AC coils emit electromagnetic pulses which create a gradient magnetic field across the patient's body. The induced AC current source is significantly smaller in magnitude (approximately 2-10%) than the one in the main DC coils and they are only activated during the imaging process. The gradient coils are orientated along three orthogonal axes (x-, y- and z-gradient coils) in order to generate variations on the magnetic field in all three spacial directions and in other directions by inducing currents in combinations of the three coils.

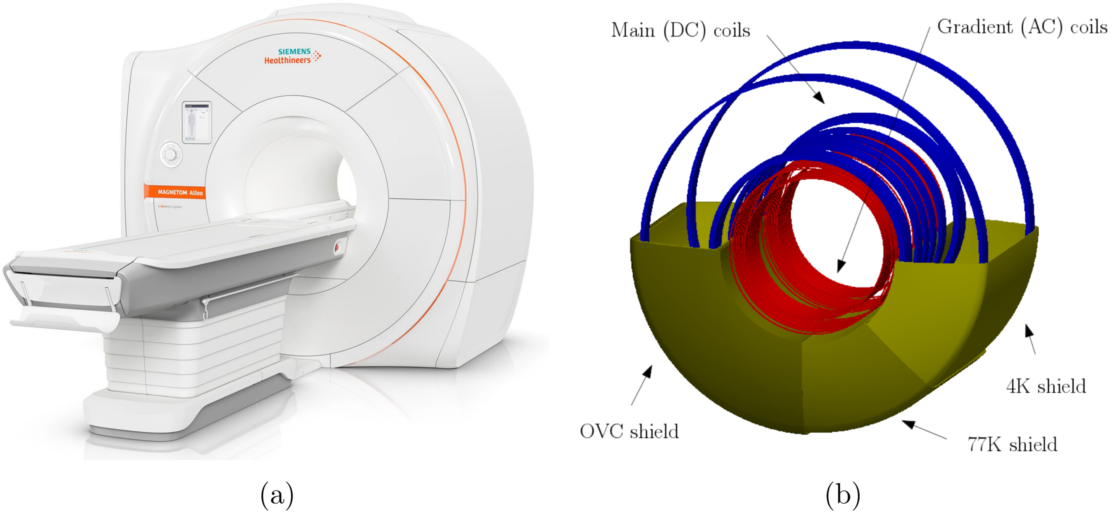

(a) (b)

Figure 1.1: MRI scanner description; (a) new MRI device model MAGNETOM Altea 1.5 T Open Bore system. (b) Simplified axisymmetric MRI components. Courtesy of Siemens Healthineers.

The industrial partner of this project, Siemens Healthineers [9], is interested in studying the gradient coil interaction taking place during the functioning of an MRI scanner. This would help designers to make sound decisions during the MRI design stage in which several material and geometrical parameters have to be varied and tested. The gradient coil interaction problem consists in studying the electro-magneto-mechanical[1] response of a simplified MRI device, where only the main components (main and gradient coils and radiation shields) are considered. This study allows Siemens Healthineers to determine the best material and geometric parameter combinations for a new MRI configuration, that will be further tested considering additional components and other physical processes such as acoustics and thermal effects [10].

1.1.1 Imaging process

This section aims to briefly describe the process followed to obtain an image from a patient through MRI technology. Some key aspects of the functioning of MRI scanners will be used later on and, thus, they are highlighted in this section.

---

[1] As it will be shown later on, the solution variables of the coupled electro-magneto-mechanical problem are the magnetic potential and the displacement field and consequently, from this point onwards it will be referred as magneto-mechanical problem.

First, the high-strength magnetic field produced by the superconducting DC coils interacts with the protons in the patient's body in a similar manner to a compass, where each proton behaves as a small magnet with a magnetic moment. Consequently, the magnetic moments of all protons align with the same direction of the induced magnetic field [5].

When the actual imaging process starts, the gradient AC coils emit electromagnetic pulses that knock the protons out of alignment. After switching off the AC coils, the protons suffer a relaxation process [7] that consists in a signal decay due to the return of protons back to alignment. All relaxation processes will be slightly different depending on the tissue and the damage level and, thus, they are usually difficult to identify. MRI relies on the contrast between tissues, which can be mapped to the spatial location and output a grey scale code to produce an image.

1.1.2 The need for computational simulation

This section motivates the need for high-accuracy computational simulation in the context of MRI scanners by presenting a set of phenomena of interest to the industrial partner of this project.

Ghosting effect

Ghosting effects or artefacts [11] consists of artificial imaging ghosts, smearing and blurry areas in the reconstructed MRI image and can have a negative impact on the image quality hindering the diagnosis. Figure 1.2 shows ghosting artefacts when imaging a large glass tube filled with water and several other smaller glass tubes. Figure 1.2a presents the image where no motion is applied during the imaging process, and Figures 1.2b and 1.2c correspond to the same imaging process, but now introducing a periodic and a random motion, respectively. It is clear from these three scans that the image quality is dramatically reduced when motion is present during scanning, where random motions are likely to disturb and create much more artefacts than a periodic motion.

The most obvious source of motion in a MRI scanner is due to patients themselves, who may move during the scanning process. Also, the respiration motion of the diaphragm and other organs have been reported to induce severe artefacts [11]. However, another factor that introduces vibrations into the system is the magneto-mechanical interaction between the coils and the radiation conducting shields, which generates vibrations in the mechanical components of the device and, thus, distort the uniform static magnetic field.

In extreme cases, the ghosting effect can potentially mislead the person in charge of diagnosing and, thus, it could compromise the medical treatment required. Hence, one of the challenges in the MRI industry consists in identifying all potential motion sources in order to minimise them.

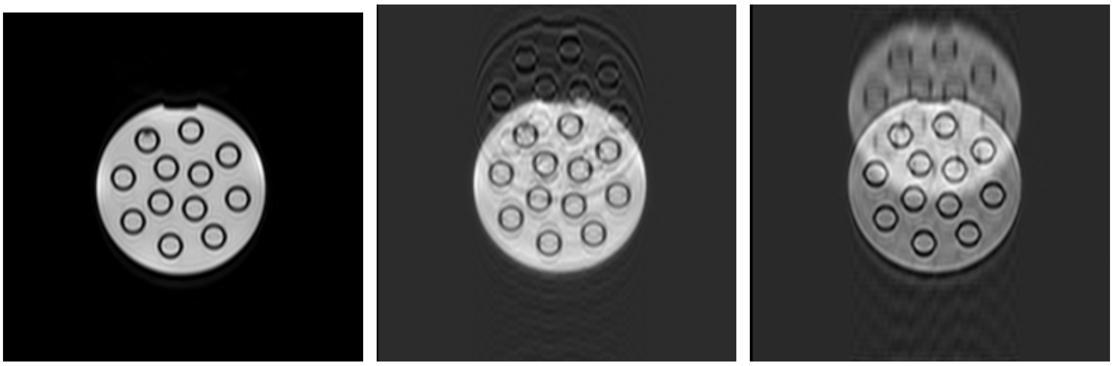

(a) Output image with no motion. (b) Output image with periodic motion. (c) Output image with random motion.

Figure 1.2: Presence of ghosting artefacts in MRI scans caused by motion. Courtesy of Siemens Healthineers.

Eddy currents

The transient magnetic field induced by the gradient AC coils penetrates into the conducting components of the MRI scanner creating loops of electrical currents known as eddy or ohmic currents [12]. The generated eddy currents are perpendicular to the magnetic field and they interact with it, perturbing the original transient field generated in the AC coils. This continuous interaction may also create image artefacts as presented in [13].

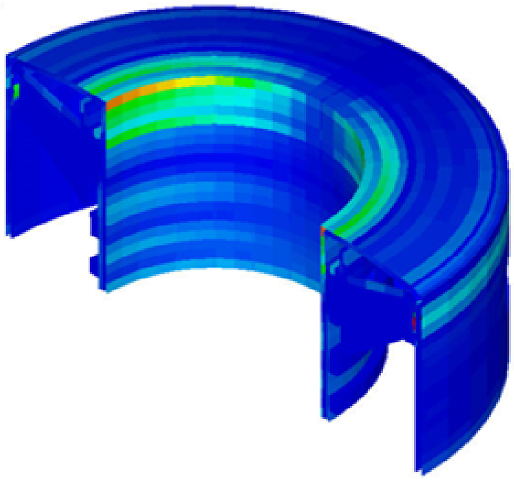

Figure 1.3: Numerical simulation of a simplified MRI configuration in order to study the eddy current generation in the radiation shields. Courtesy of Siemens Healthineers.

Figure 1.3 shows a numerical simulation of a simplified MRI configuration provided by Siemens Healthineers in which the eddy currents are plotted in one of the conducting radiation shields. In this case, numerical simulation is used in order to understand and control the eddy current generation when designing a new MRI scanner. The skin effect associated with eddy currents is the tendency of the electric current to circulate with a high current density in the surface of a conductor that decreases with greater depths [7]. The skin depth is measured as the distance at which the fields decay to $1/e$ of its value (with e being the Euler's number) within a conducting component [14] and, thus, the electric current flows mainly at the skin of the conductor for high frequencies. Therefore, the use of highly accurate numerical modes such as high-order finite elements is very appealing in order to accurately resolve the complex physics that develop in such a small skin depth.

Resonance phenomenon

One of the most relevant studies for our industrial partner consists in studying the behaviour of the magneto-mechanical system for a certain MRI geometry for a broad frequency spectrum [2]. The frequencies of excitation will vary depending on several factors, such as the part of the body that has to be scanned or the imaging process followed and, hence, Siemens Healthineers has to make sure that the different operating frequencies generate a magneto-mechanical solution that is acceptable in terms of dissipated power and mechanical vibrations. One of the problems that can occur in a newly designed MRI scanner is that the frequency of excitation may coincide with the natural frequencies of certain in-built mechanical components, leading to a resonant system exhibiting large displacements. Resonance is defined as the amplification phenomenon observed when the frequency of a periodically applied force agrees with the natural frequency of the system on which it acts [15].

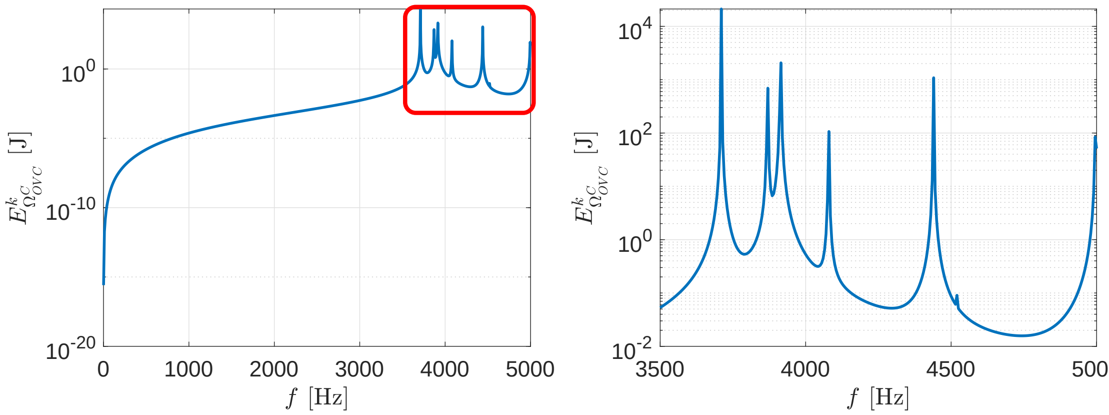

Figure 1.4: Frequency sweep study displaying mechanical resonance in the vicinity of the natural frequencies of the OVC radiation shield. Right figure shows a zoomed view in the resonance region (red rectangle).

This type of study is presented in Figure 1.4, where a particular MRI geometry is studied for a range of excitation frequencies $f \in (0, 5000]$ Hz and the kinetic energy, which is directly related to the mechanical displacements, is computed from the numerical solution. From these results it is easy to understand that an increase of three or four orders of magnitude in kinetic energy would not be acceptable and would compromise the integrity of the device and, therefore, the MRI scanner operating frequencies should not coincide with the resonant ones (or at least damped via appropriate dissipative mechanisms).

---

[2] Note that the AC coils are not necessarily excited harmonically at a single frequency, although general current signals can always be decomposed into its constituent frequencies.

Helium boil off

As mentioned previously in this chapter, the superconducting main coils are refrigerated with liquid helium in order to preserve their superconducting properties [7]. However, a common problem when operating an MRI scanner for large periods of time is that the transient magnetic field, induce eddy currents leading to mechanical vibrations in the helium vessel, which is translated into inducted heat and, thus, increase in temperature. Since the helium's boiling point is slightly higher than 4 K (-296 °C), exceeding this operating temperature implies that the helium will start to boil off and escape the device through a safety valve [16], see Figure 1.5. The main two issues associated with this phenomenon are, first, the fact that the MRI scanner may be inoperative until the device cools down and the helium is refilled and, secondly, the economic implication as each MRI scanner needs of the order of thousands of litres of helium [10]. This can translate into a considerable amount of money (Siemens Healthineers estimates around £20,000) if the entire volume of helium needs to be replaced.

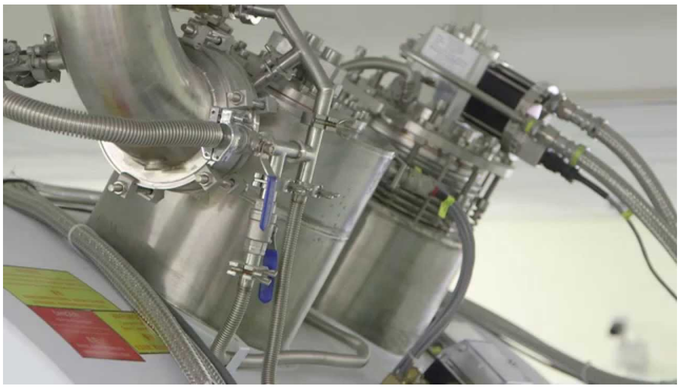

Figure 1.5: Helium safety valve for a small animal 1.5 T MRI scanner. Courtesy of Hallmarq Veterinary Imaging.

Shimming process

The importance of producing a homogeneous background DC magnetic field (for quality imaging purposes) has been motivated throughout this chapter and some factors that could potentially alter this, such as eddy currents, motion from the patient and vibrations of the mechanical components, have been already presented.

The standard practice when installing a new scanner for a client is to use shim coils on-site in order to rectify any inhomogeneities originated by ferromagnetic materials near the location of the device [7]. Therefore, the shimming process [17] consists on determining the exact location of the shim coils, see yellow arrows in Figure 1.6, which are electromagnets mounted on the ends of the main magnet bore, in order to cancel the exterior perturbations and preserve the homogeneity in the magnetic field, seeking to ultimately increase the image quality [7].

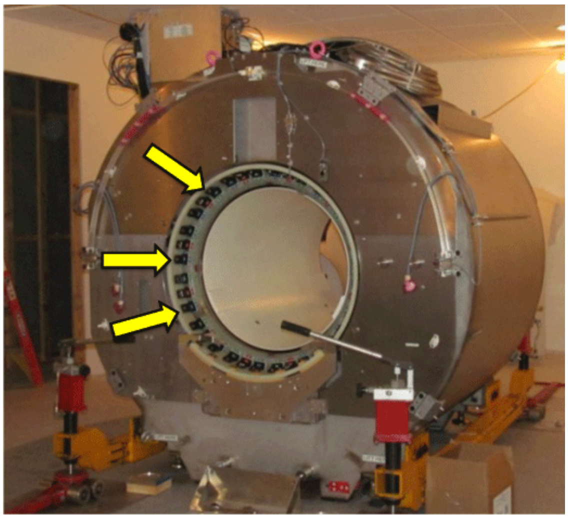

Figure 1.6: Shim elements (yellow arrows) mounted in an MRI scanner. Image taken from http://mriquestions.com/passive-shimming.html on 29/11/2019.

1.1.3 Design stage bottleneck

Latest developments in MRI scanners show how manufacturers have oriented their research towards the design and manufacturing of high-strength MRI equipment, with in-built high resolution, capable of dramatically enhance the ability of clinicians to diagnose tumours and rare illnesses [18]. Yet, according to Siemens Healthineers, one of the bottlenecks when manufacturing a new MRI scanner, such as the recent ultra high-field 7 T magnet, is the computational effort required during the design phase, which is still far from being an automatised process. Indeed, "*...the magnet was four years in the making, two of which were spent in scientific research...*" according to their design lead team [19].

A crucial part of the design stage involves the simulation of a large number of electro-magneto-mechanical problems with slight variations in the geometry and/or material parameters. The design stage can thus become very time consuming, which eventually is translated into an overall manufacturing cost increase. Reduced Order Modelling (ROM) techniques have recently gained momentum to help speed up the design optimisation process. ROM can be used in order to construct computational metamodels capable of interacting with the user in real time via multi-parametric approximations of the so-called full order solution [20]. Crucially, these multi-parametric approximations must be carefully obtained in order to avoid the well-known curse of dimensionality [21], present when attempting to solve higher-dimensional (i.e. 4D, 5D) problems through standard discretisation techniques (i.e. Finite Element Method (FEM)). An additional benefit of ROM is the speed of interaction with the user during the online stage, facilitating real time multiple-query optimisation. In this case, the computational effort lies on the marginal cost of another input-output evaluation and an increased precomputation cost is acceptable [22].

1.2 Coupled magneto-mechanics

As mentioned in Section 1.1, the main focus of this thesis is the study of the gradient coil interaction within an MRI scanner. This type of problem is modelled by Siemens Healthineers using the two main acting physics: electromagnetics and mechanics. It is now well established, from the computational modelling viewpoint, how to independently solve either of them. For instance, for high frequency problems, the displacement currents in Maxwell's equations dominate over the Ohmic currents [23]; but, when considering low frequency signals interacting with highly conducting bodies, the eddy current approximation [24–27] can be applied, which is the case of the conducting shields in an MRI scanner. In the context of mechanics, the small deformations assumption for these conducting components is considered to be valid and the theory of linear elasticity to hold [28]. However, the coupling or interaction between both physics introduce extra complexities from the modelling standpoint. First, the interaction of a transient magnetic field with conducting components generates eddy currents, which propagate and translate into undesirable deformations and vibrations. These vibrations can, in turn, perturb the surrounding magnetic field. This feedback mechanism between (*i*) transient magnetic fields, (*ii*) eddy currents and (*iii*) mechanical vibrations, results in a fully nonlinear electro-magneto-mechanical problem [10]. This complex coupled effect can yield imaging artefacts [29, 30] as well as disconcerting mechanical vibrations [31], which overall decrease the imaging quality and the lifespan of the MRI scanning equipment, see Section 1.1.2.[3] The computational modelling of this problem has been the subject of study of some authors. In [34, 35] a low order space-time finite element scheme for the solution of three-dimensional magneto-mechanical problems was presented. In previous work [32, 33, 36] and in search of highly accurate computations, a high order *hp*-finite element software was developed for axisymmetric configurations in conjunction with a stress tensor formulation and a novel linearised approach using an AC-DC splitting, which allows for its time harmonic solution in the frequency domain.

---

[3] Note that the consideration of the acoustics phenomenon has been neglected in this study. The interested reader is referred to previous works [32, 33] for all the necessary details of a fully coupled acousto-electro-magneto-mechanical problem.

1.3 Reduced Order Modelling

The dramatic increase in computational power over the last few decades and the development of numerical techniques and algorithms for solving large systems of algebraic equations have dramatically increased the number and the size of the problems that can be solved numerically. In the early stages of computational mechanics (1960s and 1970s), problems were often solved by constructing special basis functions [37], whereas nowadays refined discretisation techniques give excellent numerical results for large scale problems that could not be considered in the past due to the lack of sufficient computational resources [37].

Despite advancements in computational power, there is still a large number of problems that are not feasible to solve with a full order model approach [21], i.e. via standard discretisation techniques such as finite differences, finite volumes or finite elements. This could be due to the need to consider solutions in a high-dimensional space, for instance optimisation problems, which suffer from the curse of dimensionality: an exponential increase of the numerical complexity of the problem when considering a higher number of dimensions [21]. Moreover, another recent key demand that cannot be dealt with by a full order model approach is the need to be able to compute solutions in real time, typical of online control, optimisation and augmented reality problems, where multiple input-output evaluations are required in a very fast fashion [38].

Reduced Order Modelling (ROM) techniques were first introduced towards the end of the last century with Moore [39] and Pearson [40] among others, presenting simpler (reduced) solution basis that could accurately represent a more complex model. Another ROM approach is the so-called operational model order reduction [37], which focuses on using physical insight in order to reduce the model complexity. As examples, the authors in [41] split the blood flow system in small arteries, in which a one-dimensional flow is assumed, and large arteries, where two-dimensional models are applied. Also, within the scope of this thesis, the simplification of the Maxwell equations to the eddy currents model for relatively small frequencies [24, 27] can be understood as an operational model order reduction. Having said that, in many cases, the simplification of the model is not considered accurate enough or simply not possible at all [21]. In these cases, the automatic identification of simplifications has to be carried out by the reduced order modelling technique considered.

The calculations performed in ROM methods are often divided in two stages: offline and online [21, 38, 42]. The offline stage consists in extracting the main information from the problem, for instance, by means of the computation of a reduced basis. In contrast, the online stage uses the stored information of the previous stage to compute a real-time multi-parametric solution and will differ depending on the ROM method considered. For example, to compute solutions in the online stage could consist in solving a reduced (smaller) system of equations, that are considerably more efficient to solve than the full order model in terms of computational cost. The majority of ROM techniques can be understood as *a posteriori* methods [21, 38, 43, 44], where some *a priori* knowledge of the solution or the behaviour of the problem is known. However, in industrially relevant problems, that is often difficult to achieve and, thus, a key feature that industry seeks is the *a priori* nature of a ROM technique, where all the calculations are carried out without actually computing the solution of the problem at hand. In MRI scanner design, this is clear, as new MRI configurations are continuously tested with very different system responses. Therefore, the next two sections will focus on describing two different methods for each of the families mentioned above; *a posteriori* Proper Orthogonal Decomposition (POD) and *a priori* Proper Generalised Decomposition (PGD) methods.

1.3.1 *A posteriori* Proper Orthogonal Decomposition method

As mentioned and motivated in the previous section, the scope of this thesis focusses on *a priori* ROM techniques. However, some studies in this thesis will be conducted comparing both POD and PGD methods against the full order model. As such, this section will briefly present some key contributions as part of the state of the art of the POD technique.

The POD method was first introduced in [40] by Pearson in the field of data representation and it has been developed over the recent years under several names, such as Karhunen-Loeve Decomposition (KLD), Principal Component Analyses (PCA) and Singular Value Decomposition (SVD) [45]. The POD technique provides an ordered orthogonal truncated basis for a given set of data or numerical experiments [46] which, in the computational mechanics field, are usually referred to as snapshots of the full order model [47]. This method is often preferred due to its known optimality when separating the dimensions of the problem, meaning that there is no other basis which can give a better approximation, see [37, 46]. Note, however, that its optimality and orthogonality may be compromised when separating more than two dimensions and the High-Order SVD is in this case required [48].

The main goal of the POD method is to find the optimal set of basis given a high-dimensional set of data in order to reproduce it in a lower dimensional space [49]. With this aim, the offline POD stage consists in: (i) generation of a set of snapshots[4] that represent the behaviour of the problem within the parameter range considered, (ii) computation of the optimal basis though an SVD analysis of the generated data. The online POD stage uses the precomputed basis to (i) interpolate or project the parametric modes, known as interpolation [51] and projection [52] based POD, respectively and (ii) solve a reduced system of equations to obtain the numerical solution of the problem with the desired parameter combination. The advantages of the POD method is the non-intrusive nature of the technique, since it can be understood as a posteriori operation from the selected snapshots and, thus, it can be built wrapped around an existing piece of software. However, one of the main drawbacks is the fact that the accuracy of the POD technique is strongly dependent on the quality of the snapshots selected. To address this issue, the authors in [53,54] present a method that automatically selects the snapshots in order to maximise the information contained in the high-dimensional data set. Moreover, it is known that the computational cost related to the process of computing the POD basis is potentially very high [55]. Finally, it can be noticed that the online POD stage requires the solution of a reduced system of equations, which prevents from obtaining the desired output in real time.

---

[4] Usually known as the method of snapshots [50], these snapshots are obtained from running the full order model for the different parameters of interest.

The POD methodology has been applied to an extensive number of fields, such as transient thermal analysis [56], turbulent fluid flows [57], structural dynamics [58], signal processing and control theory [59], damage detection [60], human face recognition [61] and unsteady aerodynamics [62]. In the context of this thesis, the POD has been recently applied to coupled magneto-mechanical problems using a combined ROM-full order model approach, where a reduced basis is constructed for the electromagnetic problem and the mechanical problem is solved used the full order model, see [49]. This technique will be compared against the PGD method in Chapter 5 and it is briefly described in Appendix A for completeness. However, the reader is referred to the aforementioned publication for a full detailed description of the methodology.

1.3.2 *A priori* Proper Generalised Decomposition method

The need to develop *a priori* ROM methods, without relying on the knowledge of the solution of the problem [38], was stated in [43,63] in 2006. The core idea of the PGD method was presented by Chinesta et al., see [64,65], in order to find a space-time separated representation. The PGD methodology has been successfully implemented in numerous applications, such as Helmholtz based problems [42,66], solid mechanics [67], power distribution systems [68], flow problems [69–71], thermal problems [72,73], degenerated 3D domains such as plates and shells [74] and also in geometrical parametrisations of heat based problems [75].

This novel *a priori* ROM methodology can be understood as a multidimensional solver that is capable of incorporating extra parameters in a high-dimensional solution. Whereas the full order model approach usually considers space and time as the only dimensions of the problem, the PGD method allows to introduce boundary conditions, initial conditions, geometrical parameters and material parameters as extra coordinates of the problem [38], avoiding the curse of dimensionality.

The PGD technique can be briefly described in three steps; first, the solution field is assumed to be approximable by a separable function, which can be expressed as a finite summation of modes. Note that, although the same principle applies to POD method, in the PGD method, the separable function is computed *a priori* and, therefore, PGD can be understood as a generalisation of POD [76]. The second step consists in a Greedy algorithm [21] that enriches the solution by modal addition. Finally, for each PGD mode, the separable functions are computed using an alternating directions fixed-point algorithm [21]. In the PGD community, these computations are referred as the offline stage, where the high-dimensional separable approximation is obtained. Then, the online stage requires only a simple evaluation (particularisation) of the precomputed offline solution for the desired set of parameter values [21].

Differently from the *a posteriori* POD method, see Section 1.3.1, the PGD technique does not rely on the computation of several key snapshots that appropriately represent the problem at hand. However, the PGD accuracy will be determined by the degree of separability of the solution, since a separable expression is assumed for the solution variables. One drawback of this *a priori* technique is that it is potentially very intrusive, although some recent works, for instance [71], have focused on developing non-intrusive PGD implementations.

In the context of MRI scanner design, the PGD approach is of the utmost interest for Siemens Healthineers due to the PGD capability of efficiently dealing with multiple-query input/output evaluations during the online stage, where several MRI designs could be tested in real-time even in portable devices [44]. Moreover, another feature that is very appealing in the industry environment is the encapsulation of all numerical computations and technicalities in the offline stage, whereas the online stage can be used by non-expert users in order to obtain accurate numerical solutions in real time.

1.4 Objectives

Section 1.1.2 has motivated the need for computational simulation in the context of MRI scanner design. Additionally, Section 1.3 has presented the urgent need for the optimisation of the large number of numerical simulations performed during the design stage of a certain novel MRI configuration and how ROM could be of great use for the industrial partner of this project, Siemens Healthineers, in order to obtain fast numerical solutions without compromising the accuracy. Consequently, the main goal of this thesis is the development of a robust PGD framework for coupled magneto-mechanical problems, working towards the optimisation of the design stage of MRI scanners. This goal will be reached through the successful completion of the following objectives:

1. "*To develop a coupled magneto-mechanical formulation in a Lagrangian setting from an existing axisymmetric finite element framework*".
2. "*To develop a frequency-based PGD formulation for coupled magneto-mechanical problems*".
3. "*To propose a regularised-adaptive strategy in order to increase the PGD accuracy and robustness*".

4. "*To develop a graphical user interface for the online PGD stage that can be used in the industry environment*".
5. "*To extend the frequency-based PGD formulation to a higher-dimensional problem including now material parameters*".
6. "*To exploit the staggered nature of the coupled problem at hand*".
7. "*To assess and compare the a priori PGD and the a posteriori POD methods against the full order model*".
8. "*To include geometrical changes in the computational domain within the developed PGD framework*".

Each one of these objectives will be considered and discussed in the different chapters of this thesis.

1.5 Thesis structure

The content of this thesis is structured in seven chapters, which will address the objectives stated in Section 1.4. This section presents a brief outline of each chapter as follows:

- ***Chapter 2: Full order model.*** Presentation of the coupled-magneto mechanical problem in a Lagrangian setting. The fully non-linear coupled system is presented together with a set of numerical considerations that allow to derive the linearised time-harmonic problem under the axisymmetric assumption, which will be discretised in the context of the Finite Element Method (FEM). Moreover, two relevant MRI scanner configurations proposed by Siemens Healthineers will be fully described and a set of numerical results will be presented in order to motivate the difficulties and challenges mentioned in Chapter 1 and to better understand the problem at hand.
- ***Chapter 3: General PGD formulation.*** Description of a general PGD framework in a high-dimensional space that includes the axisymmetric two-dimensional (r, z) space and a d-dimensional parametric space, which in later chapters will be particularised for several material and geometric parameters of interest for industry. The work flow of both the offline and online PGD stages are graphically described by means of comprehensive flow charts. In addition, some important considerations on how to include non-homogeneous Dirichlet boundary conditions, scaling of the PGD modes and the convergence criteria are also presented.
- ***Chapter 4: Monolithic frequency-based PGD technique.*** Particularisation of the general PGD formulation in Chapter 3 for a parametric domain that includes the external excitation frequency and its application to the

coupled magneto-mechanical problem, see Chapter 2. A regularised-adaptive strategy that enhances the accuracy and robustness of the method is proposed. Moreover, a Graphical User Interface (GUI) will be briefly presented in order to show the potential of the online PGD stage.

- ***Chapter 5: Staggered high-dimensional PGD technique.*** Extension of the frequency-based PGD approach proposed in Chapter 4 to a higher parametric domain that now includes not only the frequency of excitation but also the electrical conductivity of the radiation shields and the strength of the static magnetic field. The staggered approach will be shown to be more efficient in terms of computational cost but also in accuracy terms with respect to the monolithic approach, in the sense that a more accurate solution is obtained for the same amount of PGD modes. A comparison on the electromagnetic solution will be performed between the *a posteriori* POD and the *a priori* PGD methods.

- ***Chapter 6: Integration of geometric parameters into the PGD methodology.*** This chapter will first present a study on how the solution of the coupled magneto-mechanical problem evolve when modifying the thickness of the conducting shields, which will highlight a highly non-linear response behaviour of the high resonant modes. Then, a collocation PGD-projection strategy will be proposed in order to incorporate geometrical changes in the computational domain, balancing efficiency and accuracy, and allowing to obtain separable expressions for the integrated quantities of interest that can then be efficiently queried in real time for different material and geometric parameter combinations.

–*Appendices*–

- ***Appendix A: EM-POD methodology.*** Two-dimensional adaptation of the EM-POD formulation developed in [49]. This formulation is presented in an appendix for completeness and to be consistent with the notation throughout the entire thesis, although the reader is referred to the aforementioned reference for a thorough presentation of the technique.

- ***Appendix B: One-dimensional mortar integral treatment.*** Brief description of the numerical implementation performed in order to deal with non-matching one-dimensional meshes. This challenge rises when exploiting the staggered nature of the equations as shown in Chapter 5.

- ***Appendix C: Efficient computation of integrated quantities.*** Description of the treatment carried out at implementation level in order to efficiently integrate the quantities of interest for industry. This treatment is shown for both the full order model and the PGD method.

- ***Appendix D: Sensitivity maps.*** Computation of sensitivity maps (response surfaces) with respect to a certain parameter of the precomputed high-dimensional PGD solution.

- ***Appendix E: GUI for the online PGD stage and code description.*** Presentation of the developed GUI in order to show the potential of the online PGD stage. A description is also provided with the main stages required in order to compute a numerical solution of the coupled magneto-mechanical problem with both the full order model and the PGD technique.

1.6 Scientific contributions

The research outcomes of the work carried out during this thesis regarding journal publications, conference presentations and research posters are listed in this section.

1.6.1 Journal publications

- **G. Barroso**, A.J. Gil, P.D. Ledger, M. Mallett and A. Huerta, "A regularised-adaptive Proper Generalised Decomposition implementation for coupled magneto-mechanical problems with application to MRI scanners", *Computer Methods in Applied Mechanics and Engineering*, vol. 358, p.112640, 2020.

- **G. Barroso**, M. Seoane, A.J. Gil, P.D. Ledger, M. Mallett, A. Huerta, "A staggered high-dimensional Proper Generalised Decomposition for coupled magneto-mechanical problems with application to MRI scanners", *Computer Methods in Applied Mechanics and Engineering.* Submitted, September 2019.

- **G. Barroso**, A.J. Gil, S. Zlotnik P.D. Ledger, M. Mallett, A. Huerta, "Integration of geometric parameters into a PGD methodology for MRI scanner design". In preparation.

1.6.2 Conference presentations

- **G. Barroso**, S. Bagwell, A.J. Gil, P.D. Ledger, M. Mallett, A. Huerta, "Towards a reduced order modelling approach for coupled acousto-magneto-mechanical problems with application to MRI scanners", *International Conference on Adaptive Modelling and Simulation (ADMOS). ECCOMAS thematic conference*, Verbania, Italy, June 2017.

- **G. Barroso**, L. Borchini, R. Ibáñez, R. Mena, G. Quaranta, M. Seoane Chouciño, V. Tsiolakis, S. Vermiglio, M. Giacomini, "Empowered decision-making in simulation-based engineering: Advanced Model Reduction for real-time, inverse and optimisation in industrial problems", *ECCM-ECFD. ECCOMAS joint conference*, Glasgow, UK, June 2018.

- **G. Barroso**, A.J. Gil, P.D. Ledger, M. Mallett, A. Huerta, “Towards a reduced order modelling approach for coupled magneto-mechanical problems with application to MRI scanners”, *ECCM-ECFD. ECCOMAS joint conference*, Glasgow, UK, June 2018.
- **G. Barroso**, A.J. Gil, P.D. Ledger, M. Mallett, A. Huerta, “Proper Generalised Decomposition for coupled magneto-mechanical problems with application to MRI scanners”, *International Conference on Adaptive Modelling and Simulation (ADMOS). ECCOMAS thematic conference*, Alicante, Spain, May 2019.

1.6.3 Research posters

- S. Bagwell, P.D. Ledger, A.J. Gil, **G. Barroso**, M. Seoane, M. Kruip, M. Mallett, “Acousto-Magneto-Mechanical simulation using *hp* finite elements for MRI scanner design”, *SIAM/UKIE Annual Conference*, Glasgow, UK, 2017.
- **G. Barroso**, S. Bagwell, A.J. Gil, P.D. Ledger, M. Mallett, “Towards a reduced order modelling approach for coupled acousto-magneto-mechanical problems with application to MRI scanners”, *International Conference on Adaptive Modelling and Simulation (ADMOS). ECCOMAS thematic conference*, Verbania, Italy, 2017.
- **G. Barroso**, A.J. Gil, P.D. Ledger, M. Mallett, “Towards a reduced order modelling approach for coupled acousto-magneto-mechanical problems with application to MRI scanners”, *ZCCE Postgraduate Student Workshop*, Swansea, UK, 2018.
- **G. Barroso**, A.J. Gil, P.D. Ledger, M. Mallett, “Towards a reduced order modelling approach for coupled acousto-magneto-mechanical problems with application to MRI scanners”, *Workshop on Numerical Methods in Applied Sciences and Engineering*, Barcelona, Spain, 2018.
- **G. Barroso**, A.J. Gil, P.D. Ledger, M. Mallett, “Proper Generalised Decomposition for coupled acousto-magneto-mechanical problems with application to MRI scanners”, *ZCCE Postgraduate Student Workshop*, Swansea, UK, 2019.

Chapter 2

Full order model

2.1 Introduction

This chapter aims to briefly present the Finite Element Method (FEM) formulation for the coupled MRI magneto-mechanical problem in a Lagrangian setting, in which ROM techniques will be developed, implemented and assessed. This FEM formulation can be understood as the "direct problem", known as the "full order model" in the ROM community. The content of this chapter aligns with the objective "*To develop a coupled magneto-mechanical formulation in a Lagrangian setting from an existing axisymmetric finite element framework*".

The equations governing the two physics considered, namely electromagnetics and mechanics, will be presented. A Eulerian formulation for coupled magneto-mechanics in the context of MRI scanners was recently developed in [32, 33, 36] and it will be here adapted to a Lagrangian setting. A set of numerical considerations and assumptions will be applied to the aforementioned equations, such as the linearisation of the transient problem, introducing the frequency domain and the axisymmetric approach. The finite element discretisation will be briefly described in order to show the system of equations that are actually solved. Finally, the last section of this chapter will introduce two industrially relevant MRI configurations that will be used throughout the entire thesis; the test magnet and the full magnet. A thorough description of the two problems will be complemented with a set of numerical results in order to motivate and discuss the difficulties of solving the coupled magneto-mechanical problem as presented in Chapter 1.

2.2 Coupled magneto-mechanical problem

In the presence of moving components (within a computational electromagnetic domain), it is customary to establish a reference position $\boldsymbol{X}$ and a time-dependent ($t \in [0, T]$) mapping $\boldsymbol{\phi}$ that links this reference state to the current position $\boldsymbol{x} = \boldsymbol{\phi}(\boldsymbol{X}, t)$. Adopting a Lagrangian viewpoint [77], the Lagrangian electromagnetic fields $\boldsymbol{H}_0$, $\boldsymbol{E}_0$ and $\boldsymbol{B}_0$ are used, which denote the magnetic field intensity, the electric field intensity and the magnetic flux density, respectively. In addition, the following considerations are made: (1) both the eddy current approximation and the constitutive laws for electromagnetics are applied in the Eulerian setting and, then, the simplified Maxwell equations are transformed to the Lagrangian description; (2) for small displacements $\boldsymbol{u}$ (although not necessarily small velocities or accelerations), Total and Updated Lagrangian descriptions coincide; (3) a vector potential formulation $\boldsymbol{A}$ is used where the gauging of the electromagnetic problem is applied to the already Lagrangian eddy current model; (4) the Cauchy stress tensor is comprised of a mechanical $\boldsymbol{\sigma}^m(\boldsymbol{u})$ and an electromagnetic interaction Maxwell stress component $\boldsymbol{\sigma}^e(\boldsymbol{A})$ defined in terms of $\boldsymbol{B}_0$.

Consequently, in the context of MRI scanners, the non-linear coupled magneto-mechanical problem, see Figure 2.1, is formulated in a Lagrangian setting with the magnetic vector potential $\boldsymbol{A}$ and the mechanical displacements $\boldsymbol{u}$ as solution variables. Thus, the governing equations can be summarised in strong form as follows: Find $(\boldsymbol{A}, \boldsymbol{u})(t) \in (\mathbb{R}^3 \times \Omega^C)[0, T]$ such that

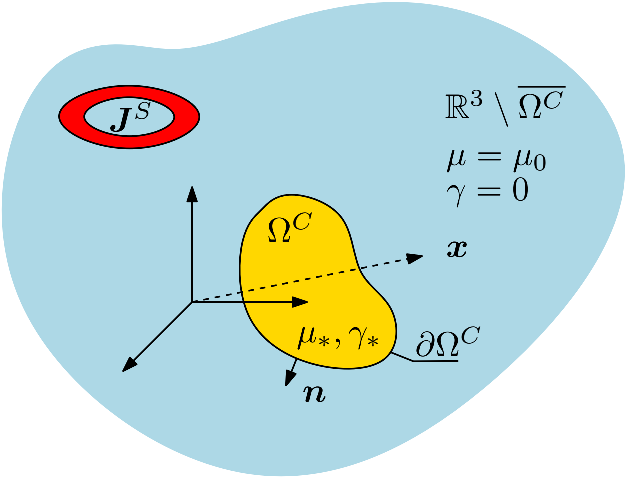

Figure 2.1: Description of a general magneto-mechanic problem; conducting component Ω^C (with magnetic permeability $\mu = \mu_*$ and electrical conductivity $\gamma = \gamma_*$) in a non-conducting three dimensional space $\mathbb{R}^3 \setminus \overline{\Omega^C}$ (with $\mu = \mu_0$ and $\gamma = 0$). Problem excited by a current source $\boldsymbol{J}^S$ acting in a series of coils.

$$\operatorname{curl}(\mu^{-1} \operatorname{curl} \boldsymbol{A}) + \gamma \frac{d\boldsymbol{A}}{dt} = \boldsymbol{J}^S \qquad \text{in } \mathbb{R}^3, \tag{2.1a}$$

$$\operatorname{div} \boldsymbol{A} = 0 \qquad \text{in } \mathbb{R}^3 \setminus \overline{\Omega^C}, \tag{2.1b}$$

$$\operatorname{div}(\boldsymbol{\sigma}^m(\boldsymbol{u}) + \boldsymbol{\sigma}^e(\boldsymbol{A})) = \rho \frac{d^2\boldsymbol{u}}{dt^2} \qquad \text{in } \Omega^C, \tag{2.1c}$$

$$\boldsymbol{A} = O\big(|\boldsymbol{x}|^{-1}\big) \qquad \text{as } |\boldsymbol{x}| \to \infty, \tag{2.1d}$$

$$\boldsymbol{u} = \boldsymbol{u}_D \qquad \text{on } \partial\Omega^C_D, \tag{2.1e}$$

$$\boldsymbol{n} \times [\boldsymbol{A}]_{\partial\Omega^C} = \boldsymbol{0} \qquad \text{on } \partial\Omega^C, \tag{2.1f}$$

$$\boldsymbol{n} \times [\mu^{-1} \operatorname{curl} \boldsymbol{A}]_{\partial\Omega^C} = \boldsymbol{0} \qquad \text{on } \partial\Omega^C, \tag{2.1g}$$

$$\big(\boldsymbol{\sigma}^m(\boldsymbol{u}) + \boldsymbol{\sigma}^e(\boldsymbol{A})\big)\big|^-_{\partial\Omega^C}\boldsymbol{n} = \boldsymbol{\sigma}^e(\boldsymbol{A})\big|^+_{\partial\Omega^C}\boldsymbol{n} \qquad \text{on } \partial\Omega^C, \tag{2.1h}$$

$$\boldsymbol{A}|_{t=0} = \boldsymbol{0} \qquad \text{in } \mathbb{R}^3, \tag{2.1i}$$

$$\boldsymbol{u}|_{t=0} = \left.\frac{d\boldsymbol{u}}{dt}\right|_{t=0} = \boldsymbol{0} \qquad \text{in } \Omega^C, \tag{2.1j}$$

where μ, γ and ρ are the magnetic permeability, the electrical conductivity and the material density, respectively. The problem is excited by a current source $\boldsymbol{J}^S$ acting on the coils, $\boldsymbol{x}$ represents the position vector and $\boldsymbol{n}$ is the outward normal vector (pointing from the conducting to the non-conducting side). Note that $\overline{\Omega^C} := \Omega^C \cup \partial\Omega^C$ and thus the overline denotes the closure of Ω^C.[1] Note that $\frac{d}{dt}$ represents the total or material derivative. The Cauchy and Maxwell stress tensors are defined as

$$\boldsymbol{\sigma}^m(\boldsymbol{u}) : = \boldsymbol{\mathcal{C}} : \boldsymbol{\varepsilon}(\boldsymbol{u}) \qquad \text{in } \Omega^C, \tag{2.2a}$$

$$\boldsymbol{\sigma}^e(\boldsymbol{A}) : = \mu^{-1}\Big((\operatorname{curl}\boldsymbol{A}) \otimes (\operatorname{curl}\boldsymbol{A}) - \frac{1}{2}|\operatorname{curl}\boldsymbol{A}|^2\boldsymbol{I}\Big) \qquad \text{in } \Omega^C, \tag{2.2b}$$

where $\boldsymbol{\varepsilon} := \big(\nabla\boldsymbol{u} + (\nabla\boldsymbol{u})^T\big)/2$ is the small strain tensor, $\boldsymbol{I}$ denotes the second order identity tensor and $\boldsymbol{\mathcal{C}}$ is the fourth other elasticity tensor that depends on the Young's modulus E and the Poisson's ratio ν as:[2]

$$\boldsymbol{\mathcal{C}} = \frac{1}{E}\begin{bmatrix} 1 & -\nu & -\nu & 0 & 0 & 0 \\ -\nu & 1 & -\nu & 0 & 0 & 0 \\ -\nu & -\nu & 1 & 0 & 0 & 0 \\ 0 & 0 & 0 & 2+2\nu & 0 & 0 \\ 0 & 0 & 0 & 0 & 2+2\nu & 0 \\ 0 & 0 & 0 & 0 & 0 & 2+2\nu \end{bmatrix}. \tag{2.3}$$

The electromagnetic problem is defined by the eddy current approximation (2.1a)-(2.1b) of the general Maxwell's equations, where the $\boldsymbol{A}$-based formulation [27] is used to define the magnetic flux density $\boldsymbol{B}_0$ as $\boldsymbol{B}_0 = \operatorname{curl}\boldsymbol{A}$. The behaviour of the embedded mechanical conducting components is described by the conservation of linear momentum (2.1c). The decay of the vector potential (2.1d), the imposed Dirichlet boundary conditions (2.1e), the interface conditions (2.1f)-(2.1h) and the set of initial conditions (2.1i)-(2.1j) are also defined to completely describe the problem. Once (2.1) is solved, the Eulerian quantities, electric field intensity $\boldsymbol{E}$ and magnetic field intensity $\boldsymbol{H}$, are recovered as[3]

$$\boldsymbol{E} = -\frac{d\boldsymbol{A}}{dt} + \boldsymbol{B}_0 \times \frac{d\boldsymbol{u}}{dt} \qquad \text{in } \Omega^C, \tag{2.4a}$$

$$\boldsymbol{H} = \mu^{-1}\boldsymbol{B}_0 = \mu^{-1}\operatorname{curl}\boldsymbol{A} \qquad \text{in } \mathbb{R}^3. \tag{2.4b}$$

---

[1] The overline is also used later in this thesis to denote the complex conjugate where no confusion arises.

[2] Note that this is the expression of $\boldsymbol{\mathcal{C}}$ for an elastic isotropic material, where the small strain tensor has been vectorised as $\boldsymbol{\varepsilon} = [\varepsilon_{11}, \varepsilon_{22}, \varepsilon_{33}, 2\varepsilon_{23}, 2\varepsilon_{13}, 2\varepsilon_{12}]$.

[3] $\boldsymbol{H} = \boldsymbol{H}_0$ is assumed due to low electric permittivities [78].

Note that the Lagrangian formulation presented in (2.1) allows the problem to be solved in a staggered manner.f This fact offers clear computational advantages with respect to the Eulerian approach [32, 33, 36] as it will discussed in this thesis. Also, note that when formulating this magneto-mechanical problem in a Lagrangian setting, the magneto-mechanical coupling does no longer appear in the electromagnetic equation as the so-called Lorentz forces, but it does appear as an extra term when recovering the electric field intensity $\boldsymbol{E}$, see (2.4).

2.3 Numerical treatment

This section contains the numerical considerations that will be applied to the coupled magneto-mechanical problem presented in Section 2.2. The reader is referred to [32, 33, 36] for a detailed description of the numerical treatment of the problem, although it is briefly described in this section for completeness. First, a linearisation of the non-linear equations about the static (DC) problem is performed. Then, taking advantage of the linearised problem, the time-harmonic assumption is introduced in order to numerically solve the magneto-mechanical equations in the frequency domain.

2.3.1 Linearisation approach

In Section 2.2, the non-linear transient problem of interest has been presented. The functioning of an MRI scanner can be divided into two main current sources, a strong static (DC) magnetic field and superimposed smaller time-dependent (AC) magnetic fields, as detailed in Section 1.1.1. Taking advantage of this fact, a linearisation of the governing equations about the static problem is advocated in [79–83] in order to obtain a linearised transient problem. Previous works [10, 33] have focused on the derivation, assessment and validation of this alternative approach with respect to solving the full non-linear transient problem, obtaining excellent results in the specific context of MRI scanners by significantly reducing the computational requirements while maintaining the same level of accuracy. The main reason for that is the fact that the static DC current source $\boldsymbol{J}^{DC}$ is several orders of magnitude stronger than the time-dependent AC current source $\boldsymbol{J}^{AC}$, leading to a problem where the mean value is driven by $\boldsymbol{J}^{DC}$ with some transient variations given by $\boldsymbol{J}^{AC}$. Hence, the total current source is written as

$$\boldsymbol{J}^{S}(t) = \boldsymbol{J}^{DC} + \boldsymbol{J}^{AC}(t). \tag{2.5}$$

As presented in Figure 2.2, the static current source $\boldsymbol{J}^{DC}$ excites the initial state to compute the non-linear static problem, which will be the initial state excited through the dynamic current source $\boldsymbol{J}^{AC}(t)$, obtaining the solution of the linearised transient problem. Once both problems are solved, the complete transient solutions fields are recovered as

$$\boldsymbol{A}(t) = \boldsymbol{A}^{DC} + \boldsymbol{A}^{AC}(t), \tag{2.6a}$$

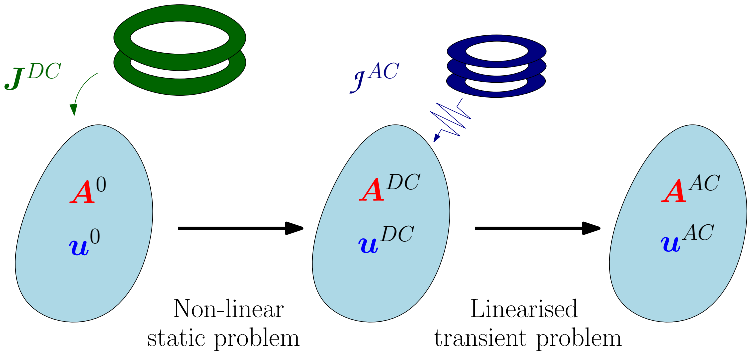

Figure 2.2: Linearisation process; initial state excited through static current source $\boldsymbol{J}^{DC}$. Solution of static problem is used as the initial state for the transient problem with time-harmonic current source $\boldsymbol{\mathcal{J}}^{AC}$.

$$\boldsymbol{u}(t) = \boldsymbol{u}^{DC} + \boldsymbol{u}^{AC}(t). \tag{2.6b}$$

2.3.2 Time-harmonic formulation

From the linearisation briefly presented in Section 2.3.1 it is clearly seen how the only time-dependent quantities are contained in the linearised transient AC problem. Due to its linear behaviour, a time-harmonic formulation can now be introduced in order to solve for the angular frequency ω of excitation. As mentioned in Section 1.1.2, although the gradient coils emit non-harmonic electromagnetic pulses, these can be decomposed into the different frequency modes using a Fourier transform, see [10]. The time-harmonic problem can then be solved for each of these frequencies and the transient solution recovered from the time-harmonic solutions. Therefore, the time-harmonic representation of the time-dependent fields is introduced by rewriting them in terms of a single angular frequency as follows

$$\boldsymbol{A}^{AC}(t) \to \boldsymbol{\mathcal{A}}^{AC} e^{\mathrm{i}\omega t}, \tag{2.7a}$$
$$\boldsymbol{u}^{AC}(t) \to \boldsymbol{\mathcal{U}}^{AC} e^{\mathrm{i}\omega t}, \tag{2.7b}$$
$$\boldsymbol{J}^{AC}(t) \to \boldsymbol{\mathcal{J}}^{AC} e^{\mathrm{i}\omega t}, \tag{2.7c}$$

where $\mathrm{i} := \sqrt{-1}$. Note that $\boldsymbol{\mathcal{A}}^{AC}$, $\boldsymbol{\mathcal{U}}^{AC}$ and $\boldsymbol{\mathcal{J}}^{AC}$ refer to the complex amplitudes of their respective time-dependent fields. Having presented this, the complete transient solutions fields are now computed as

$$\boldsymbol{A}(t) = \boldsymbol{A}^{DC} + \mathrm{Re}\left(\boldsymbol{\mathcal{A}}^{AC} e^{\mathrm{i}\omega t}\right), \tag{2.8a}$$
$$\boldsymbol{u}(t) = \boldsymbol{u}^{DC} + \mathrm{Re}\left(\boldsymbol{\mathcal{U}}^{AC} e^{\mathrm{i}\omega t}\right), \tag{2.8b}$$

which are equivalent to (2.6) in the time-harmonic setting.

2.4 Time-harmonic magneto-mechanical problem

From the full non-linear coupled magneto-mechanical problem presented in (2.1), the numerical considerations described in Section 2.3 are applied in order to obtain first a non-linear static DC problem and a linearised time-harmonic AC problem, which are presented in this Section.

2.4.1 Non-linear static DC problem

The non-linear[4] static problem is defined through the following strong from: Find $(\boldsymbol{A}^{DC}, \boldsymbol{u}^{DC}) \in (\mathbb{R}^3 \times \Omega^C)$ such that

$$\operatorname{curl}(\mu^{-1} \operatorname{curl} \boldsymbol{A}^{DC}) = \boldsymbol{J}^{DC} \qquad \text{in } \mathbb{R}^3, \tag{2.9a}$$

$$\operatorname{div} \boldsymbol{A}^{DC} = 0 \qquad \text{in } \mathbb{R}^3, \tag{2.9b}$$

$$\operatorname{div} \big(\boldsymbol{\sigma}^m(\boldsymbol{u}^{DC}) + \boldsymbol{\sigma}^e(\boldsymbol{A}^{DC})\big) = \boldsymbol{0} \qquad \text{in } \Omega^C, \tag{2.9c}$$

$$\boldsymbol{A}^{DC} = O\big(|\boldsymbol{x}|^{-1}\big) \qquad \text{as } |\boldsymbol{x}| \to \infty, \tag{2.9d}$$

$$\boldsymbol{u}^{DC} = \boldsymbol{u}_D^{DC} \qquad \text{on } \partial\Omega_D^C, \tag{2.9e}$$

$$\boldsymbol{n} \times [\boldsymbol{A}^{DC}]_{\partial\Omega^C} = \boldsymbol{0} \qquad \text{on } \partial\Omega^C, \tag{2.9f}$$

$$\boldsymbol{n} \times [\mu^{-1} \operatorname{curl} \boldsymbol{A}^{DC}]_{\partial\Omega^C} = \boldsymbol{0} \qquad \text{on } \partial\Omega^C, \tag{2.9g}$$

$$\big(\boldsymbol{\sigma}^m(\boldsymbol{u}^{DC}) + \boldsymbol{\sigma}^e(\boldsymbol{A}^{DC})\big)\big|_{\partial\Omega^C}^{-} \boldsymbol{n} = \boldsymbol{\sigma}^e(\boldsymbol{A}^{DC})\big|_{\partial\Omega^C}^{+} \boldsymbol{n} \qquad \text{on } \partial\Omega^C, \tag{2.9h}$$

which will be solved through the iterative Newton-Raphson strategy. The complete details can be found in [10], where a linearisation of this non-linear static problem is carried out using the concept of directional derivatives [84] and incrementally solving for the updated solution fields. Note that rather than using a monolithic approach, the authors in [49,77] advocate for a staggered approach, that in this thesis will only be considered in the linearised time-harmonic AC problem.

2.4.2 Linearised time-harmonic AC problem

The governing equations for the linearised transient problem are derived in [10] and the strong form is defined as: Find $(\boldsymbol{\mathfrak{A}}^{AC}, \boldsymbol{\mathfrak{u}}^{AC}) \in (\mathbb{C}^3 \times \Omega^C)$ such that

$$\operatorname{curl}(\mu^{-1} \operatorname{curl} \boldsymbol{\mathfrak{A}}^{AC}) + \mathrm{i}\omega\gamma \boldsymbol{\mathfrak{A}}^{AC} = \boldsymbol{\mathfrak{J}}^{AC} \qquad \text{in } \mathbb{R}^3, \tag{2.10a}$$

$$\operatorname{div} \boldsymbol{\mathfrak{A}}^{AC} = 0 \qquad \text{in } \mathbb{R}^3 \setminus \overline{\Omega^C}, \tag{2.10b}$$

$$\operatorname{div} \big(\boldsymbol{\sigma}^m(\boldsymbol{\mathfrak{u}}^{AC}) + \mu^{-1}\boldsymbol{T}(\boldsymbol{A}^{DC}, \boldsymbol{\mathfrak{A}}^{AC})\big) = -\rho\omega^2 \boldsymbol{\mathfrak{u}}^{AC} \qquad \text{in } \Omega^C, \tag{2.10c}$$

$$\boldsymbol{\mathfrak{A}}^{AC} = O\big(|\boldsymbol{x}|^{-1}\big) \qquad \text{as } |\boldsymbol{x}| \to \infty, \tag{2.10d}$$

$$\boldsymbol{\mathfrak{u}}^{AC} = \boldsymbol{\mathfrak{u}}_D^{AC} \qquad \text{on } \partial\Omega_D^C, \tag{2.10e}$$

$$\boldsymbol{n} \times [\boldsymbol{\mathfrak{A}}^{AC}]_{\partial\Omega^C} = \boldsymbol{0} \qquad \text{on } \partial\Omega^C, \tag{2.10f}$$

---

[4] The non-linearity of the problem is driven by the Maxwell stress tensor $\boldsymbol{\sigma}^e(\boldsymbol{A}^{DC})$ defined in (2.2b).

$$\boldsymbol{n} \times [\mu^{-1} \operatorname{curl} \boldsymbol{\mathcal{A}}^{AC}]_{\partial\Omega^C} = \boldsymbol{0} \qquad \text{on } \partial\Omega^C, \tag{2.10g}$$

$$\left(\boldsymbol{\sigma}^m(\boldsymbol{\mathcal{U}}^{AC}) + \boldsymbol{T}(\boldsymbol{A}^{DC}, \boldsymbol{\mathcal{A}}^{AC})\right)\Big|^{-}_{\partial\Omega^C} \boldsymbol{n} = \boldsymbol{T}(\boldsymbol{A}^{DC}, \boldsymbol{\mathcal{A}}^{AC})\Big)\Big|^{+}_{\partial\Omega^C} \boldsymbol{n} \qquad \text{on } \partial\Omega^C, \tag{2.10h}$$

where in (2.10c) and (2.10h) the linearised electromagnetic stress tensor is introduced and defined as

$$\begin{aligned} \boldsymbol{T}(\boldsymbol{A}^{DC}, \boldsymbol{\mathcal{A}}^{AC}) := \mu^{-1}\big(&(\operatorname{curl} \boldsymbol{A}^{DC}) \otimes (\operatorname{curl} \boldsymbol{\mathcal{A}}^{AC}) + (\operatorname{curl} \boldsymbol{\mathcal{A}}^{AC}) \otimes (\operatorname{curl} \boldsymbol{A}^{DC}) \\ &- (\operatorname{curl} \boldsymbol{A}^{DC} \cdot \operatorname{curl} \boldsymbol{\mathcal{A}}^{AC})\boldsymbol{I}\big). \end{aligned} \tag{2.11}$$

Once the linearised transient problem (2.10) is solved, the Eulerian electric and magnetic AC fields can be computed as

$$\boldsymbol{\mathcal{E}}^{AC} = -\mathrm{i}\omega \boldsymbol{\mathcal{A}}^{AC} + \mathrm{i}\omega \boldsymbol{B}_0^{DC} \times \boldsymbol{\mathcal{U}}^{AC} \qquad \text{in } \mathbb{R}^3, \tag{2.12a}$$

$$\boldsymbol{\mathcal{H}}^{AC} = \mu^{-1} \boldsymbol{\mathcal{B}}_0^{AC} = \mu^{-1} \operatorname{curl} \boldsymbol{\mathcal{A}}^{AC} \qquad \text{in } \mathbb{R}^3. \tag{2.12b}$$

Finally, the complete time-dependent solution of the problem (2.1) can be written as

$$\boldsymbol{E} = \operatorname{Re}\left(\boldsymbol{\mathcal{E}}^{AC} e^{\mathrm{i}\omega t}\right) = \operatorname{Re}\left((-\mathrm{i}\omega \boldsymbol{\mathcal{A}}^{AC} + \mathrm{i}\omega \boldsymbol{B}_0^{DC} \times \boldsymbol{\mathcal{U}}^{AC}) e^{\mathrm{i}\omega t}\right) \qquad \text{in } \Omega^C, \tag{2.13a}$$

$$\boldsymbol{H} = \boldsymbol{H}^{DC} + \operatorname{Re}\left(\boldsymbol{\mathcal{H}}^{AC} e^{\mathrm{i}\omega t}\right) = \mu^{-1}\left(\operatorname{curl} \boldsymbol{A}^{DC} + \operatorname{Re}\left((\operatorname{curl} \boldsymbol{\mathcal{A}}^{AC}) e^{\mathrm{i}\omega t}\right)\right) \qquad \text{in } \mathbb{R}^3, \tag{2.13b}$$

which is equivalent to (2.4) in a time-harmonic setting. Later in this thesis, two different approaches, monolithic and staggered, will be presented and assessed in order to solve the AC problem (2.10).

2.5 Axisymmetric time-harmonic problem

During the design stage of MRI scanners several simplifications are introduced into the numerical model in order to obtain relatively fast results that help tuning the geometry and material parameters. One of these simplifications is the consideration of an axisymmetric geometry, which certainly makes sense in the context of MRI scanners as a first attempt to design a novel MRI configuration. Figure 2.3 shows first a real MRI device that is simplified by using a three-dimensional axisymmetric geometry, which may be represented using a single two-dimensional meridional plane Ω_p.

In a typical MRI device, there are three different sets of gradient coils; the x-, y- and z-gradient coils. However, only the z-gradient coils are axisymmetric and, thus, they will be the only set of gradient coils considered.

An axisymmetric (r, ϕ, z) representation is assumed when deriving the weak forms of above strong forms (2.9)-(2.10) and the problem is formulated in the meridian two-dimensional plane Ω_p as shown in Figure 2.4. The unbounded domain is

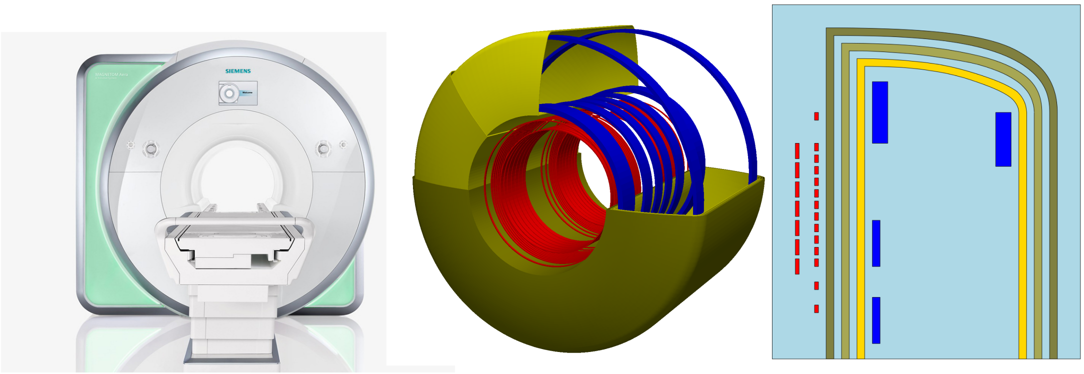

(a) Real MRI scanner device. (b) Three-dimensional simplified axisymmetric. (c) Two-dimensional meridional plane Ω_p.

Figure 2.3: Axisymmetric reduction of a real three-dimensional problem.

truncated at a finite distance away from the conducting embedded domain Ω_p^C and the decay conditions for $\boldsymbol{A}^{DC}$ and $\boldsymbol{\mathcal{A}}^{AC}$ apply. In addition, the transient current source is represented as $\boldsymbol{\mathcal{J}}^{AC}(r,\phi,z) = \mathcal{J}_\phi^S(r,z)\boldsymbol{e}_\phi$ and, thus, the solution variables become

$$\boldsymbol{\mathcal{A}}^{AC} = r\mathcal{A}_\phi(r,z)\boldsymbol{e}_\phi, \tag{2.14a}$$

$$\boldsymbol{\mathcal{U}}^{AC} = \boldsymbol{\mathcal{U}} = r\,\mathcal{U}_r(r,z)\boldsymbol{e}_r + \mathcal{U}_z(r,z)\boldsymbol{e}_z, \tag{2.14b}$$

where the upper index AC in the fields $\{\mathcal{A}_\phi, \boldsymbol{\mathcal{U}}\}$ is dropped for simplicity and with $\boldsymbol{e}_r$, $\boldsymbol{e}_\phi$ and $\boldsymbol{e}_z$ denoting the basis vectors in the r, ϕ and z directions, respectively. In addition, solution fields are scaled in order to avoid singularities along the $r = 0$ axis [36]. In what follows, the axisymmetric AC weak form of problem (2.10) is presented, as this will form the basis of our frequency (ω) based Proper Generalised Decomposition (PGD) method. Notice that, although the solution to the DC stage is still required, this is independent of the PGD parameter of interest, namely, the frequency ω, and so it is omitted and the reader is referred to [10, 36] for further details.

2.5.1 Monolithic formulation

The first option in order to solve the linearised time-harmonic AC problem (2.10) is to construct a solution field containing both the vector potential and the mechanical displacement as $\boldsymbol{\mathcal{Q}}(r,z) = [\mathcal{A}_\phi, \boldsymbol{\mathcal{U}}]^T$ and solve the system monolithically: Find $\boldsymbol{\mathcal{Q}} \in X(\mathcal{A}_{\phi,D}) \times Y(\boldsymbol{\mathcal{U}}_D)$ such that

$$W_K(\boldsymbol{\mathcal{Q}}, \delta\boldsymbol{\mathcal{Q}}) + \mathrm{i}\omega W_C(\boldsymbol{\mathcal{Q}}, \delta\boldsymbol{\mathcal{Q}}) - \omega^2 W_M(\boldsymbol{\mathcal{Q}}, \delta\boldsymbol{\mathcal{Q}}) = S(\delta\boldsymbol{\mathcal{Q}}) \qquad \forall \delta\boldsymbol{\mathcal{Q}} \in X(0) \times Y(\boldsymbol{0}), \tag{2.15}$$

where the functional spaces are defined as

$$X(\mathcal{A}_{\phi,D}) := \{\mathcal{A}_\phi : \mathcal{A}_\phi \in H^1(\Omega_p), \mathcal{A}_\phi = \mathcal{A}_{\phi,D} \text{ on } \partial\Omega_{p,D}\}, \tag{2.16a}$$

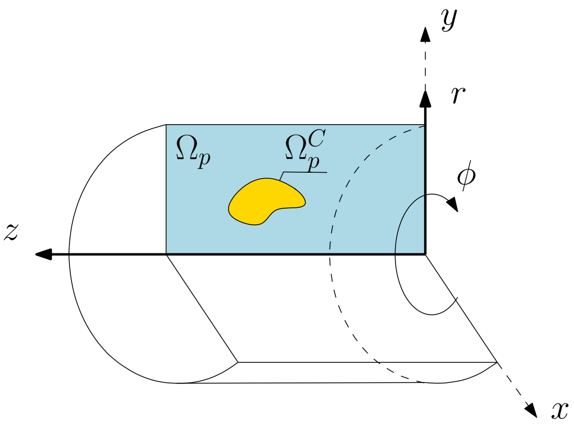

Figure 2.4: Axisymmetric $\{r, \phi, z\}$ representation of the problem; a conducting component Ω_p^C in a non-conducting domain Ω_p.

$$Y(\boldsymbol{\mathcal{U}}_D) := \{\boldsymbol{\mathcal{U}} : \boldsymbol{\mathcal{U}} \in (H^1(\Omega_p^C))^2, \boldsymbol{\mathcal{U}} = \boldsymbol{\mathcal{U}}_D \text{ on } \partial\Omega_{p,D}^C\}, \tag{2.16b}$$

with $\partial\Omega_{p,D}$ and $\partial\Omega_{p,D}^C$ denoting the Dirichlet part of the electromagnetic and mechanical boundaries, respectively. In addition, the compact forms appearing in (2.15) are defined as

$$W_K(\boldsymbol{Q}, \delta\boldsymbol{Q}) := W_K^A(\mathscr{A}_\phi, \delta\mathscr{A}_\phi) + W_K^u(\boldsymbol{\mathcal{U}}, \delta\boldsymbol{\mathcal{U}}) + S^u(\mathscr{A}_\phi, \delta\boldsymbol{\mathcal{U}}), \tag{2.17a}$$

$$W_C(\boldsymbol{Q}, \delta\boldsymbol{Q}) := W_C^A(\mathscr{A}_\phi, \delta\mathscr{A}_\phi), \tag{2.17b}$$

$$W_M(\boldsymbol{Q}, \delta\boldsymbol{Q}) := W_M^u(\boldsymbol{\mathcal{U}}, \delta\boldsymbol{\mathcal{U}}), \tag{2.17c}$$

$$S(\delta\boldsymbol{Q}) := S^A(\delta\mathscr{A}_\phi), \tag{2.17d}$$

with

$$W_K^A(a, b) := \int_{\Omega_p} \frac{\mu^{-1}}{r} \nabla_p(r^2 a) \cdot \nabla_p(r^2 \overline{b}) \, \mathrm{d}\Omega, \tag{2.18a}$$

$$W_C^A(a, b) := \int_{\Omega_p^C} \gamma a \overline{b} r^3 \, \mathrm{d}\Omega, \tag{2.18b}$$

$$S^A(b) := \int_{\Omega_p} \mathscr{J}_\phi^S \overline{b} r^2 \, \mathrm{d}\Omega, \tag{2.18c}$$

$$W_K^u(\boldsymbol{a}, \boldsymbol{b}) := \int_{\Omega_p^C} \boldsymbol{\sigma}^m(\boldsymbol{a}) : \nabla \overline{\boldsymbol{b}} \, r \, \mathrm{d}\Omega, \tag{2.18d}$$

$$W_M^u(\boldsymbol{a}, \boldsymbol{b}) := \int_{\Omega_p^C} \rho \boldsymbol{a} \cdot \overline{\boldsymbol{b}} \, r \, \mathrm{d}\Omega, \tag{2.18e}$$

$$S^u(a, \boldsymbol{b}) := \int_{\Omega_p^C} \mu^{-1} \boldsymbol{T}(\mathscr{A}_\phi^{DC}, a) : \nabla \overline{\boldsymbol{b}} \, r \, \mathrm{d}\Omega - \int_{\partial\Omega_p^{C,N}} \mu_0^{-1} \boldsymbol{T}(\mathscr{A}_\phi^{DC}, a)\big|^{+} \boldsymbol{n} \cdot \overline{\boldsymbol{b}} \, r \, \mathrm{d}S, \tag{2.18f}$$

Note that $(\overline{\cdot})$ denotes now the complex conjugate of a given field and that the gradient of the scalar potential in the meridian plane is defined as $\nabla_p \mathscr{A}_\phi := \frac{\partial \mathscr{A}_\phi}{\partial r} \boldsymbol{e}_r + \frac{\partial \mathscr{A}_\phi}{\partial z} \boldsymbol{e}_z$ [10].

Introduction of numerical regularisation

When simulating coupled magneto-mechanical problems, numerical singularities may arise in the vicinity of the conductors' resonant modes as motivated in Section 1.1.2, see Figure 1.4. As it will be shown later in this thesis, the introduction of numerical regularisation through the mass proportional Rayleigh damping coefficient [28] will help to reduce the ill-conditioning of the system of equations whilst preserving the overall behaviour of the coupled magneto-mechanical problem. The Rayleigh damping coefficient [28] α_M is defined as

$$\alpha_M = 2\omega\xi, \tag{2.19}$$

being ξ a dimensionless ratio that allows to control the amount of damping added to the system. This coefficient is introduced in the monolithic weak formulation (2.15) through a damping term

$$\mathrm{i}\omega W_C^u(\boldsymbol{\mathcal{U}}, \delta\boldsymbol{\mathcal{U}}) := \mathrm{i}\omega\alpha_M W_M^u(\boldsymbol{\mathcal{U}}, \delta\boldsymbol{\mathcal{U}}) = 2\mathrm{i}\omega^2\xi W_M^u(\boldsymbol{\mathcal{U}}, \delta\boldsymbol{\mathcal{U}}), \tag{2.20}$$

and, thus, the only compact form that needs to be modified in (2.17) is

$$W_M(\boldsymbol{\mathcal{Q}}, \delta\boldsymbol{\mathcal{Q}}) := W_M^u(\boldsymbol{\mathcal{U}}, \delta\boldsymbol{\mathcal{U}}) - \underbrace{\mathrm{i}W_C^u(\boldsymbol{\mathcal{U}}, \delta\boldsymbol{\mathcal{U}})}_{\text{damping term}}, \tag{2.21}$$

with

$$W_C^u(\boldsymbol{a}, \boldsymbol{b}) := 2\xi \int_{\Omega_p^C} \rho\boldsymbol{a} \cdot \overline{\boldsymbol{b}}\, r \,\mathrm{d}\Omega, \tag{2.22}$$

A study on the effect of introducing numerical regularisation in the coupled magneto-mechanical problem at hand will be performed in Section 2.7.

2.5.2 Staggered formulation

An alternative to the monolithic procedure presented in Section 2.5.1 consists in exploiting the staggered nature of the problem by solving first the electromagnetic problem and then using the electromagnetic solution in order to excite the mechanical problem through a source type term.

Electromagnetics

The full order electromagnetic AC problem is obtained from (2.10) in an axisymmetric configuration as: Find $\mathcal{A}_\phi(r,z) \in X(\mathcal{A}_{\phi,D})$ such that

$$W_K^A(\mathcal{A}_\phi, \delta\mathcal{A}_\phi) + \mathrm{i}\omega W_C^A(\mathcal{A}_\phi, \delta\mathcal{A}_\phi) = S^A(\delta\mathcal{A}_\phi) \qquad \forall\delta\mathcal{A}_\phi \in X(0), \tag{2.23}$$

which can be solved independently from mechanics.

Mechanics in embedded conductors

Once the electromagnetic field is known, the axisymmetric mechanical AC problem is also obtained from (2.10) as: Find $\boldsymbol{\mathcal{U}}(r,z) \in Y(\boldsymbol{\mathcal{U}}_D)$ such that

$$W_K^u(\boldsymbol{\mathcal{U}}, \delta\boldsymbol{\mathcal{U}}) - \omega^2 W_M^u(\boldsymbol{\mathcal{U}}, \delta\boldsymbol{\mathcal{U}}) = -S^u(\mathcal{A}_\phi, \delta\boldsymbol{\mathcal{U}}) \quad \forall \delta\boldsymbol{\mathcal{U}} \in Y(\mathbf{0}), \tag{2.24}$$

where the electromagnetic field $\mathcal{A}_\phi$ appears on the right-hand side as a source term.

Regularised mechanical problem

As mentioned in Section 2.5.1, the addition of numerical regularisation will be shown to be beneficial when solving the coupled magneto-mechanical system. With this purpose, the mechanical problem may be formulated as: Find $\boldsymbol{\mathcal{U}}(r,z) \in Y(\boldsymbol{\mathcal{U}}_D)$ such that

$$W_K^u(\boldsymbol{\mathcal{U}}, \delta\boldsymbol{\mathcal{U}}) + \mathrm{i}\omega^2 W_C^u(\boldsymbol{\mathcal{U}}, \delta\boldsymbol{\mathcal{U}}) - \omega^2 W_M^u(\boldsymbol{\mathcal{U}}, \delta\boldsymbol{\mathcal{U}}) = -S^u(\mathcal{A}_\phi, \delta\boldsymbol{\mathcal{U}}) \quad \forall \delta\boldsymbol{\mathcal{U}} \in Y(\mathbf{0}), \tag{2.25}$$

where, similarly to the monolithic approach, the frequency-proportional damping term $\mathrm{i}\omega^2 W_C^u(\boldsymbol{\mathcal{U}}, \delta\boldsymbol{\mathcal{U}})$ is clearly observed in the weak form.

2.6 Finite element discretisation

The finite element method requires a numerical discretisation [28] in order to obtain an approximated solution of the DC and AC problems previously explained. As mentioned, the focus will be on the AC problem since it is the one in which the PGD methodology will be applied to. Having said that, first the unbounded domain $\mathbb{R}^3$ is truncated by introducing a finite computational discretisation of the truncated meridian plane denoted by Ω_p which, throughout this thesis, will be partitioned using a 2D unstructured triangular mesh of non-overlapping elements as $\Omega_p = \bigcup_{e=1}^{E} \Omega_p^e$, where Ω_p^e refers to the computational domain within a triangular finite element e and E is the total number of elements in the mesh, where $\mathcal{A}_\phi = \mathcal{A}_{\phi,D}$ and $\boldsymbol{\mathcal{U}} = \boldsymbol{\mathcal{U}}_D$ in the truncated boundary. As presented in Section 2.5, the formulation can be solved monolithically or in a staggered manner, although the discretisation process is carried out in the same way. Hence, focusing first on the monolithic approach, the continuous solution field $\boldsymbol{\mathcal{Q}}$ and the virtual field $\delta\boldsymbol{\mathcal{Q}}$ are written in terms of discrete values as

$$\boldsymbol{\mathcal{Q}} = \sum_{b=1}^{n_{dof}} N^b \mathbf{Q}^b, \tag{2.26a}$$

$$\delta\boldsymbol{\mathcal{Q}} = L^a \delta\mathbf{Q}^a \qquad \forall a = 1, 2, \cdots, n_w, \tag{2.26b}$$

where $L^a, N^b \in H^1(\Omega_p)$, $\mathbf{Q}^b$ and $\delta\mathbf{Q}^a$ are the discrete values associated to the degrees of freedom of the solution field $\boldsymbol{\mathcal{Q}}$ and the virtual field $\delta\boldsymbol{\mathcal{Q}}$, respectively, n_{dof} is the number of degrees of freedom of the problem and n_w is the number of weighting functions. The standard Galerkin discretisation approach is followed in this problem, which implies $L^a = N^a$ and $n_w = n_{dof}$, although hierarchical shape functions [85] are used. The discrete approximation is then inserted in the monolithic weak form (2.15) to obtain its discretised version: Find $\mathbf{Q}$ such that

$$\left(\mathbf{K} + \mathrm{i}\omega\mathbf{C} - \omega^2\mathbf{M}\right)\mathbf{Q} = \mathbf{s}, \tag{2.27}$$

with

$$\mathbf{K} = \operatorname*{\mathsf{A}}_{e=1}^{E} \mathbf{K}^e, \;\; \mathbf{C} = \operatorname*{\mathsf{A}}_{e=1}^{E} \mathbf{C}^e, \;\; \mathbf{M} = \operatorname*{\mathsf{A}}_{e=1}^{E} \mathbf{M}^e \;\text{ and }\; \mathbf{s} = \operatorname*{\mathsf{A}}_{e=1}^{E} \mathbf{s}^e, \tag{2.28}$$

where A denotes the standard Finite Element assembly procedure [28]. Moreover, the definitions of each entry of the assembled (global) matrices and vector are

$$\mathrm{K}^{ab} := W_K(N^a, N^b), \tag{2.29a}$$
$$\mathrm{C}^{ab} := W_C(N^a, N^b), \tag{2.29b}$$
$$\mathrm{M}^{ab} := W_M(N^a, N^b), \tag{2.29c}$$
$$\mathrm{s}^{a} := S(N^a). \tag{2.29d}$$

The discretised system (2.27) can be written in terms of the different matrix blocks of $\mathbf{K}$, $\mathbf{C}$ and $\mathbf{M}$ related to both physics as

$$\left(\begin{bmatrix}\mathbf{K}_{AA} & \mathbf{0}\\ \mathbf{K}_{uA} & \mathbf{K}_{uu}\end{bmatrix} + \mathrm{i}\omega\begin{bmatrix}\mathbf{C}_{AA} & \mathbf{0}\\ \mathbf{0} & \mathbf{0}\end{bmatrix} - \omega^2\begin{bmatrix}\mathbf{0} & \mathbf{0}\\ \mathbf{0} & \mathbf{M}_{uu} - \mathrm{i}\mathbf{C}_{uu}\end{bmatrix}\right)\begin{bmatrix}\boldsymbol{\mathcal{A}}_\phi\\ \boldsymbol{\mathcal{U}}\end{bmatrix} = \begin{bmatrix}\mathbf{s}_A\\ \mathbf{0}\end{bmatrix}, \tag{2.30}$$

where $\boldsymbol{\mathcal{A}}_\phi$ and $\boldsymbol{\mathcal{U}}$ are the discrete nodal solution values for electromagnetics and mechanics, respectively. Note that each entry of these matrix blocks is defined from the compact forms (2.18) as

$$\begin{aligned} \mathbf{K}_{AA}^{ab} &= W_K^A(N^a, N^b), & \mathbf{C}_{AA} &= W_C^A(N^a, N^b),\\ \mathbf{K}_{uu}^{ab} &= W_K^u(N^a, N^b), & \mathbf{C}_{uu} &= W_C^u(N^a, N^b),\\ \mathbf{K}_{uA}^{ab} &= S^u(N^a, N^b), & \mathbf{M}_{uu} &= W_M^u(N^a, N^b). \end{aligned} \tag{2.31}$$

From (2.30) it is immediate to observe that the above system of equations can be solved in a two-step process, when the vector of unknown nodal values of $\mathcal{A}_\phi$ is obtained first as: Find $\boldsymbol{\mathcal{A}}_\phi$ such that

$$\left(\mathbf{K}_{AA} + \mathrm{i}\omega\mathbf{C}_{AA}\right)\boldsymbol{\mathcal{A}}_\phi = \mathbf{s}_A, \tag{2.32}$$

in order to excite the mechanical problem though a source term: Find $\boldsymbol{\mathcal{U}}$ such that

$$\left(\mathbf{K}_{uu} - \omega^2(\mathbf{M}_{uu} - \mathrm{i}\mathbf{C}_{uu})\right)\boldsymbol{\mathcal{U}} = \mathbf{s}_u, \tag{2.33}$$

where now the term $\mathbf{s}_u := \mathbf{K}_{uA}\boldsymbol{\mathcal{A}}_\phi$ appearing in (2.33) is a known quantity that is presented as a mechanical source term.

2.7 Effect of the addition of numerical regularisation

As motivated in Section 1.1.2, the solution of the coupled MRI magneto-mechanical problem may feature the resonance phenomenon, where the resulting system of equations becomes ill-conditioned near the conductors' resonant modes. To study the effect of introducing numerical regularisation to the problem at hand, Figure 2.5a presents a simplified coupled magneto-mechanical MRI test problem consisting of a conducting mechanical shell Ω_p^C embedded in a non-conducting domain.

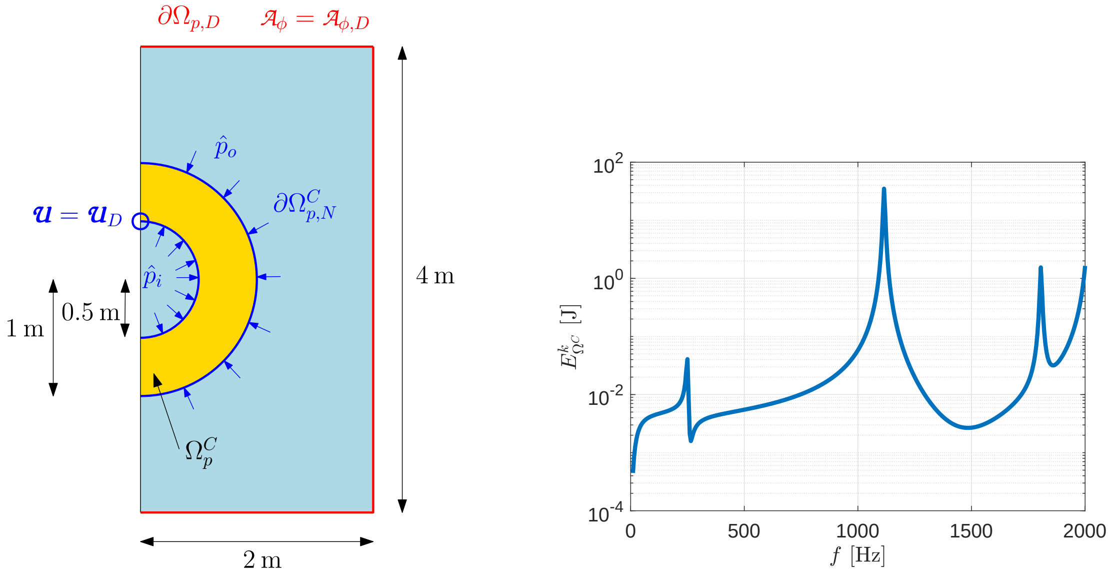

(a) Geometry and boundary conditions description.

(b) Kinetic energy $E^k_{\Omega^C}$ in the conducting mechanical shell. Mesh of 351 triangular elements with polynomial order $p = 3$.

Figure 2.5: Magneto-mechanical test problem; geometry description and kinetic energy in the conducting mechanical shell.

Figure 2.5b shows a frequency sweep in the frequency spectrum $f \in (0, 2000]$ Hz, where the resonant frequencies are clearly depicted through the visualisation of the kinetic energy $E^k_{\Omega^C}$ presented in (2.34). These sharp changes in the solution fields are produced due to an ill-conditioned system in the proximity of the resonance modes, which can be alleviated using numerical regularisation.

As described in Section 2.5.1, numerical regularisation is simply introduced in the algorithm through the addition of mechanical damping which, in its simplest form, can be formulated as Rayleigh mass based damping [28], where a damping contribution proportional to the mass of the system is considered, as presented in [10]. Consequently, this study seeks to determine the influence of the damping ratio ξ on the numerical solution computed using the full order model. In Figure 2.6, the kinetic energy in the conducting mechanical shell Ω_p^C is plotted for different values of the damping ratio ξ. The mesh used for these simulations consists of 351 triangular elements with polynomial order $p = 3$, which produces a fully resolved full order solution. It is interesting to observe that the value of the resonant frequencies remain unaffected regardless of the damping introduced but with lower energetic contributions. This shows how the use of numerical regularisation helps reduce the ill-conditioning of the overall system near resonant modes, without modifying the overall energy spectrum [28].

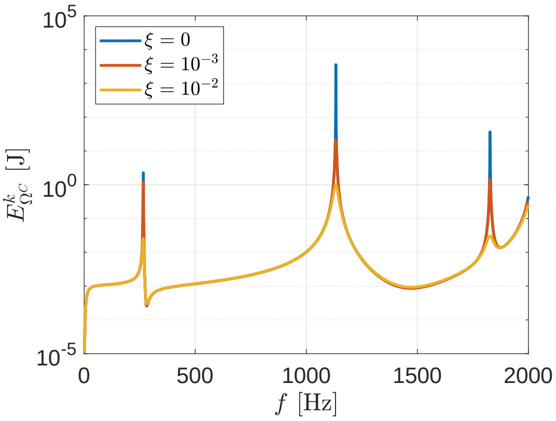

Figure 2.6: Magneto-mechanical test problem; values of the kinetic energy $E^k_{\Omega^C}$ in the mechanical shell Ω^C_p for different damping ratios ξ.

2.8 Description of industrially relevant problems

This section aims to present and motivate two problems of interest that represent possible axisymmetric MRI scanner geometries and that are relevant from the industrial point of view. First, a simplified tailor-made MRI (test) magnet problem followed by a realistic and more challenging (full) MRI configuration, with closed shells representing the conducting shields. The full order problem will be solved by applying the numerical approach described in Section 2.5 and the full order solution obtained will highlight the challenges involved in the design stage of these devices. The numerical difficulties regarding the appearance of the resonance phenomenon will also be discussed, together with its implication when applying reduced order modelling techniques to this type of problems.

2.8.1 Test magnet problem

The test magnet problem corresponds to a simplified MRI scanner geometry, which consists of three conducting shields embedded in a non conducting rectangular domain, see Figure 2.7. The three shields are known as the Outer Vacuum Chamber (OVC) shield Ω^C_{OVC}, the 77K radiation shield Ω^C_{77K} and the 4K helium vessel shield Ω^C_{4K} and they have different material parameters that cannot be exactly specified due to confidentiality issues. However, the approximate values are $\mu_* \approx 10^{-7}$ H/m, $\gamma_* \approx 10^6$ S/m, $\rho \approx 10^3$ Kg/m^3, $E \approx 10^9$ Pa, $\nu \approx 0.3$. The thickness of each shield is slightly different and it is of the order of a few millimetres. Regarding the boundary conditions, displacements $\boldsymbol{\mathcal{U}} = \boldsymbol{\mathcal{U}}_D = \mathbf{0}$ are fixed to a small part in the centre of each shield and the component of the vector potential is set to $\mathcal{A}_\phi = \mathcal{A}_{\phi,D} = 0$ far away from the conducting objects. Note that the axisymmetric formulation [36] follows from assuming rotational symmetry of the weak form expressed in 3D cylindrical coordinates and, as such, $r = 0$ does not form a boundary of the computational domain Ω_p.

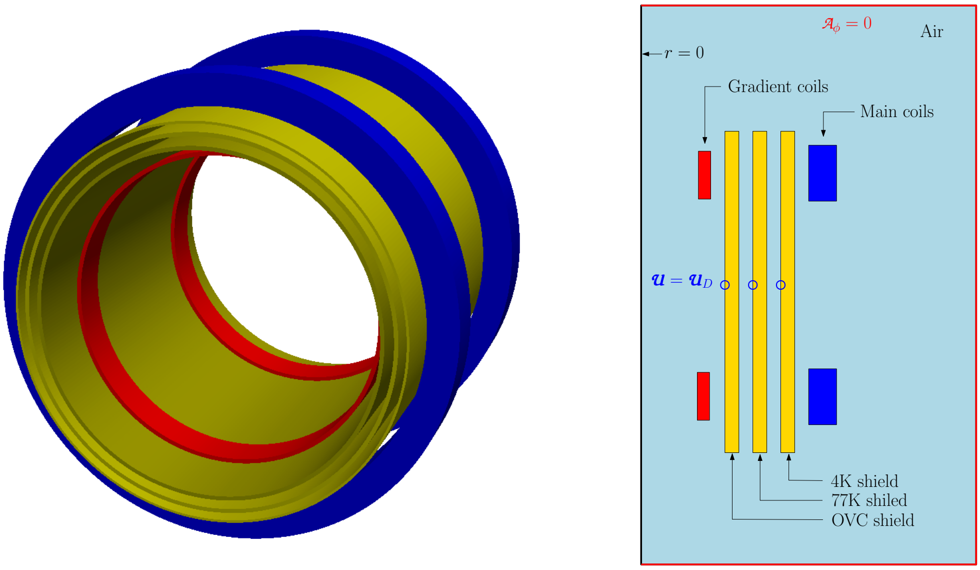

Figure 2.7: Test magnet problem; geometry description. 3D view (left) and 2D axisymmetric view (right) with components names and boundary conditions.

The main study regarding the shield-coil interaction in the design stage of MRI scanners consists in performing numerical simulations for a wide range of frequencies in order to obtain the complex physical solution of the system. Once the solution fields are obtained, a post-process is needed in order to obtain the integrated quantities of interest, the dissipated Power $P^0_{\Omega^C}$ and the kinetic energy $E^k_{\Omega^C}$ computed as

$$P^0_{\Omega^C} = \frac{1}{2}\int_{\Omega^C} \gamma |\boldsymbol{\mathcal{E}}^{AC}|^2 \mathrm{d}\Omega, \qquad E^k_{\Omega^C} = \frac{1}{2}\int_{\Omega^C} \rho\omega^2 |\boldsymbol{\mathcal{U}}^{AC}|^2 \mathrm{d}\Omega, \tag{2.34}$$

which are integrated in the conducting components for both, electromagnetics and mechanics, respectively. The reader is referred to Section C.1.1 in Appendix C for a brief description on how these quantities are computed in an efficient manner using the full order model approach. These quantities provide very valuable information as to the amount of energy generated in the system for a certain frequency of excitation. Hence, they serve to quantify the resonance behaviour of each conducting shield and locate the frequencies in which the MRI scanner should not operate in order to maximise its lifespan. The problems in terms of medical imaging associated to the existence of vibrations and resonance have been presented in Section 1.1.2. Moreover, resonance frequencies are found to be driven by the eigenvalues of the mechanical problem and they provide information on the vibration modes or mode shapes of the shields forming the scanner.

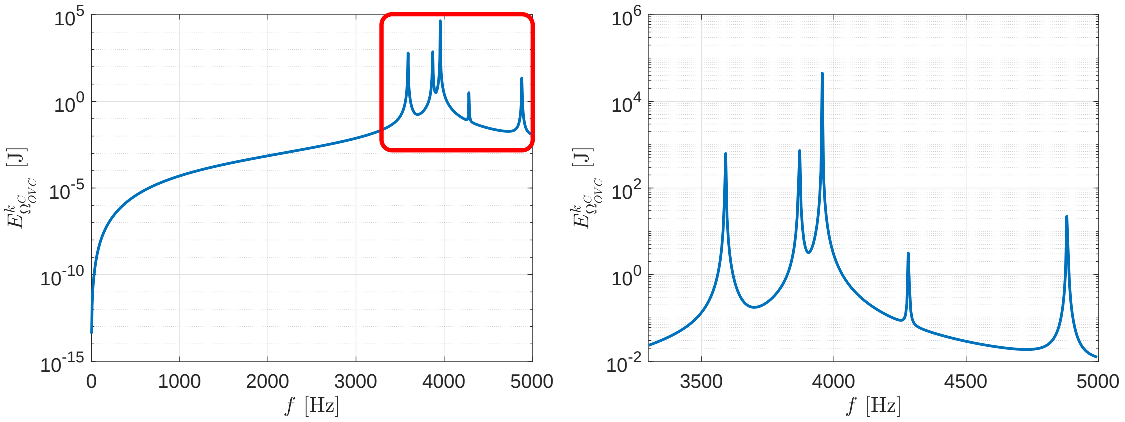

Figure 2.8: Test magnet problem; value of the dissipated Power $E^k_{\Omega^C_{OVC}}$ in the OVC shield for different frequencies from 1 to 5000 Hz. Right Figure shows a zoomed view in the resonance region (red rectangle). Results shown are for a mesh of 2.9K triangular elements using a polynomial order $p = 4$.

Figure 2.8 shows the frequency sweep applied to the test magnet geometry excited through the current sources $\boldsymbol{J}^{DC}$ and $\boldsymbol{\mathcal{J}}^{AC}$ that create a uniform magnetic field of strength $B_0 = \max(\left|\boldsymbol{B}_0^{DC}|_{r=0}\right|) = 1.5$ T and a gradient magnetic field along the $r = 0$ axis of value $\left|\partial \boldsymbol{\mathcal{B}}_0^{AC}|_{r=0}/\partial z\right| = 100$ mT/m, respectively. The range of interest in this geometry is $f \in \Omega_\omega = (0, 5000]$ Hz due to the fact that the focus lies on the first resonant frequencies of the system. In this figure, it can be seen how, for this geometry, the kinetic energy grows monotonically as the frequency is increased, and the resonance region is concentrated within the range between 3500 and 5000 Hz. Since this information is not known *a priori*, the frequency sweeps for different geometries have to be performed with small frequency increments. Otherwise, the thin spikes may be either partially or not captured at all by the full order solution, leading to a misdiagnosed design and, potentially, wrong manufacturing decisions.

Convergence of the numerical solution

Before moving to other studies, this section aims to discuss the convergence of the fields in order to prove that the full order model solution is well resolved. The Finite Element Method [28] allows to compute more accurate solutions as the mesh is refined either by decreasing the mesh size (h-refinement) or by increasing the polynomial order of interpolation (p-refinement). Naturally, the finite element solution should reach convergence with both approaches, meaning that no changes are appreciated in the numerical solution with a sufficient h- or p-refinement.

The two refinement approaches are presented in Figure 2.9 in order to demonstrate the consistency of the numerical scheme employed. This analysis is important prior to further investigations in order to ensure that the full order model can be

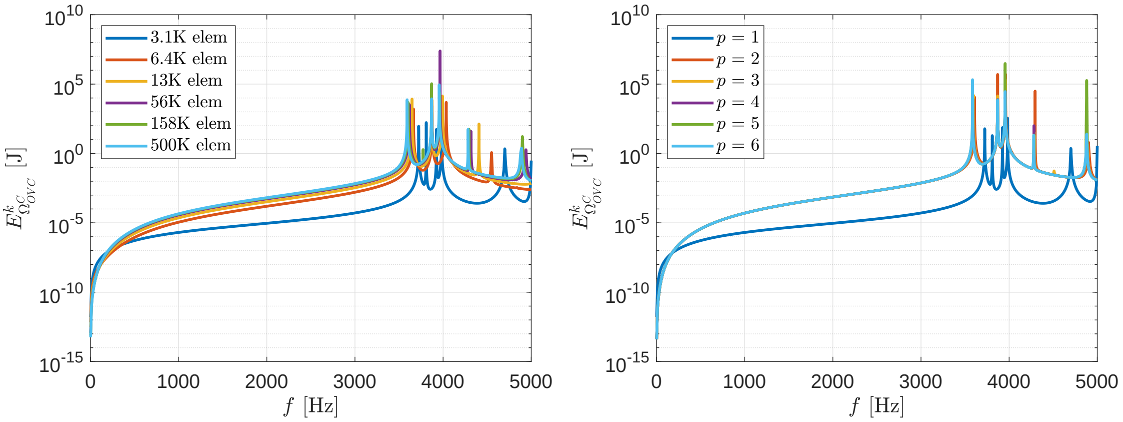

Figure 2.9: Test magnet problem; h-refinement (left) using a polynomial order $p = 1$ and p-refinement (right) with a mesh of 2.9K elements.

used as the reference solution for benchmarking proposes. Comparison of Figures 2.9 (left) and (right), demonstrates that p-refinement leads more efficiently to a converged solution in terms of degrees of freedom. Figure 2.10 shows the converged solution obtained with both refinement strategies, which agree very well. However, whilst the 500K element mesh and $p = 1$ results in 695K degrees of freedom (ndof), only 77K ndof are used in 2.9K element mesh and $p = 6$. Note that although some minor differences are observed in the magnitude of the resonance spikes, it is important to emphasise that the importance lies on their location and not so much in their magnitude, which should tend to infinity, anyway, at the theoretical level in the absence of damping mechanisms. In this case, the results suggest that increasing the polynomial order p is a good strategy to accurately capture the skin depth effect inside the thin conducting shields without the need to resort to a prohibitively large number of degrees of freedom.

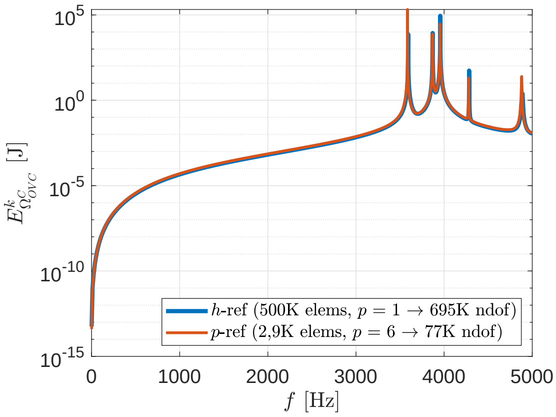

Figure 2.10: Test magnet problem; comparison between solutions obtained with a mesh with 500K elements with $p = 1$ and a mesh with $p = 6$ with 2.9K elements.

Sampling points in frequency

As mentioned in Section 2.8.1, the number of sampling points used to compute the integrated quantities (2.34) is key in order to accurately represent the problem throughout the entire frequency spectrum. In other words, it is pointless to optimise the spatial discretisation in order to ensure an accurate finite element analysis if a sufficiently large range of frequencies is not sampled. Therefore, the following study explores the number of frequency sampling points required in order to obtain an accurate energy spectrum. Figures 2.8, 2.9 and 2.10 have been obtained sweeping over the frequency range with sampling points every 5 Hz. In order to certify that a 5 Hz spacing is sufficient, Figure 2.11 is presented, where frequency energy spectra for five different frequency spacings are displayed, namely, every 0.5, 1, 5, 10 and 20 Hz. The main conclusion than can be extracted from these results is that a 5 Hz spacing is sufficient to accurately represent the spectrum and capture the resonance modes.

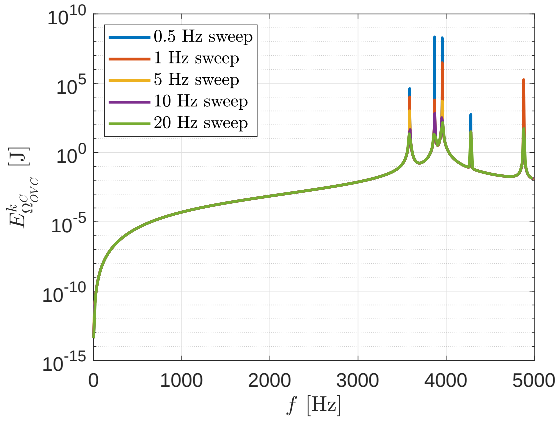

Figure 2.11: Test magnet problem; study on the number sampling of points in the frequency interval required to accurately capture the solution.

Modal shapes

From the results presented in Figure 2.8, the resonance frequencies may be easily located, allowing the visualisation of the modal shapes of each radiation shield in the MRI configuration. Figure 2.12 shows both the magnetic field in the (r, z) plane as well as the displacement field in the field, which has been plotted in an axisymmetric three-dimensional domain for visualisation proposes. The six subfigures correspond to six different frequencies, one at the pre-resonant frequency of 2000 Hz and the other five at resonance frequencies of 3590, 3870, 3955, 4280 and 4880 Hz. Regarding electromagnetics, the magnitude of the transient magnetic field $|\boldsymbol{\mathcal{B}}_0^{AC}|$ in the axisymmetric plane is visualised in the form of contour lines, where major changes are not visible when increasing the excitation frequency. Yet, it is interesting to notice how this magnetic field is generated in the gradient coils and travels through the free space permeating across the conducting shields.

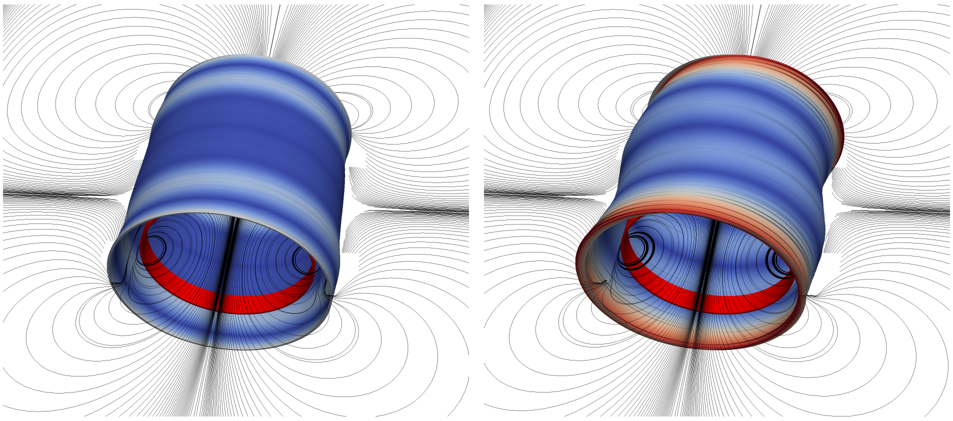

(a) $f = 2000$ Hz. (b) $f = 3590$ Hz.

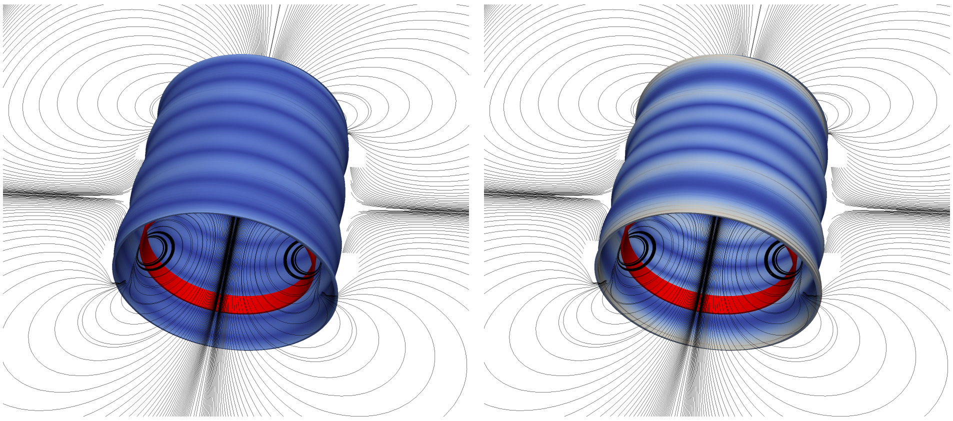

(c) $f = 3870$ Hz. (d) $f = 3955$ Hz.

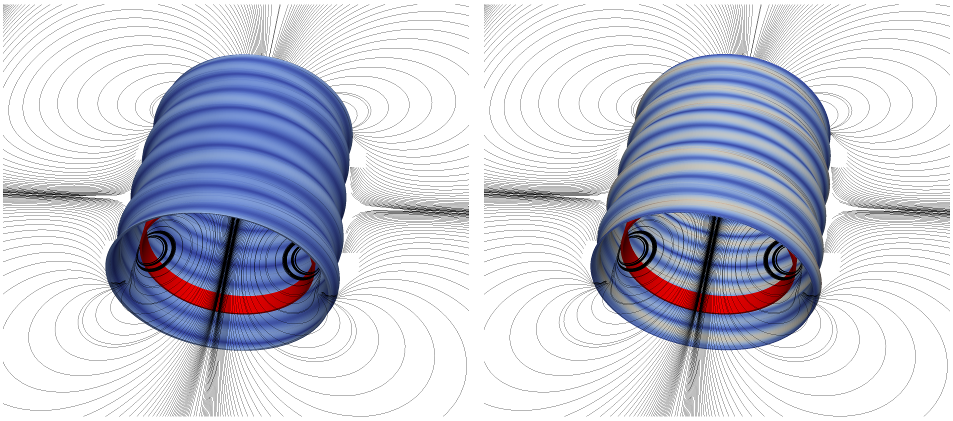

(e) $f = 4280$ Hz. (f) $f = 4880$ Hz.

Figure 2.12: Test magnet problem; visualisation of the magnetic field $|\boldsymbol{\mathcal{B}}_0^{AC}|$ contour lines on the axisymmetric plane and the magnitude of the displacements $|\boldsymbol{\mathcal{U}}|$ in the OVC shield. Plot of the deformed OVC shield for different frequencies.

On the other hand, major changes can be seen in the magnitude of the mechanical displacement field $|\boldsymbol{\mathcal{U}}|$. Figure 2.12a represents the displacement that would be typically observed for frequencies in the pre-resonance region, where the maximum values are concentrated in regions near the gradient coils that generate the transient magnetic field. Figures 2.12b-2.12f, display the displacement fields for the first resonant modes of the spectrum, where the typical increasing modal vibrations can be seen.

2.8.2 Full magnet problem

The full magnet problem depicts a considerably more complex geometry, being this a better representation of a MRI scanner configuration, see Figure 2.13. This problem also contains the main and gradient coils and the three conducting shields (OVC, 77K and 4K) which are now shown more realistically as closed cylindrical shells. Again, each shield has different material parameters that cannot be exactly specified due to confidentiality issues. However, the approximate values are $\mu_* \approx 10^{-7}$ H/m, $\gamma_* \approx 10^6$ S/m, $\rho \approx 10^3$ Kg/m^3, $E \approx 10^9$ Pa and $\nu \approx 0.3$. The thickness of each shield is slightly different and it is of the order of a few millimetres. The Dirichlet boundary conditions are shown in Figure 2.13 (only the top half of the axisymmetric domain is presented due to symmetry), where the outer boundary is set to $\mathcal{A}_\phi = \mathcal{A}_{\phi,D} = 0$ (electromagnetics) and the mechanical conducting shields are fixed $\boldsymbol{\mathcal{U}} = \boldsymbol{\mathcal{U}}_D = \mathbf{0}$ (displacements) in the rear part of each shield. In the same way than for the test magnet geometry, see Section 2.8.1, the axisymmetric formulation [36] follows from the assumption of rotational symmetry of the weak form expressed in 3D cylindrical coordinates and, as such, $r = 0$ does not form a boundary of the computational domain Ω_p.

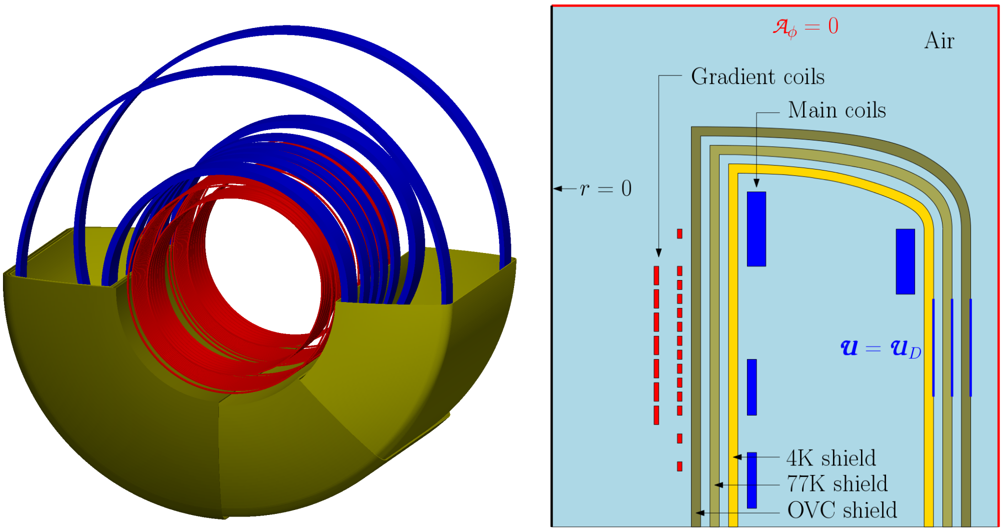

Figure 2.13: Full magnet problem; geometry description. 3D view (left) and 2D axisymmetric view (right) with components names and boundary conditions (only the top half of the axisymmetric domain is presented due to symmetry).

AC/DC splitting

The linearisation process has been described in Section 2.3.1, where the operating conditions of an MRI scanner are used in order to linearise the transient (AC) problem about the strong static (DC) magnetic field on the background and, thus, the complete fields are obtained as the sum of both DC and AC stages. It is interesting to observe the solution of both problems as presented in Figure 2.14, where a mesh of 17.4K triangular elements with $p = 4$ is used. First, the DC problem is obtained excited through a static current source that generates a strong static magnetic field which is as uniform as possible on the imaging bore axis ($r = 0$). Figure 2.14a shows this static solution and how it is indeed uniform in the interior of the MRI scanner. Note that the magnetic field $\boldsymbol{B}_0^{DC}$ is generated in the supercooled main coils, located inside the 4K Helium vessel. In addition, this Figure shows the static magnetic field magnitude in the OVC shield, with maximum values near the set of main coils. Once the static solution is obtained, this will become the initial state of the dynamic problem, which will be solved considering a dynamic current source several orders of magnitude lower than the static one, in this particular case $|\boldsymbol{\mathcal{J}}^{AC}|/|\boldsymbol{J}^{DC}| \approx 2\%$. The solution of the AC problem is presented in Figure 2.14b, where the displacements $|\boldsymbol{\mathcal{U}}|$ are plotted in the OVC shield and the magnitude of the dynamic magnetic field $|\boldsymbol{\mathcal{B}}_0^{AC}|$ is represented through contour lines. In this Figure, it can be seen how the magnetic field is generated in the gradient coils and it is no longer uniform. The displacements have its maximum values in the interior of the MRI device around the gradient coils.

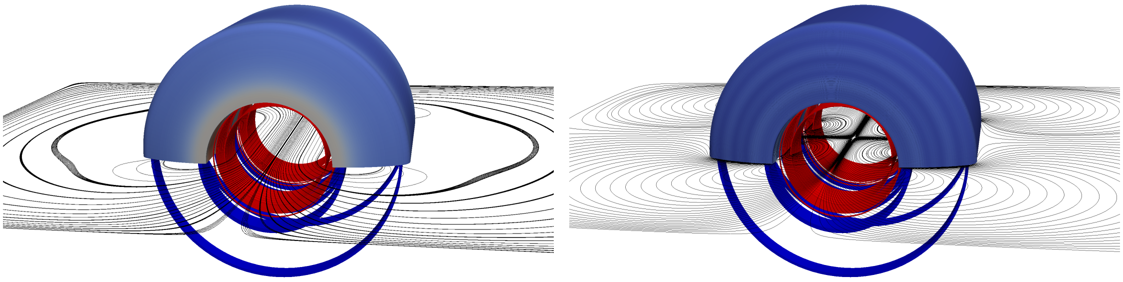

(a) DC problem; visualisation of $|\boldsymbol{B}_0^{DC}|$ in the OVC shield and streamlines.

(b) AC problem; visualisation of $|\boldsymbol{\mathcal{U}}|$ in the OVC shield and streamlines of $|\boldsymbol{\mathcal{B}}_0^{AC}|$.

Figure 2.14: Full magnet problem; full order solution of both DC and AC problems for a frequency of 1000 Hz.

The current sources $\boldsymbol{J}^{DC}$ and $\boldsymbol{J}^{AC}$ have been selected in the same way than for the previous geometry so they generate a uniform magnetic field of strength $B_0 = \max(\left|\boldsymbol{B}_0^{DC}|_{r=0}\right|) = 1.5$ T and a gradient along the $r = 0$ axis of $\left|\partial\boldsymbol{\mathcal{B}}_0^{AC}|_{r=0}/\partial z\right| = 100$ mT/m, respectively. To visualise these quantities, Figure 2.15 is presented, where a line plot has been generated for both, static and transient problems, along the

$r = 0$ axis. This Figure clearly shows how, first, the static magnetic field $\boldsymbol{B}_0^{DC}$ is indeed uniform in the scanning region, in the $r = 0$ axis and in the vicinity of the axial $z = 0$ coordinate. Note that the value of this uniform area is that defines the strength of the magnet B_0 quantity, which in this case is indeed 1.5 T. On the other hand, the gradient $\left|\partial \boldsymbol{\mathcal{B}}_0^{AC}|_{r=0} / \partial z\right|$ along the $r = 0$ axis can be easily computed in the vicinity of the $z = 0$ coordinate, obtaining a gradient of 100 mT/m as previously mentioned.

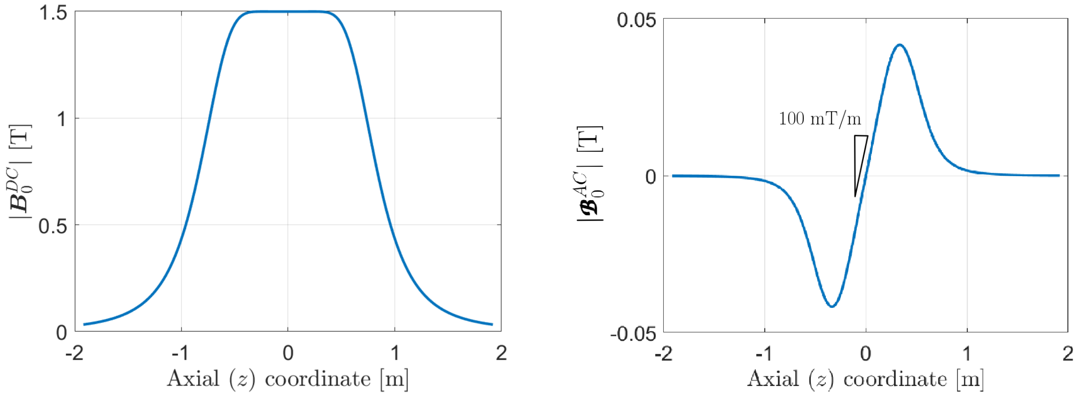

Figure 2.15: Full magnet problem; line plot of both static (DC) and transient (AC) magnetic fields along the $r = 0$ axis for a frequency of 1000 Hz.

2.9 Chapter summary

This chapter has presented a linearised axisymmetric computational FEM framework for Lagrangian coupled magneto-mechanics in the context of MRI scanners, where the transient governing equations are solved in the frequency domain. Two MRI configurations, recurrently used throughout this thesis, have been comprehensively described and carefully studied through a set of tailor-made numerical simulations in order to motivate the challenges and numerical difficulties stated in Chapter 1. With this chapter, it can be concluded that the objective "*To develop a coupled magneto-mechanical formulation in a Lagrangian setting from an existing axisymmetric finite element framework*" has been achieved. The following chapters will focus on developing and implementing the PGD technique to these governing equations.

Chapter 3

General Proper Generalised Decomposition formulation

3.1 Introduction

The Proper Generalised Decomposition (PGD) method is an *a priori* Reduced Order Model (ROM) technique which allows the consideration of multiple material and geometric parameters as extra coordinates of a high-dimensional parametric solution, as presented in Section 1.3.2. The goal of this chapter is the derivation of a general PGD formulation for the full order problem at hand, considering an axisymmetric two-dimensional (r, z) space Ω_p, see the full order model Section 2.5, and a d-dimensional parametric space Ω_q which can be represented as a set of one-dimensional parametric spaces, that is $\Omega_q = \Omega_{w_1} \times \cdots \times \Omega_{w_d}$. This chapter will briefly introduce key concepts which will be exploited in Chapters 4 and 5.

With this aim, the first step before presenting the actual PGD formulation, is the slight modification of the weak form of the full order model (2.15) by incorporating the new parametric domain Ω_q into the solution process. This new problem statement can be understood as an augmented high-dimensional weak form. Subsequently, the PGD formulation will be derived and the iterative algorithms needed in order to compute the high-dimensional parametric solution will be presented. Moreover, some important numerical considerations that have to be taken into account during the offline stage will be discussed, such as the inclusion of non-homogeneous Dirichlet boundary conditions, the scaling of the PGD modes and the convergence criteria used for the iterative algorithms. Finally, this chapter will also explain the online stage, in which the precomputed high-dimensional parametric solution is evaluated (particularised) for the desired set of design parameters in real time.

3.2 Augmented weak formulation

The standard weak formulation of the full order model problem (2.15) is established via integration over the spatial domain Ω_p. In contrast, the high-dimensional weak formulation necessary for the PGD implementation consists on further integrating the weak form of the full order model problem over the set of one-dimensional parametric spaces $\Omega_q = \Omega_{w_1} \times \cdots \times \Omega_{w_d}$. Consequently, the augmented high-dimensional weak formulation version of (2.15) is formulated as: Find $\boldsymbol{\mathcal{Q}}(r, z, w_1, \dots, w_d) \in \mathcal{X}(\mathcal{A}_{\phi,D}) \times \mathcal{Y}(\boldsymbol{\mathcal{U}}_D)$ such that[1]

$$\mathcal{W}_K(\boldsymbol{\mathcal{Q}}, \delta\boldsymbol{\mathcal{Q}}) + \mathrm{i}\omega\mathcal{W}_C(\boldsymbol{\mathcal{Q}}, \delta\boldsymbol{\mathcal{Q}}) - \omega^2\mathcal{W}_M(\boldsymbol{\mathcal{Q}}, \delta\boldsymbol{\mathcal{Q}}) = \mathcal{S}(\delta\boldsymbol{\mathcal{Q}}) \quad \forall \delta\boldsymbol{\mathcal{Q}} \in \mathcal{X}(0) \times \mathcal{Y}(\mathbf{0}), \tag{3.1}$$

where the calligraphic font denotes integration in a higher dimensional space defined as

$$\mathcal{W}_K(\boldsymbol{\mathcal{Q}}, \delta\boldsymbol{\mathcal{Q}}) := \int_{\Omega_{w_1}} \cdots \int_{\Omega_{w_d}} W_K(\boldsymbol{\mathcal{Q}}, \delta\boldsymbol{\mathcal{Q}})\, \mathrm{d}w_1 \dots \mathrm{d}w_d, \tag{3.2a}$$

$$\mathcal{W}_C(\boldsymbol{\mathcal{Q}}, \delta\boldsymbol{\mathcal{Q}}) := \int_{\Omega_{w_1}} \cdots \int_{\Omega_{w_d}} W_C(\boldsymbol{\mathcal{Q}}, \delta\boldsymbol{\mathcal{Q}})\, \mathrm{d}w_1 \dots \mathrm{d}w_d, \tag{3.2b}$$

$$\mathcal{W}_M(\boldsymbol{\mathcal{Q}}, \delta\boldsymbol{\mathcal{Q}}) := \int_{\Omega_{w_1}} \cdots \int_{\Omega_{w_d}} W_M(\boldsymbol{\mathcal{Q}}, \delta\boldsymbol{\mathcal{Q}})\, \mathrm{d}w_1 \dots \mathrm{d}w_d, \tag{3.2c}$$

$$\mathcal{S}(\delta\boldsymbol{\mathcal{Q}}) := \int_{\Omega_{w_1}} \cdots \int_{\Omega_{w_d}} S(\delta\boldsymbol{\mathcal{Q}})\, \mathrm{d}w_1 \dots \mathrm{d}w_d, \tag{3.2d}$$

with the spatial integration already included inside the terms defined in (2.17). Note that, since now the integration is performed over a higher-dimensional space, the functional subspaces are defined as

$$\begin{aligned}\mathcal{X}(\mathcal{A}_{\phi,D}) :=& \{\mathcal{A}_\phi : \mathcal{A}_\phi \in H^1(\Omega_p \times \Omega_{w_1} \times \cdots \times \Omega_{w_d}),\\ & \mathcal{A}_\phi = \mathcal{A}_{\phi,D} \text{ on } \partial\Omega_{p,D} \times \Omega_{w_1} \times \cdots \times \Omega_{w_d}\},\end{aligned} \tag{3.3a}$$

$$\begin{aligned}\mathcal{Y}(\boldsymbol{\mathcal{U}}_D) :=& \{\boldsymbol{\mathcal{U}} : \boldsymbol{\mathcal{U}} \in \left(H^1(\Omega_p^C \times \Omega_{w_1} \times \cdots \times \Omega_{w_d})\right)^2,\\ & \boldsymbol{\mathcal{U}} = \boldsymbol{\mathcal{U}}_D \text{ on } \partial\Omega_{p,D}^C \times \Omega_{w_1} \times \cdots \times \Omega_{w_d}\}.\end{aligned} \tag{3.3b}$$

3.3 Offline high-dimensional parametric PGD formulation

This section presents the PGD formulation when applied to a general high-dimensional $\Omega_p \times \Omega_q$ parametric problem. The core idea of the PGD technique [21] is the approximation of a particular solution field $\boldsymbol{\mathcal{Q}} = \boldsymbol{\mathcal{Q}}(r, z, w_1, \dots, w_d)$ by assuming its separability follows as

---

[1] Note that the calligraphic font is used to denote the integration over a high-dimensional domain, whereas the terms appearing in the classical weak formulation (2.15) are written in the standard maths font.

$$\boldsymbol{\mathcal{Q}}(r,z,w_1,\ldots,w_d) \approx \boldsymbol{\mathcal{Q}}^N(r,z,w_1,\ldots,w_d) = \sum_{n=1}^{N} \beta^n \boldsymbol{\mathcal{F}}^n(r,z) \prod_{i=1}^{d} \mathcal{G}_i^n(w_i), \tag{3.4}$$

where N is the total number of modes computed. The spatial modes $\boldsymbol{\mathcal{F}}^n(r,z)$ are represented by normalised vectorial functions, the parametric modes $\mathcal{G}_i^n(w_i)$ are denoted by normalised scalar functions and the mode weights β^n are scalar coefficients computed via L^2 projection once all spatial and parametric modes are known [42], see Section 3.5. Note that the choice made uses a single vectorial modal function $\boldsymbol{\mathcal{F}}^n(r,z)$ that accounts for the spatial (r,z) space Ω_p, whilst a set of separated scalar functions $\prod_{i=1}^{d} \mathcal{G}_i^n(w_i)$ are chosen to model the one-dimensional parametric domains $\Omega_p = \Omega_{w_1} \times \cdots \times \Omega_{w_d}$. Other works [86] have explored the further separation of the spatial modal functions into the product of one-dimensional modal functions depending upon the individual spatial directions, namely, $\boldsymbol{\mathcal{F}}^n(r,z) = \boldsymbol{\mathcal{F}}_r^n(r) \odot \boldsymbol{\mathcal{F}}_z^n(z)$, where $\odot$ represents the element-wise Hadamard product as defined in [87]. This approach can give excellent results as certain 2D or 3D domains (i.e. plates/beams) can easily be decomposed into a set of 1D domains, obtaining thus a great reduction in terms of computational effort. However, the drawback is that only simple geometries, typically with edges parallel to the Cartesian axis can be considered. Hence, in the context of MRI scanners where the goemetries are complex, the most appropriate choice is to represent the modal spatial function without assuming separability in space.

In (3.4), each term n of the modal series is sequentially computed through a Greedy algorithm [38]. For a given n^{th} term, the accumulated solution $\boldsymbol{\mathcal{Q}}^n = \boldsymbol{\mathcal{Q}}^n(r,z,w_1,\ldots,w_d)$ is expressed as

$$\begin{aligned} \boldsymbol{\mathcal{Q}}^n(r,z,w_1,\ldots,w_d) &= \sum_{m=1}^{n-1} \beta^m \boldsymbol{\mathcal{F}}^m(r,z) \prod_{i=1}^{d} \mathcal{G}_i^m(w_i) + \boldsymbol{f}(r,z) \prod_{i=1}^{d} \mathscr{g}_i(w_i) \\ &= \boldsymbol{\mathcal{Q}}^{n-1}(r,z,w_1,\ldots,w_d) + \boldsymbol{f}(r,z) \prod_{i=1}^{d} \mathscr{g}_i(w_i), \end{aligned} \tag{3.5}$$

where the approximation $\boldsymbol{f}(r,z) \prod_{i=1}^{d} \mathscr{g}_i(w_i)$ (lowercase) is assumed to converge to $\beta^m \boldsymbol{\mathcal{F}}^m(r,z) \prod_{i=1}^{d} \mathcal{G}_i^m(w_i)$ (uppercase) via a fixed-point Alternating Direction Scheme (ADS). When applying a standard Galerkin method [28] to the augmented weak form (3.1), a compatible virtual field to the field $\boldsymbol{\mathcal{Q}}(r,z,w_i,\ldots,w_d)$ is defined as

$$\begin{aligned} \delta\boldsymbol{\mathcal{Q}}(r,z,w_i,\ldots,w_d) :&= \delta\boldsymbol{f}(r,z) \prod_{i=1}^{d} \mathscr{g}_i(w_i) + \boldsymbol{f}(r,z)\delta\mathscr{g}_1(w_1) \prod_{i=2}^{d} \mathscr{g}_i(w_i) + \cdots \\ &+ \boldsymbol{f}(r,z) \prod_{i=1}^{d-1} \mathscr{g}_i(w_i)\delta\mathscr{g}_d(w_d), \end{aligned} \tag{3.6}$$

with the same separability as that of equation (3.4). The expressions for these two fields (3.5) and (3.6) can be substituted in the augmented weak form (3.1) in order to obtain the $d+1$ residual equations than will be solved during the offline stage, yielding the functions constituting the high-order parametric solution (3.4). These residuals are obtained by using the separability introduced in (3.5) and (3.6) as: Find $(\boldsymbol{f}, g_1, \dots, g_d) \in H^1(\Omega_p) \times L^2(\Omega_{w_1}) \times \dots \times L^2(\Omega_{w_d})$ such that

$$\mathcal{R}_{\boldsymbol{f}}(\delta \boldsymbol{f}; \boldsymbol{\mathcal{Q}}^{n-1}, \boldsymbol{f}, g_1, \dots, g_d) + \sum_{i=1}^{d} \mathcal{R}_{g_i}(\delta g_i; \boldsymbol{\mathcal{Q}}^{n-1}, \boldsymbol{f}, g_1, \dots, g_d) = 0, \tag{3.7}$$

for all $\delta \boldsymbol{f}, \delta g_i \in H^1_0(\Omega_p) \times L^2(\Omega_{\omega_1}) \times \dots \times L^2(\Omega_{\omega_d})$.

The Greedy algorithm starts by including first the Dirichlet boundary conditions in the first mode ($n = 1$), where the parametric functions $\prod_{i=1}^{d} \mathcal{G}_i^1$ are set equal to one, and $\mathcal{R}_{\boldsymbol{f}} = 0$ is solved in order to obtain $\boldsymbol{\mathcal{F}}^1$, which contains the correct values associated to the Dirichlet boundary, see Section 3.4. Subsequently, the fixed-point ADS algorithm is used to compute the converged quantities by updating one function at a time and assuming that the others are known. The steps followed are summarised as:

1. Assume that $\boldsymbol{f}^{[k]}$ and $g_2^{[k]}, \dots, g_d^{[k]}$ are known and solve a linear 1D problem to compute $g_1^{[k+1]} \in L^2(\Omega_{w_1})$ such that

$$\mathcal{R}_{g_1}(\delta g_1; \boldsymbol{\mathcal{Q}}^{n-1}, \boldsymbol{f}^{[k]}, g_1^{[k+1]}, g_2^{[k]}, \dots, g_d^{[k]}) = 0 \quad \forall \delta g_1 = 0, \tag{3.8}$$

and normalise the updated quantity $g_1^{[k+1]}$.

⋮ (Solve $\mathcal{R}_{g_i} = 0$ for $i = 2, \dots, d-1$.)

2. Assume that $\boldsymbol{f}^{[k]}$ and $g_1^{[k+1]}, \dots, g_{d-1}^{[k+1]}$ are known and solve a linear 1D problem to compute $g_d^{[k+1]} \in L^2(\Omega_{w_d})$ such that

$$\mathcal{R}_{g_d}(\delta g_d; \boldsymbol{\mathcal{Q}}^{n-1}, \boldsymbol{f}^{[k]}, g_1^{[k+1]}, \dots, g_d^{[k+1]}) = 0 \quad \forall \delta g_d = 0, \tag{3.9}$$

and normalise the updated quantity $g_d^{[k+1]}$.

3. Assume that $g_1^{[k+1]}, \dots, g_d^{[k+1]}$ are known and solve a 2D problem to compute $\boldsymbol{f}^{[k+1]} \in H^1(\Omega_p)$ such that

$$\mathcal{R}_{\boldsymbol{f}}(\delta \boldsymbol{f}; \boldsymbol{\mathcal{Q}}^{n-1}, \boldsymbol{f}^{[k+1]}, g_1^{[k+1]}, \dots, g_d^{[k+1]}) = 0 \quad \forall \delta \boldsymbol{f} = 0. \tag{3.10}$$

Note that $\boldsymbol{f}^{[k+1]}$ is only normalised when the ADS for a particular mode n is terminated.

The presented fixed-point ADS algorithm computes and normalises first the updated parametric functions g_i, whilst the spatial function $\boldsymbol{f}$ is updated at the end of the loop. The spatial function is only normalised when the ADS convergence is reached, where the converged functions are denoted with the superscript $(\cdot^{\infty})$. Then, the $n+1$ Greedy step is performed until convergence is achieved for this second iterative procedure. Note that the normalisation is described in Section 3.5 and the convergence criteria is detailed in Section 3.6.

The presented residual form is discretised using FEM, which will be thoroughly presented in Chapters 4 and 5. The generic high-dimensional PGD algorithm is graphically described in Figure 3.1.

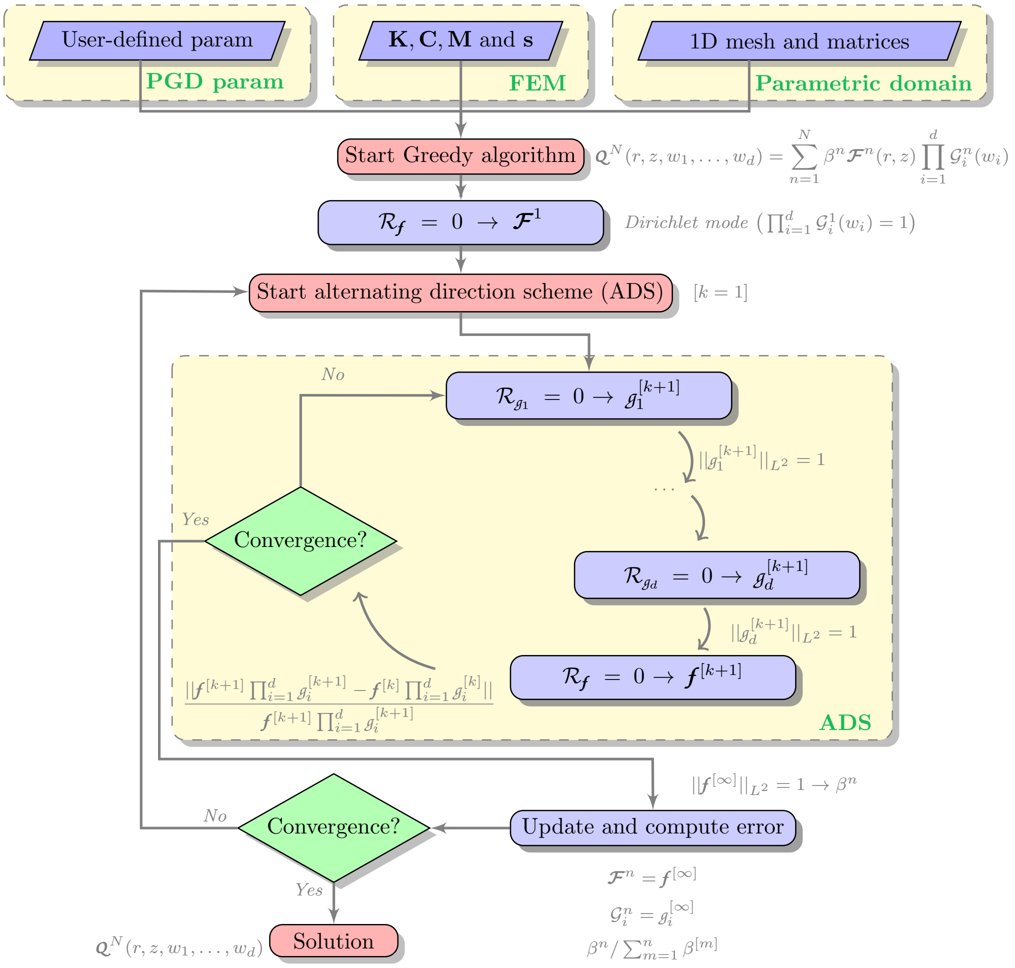
User-defined param
PGD param
$\mathbf{K}, \mathbf{C}, \mathbf{M}$ and $\mathbf{s}$
FEM
1D mesh and matrices
Parametric domain
Start Greedy algorithm
$\mathcal{Q}^N(r,z,w_1,\ldots,w_d) = \sum_{n=1}^{N} \beta^n \mathcal{F}^n(r,z) \prod_{i=1}^{d} \mathcal{G}_i^n(w_i)$
$\mathcal{R}_f = 0 \rightarrow \mathcal{F}^1$
Dirichlet mode $(\prod_{i=1}^d \mathcal{G}_i^1(w_i) = 1)$
Start alternating direction scheme (ADS)
$[k=1]$
No
$\mathcal{R}_{g_1} = 0 \rightarrow g_1^{[k+1]}$
$||g_1^{[k+1]}||_{L^2} = 1$
...
Yes
Convergence?
$\mathcal{R}_{g_d} = 0 \rightarrow g_d^{[k+1]}$
$||g_d^{[k+1]}||_{L^2} = 1$
$\mathcal{R}_f = 0 \rightarrow f^{[k+1]}$
$\frac{||f^{[k+1]} \prod_{i=1}^d g_i^{[k+1]} - f^{[k]} \prod_{i=1}^d g_i^{[k]}||}{f^{[k+1]} \prod_{i=1}^d g_i^{[k+1]}}$
ADS
$||f^{[\infty]}||_{L^2} = 1 \rightarrow \beta^n$
No
Convergence?
Update and compute error
Yes
$\mathcal{F}^n = f^{[\infty]}$
$\mathcal{G}_i^n = g_i^{[\infty]}$
$\beta^n / \sum_{m=1}^n \beta^{[m]}$
$\mathcal{Q}^N(r,z,w_1,\ldots,w_d)$
Solution

Figure 3.1: Flow chart algorithm; description of the d-dimensional PGD algorithm.

3.4 Non-homogeneous Dirichlet boundary conditions

The usual strategy in order to account for non-homogeneous Dirichlet boundary conditions consists in incorporating them into the first mode followed by the computation of the subsequent modes considering homogeneous Dirichlet boundary conditions [21]. Therefore, the PGD algorithm presented in Section 3.3 is implemented by separating the first mode form the summation as

$$\boldsymbol{\mathcal{Q}}^N(r,z,w_1,\dots,w_d) = \beta^1 \boldsymbol{\mathcal{F}}^1(r,z)\prod_{i=1}^{d}\mathcal{G}_i^1(w_i) + \sum_{n=2}^{N}\beta^n\boldsymbol{\mathcal{F}}^n(r,z)\prod_{i=1}^{d}\mathcal{G}_i^n(w_i), \qquad (3.11)$$

where the only difference is that in the first mode ($n = 1$), the parametric functions $\prod_{i=1}^{d}\mathcal{G}_i^1(w_i)$ are set equal to one and the spatial function $\boldsymbol{\mathcal{F}}^1(r,z)$ is sought in the space $X(\mathcal{A}_{\phi,D})\times Y(\boldsymbol{\mathcal{U}}_D)$, identical to the full order model problem (2.15), in order to satisfy the Dirichlet boundary conditions. Subsequently, the following modes ($n > 1$) are computed using the standard PGD algorithm, where the spatial functions $\boldsymbol{\mathcal{F}}^n(r,z)$ are computed assuming homogeneous Dirichlet boundary conditions in the space $X(0)\times Y(\mathbf{0})$, so they do not interact with the values obtained in the first mode in the non-homogenous Dirichlet boundary. Note that for the sake of simplicity, the PGD definition used later on in this thesis is given by equation (3.4), where no explicit distinction is made between the first and the rest of the modes.

3.5 Modal scaling

The spatial and parametric modes are normalised by a L^2 projection as mentioned in Section 3.3. The main computational advantage of this scaling is a better convergence of the algorithm as it will be discussed in Section 3.6. Hence, this section aims to detail the procedure in order to obtain the converged scaled modes and its scaling coefficients.

The fixed-point ADS starts with the approximation $\boldsymbol{f}^0(r,z)\prod_{i=1}^{d} g_i^0(w_i)$, where the superscript $(\cdot^0)$ indicates the initial guess for this iterative procedure. Then, the algorithm iterates until convergence is reached, where the converged functions $\boldsymbol{f}^\infty(r,z)\prod_{i=1}^{d} g_i^\infty(w_i)$ are obtained. As it can be seen in Figure 3.1, the parametric functions g_i, with $i = 1,\dots,d$ are normalised inside the iterative procedure, while the spatial function is only normalised once convergence is achieved. Thus, the scaling coefficients β^n appearing in (3.4) for a particular mode n are obtained only through the spatial functions as[2]

$$\beta^n = ||\boldsymbol{f}^{[\infty]}(r,z)||_{L^2(\Omega_p)}. \qquad (3.12)$$

In the literature [21,38,42,44], this quantity β^n is sometimes referred as amplitude of the n^{th} term of (3.4). Note that some further subtleties related to the computation of the scaling coefficients will be highlighted when presenting the PGD technique applied to the coupled magneto-mechanical problem in Section 4.3.2.

3.6 Convergence criteria

Two iterative algorithms are involved in the computation of the PGD approximation formulated in Section 3.3, namely, the Greedy algorithm that adds an

---

[2] Recall that the notation $(\cdot^\infty)$ was defined in Section 3.3.

n^{th} mode to the solution and the fixed-point alternating directions scheme which computes the converged functions $\beta^m \boldsymbol{\mathcal{F}}^m(r,z)\prod_{i=1}^d \mathcal{G}_i^m(w_i)$ from the approximation $\boldsymbol{f}(r,z)\prod_{i=1}^d g_i(w_i)$. Therefore, two stopping criteria will be defined in this section in order to determine when convergence is reached for a given tolerance.

3.6.1 Alternating Direction Scheme (ADS)

The fixed-point ADS computes new parametric and spatial functions iteratively by updating one function assuming that the others are known. As shown in Figure 3.1, this iterative procedure computes an updated function $[k+1]$ from an already known $[k]$. An option widely used, see [21], in order to stop the ADS is the measurement of the difference between iterations $[k+1]$ and $[k]$ and the check of whether this difference is less than a given tolerance tol_{FP}. Using this criterion, the errors are computed as

$$e_{FP}^{\boldsymbol{f}} = \frac{||\Delta \boldsymbol{f}||_{L^2(\Omega_p)}}{||\boldsymbol{f}^{[k+1]}||_{L^2(\Omega_p)}} \leq tol_{FP}, \quad e_{FP}^{g_i} = \frac{||\Delta g_i||_{L^2(\Omega_{w_i})}}{||g_i^{[k+1]}||_{L^2(\Omega_{w_i})}} \leq tol_{FP}, \tag{3.13}$$

for $i = 1,\ldots,d$, where the incremental functions are defined as $\Delta \boldsymbol{f} := \boldsymbol{f}^{[k+1]} - \boldsymbol{f}^{[k]}$ and $\Delta g_i := g_i^{[k+1]} - g_i^{[k]}$.

However, the solution of the linearised frequency-based (2.10) is complex and thus, some numerical difficulties may arise when using the stopping criterion (3.13). For instance, it has been noticed how the spatial $\boldsymbol{f}(r,z)$ and parametric $g_i(w_i)$ functions may be increasing and decreasing their magnitude[3], respectively, where in that case the criterion (3.13) would be never satisfied. When looking at the accumulated PGD definition (3.5), it can be seen that the important quantity that has to reach convergence is the product of both functions $\boldsymbol{f}(r,z)\prod_{i=1}^d g_i(w_i)$. Therefore, an alternative measure of the ADS error for a particular mode n is presented as

$$e_{FP}^{n} = \frac{||\boldsymbol{f}^{[k+1]}\prod_{i=1}^d g_i^{[k+1]} - \boldsymbol{f}^{[k]}\prod_{i=1}^d g_i^{[k]}||_{L^2(\Omega)}}{||\boldsymbol{f}^{[k+1]}\prod_{i=1}^d g_i^{[k+1]}||_{L^2(\Omega)}} \leq tol_{FP}, \tag{3.14}$$

which overcomes the issues previously mentioned. Note that although the L^2 norm is now computed in the entire space $\Omega = \Omega_p \times \Omega_q$, the expression (3.14) can be easily separated. For instance, in terms of implementation, the denominator is expanded as[4]

---

[3] Note that $\boldsymbol{f}(r,z)$ and $g_i(w_i)$ will be complex quantities in the context of this thesis and, thus, their magnitude may increase and decrease whilst the overall product converges.

$$
\begin{aligned}
&||\boldsymbol{\mathscr{f}}^{[k+1]} \prod_{i=1}^{d} \mathscr{g}_i^{[k+1]} ||_{L^2(\Omega)} \\
=&\Big(\int_{\Omega_p} \int_{\Omega_{w_1}} \cdots \int_{\Omega_{w_d}} \boldsymbol{\mathscr{f}}^{[k+1]} \prod_{i=1}^{d} \mathscr{g}_i^{[k+1]} \,\mathrm{d}\Omega \Big) \Big(\int_{\Omega_p} \int_{\Omega_{w_1}} \cdots \int_{\Omega_{w_d}} \overline{\boldsymbol{\mathscr{f}}}^{[k+1]} \prod_{i=1}^{d} \overline{\mathscr{g}}_i^{[k+1]} \,\mathrm{d}\Omega \Big) \\
=&\int_{\Omega_p} \boldsymbol{\mathscr{f}}^{[k+1]} \cdot \overline{\boldsymbol{\mathscr{f}}}^{[k+1]} \,\mathrm{d}\Omega_p \prod_{i=1}^{d} \Big[\int_{\Omega_{w_i}} \mathscr{g}_i^{[k+1]} \overline{\mathscr{g}}_i^{[k+1]} \,\mathrm{d}\Omega_{w_i} \Big],
\end{aligned}
\tag{3.15}
$$

where now each integral can be integrated in the separated domains.

3.6.2 Greedy algorithm

Once the ADS has reached a converged modal solution n and thus, (3.14) is satisfied, the PGD algorithm jumps into the next modal computation $n+1$. This second iterative process will enrich the accumulated solution and hence, a second stopping criterion has to be defined in order to stop this modal addition. With this aim, it is presented in [21] the convergence measure e_N^n that computes the importance of a certain computed mode n with respect to the total accumulated solution. This convergence measure is computed as

$$
\begin{aligned}
e_N^n &= \frac{||\beta^n \boldsymbol{\mathcal{F}}^n(r,z) \prod_{i=1}^{d} \mathcal{G}_i^n(w_i) ||_{L^2(\Omega)}}{||\boldsymbol{q}^n(r,z,w_1,\ldots,w_d)||_{L^2(\Omega)}} \\
&= \frac{||\beta^n \boldsymbol{\mathcal{F}}^n(r,z) \prod_{i=1}^{d} \mathcal{G}_i^n(w_i) ||_{L^2(\Omega)}}{\sum_{m=1}^{n} ||\beta^{[m]} \boldsymbol{\mathcal{F}}^{[m]}(r,z) \prod_{i=1}^{d} \mathcal{G}_i^{[m]}(w_i) ||_{L^2(\Omega)}} \leq tol_N,
\end{aligned}
\tag{3.16}
$$

where tol_N is the required tolerance in order to stop this iterative procedure. This error measure will start at value equal to 1 and it will be descending towards 0 until the specified tolerance is reached. However, since both spatial and parametric functions have been L^2 normalised the expression (3.16) can be simplified to avoid computing several L^2 norms inside each iterative loop. Therefore, the expression that will be in fact implemented is a much simpler one, that reads

$$
e_N^n = \frac{\beta^n}{\sum_{m=1}^{n} \beta^{[m]}} \leq tol_N, \tag{3.17}
$$

where the importance of the modal scaling is now clearly stated, since the expression has been simplified to a simple calculation. This quantity can also be understood as the relative amplitude of the term n with respect to the total solution computed. Note that this expression will be slightly modified when applying the PGD algorithm to the problem of interest, a coupled magneto-mechanical problem in Chapters 4 and 5.

---

[4] Recall that the overline symbol $(\overline{\cdot})$ denotes the complex conjugate of a certain quantity.

3.7 Online PGD stage

The main advantage of the PGD technique is that it enables the encapsulation of all the costly computations in the so-called offline stage described in Section 3.3, obtaining an offline solution that includes all the dimensions considered. For the case presented, the $d+2$ dimensional space $\Omega = \Omega_p \times \Omega_q$ depends on $(r, z, w_1, \dots, w_d)$. Once the single offline computation is stored, the online PGD stage consists of two computationally efficient steps:

1. Specification of the parameters of interest: the offline information has been computed for the whole range of parameters $(r, z, w_1, \dots, w_d)$ of interest, and thus, the first step is to define a set of discrete vectors $(\mathbf{r}, \mathbf{z}, \mathbf{w}_1, \dots, \mathbf{w}_d)$[5] containing the desired values that will be interpolated in the online stage.

2. Interpolation and construction of the accumulated solution: the second step can be divided in two sub-steps that will be performed sequentially for $n = 1, \dots, N$:

    (a) Particularisation of $\boldsymbol{\mathcal{F}}^n(r, z)$ and $\prod_{i=1}^{d} \mathcal{G}_i^n(w_i)$: the computed spatial and parametric functions are interpolated for the desired set of parameters $(\mathbf{r}, \mathbf{z}, \mathbf{w}_1, \dots, \mathbf{w}_d)$, obtaining the particularised spatial and parametric functions $\boldsymbol{\mathcal{F}}^n(\mathbf{r}, \mathbf{z})$ and $\prod_{i=1}^{d} \mathcal{G}_i^n(\mathbf{w}_i)$, respectively.

    (b) Modal addition: a simple modal enrichment is performed in order to increase the accuracy of the solution $\boldsymbol{\mathcal{Q}}^n(\mathbf{r}, \mathbf{z}, \mathbf{w}_1, \dots, \mathbf{w}_d)$, obtaining the final solution $\boldsymbol{\mathcal{Q}}^N(\mathbf{r}, \mathbf{z}, \mathbf{w}_1, \dots, \mathbf{w}_d)$ at the end of the loop $(n = N)$.

The flow chart algorithm of the online PGD stage is presented in Figure 3.2. The great advantage of this online stage is that it is computationally very efficient, being able to achieve real-time simulations and multiple-query input/output evaluations. Since the online PGD stage involves a minimal computational cost, this stage can be performed in portable devices such as smartphones or tablets. See Appendix E for an example of a graphical user interface for the online PGD stage in the context of MRI scanner design.

---

[5] The Roman bold font denotes the set of values of a certain dimension that will be evaluated in the online PGD stage.

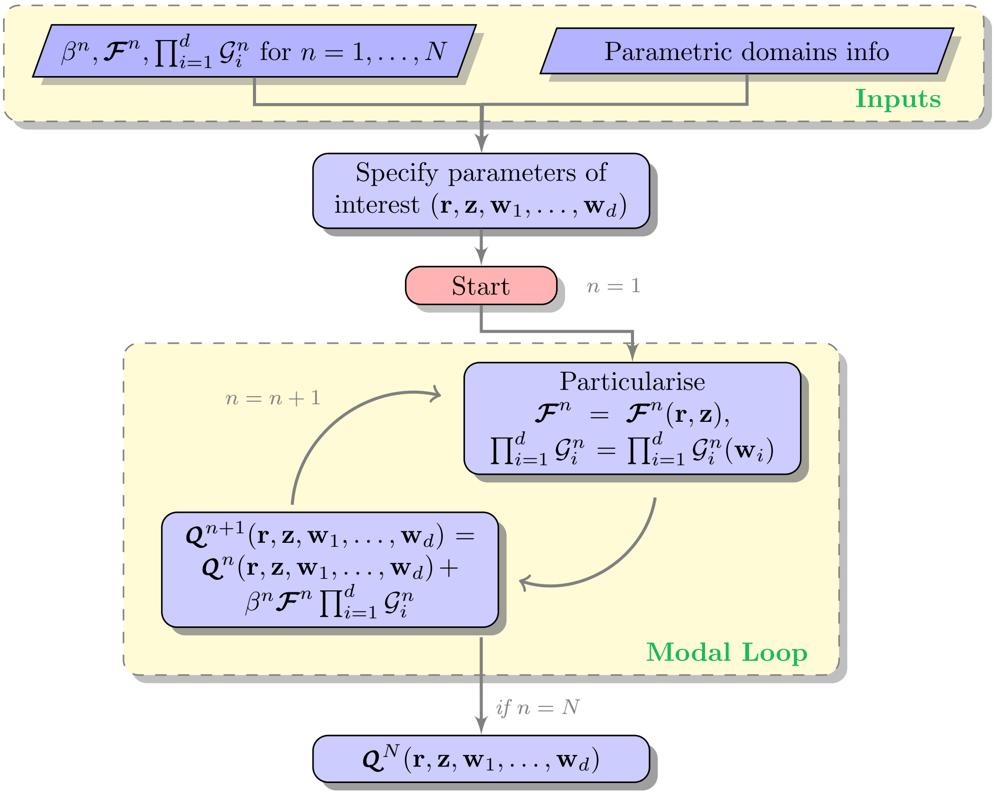
$\beta^n, \boldsymbol{\mathcal{F}}^n, \prod_{i=1}^d \mathcal{G}_i^n$ for $n = 1, \dots, N$
Parametric domains info
Inputs
Specify parameters of interest $(\mathbf{r}, \mathbf{z}, \mathbf{w}_1, \dots, \mathbf{w}_d)$
Start
$n = 1$
$n = n + 1$
Particularise $\boldsymbol{\mathcal{F}}^n = \boldsymbol{\mathcal{F}}^n(\mathbf{r}, \mathbf{z})$, $\prod_{i=1}^d \mathcal{G}_i^n = \prod_{i=1}^d \mathcal{G}_i^n(\mathbf{w}_i)$
$\boldsymbol{\mathcal{Q}}^{n+1}(\mathbf{r}, \mathbf{z}, \mathbf{w}_1, \dots, \mathbf{w}_d) = \boldsymbol{\mathcal{Q}}^n(\mathbf{r}, \mathbf{z}, \mathbf{w}_1, \dots, \mathbf{w}_d) + \beta^n \boldsymbol{\mathcal{F}}^n \prod_{i=1}^d \mathcal{G}_i^n$
Modal Loop
if $n = N$
$\boldsymbol{\mathcal{Q}}^N(\mathbf{r}, \mathbf{z}, \mathbf{w}_1, \dots, \mathbf{w}_d)$

Figure 3.2: Flow chart algorithm; description of the d-dimensional online PGD stage.

3.8 Chapter summary

This chapter has presented a general ROM framework for coupled magneto-mechanical problems through the use of the PGD technique, which includes the axisymmetric two-dimensional (r, z) space Ω_p and a generic d-dimensional parametric space Ω_q to find an offline solution in a high-dimensional space $\Omega_p \times \Omega_q$. The formulation presented together with some numerical considerations regarding the inclusion of non-homogeneous Dirichlet boundary conditions, the scaling of the PGD modes and the convergence criteria of the iterative algorithms, constitute the so-called offline PGD stage. On the other hand, the online stage has been also described, which consists in a fast evaluation of the precomputed high-dimensional parametric solution that can be performed in real time.

This generic framework will be particularised in Chapters 4 and 5 for the problem of interest by using two different approaches; a monolithic frequency-based formulation and a staggered high-dimensional formulation, respectively. Both formulations will be validated and discussed in the context of MRI scanner design using the two industrially relevant problems presented in Section 2.8.

Chapter 4

Monolithic frequency-based Proper Generalised Decomposition technique

4.1 Introduction

One crucial study performed by the industrial partner Siemens Healthineers consists in the repetitive computation of the solution of the coupled MRI magneto-mechanical problem for a range of exciting angular frequencies ω, resulting in a frequency sweep in which the solution fields are postprocessed in order to obtain quantities of interest, namely, dissipated power and kinetic energy (2.34). As stated in Section 1.1.3, a large number of evaluations of the problem can lead to a prohibitively high increase in computational cost and, thus, the PGD technique is seen as a fundamental tool in order to drastically reduce the cost by circumventing the solution of the full order model (direct problem) for each frequency of interest.

From the goals of the thesis stated in Section 1.4, this chapter aligns with the following objectives: "*To develop a frequency-based PGD formulation for coupled magneto-mechanical problems*", "*To propose a regularised-adaptive strategy in order to increase the PGD accuracy and robustness*" and "*To develop a graphical user interface for the online PGD stage that can be used in the industry environment*". The content of this chapter summarises the work published by the author of the thesis in [88].

As a first step, this chapter presents a particularisation of the general PGD formulation, see Chapter 3, for a high-dimensional space $\Omega_p \times \Omega_q$, where the parametric space is now a one-dimensional domain $\Omega_q = \Omega_\omega$ whilst the spatial space remains the same, a two-dimensional axisymmetric (r, z) domain. Note that a monolithic approach, see Section 2.5.1, is first pursued in order to compute a single offline PGD solution for the entire problem.

4.2 Augmented weak formulation

The monolithic approach is chosen as a first attempt to implement the frequency-based PGD technique and therefore, the augmented weak formulation is constructed from the monolithic space-based weak form (2.15) by integrating over frequency and space as follows: Find $\boldsymbol{\mathcal{Q}} \in \mathcal{X}(\mathcal{A}_{\phi,D}) \times \mathcal{Y}(\boldsymbol{\mathcal{U}}_D)$ such that

$$\mathcal{W}_K(\boldsymbol{\mathcal{Q}}, \delta\boldsymbol{\mathcal{Q}}) + \mathrm{i}\mathcal{W}_C(\boldsymbol{\mathcal{Q}}, \delta\boldsymbol{\mathcal{Q}}) - \mathcal{W}_M(\boldsymbol{\mathcal{Q}}, \delta\boldsymbol{\mathcal{Q}}) = \mathcal{S}(\delta\boldsymbol{\mathcal{Q}}) \qquad \forall \delta\boldsymbol{q} \in \mathcal{X}(0) \times \mathcal{Y}(0), \tag{4.1}$$

where the augmented compact forms are defined as

$$\mathcal{W}_K(\boldsymbol{\mathcal{Q}}, \delta\boldsymbol{\mathcal{Q}}) := \mathcal{W}_K^A(\mathcal{A}_\phi, \delta\mathcal{A}_\phi) + \mathcal{W}_K^u(\boldsymbol{\mathcal{U}}, \delta\boldsymbol{\mathcal{U}}) + \mathcal{S}^u(\mathcal{A}_\phi, \delta\boldsymbol{\mathcal{U}}), \tag{4.2a}$$

$$\mathcal{W}_C(\boldsymbol{\mathcal{Q}}, \delta\boldsymbol{\mathcal{Q}}) := \mathcal{W}_C^A(\mathcal{A}_\phi, \delta\mathcal{A}_\phi), \tag{4.2b}$$

$$\mathcal{W}_M(\boldsymbol{\mathcal{Q}}, \delta\boldsymbol{\mathcal{Q}}) := \mathcal{W}_M^u(\boldsymbol{\mathcal{U}}, \delta\boldsymbol{\mathcal{U}}), \tag{4.2c}$$

$$\mathcal{S}(\delta\boldsymbol{\mathcal{Q}}) := \mathcal{S}^A(\delta\mathcal{A}_\phi). \tag{4.2d}$$

with

$$\mathcal{W}_K^A(a, b) := \int_{\Omega_\omega} W_K^A(a, b)\, \mathrm{d}\omega, \tag{4.3a}$$

$$\mathcal{W}_C^A(a, b) := \int_{\Omega_\omega} \omega W_C^A(a, b)\, \mathrm{d}\omega, \tag{4.3b}$$

$$\mathcal{S}^A(b) := \int_{\Omega_\omega} S^A(b)\, \mathrm{d}\omega, \tag{4.3c}$$

$$\mathcal{W}_K^u(\boldsymbol{a}, \boldsymbol{b}) := \int_{\Omega_\omega} W_K^{uu}(\boldsymbol{a}, \boldsymbol{b})\, \mathrm{d}\omega, \tag{4.3d}$$

$$\mathcal{W}_M^u(\boldsymbol{a}, \boldsymbol{b}) := \int_{\Omega_\omega} \omega^2 W_M^{uu}(\boldsymbol{a}, \boldsymbol{b})\, \mathrm{d}\omega, \tag{4.3e}$$

$$\mathcal{S}^u(a, \boldsymbol{b}) := \int_{\Omega_\omega} W_K^{uA}(a, \boldsymbol{b})\, \mathrm{d}\omega, \tag{4.3f}$$

4.3 PGD for magneto-mechanical problems

In this section, the Proper Generalised Decomposition described in Chapter 3 is applied to the coupled magneto-mechanical problem presented in Chapter 2 by considering the angular frequency ω as a parameter in the offline PGD computation. Therefore, the three-dimensional parametric solution $\boldsymbol{\mathcal{Q}} = \boldsymbol{\mathcal{Q}}(r, z, \omega)$ is sought in the higher-dimensional space $\Omega_p \times \Omega_q$, where in this case $\Omega_q = \Omega_\omega$ as mentioned in Section 4.1. The general high-dimensional expression (3.4) is then written as

$$\boldsymbol{\mathcal{Q}}(r, z, \omega) \approx \boldsymbol{\mathcal{Q}}^N(r, z, \omega) = \sum_{n=1}^{N} \boldsymbol{\beta}^n \odot \boldsymbol{F}^n(r, z) G^n(\omega), \tag{4.4}$$

where each n^{th} term of the above series is the product of normalised separable functions $\boldsymbol{F}^n(r, z) \in X(0) \times Y(\boldsymbol{0})$ and $G^n(\omega) \in Z = L^2(\Omega_\omega)$. As mentioned in

Section 3.4, the non-homogeneous Dirichlet boundary conditions are incorporated within the first PGD mode. In addition, a subtle difference between (3.4) and (4.4) is that the scaling coefficients or modal weights $\boldsymbol{\beta}^n$ are no longer scalars but vectors, with $\odot$ representing the element-wise Hadamard product introduced in Section 3.3. The PGD definition (4.4) may then be written as

$$\boldsymbol{\mathcal{Q}}^N(r,z,\omega) = \begin{bmatrix} \mathcal{A}_\phi \\ \mathcal{U}_r \\ \mathcal{U}_z \end{bmatrix}^n (r,z,\omega) = \sum_{n=1}^{N} \begin{bmatrix} \beta_{\mathcal{A}_\phi} \\ \beta_{\boldsymbol{\mathcal{U}}} \\ \beta_{\boldsymbol{\mathcal{U}}} \end{bmatrix}^n \odot \begin{bmatrix} F_{\mathcal{A}_\phi} \\ F_{\mathcal{U}_r} \\ F_{\mathcal{U}_z} \end{bmatrix}^n (r,z) G^n(\omega), \tag{4.5}$$

where the importance of exploiting vectorial scaling lies on the fact that the two different physics can exhibit different scales and lead to ill-conditioning of the overall problem. For a given n^{th} term of above series (4.4), the accumulated solution $\boldsymbol{\mathcal{Q}}^n(r,z,\omega)$ can be written as

$$\boldsymbol{\mathcal{Q}}^n(r,z,\omega) = \boldsymbol{\mathcal{Q}}^{n-1}(r,z,\omega) + \boldsymbol{f}(r,z)g(\omega) \qquad\qquad n = 1,2\cdots N, \tag{4.6}$$

where $\boldsymbol{f}(r,z)g(\omega)$ denotes an approximation which is assumed to converge to $\boldsymbol{\beta}^n \odot \boldsymbol{F}^n(r,z)G^n(\omega)$ as detailed in Chapter 3. A compatible virtual field for $\boldsymbol{f}(r,z)g(\omega)$ is then chosen with the same separability of (4.6) as

$$\delta\boldsymbol{\mathcal{Q}}(r,z,\omega) = \delta\boldsymbol{f}(r,z)g(\omega) + \boldsymbol{f}(r,z)\delta g(\omega), \tag{4.7}$$

with $\delta\boldsymbol{f}(r,z) \in X(0) \times Y(\boldsymbol{0})$ and $\delta g(\omega) \in Z$. In this case, substitution of (4.6) and (4.7) into the augmented weak form (4.1), permits the alternating directions fixed-point algorithm for the computation of the n^{th} term in (4.4) to be formulated as: Find $(\boldsymbol{f}, g) \in X(0) \times Y(\boldsymbol{0}) \times Z$ such that

$$\mathcal{R}_f(\delta\boldsymbol{f}; \boldsymbol{q}^{n-1}, \boldsymbol{f}, g) + \mathcal{R}_g(\delta g; \boldsymbol{q}^{n-1}, \boldsymbol{f}, g) = 0 \qquad \forall(\delta\boldsymbol{f}, \delta g) \in X(0) \times Y(0) \times Z, \tag{4.8}$$

with

$$\begin{aligned} \mathcal{R}_f(\delta\boldsymbol{f}; \boldsymbol{q}^{n-1}, \boldsymbol{f}, g) :=\ & G_0(g,g)W_K(\boldsymbol{f}, \delta\boldsymbol{f}) + \mathrm{i}G_1(g,g)W_C(\boldsymbol{f}, \delta\boldsymbol{f}) \\ & - G_2(g,g)W_M(\boldsymbol{f}, \delta\boldsymbol{f}) - G_0(1,g)S(\delta\boldsymbol{f}) \qquad\qquad (4.9\text{a}) \\ & + \mathcal{W}_K(\boldsymbol{q}^{n-1}, g\delta\boldsymbol{f}) + \mathrm{i}\mathcal{W}_C(\boldsymbol{q}^{n-1}, g\delta\boldsymbol{f}) - \mathcal{W}_M(\boldsymbol{q}^{n-1}, g\delta\boldsymbol{f}), \\ \mathcal{R}_g(\delta g; \boldsymbol{q}^{n-1}, \boldsymbol{f}, g) :=\ & G_0(g,\delta g)W_K(\boldsymbol{f}, \boldsymbol{f}) + \mathrm{i}G_1(g,\delta g)W_C(\boldsymbol{f}, \boldsymbol{f}) \\ & - G_2(g,\delta g)W_M(\boldsymbol{f}, \boldsymbol{f}) - G_0(1,\delta g)S(\boldsymbol{f}) \qquad\qquad (4.9\text{b}) \\ & + \mathcal{W}_K(\boldsymbol{q}^{n-1}, \boldsymbol{f}\delta g) + \mathrm{i}\mathcal{W}_C(\boldsymbol{q}^{n-1}, \boldsymbol{f}\delta g) - \mathcal{W}_M(\boldsymbol{q}^{n-1}, \boldsymbol{f}\delta g), \end{aligned}$$

where

$$G_0(a,b) := \int_{\Omega_\omega} a\bar{b}\,\mathrm{d}\omega, \quad G_1(a,b) := \int_{\Omega_\omega} a\bar{b}\omega\,\mathrm{d}\omega, \quad G_2(a,b) := \int_{\Omega_\omega} a\bar{b}\omega^2\,\mathrm{d}\omega. \tag{4.10}$$

4.3.1 Alternating direction scheme

In order to solve (4.8), the $[k]$-iterative ADS method is typically preferred [21]; first solving for $\boldsymbol{f}^{[k+1]}$ based on a known value of $g^{[k]}$ and then updating $g^{[k+1]}$ with the newly computed $\boldsymbol{f}^{[k+1]}$. The ADS method can be summarised as: Find $(\boldsymbol{f}^{[k+1]}, g^{[k+1]}) \in X(0) \times Y(\boldsymbol{0}) \times Z$ such that

$$\mathcal{R}_{\boldsymbol{f}}(\delta \boldsymbol{f}; \boldsymbol{q}^{n-1}, \boldsymbol{f}^{[k+1]}, g^{[k]}) = 0, \quad \mathcal{R}_g(\delta g; \boldsymbol{q}^{n-1}, \boldsymbol{f}^{[k+1]}, g^{[k+1]}) = 0, \tag{4.11}$$

for all $(\delta \boldsymbol{f}, \delta g) \in X(0) \times Y(0) \times Z$, where $[k] = 1, 2, \ldots$ denotes the fixed-point iteration. The stopping criteria was presented in Section 3.6. Alternatively, the solution fields $\boldsymbol{f}^{[k+1]}$ and $g^{[k+1]}$ can be written as

$$\boldsymbol{f}^{[k+1]} = \boldsymbol{f}^{[k]} + \Delta \boldsymbol{f}, \quad g^{[k+1]} = g^{[k]} + \Delta g, \tag{4.12}$$

and, thus, (4.11) can be re-written by making use of the concept of directional derivatives [84] as: Find $(\Delta \boldsymbol{f}, \Delta g) \in X(0) \times Y(\boldsymbol{0}) \times Z$ such that

$$D\mathcal{R}_{\boldsymbol{f}}(\delta \boldsymbol{f}; \boldsymbol{f}^{[k]}, g^{[k]})[\Delta \boldsymbol{f}] = -\mathcal{R}_{\boldsymbol{f}}(\delta \boldsymbol{f}; \boldsymbol{q}^{n-1}, \boldsymbol{f}^{[k]}, g^{[k]}), \tag{4.13a}$$

$$D\mathcal{R}_g(\delta g; \boldsymbol{f}^{[k+1]}, g^{[k]})[\Delta g] = -\mathcal{R}_g(\delta g; \boldsymbol{q}^{n-1}, \boldsymbol{f}^{[k+1]}, g^{[k]}), \tag{4.13b}$$

for all $(\delta \boldsymbol{f}, \delta g) \in X(0) \times Y(\boldsymbol{0}) \times Z$. The above residual equations (4.13) can be sequentially solved for $\Delta \boldsymbol{f}$ and Δg in order to iteratively evolve the ADS algorithm as shown in (4.12). The directional derivatives appearing in (4.13) can be expanded as

$$\begin{aligned} D\mathcal{R}_{\boldsymbol{f}}(\delta \boldsymbol{f}; \boldsymbol{f}, g)[\Delta \boldsymbol{f}] = {} & G_0(g,g) W_K(\Delta \boldsymbol{f}, \delta \boldsymbol{f}) + G_1(g,g) W_C(\Delta \boldsymbol{f}, \delta \boldsymbol{f}) \\ & - G_2(g,g) W_M(\Delta \boldsymbol{f}, \delta \boldsymbol{f}) \end{aligned} \tag{4.14a}$$

$$\begin{aligned} D\mathcal{R}_g(\delta g; \boldsymbol{f}, g)[\Delta g] = {} & W_K(\boldsymbol{f}, \boldsymbol{f}) G_0(\Delta g, \delta g) + W_C(\boldsymbol{f}, \boldsymbol{f}) G_1(\Delta g, \delta g) \\ & - W_M(\boldsymbol{f}, \boldsymbol{f}) G_2(\Delta g, \delta g), \end{aligned} \tag{4.14b}$$

and the residuals have been already defined in (4.9).

4.3.2 Greedy algorithm convergence

The generic stopping criteria used to monitor and control the number of modes added to the series of the generic PGD definition (3.4) has been defined in Section 3.6.2. Following the same idea previously presented, the monolithic frequency-based PGD technique (4.4) requires the monitoring of the following two error norms

$$e^n_{EM,N} = \frac{\beta^n_{\mathcal{A}_\phi}}{\sum_{m=1}^{n} \beta^{[m]}_{\mathcal{A}_\phi}} \leq tol_N, \qquad e^n_{M,N} = \frac{\beta^n_{\boldsymbol{u}}}{\sum_{m=1}^{n} \beta^{[m]}_{\boldsymbol{u}}} \leq tol_N, \tag{4.15}$$

which allows the independent control of the convergence of the vector potential and the displacement field vectors of the PGD approximation.

4.3.3 Finite element discretisation

This Section briefly presents the discretised problem (4.13) using the standard finite element Bubnov-Galerkin approximation (often known as simply Galerkin). The computational domain will be discretised into an unstructured triangular mesh, defining a non-overlapping partition $(\mathcal{V}, \mathcal{E}, \mathcal{I})$, where $\mathcal{V}$ denotes the set of vertices, $\mathcal{E}$ the set of edges and $\mathcal{I}$ the set of elements. In each element, the H^1 conforming hierarchic finite element basis functions [89] are employed. Hence, the spatial discretisation of the fields $\mathcal{A}_\phi$ and $\boldsymbol{\mathcal{U}}$ allows an arbitrary increase in element order p and local refinement of the mesh spacing h. The discretised system is obtained by replacing the fields $\Delta \boldsymbol{f}$, $\delta \boldsymbol{f}$, Δg and δg in (4.13) by the discretised fields

$$\begin{aligned} \Delta \boldsymbol{f} &= \sum_{a=1}^{P} N_a \Delta \mathbf{f}_a, & \delta \boldsymbol{f} &= \sum_{b=1}^{P} N_b \delta \mathbf{f}_b, \\ \Delta g &= \sum_{a=1}^{Q} N_a \Delta \mathrm{g}_a, & \delta g &= \sum_{b=1}^{Q} N_b \delta \mathrm{g}_b, \end{aligned} \tag{4.16}$$

where N_a is a typical shape function and $P = P_{\mathcal{V}} + P_{\mathcal{E}} + P_{\mathcal{I}}$ and $Q = Q_{\mathcal{V}} + Q_{\mathcal{E}} + Q_{\mathcal{I}}$ are the number of degrees of freedom of the spatial and frequency (parametric) problems, respectively. The global system is constructed from the elemental matrices and vectors by a standard assembly procedure [28]. Thus, the global discrete expression of the spatial problem (4.13a) is

$$(g_0 \mathbf{K} + \mathrm{i} g_1 \mathbf{C} - g_2 \mathbf{M}) \Delta \mathbf{f} = -\mathbf{R}_{\boldsymbol{f}}(\boldsymbol{f}^{[k]}, g^{[k]}). \tag{4.17}$$

Note that here, and in the following, Roman boldface font is used to describe discrete matrix/vector quantities. The discretised version of the residual is defined as

$$\mathbf{R}_{\boldsymbol{f}}(\boldsymbol{f}, g) := (g_0 \mathbf{K} + \mathrm{i} g_1 \mathbf{C} - g_2 \mathbf{M}) \mathbf{f} - g_0^s \mathbf{s} + \sum_{m=1}^{n-1} \left[g_0^{[m]} \mathbf{K} + \mathrm{i} g_1^{[m]} \mathbf{C} - g_2^{[m]} \mathbf{M} \right] \mathbf{F}^{[m]}, \tag{4.18}$$

with the following scalar quantities

$$\begin{aligned} g_0 &:= G_0(g, g), & g_0^{[m]} &:= G_0(G^{[m]}, g), \\ g_1 &:= G_1(g, g), & g_1^{[m]} &:= G_1(G^{[m]}, g), \\ g_2 &:= G_2(g, g), & g_2^{[m]} &:= G_2(G^{[m]}, g). \\ g_0^s &:= G_0(1, g), \end{aligned} \tag{4.19}$$

Similarly, the problem on the frequency domain (4.13b) can be written in its discrete from as

$$(k \mathbf{G}_0 + \mathrm{i} c \mathbf{G}_1 - m \mathbf{G}_2) \Delta \mathbf{g} = -\mathbf{R}_g(\boldsymbol{f}^{[k+1]}, g^{[k]}), \tag{4.20}$$

where the residual is defined as

$$\begin{aligned}\mathbf{R}_g(\boldsymbol{f}, g) := {}& (k\mathbf{G}_0 + \mathrm{i}c\mathbf{G}_1 - m\mathbf{G}_2)\mathbf{g} - s\mathbf{g}_1 \\ &+ \sum_{m=1}^{n-1} \left[k^{[m]}\mathbf{G}_0 + \mathrm{i}c^{[m]}\mathbf{G}_1 - m^{[m]}\mathbf{G}_2\right]\mathbf{G}^{[m]},\end{aligned} \tag{4.21}$$

with the following scalar quantities

$$\begin{aligned} k &:= W_K(\boldsymbol{f}, \boldsymbol{f}), \\ c &:= W_C(\boldsymbol{f}, \boldsymbol{f}), \\ m &:= W_M(\boldsymbol{f}, \boldsymbol{f}), \\ s &:= S(\boldsymbol{f}), \end{aligned} \qquad \begin{aligned} k^{[m]} &:= W_K(\boldsymbol{F}^{[m]}, \boldsymbol{f}), \\ c^{[m]} &:= W_C(\boldsymbol{F}^{[m]}, \boldsymbol{f}), \\ m^{[m]} &:= W_M(\boldsymbol{F}^{[m]}, \boldsymbol{f}). \end{aligned} \tag{4.22}$$

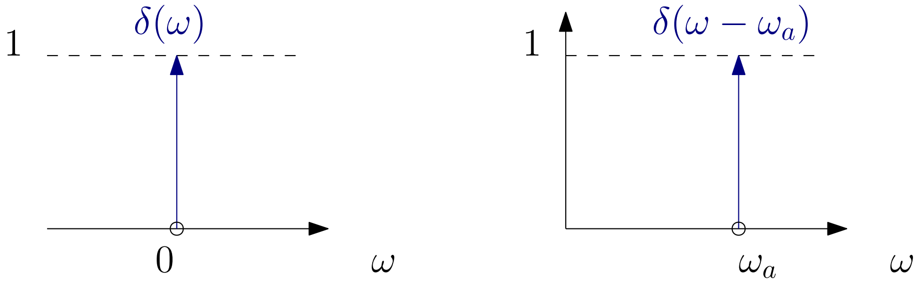

Figure 4.1: Visualisation of the dirac Delta function, which has a value equal to one in a particular point ω_a and zero everywhere else.

The monolithic frequency-based PGD technique has been found to perform with better accuracy when using an alternative Petrov-Galerkin methodology [90] when solving (4.13b), where the test function δg associated to a frequency ω_a is chosen to be the Dirac delta distribution defined as $\delta g = \delta(\omega - \omega_a)$, see Figure 4.1. This alternative approach allows to completely decouple each node of the one-dimensional parametric mesh, which helps to capture the resonance singularities in the frequency domain. Thus, the discretised system (4.20) becomes

$$(k\mathbf{I} + \mathrm{i}c\boldsymbol{\omega} - m\boldsymbol{\omega}^2)\Delta\mathbf{g} = -\mathbf{R}_g(\boldsymbol{f}^{[k+1]}, g^{[k]}), \tag{4.23}$$

where the new residual is defined as

$$\mathbf{R}_g(\boldsymbol{f}, g) = (k\mathbf{I} + \mathrm{i}c\boldsymbol{\omega} - m\boldsymbol{\omega}^2)\mathbf{g} - s\mathbf{1} + \sum_{m=1}^{n-1} \left[k^{[m]}\mathbf{I} + \mathrm{i}c^{[m]}\boldsymbol{\omega} - m^{[m]}\boldsymbol{\omega}^2\right]\mathbf{G}^{[m]}, \tag{4.24}$$

with $\mathbf{I}$ is the identity matrix of dimension the size of the parametric domain N_ω, $\mathbf{1}$ is a vector of ones of dimension N_ω and $\boldsymbol{\omega} = \mathrm{diag}(\omega_1, \cdots, \omega_{N_\omega})$ contains the discretised frequency domain.

4.4 Monolithic adaptive frequency splitting

As mentioned throughout this thesis, the resonance associated to the mechanical modes implies sharp changes in the solution fields and, thus, it is a challenge for any ROM technique aiming to predict the physical response of this coupled system. Indeed, if the workflow as described in Chapter 3 was to be applied directly using the frequency as extra parameter, it would not immediately yield an accurate approximation of the solution. For instance, in Figure 4.2, the frequency-based PGD formulation has been applied to the magneto-mechanical shell problem, see Section 2.7.

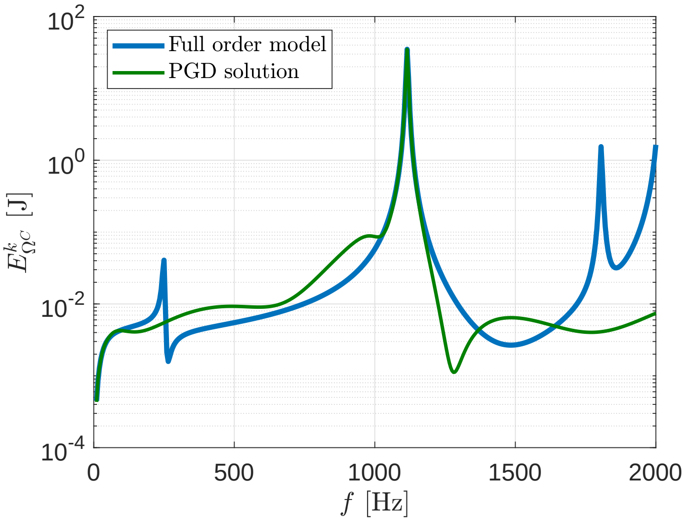

Figure 4.2: Magneto-mechanical test problem; comparison between the full order model and the PGD approximation obtained considering the entire frequency domain $f \in (0, 5000]$ Hz.

In Figure 4.2 it is clearly seen how the PGD solution is not accurate within the frequency spectrum and it is not able to capture all the resonance singularities. The two main factors that are detrimental to the PGD accuracy are, first, the presence of numerical singularities associated with the resonance effect. The more spikes appearing in the solution, the worse the PGD algorithm will perform trying to capture the solution. The second factor is the large frequency domain that is considered in the PGD offline stage, where a frequency $f \in (0, 5000]$ Hz corresponds to an angular frequency $\omega = 2\pi f$ range of $\omega \in (0, 31516]$ rad/s. The fact that the PGD algorithm has to approximate a large frequency spectrum also decreases its accuracy. Therefore, the strategy that will be followed consists of splitting the frequency domain Ω_ω in an automatic manner, identifying where the singularities are and carrying out adaptive refinement in the neighbourhood. With this, the PGD algorithm will seek parametric solutions in reduced frequency intervals of interest (subdomains) $\Omega_\omega = \cup_{i=1}^{N_\omega^{sub}} \Omega_{\omega_i}$ and a reduced number of singularities per subdomain, increasing its overall accuracy.

The first global PGD approximation is known to lack accuracy. Nonetheless, it can still be used in order to approximately identify the location of the largest (in response) resonant mode, without any *a priori* knowledge of the true solution, see Figure 4.3a. Once a singularity (or several singularities) has (have) been identified, partitioned frequency subdomains (clusters) can be defined and a refined PGD solution is computed within these subdomains, that can better capture the overall solution, see Figure 4.3b. This three-step process of *i*) identification of resonance modes (in green), *ii*) frequency interval splitting and *iii*) adaptive PGD calculation (in orange), might need to be repeated several times until convergence is achieved, namely, after no further resonance frequencies are detected. For the example considered here, the process was repeated three times before converging to the final PGD approximation displayed in Figure 4.3d. As can be observed, differences between the full and the PGD solutions are virtually undistinguishable. Notice that the splitting in step *ii*) is carried out by setting a tolerance value tol^{ω}_{split} that controls the size of the subdomains, obtaining frequency subdomains that are neither too small nor too large. Once the singularities are approximately identified (in green), the refined PGD solution (in orange) is used to accurately approximate the full order model.

Table 4.1: Magneto-mechanical test problem; user-defined parameters for the monolithic frequency-based PGD method.

Global PGD				Refined PGD				Ω_p			Ω_q	
I_N	tol_N	I_{FP}	tol_{FP}	I_N	tol_N	I_{FP}	tol_{FP}	h_{Ω_p}	p	ξ	h_ω	tol_ω^{split}
10	10^{-4}	5	10^{-2}	20	10^{-4}	10	10^{-2}	0.06	3	10^{-3}	$5 \cdot 10^{-6}$	20%

For this problem, the user-defined parameters are shown in Table 4.1. I_N and I_{FP} denote the maximum number of PGD modes and fixed-point iterations, respectively; tol_N and tol_{FP} are the tolerance values used for the stopping criteria of the Greedy and ADS algorithms, respectively. The parametric domains are defined by a dimensionless mesh size parameter h_Ω that is computed as the maximum (FEM) element size divided by a reference size of the domain. For instance, for the frequency domain Ω_ω, the dimensionless mesh size is $h_\omega = 0.01/2000 = 5 \cdot 10^{-6}$. The remaining user-defined parameters refer to the spatial problem Ω_p, where h_{Ω_p} is the mesh size parameter as previously explained, p is the polynomial order used in the FEM discretisation and ξ, the dimensionless damping ratio, is used to account both for physical (i.e. classical damping) and numerical regularisation [88]. Note that the parameters I_N, I_{FP} used for the refined PGD solution are larger than those used for the less accurate global PGD solution (employed for the localisation of resonant modes). The reduction in ADS iterations and the coarsening of the computational frequency interval implies less computational cost without sacrificing numerical accuracy.

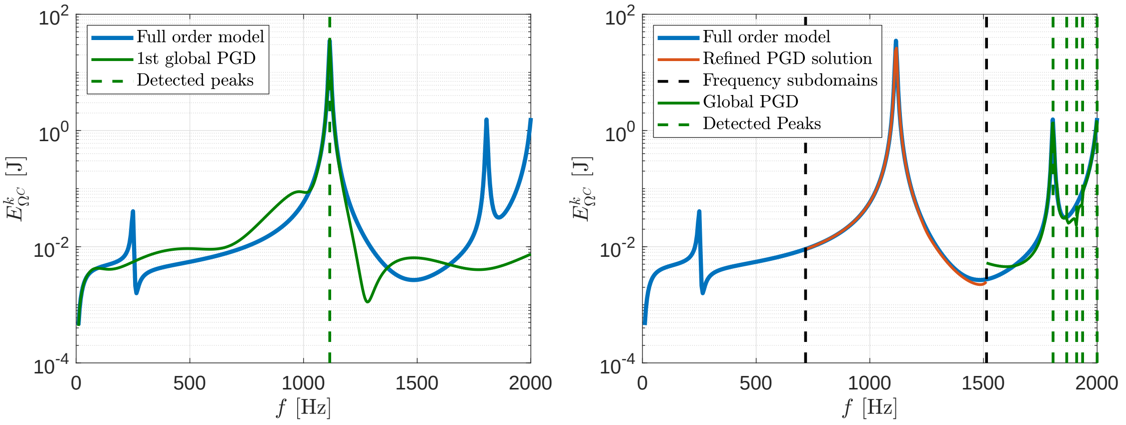

(a) 1^{st} step; global PGD over the entire interval of interest. Low accuracy of the approximation but good identification of some singularities.

(b) 2^{nd} step; refined PGD solution around resonant frequencies and global PGD to next domain (repeat until all subdomains have a refined PGD solution).

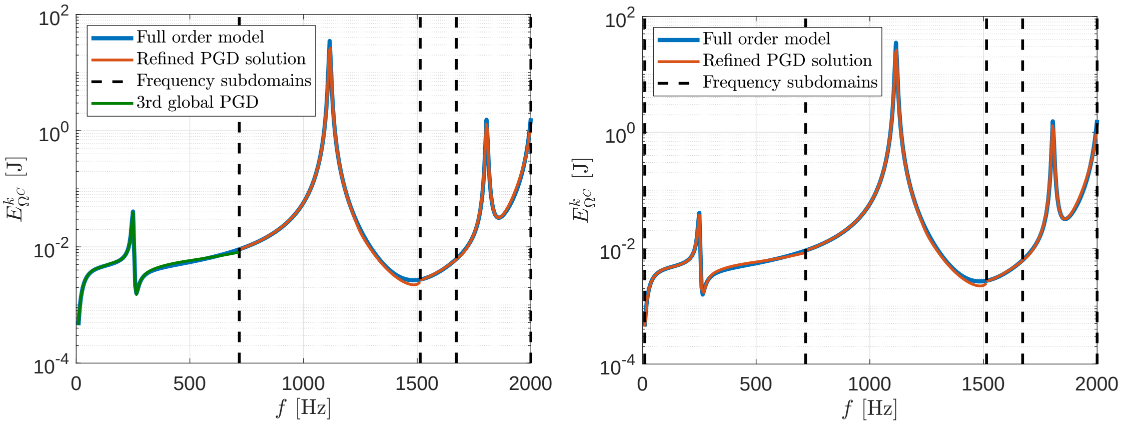

(c) 3^{rd} step; refined PGD solution around resonant frequencies and global PGD to next domain (repeat until all subdomains have a refined PGD solution).

(d) 4^{th} step; solution of the regularised-adaptive PGD.

Figure 4.3: Magneto-mechanical test problem; description of the automatic splitting process performed to locate the resonance frequencies and refine around them. Plot of kinetic energy $E^k_{\Omega^C}$ in the conducting mechanical shell with a damping coefficient $\alpha = 50$.

4.5 Test magnet problem

The monolithic frequency-based PGD algorithm will first be applied to the simplified test magnet geometry described in Section 2.8.1. This geometry is relevant in the early design stage of MRI scanners since it allows to see the behaviour of the most interesting part of the shield (closer to the coils). The user-defined parameters used to run the PGD algorithm are presented in Table 4.2.

The developed automatic adaptive splitting, see Section 4.4, has been successfully applied to the test magnet geometry in the frequency range $f \in (0, 5000]$

Table 4.2: Test magnet problem; user-defined parameters for the monolithic frequency-based PGD method.

Global PGD				Refined PGD				Ω_p			Ω_q	
I_N	tol_N	I_{FP}	tol_{FP}	I_N	tol_N	I_{FP}	tol_{FP}	h_{Ω_p}	p	ξ	h_ω	tol_ω^{split}
10	10^{-4}	5	10^{-2}	50	10^{-6}	10	10^{-2}	0.25	4	10^{-3}	0.01	5%

Hz, obtaining five different frequency subdomains as shown in Figure 4.4. The frequency subdomains generated are $[1, 3331]$, $[3331, 3817]$, $[3817, 4017]$, $[4017, 4582]$ and $[4582, 5000]$ Hz. Notice that the algorithm automatically identifies that no singularities appear within the first half of the interval, whilst it detects the resonance effect at the end of the frequency interval and refines accordingly. It has been found that the overall accuracy of the PGD approximation improves when the resonance spikes are located as centred as possible within each frequency subdomain and thus, the algorithm was designed satisfying this criterion.

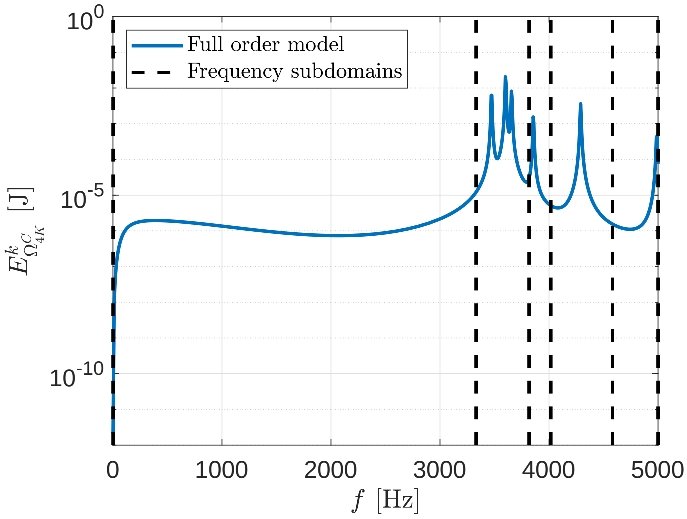

Figure 4.4: Test magnet problem; splitting of the frequency domain to increase PGD accuracy.

The results presented in the following sections contain the PGD convergence of both Greedy and ADS algorithms, the visualisation of the computed spatial and parametric modes and a comparison between full order solution and PGD approximation. The main goal is to visualise the main elements that define the offline PGD solution and to validate the frequency-based PGD implementation by benchmarking the solution against the full order (reference) model.

4.5.1 PGD algorithm convergence

Section 3.6 has presented the stopping criteria followed for the two iterative procedures that feature in the PGD offline computation; the Greedy algorithm and the fixed-point Alternating Direction Scheme. In the Greedy algorithm, the solution is enriched by modal addition until the amplitude of the most recently computed mode falls under a specified tolerance, see Section 3.6.2. Figure 4.5 shows the relative amplitude (3.17) of a new mode with respect to the accumulated solution, where each subfigure corresponds to one of the five frequency subdomains and contains the electromagnetic $e^n_{EM,N}$ and mechanical amplitudes $e^n_{M,N}$ for a certain computed mode n. Both electromagnetic and mechanic convergence curves have a decreasing trend, although not monotonically decreasing, namely, not always the last computed mode has a smaller amplitude than the previously computed. This fact results from the non-orthogonality of the PGD modes, where a new computed mode may contain new but also redundant information with respect to that contained in the previously computed modes. Another conclusion that these results suggest is that the electromagnetic problem seems to converge slightly faster than the mechanical problem, which makes perfect sense since the resonance phenomenon is associated with mechanics.

When looking at the frequency subdomains automatically generated by the splitting algorithm in Figure 4.4, one could think that some frequency subdomains are going to be computationally easier for the PGD algorithm, where no singularities are found. This idea agrees with the Greedy algorithm convergence showed in Figure 4.5, where in the first and last frequency subdomains convergence is reached with less than 40 modes and with amplitudes smaller than 10^{-6}. Note that although it looks like the last interval is very close to a singularity (after the range of interest $(0, 5000]$ Hz), the PGD algorithm does not have to reproduce a solution that is sharply increasing and decreasing afterwords, which may be the reason why a fast convergence is also observed in the 6^{th} frequency subdomain.

The second iterative algorithm that features in the offline PGD calculations is the computation of the spatial and parametric functions within a mode using the Alternating Directions Scheme (ADS), see Section 4.3.1. The ADS convergence is measured as (3.14) and Figure 4.6 shows, for a computed mode (one coloured line), the evolution of the error e^n_{FP} for each ADS iteration. Similarly to above, each subfigure corresponds to one frequency subdomain. Observing the five subfigures it can be seen that the trend is similar in all frequency subdomains, where some modes are converging (tolerance set to $tol_{FP} = 10^{-2}$) while others do not. Different strategies can be followed at this point; allowing a greater number of ADS iterations whilst computing fewer PGD modes containing more accurate information, or computing more PGD modes with just a few ADS iterations each. For the problems studied in this thesis, the second approach has been found to be more computationally efficient, allowing the computation of more PGD modes but only with a few ADS iterations (order of magnitude of 10). Note that a similar strategy was pursued in [42], where

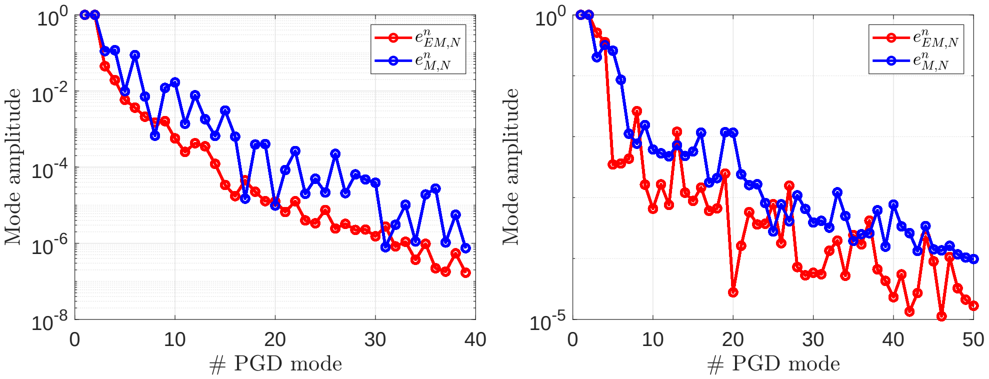

(a) Subdomain 1: $[1, 3331]$ Hz. (b) Subdomain 2: $[3331, 3817]$ Hz.

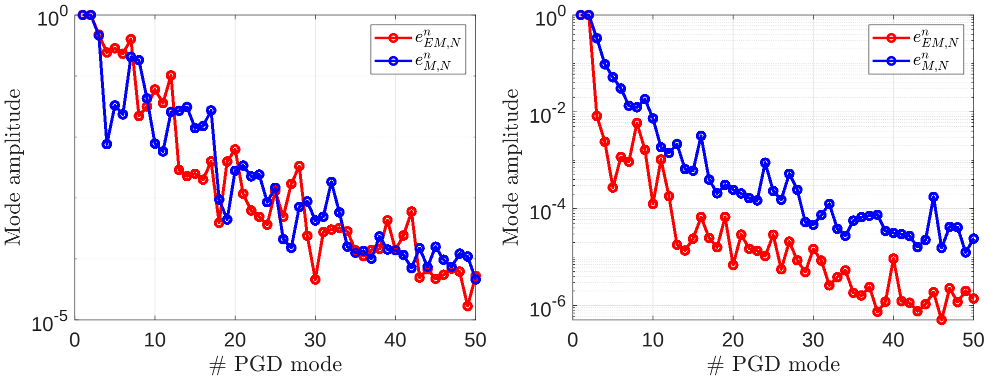

(c) Subdomain 3: $[3817, 4017]$ Hz. (d) Subdomain 4: $[4017, 4582]$ Hz.

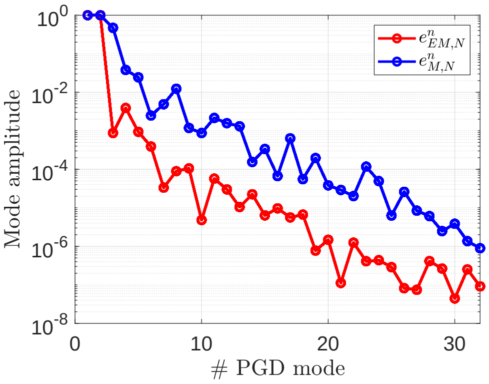

(e) Subdomain 5: $[4582, 5000]$ Hz.

Figure 4.5: Test magnet problem; Greedy algorithm convergence for all frequency subdomains.

the authors advocate for this technique claiming that it is more efficient to compute a mode that has not reached convergence and let the following modes correct possible errors rather than trying to compute always a converged mode.

Once both iterative algorithms are stopped, the spatial and parametric modes are obtained and thus, the offline calculation is complete. Note that in the context of magneto-mechanical problems featuring resonance, the Greedy algorithm convergence is not a clear indicator that can ensure that the PGD solution will capture all the singularities in the resonant frequencies. The reason is that $e^n_{EM,N}$ and $e^n_{M,N}$

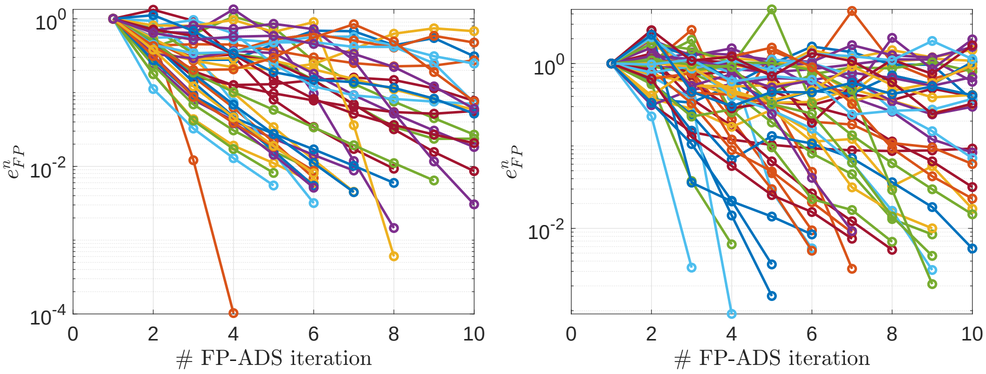

(a) Subdomain 1: $[1, 3331]$ Hz. (b) Subdomain 2: $[3331, 3817]$ Hz.

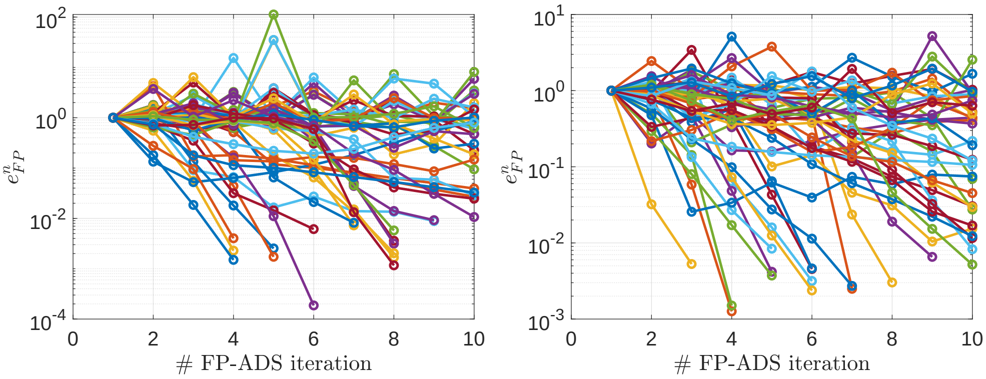

(c) Subdomain 3: $[3817, 4017]$ Hz. (d) Subdomain 4: $[4017, 4582]$ Hz.

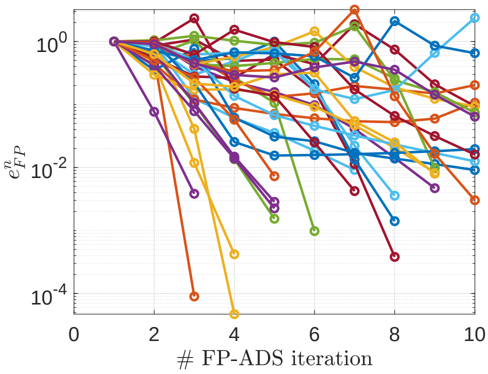

(e) Subdomain 5: $[4582, 5000]$ Hz.

Figure 4.6: Test magnet problem; fixed-point alternating direction scheme convergence for all frequency subdomains.

are global measures that consider the solution in the entire frequency subdomain and thus, small changes such as capturing a particular spike or not will not have a significant effect on these two convergence quantities. Having said that, the Greedy algorithm convergences does indicate if the overall solution is being captured with the already computed modes.

4.5.2 Modes visualisation

The offline PGD stage is complete when both spatial and parametric modes are obtained and hence, all terms in (4.4) are known. The online PGD stage is then a simple operation that can be done in real time, see Section 3.7. Before moving to the online PGD stage and obtain the desired PGD approximation, the computed modes, both spatial $\boldsymbol{F}(r,z)$ and parametric $G(\omega)$, will be presented and discussed in this section.

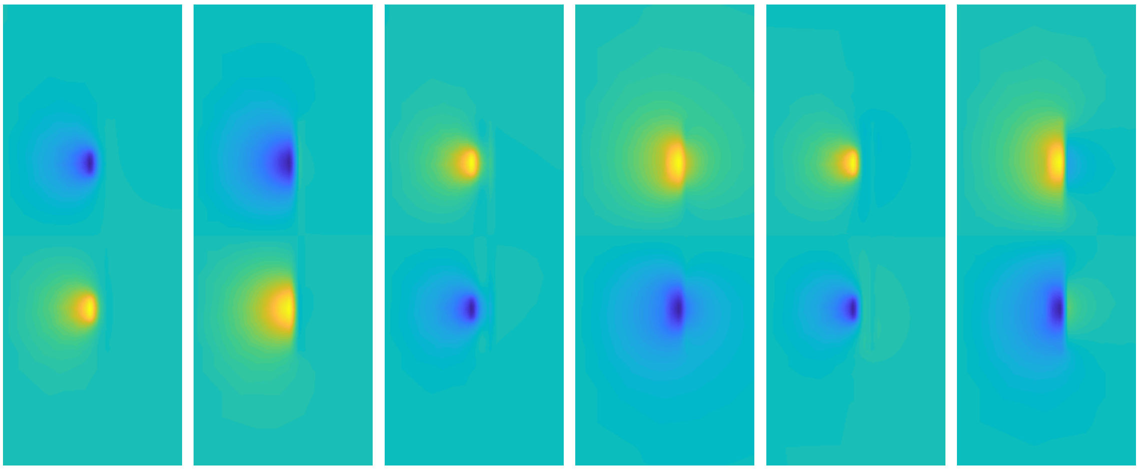

1^{st} mode. 2^{nd} mode. 3^{rd} mode. 4^{th} mode. 5^{th} mode. 6^{th} mode.

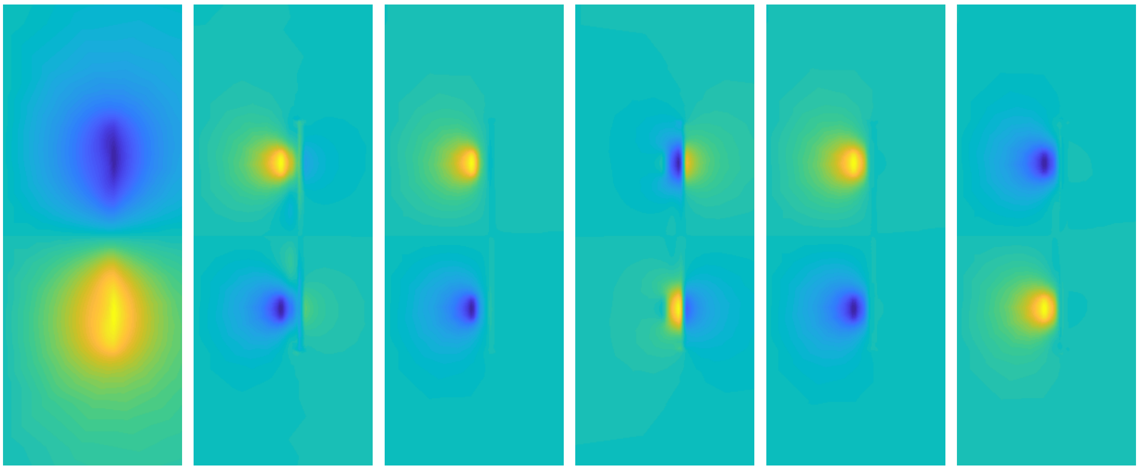

7^{th} mode. 8^{th} mode. 9^{th} mode. 10^{th} mode. 11^{th} mode. 12^{th} mode.

Figure 4.7: Test magnet problem; first 12 computed electromagnetic spatial modes $F_{\mathcal{A}_\phi}(r,z)$ for the first frequency subdomain $f \in [1, 3331]$ Hz. Same colour scale for all subfigures.

The spatial modes $\boldsymbol{F} = [F_{\mathcal{A}_\phi}, F_{\mathcal{U}_r}, F_{\mathcal{U}_z}]^T$ will be split between electromagnetic component $F_{\mathcal{A}_\phi}$ and module of the two mechanical components $F_{\boldsymbol{u}} = \sqrt{F_{\mathcal{U}_r}^2 + F_{\mathcal{U}_z}^2}$. The normalised electromagnetic spatial two-dimensional modes $F_{\mathcal{A}_\phi}(r,z)$ are plotted in Figure 4.7, where the view has been zoomed in the vicinity of the coils and conducing shields. Note that this figure only presents the first 12 computed modes within the first frequency subdomain $f \in [1, 3331]$ Hz because no additional information is obtained from visualising the complete set of computed modes. Moreover, the computed modes do not include the first Dirichlet mode, which is set such that it satisfies the Dirichlet boundary conditions. Having said that, the plots in Figure 4.7 show a smooth two-dimensional field that is originated in the gradient coils as expected. Also, these results suggest that the modes do not follow a particular order when being computed and that it is possible that some repeated information is contained among them.

In a similar way, the normalised two-dimensional mechanical modes $F_{\boldsymbol{u}}(r, z)$ are presented in Figure 4.8, where similarly than for electromagnetics, a smooth field is obtained from the ADS algorithm. Another similarity is that it seems that the computation does not follow a particular order, where a high-frequency mode may be computed prior to a low-frequency one (see 8^{th} and 9^{th} modes).

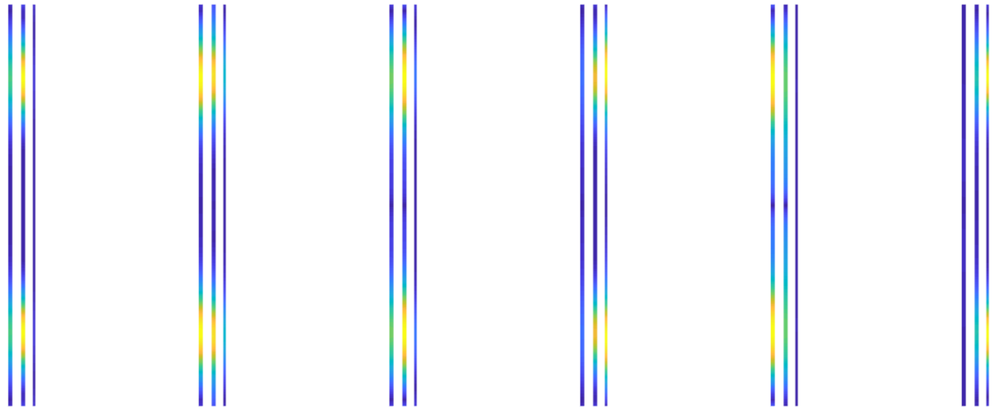

1^{st} mode. 2^{nd} mode. 3^{rd} mode. 4^{th} mode. 5^{th} mode. 6^{th} mode.

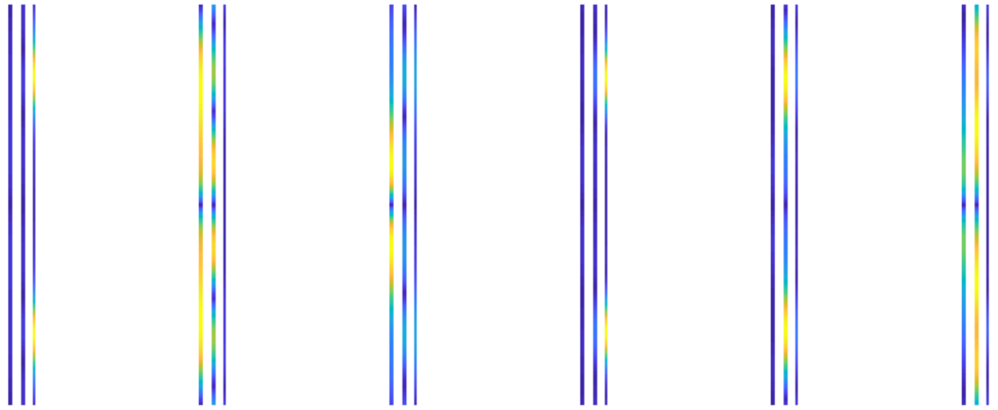

7^{th} mode. 8^{th} mode. 9^{th} mode. 10^{th} mode. 11^{th} mode. 12^{th} mode.

Figure 4.8: Test magnet problem; first 12 computed mechanical spatial modes $F_{\boldsymbol{u}}(r, z)$ for the first frequency subdomain $f \in [1, 3331]$ Hz. Same colour scale for all subfigures.

The last computed quantities are the normalised one-dimensional parametric modes $G(\omega)$ represented in Figure 4.9, where again each subfigure represents one frequency subdomain. A lot of information is contained in this figure, although the main point is to highlight that these modes are non-smooth in some parts of the 1D frequency domain, which suggests that they are indeed containing the information to detect the resonance singularities in the actual solution. However, thanks to the automatic splitting in frequency there are no spikes in the first frequency subdomain, which is by far the largest one.

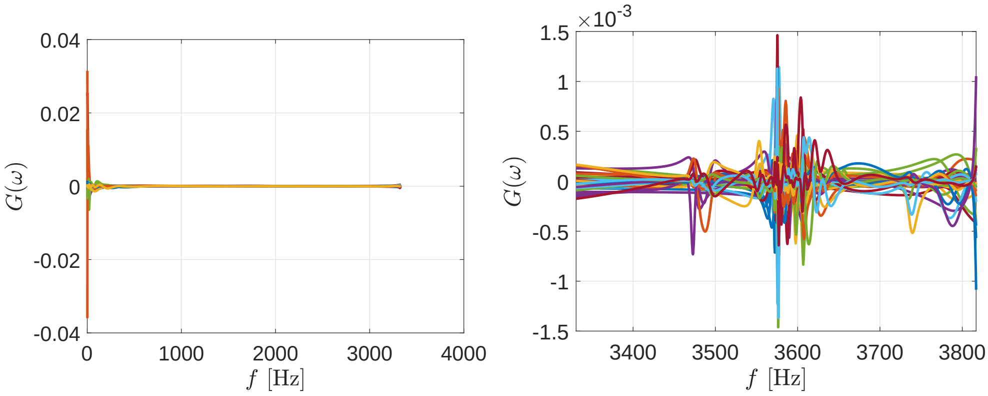

(a) Subdomain 1: $[1, 3331]$ Hz. (b) Subdomain 2: $[3331, 3817]$ Hz.

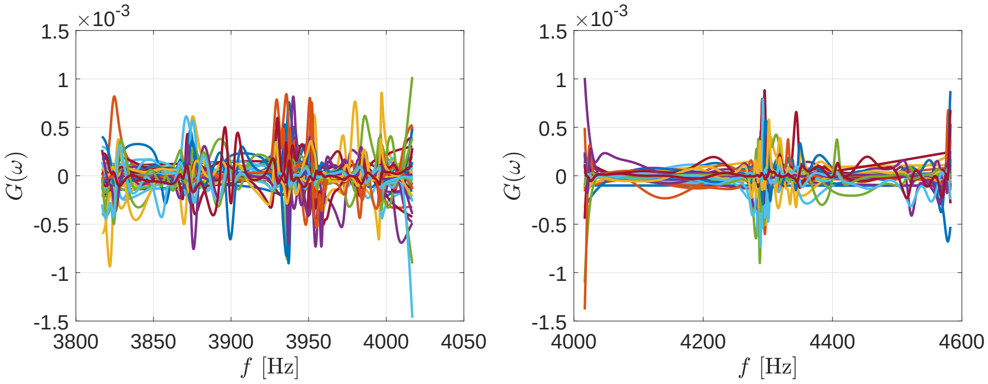

(c) Subdomain 3: $[3817, 4017]$ Hz. (d) Subdomain 4: $[4017, 4582]$ Hz.

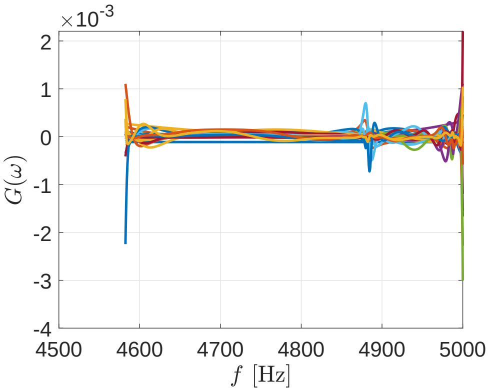

(e) Subdomain 5: $[4582, 5000]$ Hz.

Figure 4.9: Test magnet problem; parametric modes $G(\omega)$ computed for each frequency subdomain.

Notice that the changes in $G(\omega)$ for a particular frequency subdomain will determine all the spikes of all conducting shields, which means that the parametric modes $G(\omega)$ have to adapt to all conducting components. This will be completely different when applying the high-dimensional staggered PGD in Chapter 5.

The combination of the normalised spatial and parametric modes times the modal amplitudes will provide the PGD approximation of the solution fields as detailed in Section 3.7.

4.5.3 Validation of the PGD method

Once computed and stored all the modes contained in the PGD definition (4.4), the online PGD stage can be used in order to interpolate the solution for a given set of parameters, in this case (r, z, ω). The goal is now to assess and validate the PGD technique using the full order model as a reference solution. The solution fields, the vector potential and the mechanical displacements, obtained with both methodologies, will be compared, but also the main quantities of interest, dissipated power $P^0_{\Omega^C}$ and kinetic energy $E^k_{\Omega^C}$, will be computed, since they are of high interest in an industrial context. Note that all results shown were generated using the user-defined PGD parameters presented in Table 4.2.

Figure 4.10 shows the comparison between the PGD approximation and the full order solution for a frequency $f = 4000$ Hz using three different quantities, the AC magnetic field $\boldsymbol{\mathcal{B}}^{AC}_0$, the displacement field $\boldsymbol{\mathcal{U}}$ and the eddy currents $\boldsymbol{J}^e$ computed as $\boldsymbol{J}^e = \gamma \boldsymbol{\mathcal{E}}^{AC}$. Note that the subscript $(\cdot_{full})$ and $(\cdot_{PGD})$ denote that a certain quantity has been obtained using the full order model or the PGD technique, respectively. The errors obtained are approximately between 1% and 0.1%, which suggests that the PGD has been developed and implemented correctly. Moreover, it is interesting to see the skin depth effect in the eddy current field $\boldsymbol{J}^e$, which appears due to the high frequency of excitation of the problem ($f = 4000$ Hz).

Since the integrated quantities (2.34) are extremely relevant in the design stage of MRI scanners, Figure 4.11 presents the comparison of both, dissipated power and kinetic energy, between PGD approximation and the full order solution for each conducting shield, OVC, 77K and 4K. An efficient computation of the integrated quantities is described in Appendix C. These results clearly show a very high accurate PGD approximation that is able to reproduce all the resonant frequencies appearing in the full order model. Whilst a high number of full order solutions are necessary in order to generate the full order model curve, the PGD approximation only needs the fast online PGD interpolation to interpolate in real-time a high number of points in the frequency sweep to create the PGD approximation curve.

4.6 Full magnet problem

The full magnet problem consists of a more realistic geometry with closed cylindrical shells instead of radiation shields. This problem set up is detailed in Section 2.8.2 and it is used as a more accurate representation of a real MRI scanner. The user-defined PGD parameters for this full magnet geometry are shown in Table 4.3. Note that all parameters are identical to the previous test magnet problem except

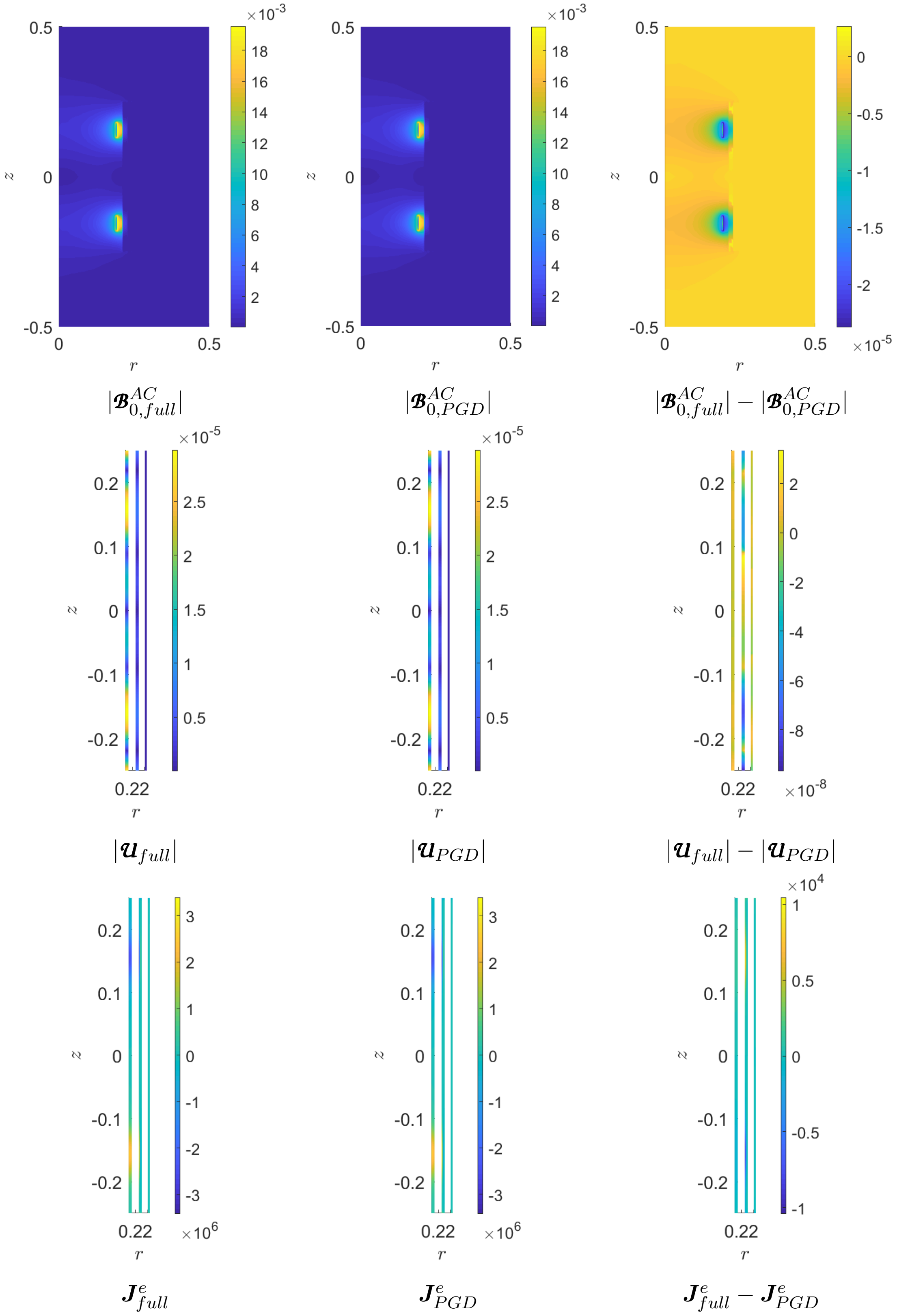

Figure 4.10: Test magnet problem; comparison between PGD approximation and full order model for $f = 4000$ Hz.

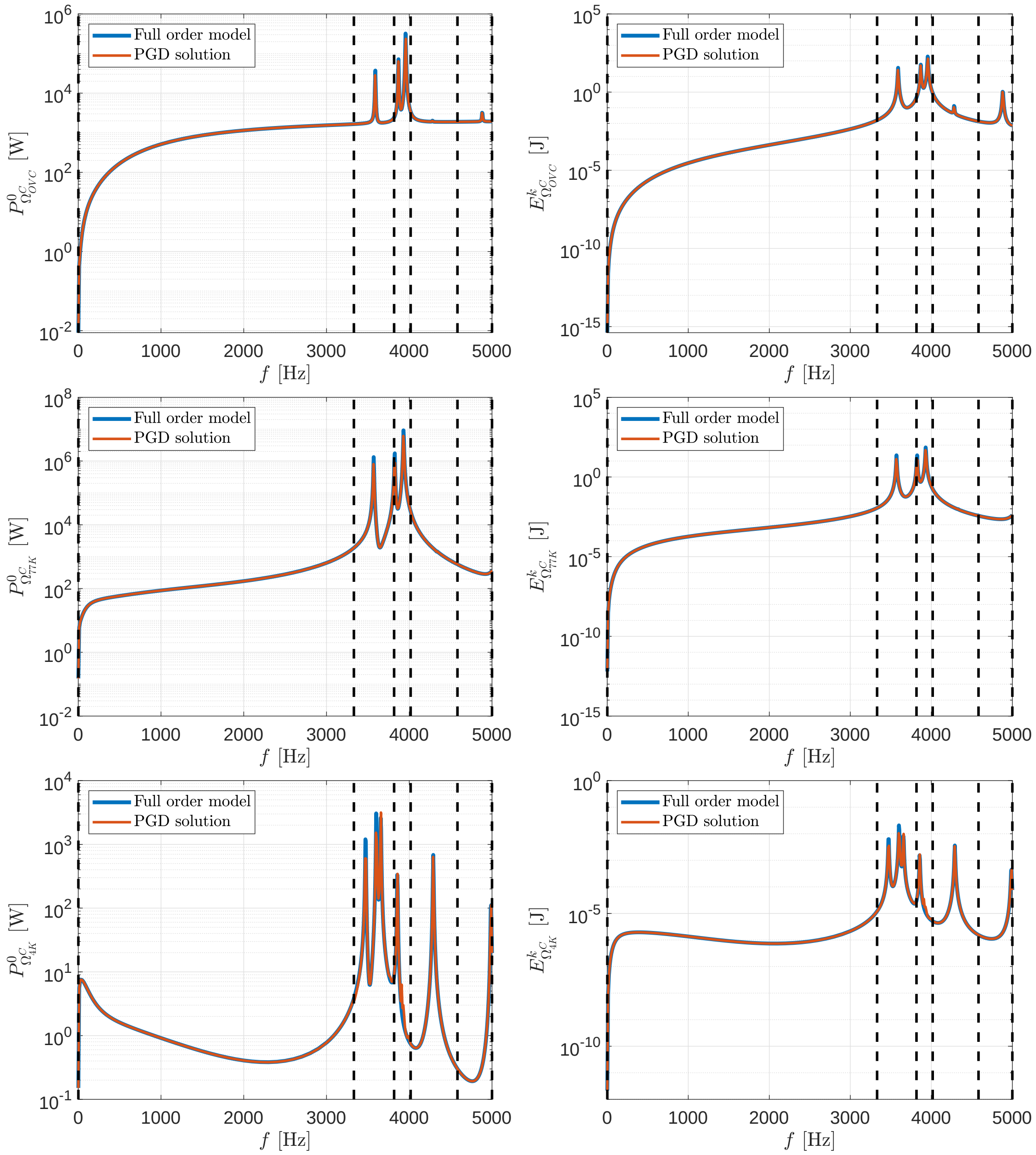

Figure 4.11: Test magnet problem; comparison between PGD approximation and full order model. Plot of dissipated power $P^0_{\Omega^C}$ and kinetic energy $E^k_{\Omega^C}$ in the three conducting shields OVC, 77K and 4K.

the ones related to the refined PGD. In this section it will be shown that although it is a more complex geometry, this problem needs fewer modes than the test magnet geometry in order to obtain an accurate approximation of the solution fields. As it will be discussed later on, this fact may be related to the smaller size of frequency subdomains that are computed in this problem.

The frequency splitting algorithm applied to the monolithic PGD has been presented in Section 4.4 and it has been applied in this geometry in order to split the global frequency range of interest $f \in (0, 2000]$ Hz, see Figure 4.12. Although

Table 4.3: Full magnet problem; user-defined parameters for the monolithic frequency-based PGD method.

Global PGD				Refined PGD				Ω_p			Ω_q	
I_N	tol_N	I_{FP}	tol_{FP}	I_N	tol_N	I_{FP}	tol_{FP}	h_{Ω_p}	p	ξ	h_ω	tol_ω^{split}
10	10^{-4}	5	10^{-2}	20	10^{-4}	10	10^{-2}	0.25	4	10^{-3}	0.01	5%

this geometry behaves in a completely different way than the previous test problem, where the resonance phenomenon is now present throughout the entire frequency spectrum, the automatic frequency splitting algorithm is capable of identifying the singularities and divide the frequency domain accordingly. The seven resulting frequency subdomains are $[1, 167]$, $[167, 473]$, $[473, 819]$, $[819, 1154]$, $[1154, 1336]$, $[1336, 1685]$ and $[1685, 2000]$ Hz, are now smaller than for the test magnet problem due to the large amount of singularities. Note that the global frequency range of interest is reduced for this geometry since the goal is to identify and represent the solution within the first more dominant resonant modes.

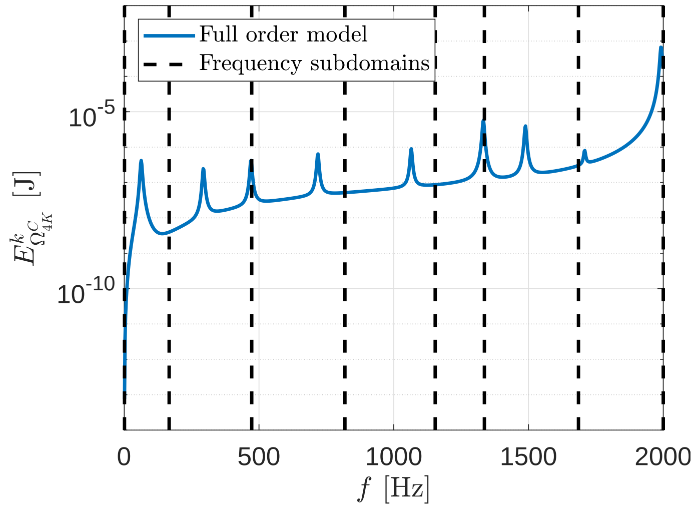

Figure 4.12: Test magnet problem; splitting of the frequency domain to increase PGD accuracy.

The results for this geometry will follow the same structure as those for the test magnet problem; first the Greedy algorithm and ADS convergences will be presented together with the visualisation of the first modes computed, both spatial and parametric. Finally, the PGD algorithm will be benchmarked and validated against the full order model.

4.6.1 PGD algorithm convergence

As detailed in Chapter 3, the PGD algorithm consists of two iterative procedures, the Greedy algorithm and the Alternating Direction Scheme (ADS), that will compute the required PGD modes with all the functions appearing in the PGD definition (4.4). First, the convergence of the Greedy algorithm is presented in Figure 4.13 for the full magnet geometry, where each subfigure corresponds to each one of the seven frequency subdomains. This figure shows that both physics have a descending overall trend although it converges faster for the case of electromagnetics. The same behaviour was obtained in the test magnet problem, see Figure 4.5, which is related to the fact that resonant singularities only appear in the mechanical problem, which is indeed the more challenging one. Note however that the mechanical problem for the full magnet geometry is significantly more challenging than in the previous test magnet case, where the mechanical mode amplitudes are now reaching values around 10^{-2} instead of 10^{-5}.

The ADS is executed within a PGD mode in order to compute the separable functions in the PGD definition (4.4), in this case $\boldsymbol{F}^n$ and G^n. The convergence obtained after running this iterative process is shown in Figure 4.14, where it can be seen how some modes reach the specified tolerance ($tol_N = 10^{-2}$) before exceeding the maximum number of iterations allowed ($I_{FP} = 10$). These results are consistent with what was observed in the test magnet geometry, where the strategy adopted is to allow just a few iterations, even though all modes may not be fully converged.

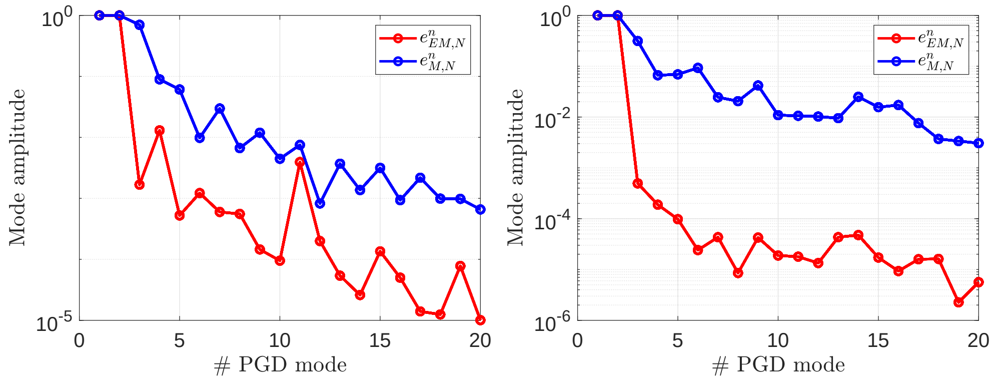

(a) Subdomain 1: [1, 167] Hz. (b) Subdomain 2: [167, 473] Hz.

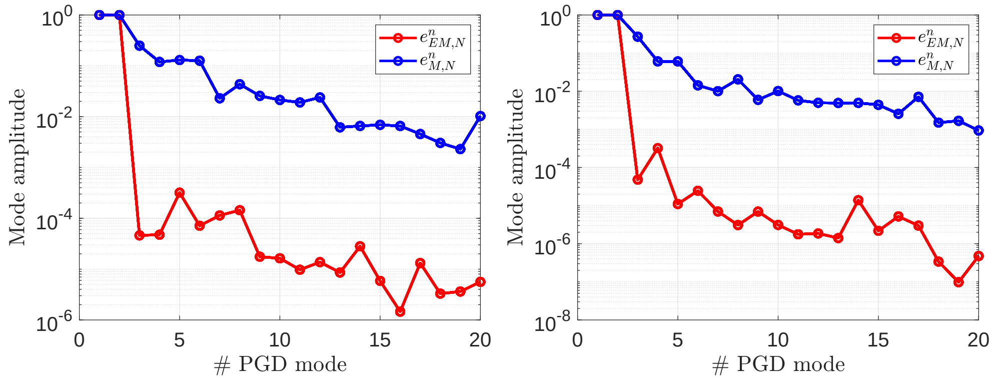

(c) Subdomain 3: [473, 819] Hz. (d) Subdomain 4: [819, 1154] Hz.

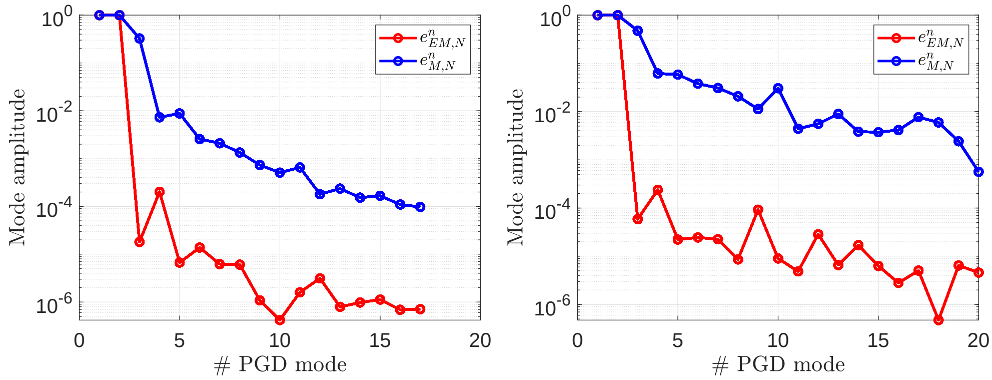

(e) Subdomain 5: [1154, 1336] Hz. (f) Subdomain 6: [1336,1685] Hz.

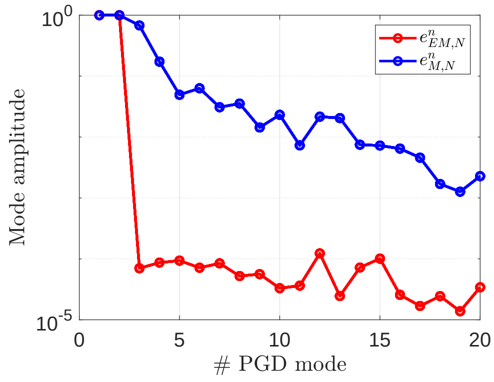

(g) Subdomain 7: [1685, 2000] Hz.

Figure 4.13: Full magnet problem; Greedy algorithm convergence for all frequency subdomains.

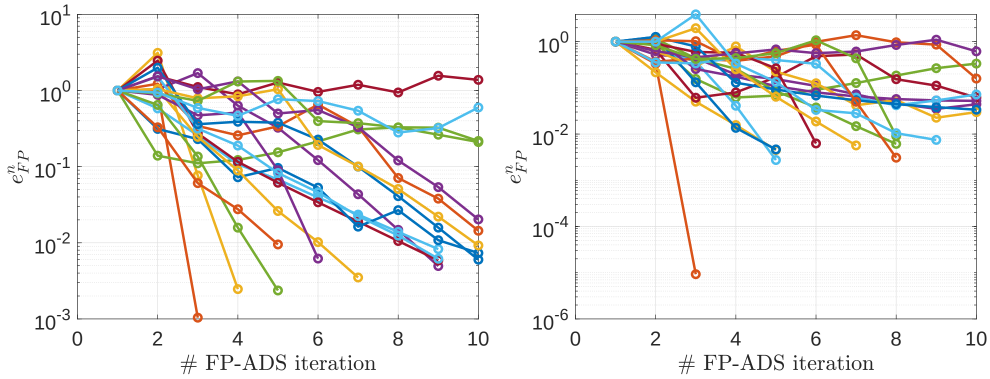

(a) Subdomain 1: [1, 167] Hz.

(b) Subdomain 2: [167, 473] Hz.

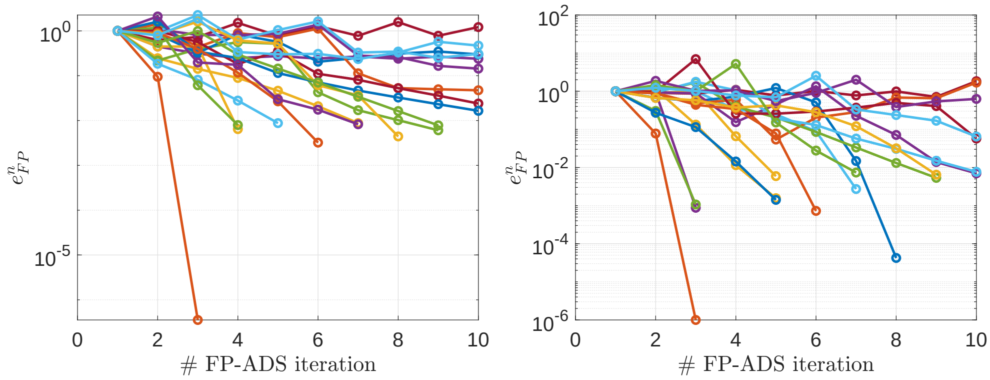

(c) Subdomain 3: [473, 819] Hz.

(d) Subdomain 4: [819, 1154] Hz.

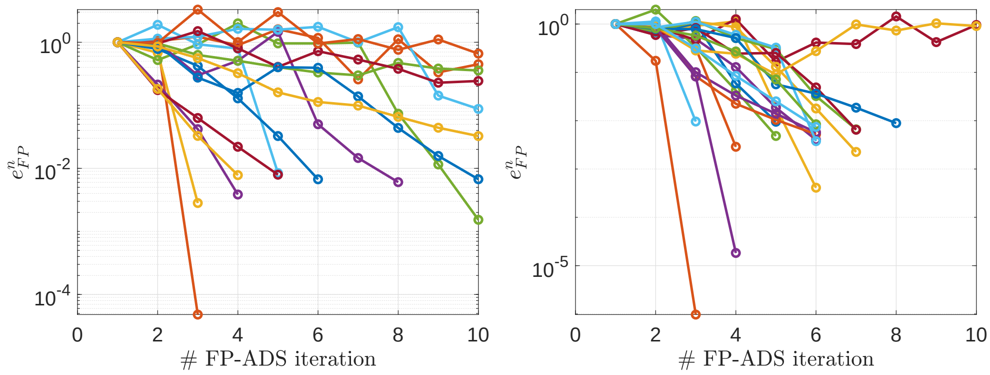

(e) Subdomain 5: [1154, 1336] Hz.

(f) Subdomain 6: [1336,1685] Hz.

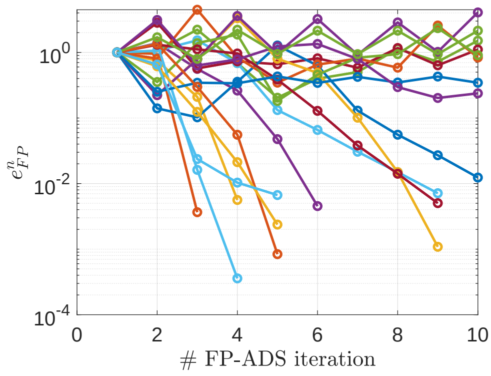

(g) Subdomain 7: [1685, 2000] Hz.

Figure 4.14: Full magnet problem; fixed-point alternating direction scheme convergence for all frequency subdomains.

4.6.2 Modes visualisation

This section aims to graphically visualise the spatial and parametric PGD modes computed, which will be used later on in order to approximate the solution fields in the online PGD stage, see Section 3.7. For the sake of brevity, only the first eight PGD modes are presented since no additional information would be obtained from visualising them entirely. The spatial modes will be presented as $\boldsymbol{F} = [F_{\mathcal{A}_\phi}, F_{\boldsymbol{u}}]^T$, where $F_{\boldsymbol{u}} = \sqrt{F_{\mathcal{U}_r}^2 + F_{\mathcal{U}_z}^2}$. The electromagnetic spatial modes $F_{\mathcal{A}_\phi}(r,z)$ are shown in Figure 4.15, where both low and high frequency smooth modes are observed. Note that, similarly than for the test magnet configuration, the modes do not follow any particular order in terms of sign or frequency.

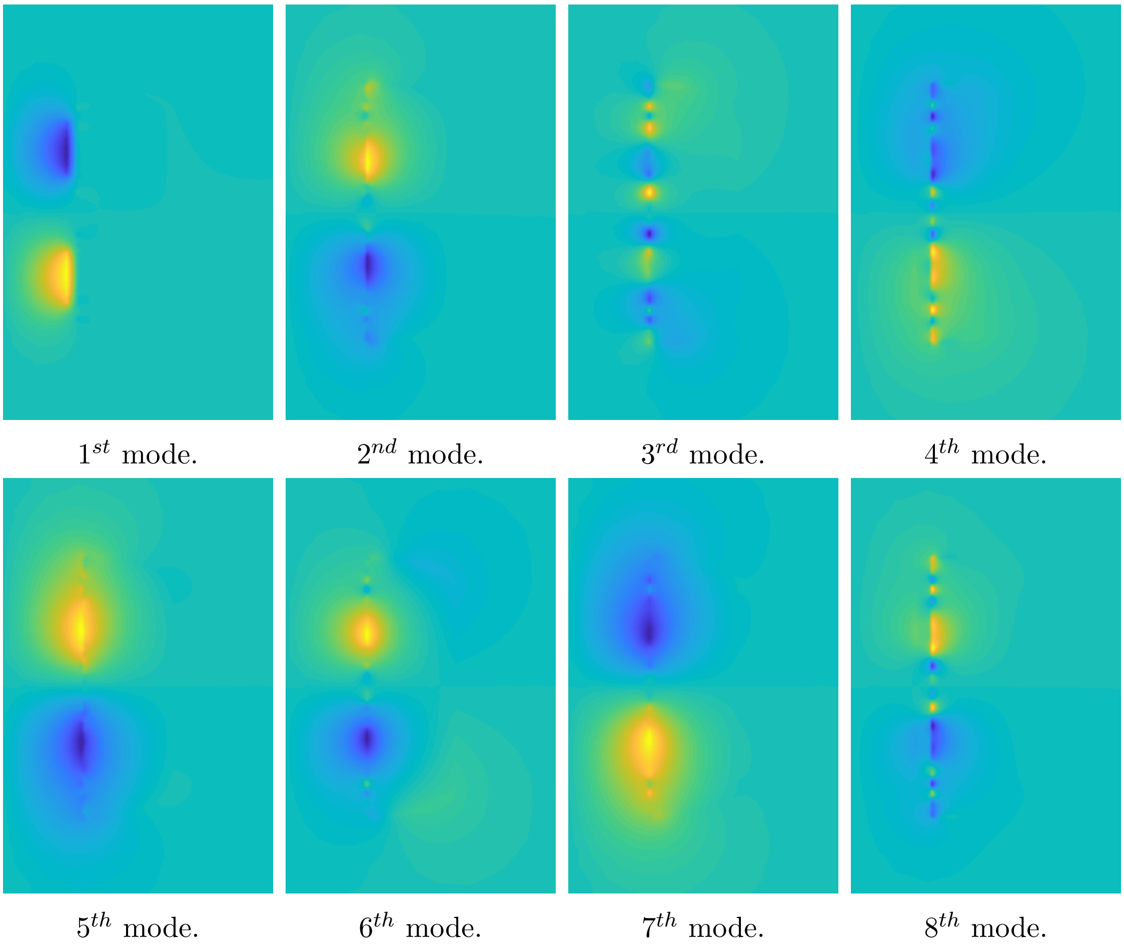

1^{st} mode. 2^{nd} mode. 3^{rd} mode. 4^{th} mode.

5^{th} mode. 6^{th} mode. 7^{th} mode. 8^{th} mode.

Figure 4.15: Full magnet problem; first 8 computed electromagnetic spatial modes $F_{\mathcal{A}_\phi}(r,z)$ for the first frequency subdomain $f \in [1,167]$ Hz. All modes have been L^2 normalised. Same colour scale for all subfigures.

Figure 4.16 shows the mechanical spatial modes $F_{\boldsymbol{u}}(r,z)$, which are smooth two-dimensional fields within the conducting shields. Note how each mode acts on different shields and different areas within the same shield.

The one-dimensional parametric modes $G(\omega)$ obtained from the ADS are plotted in Figure 4.17, with one subfigure per frequency subdomain. In this case is clear that

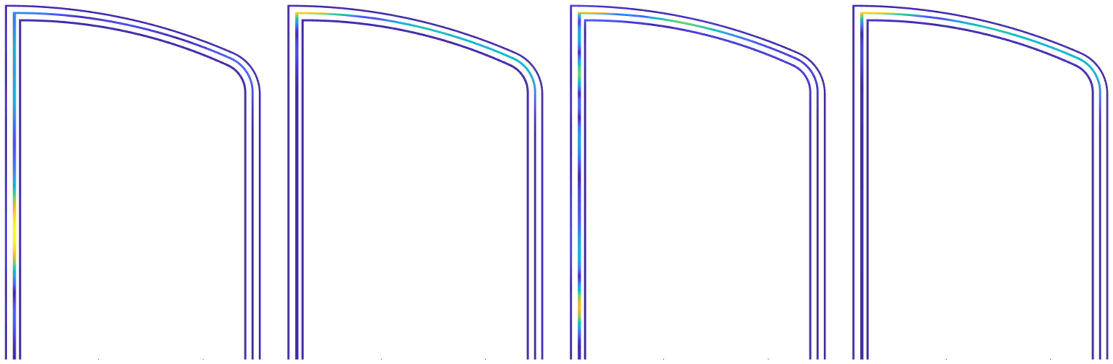

1^{st} mode. 2^{nd} mode. 3^{rd} mode. 4^{th} mode.

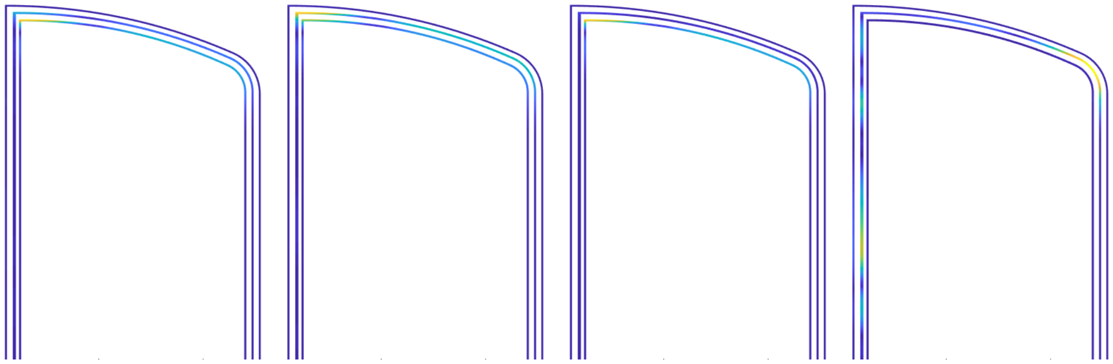

5^{th} mode. 6^{th} mode. 7^{th} mode. 8^{th} mode.

Figure 4.16: Full magnet problem; first 8 computed mechanical spatial modes $F_{\boldsymbol{u}}(r, z)$ for the first frequency subdomain $f \in [1, 167]$ Hz. All modes have been L^2 normalised. Same colour scale for all subfigures.

the information related to the resonant modes is contained within the parametric modes since non-smooth behaviour is observed. Also note that the parametric modes are the same for all shields, so $G(\omega)$ has to represent all singularities contained in the three conducting shields appearing in the computational domain. These results agree with the conclusions reached for the test magnet problem.

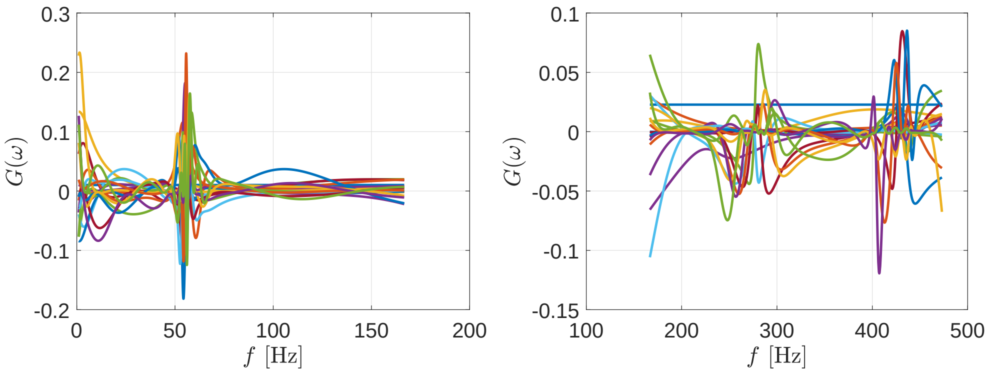

(a) Subdomain 1: $[1, 167]$ Hz.

(b) Subdomain 2: [167,473] Hz.

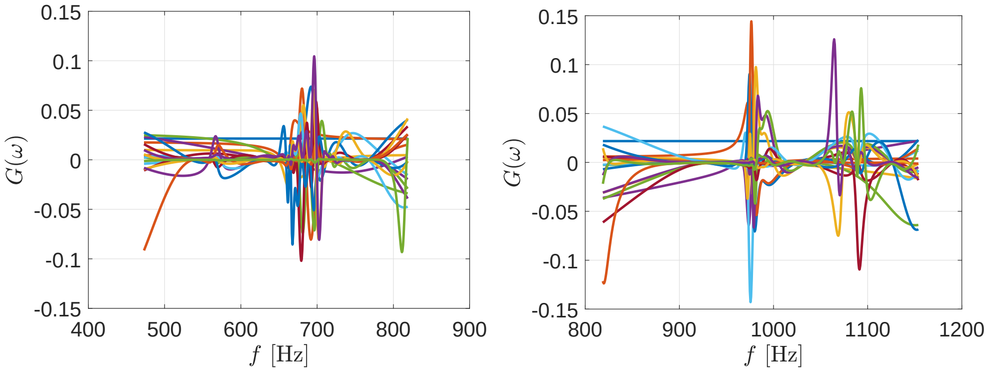

(c) Subdomain 3: [473, 819] Hz.

(d) Subdomain 4: [819, 1154] Hz.

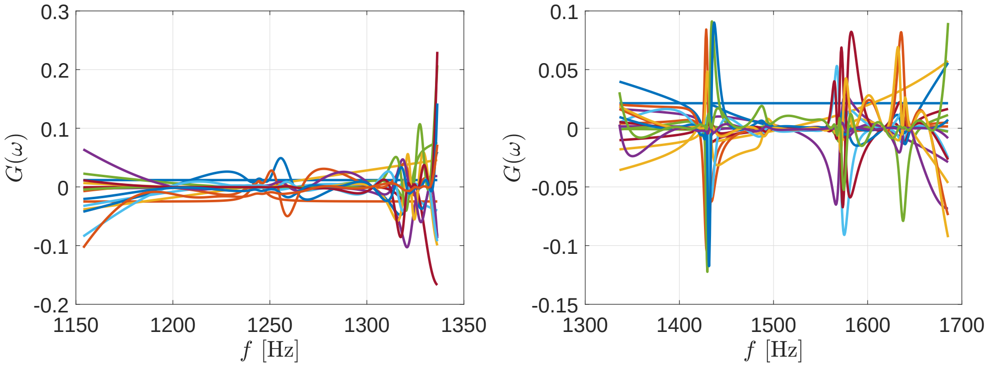

(e) Subdomain 5: [1154, 1336] Hz.

(f) Subdomain 6: [1336,1685] Hz.

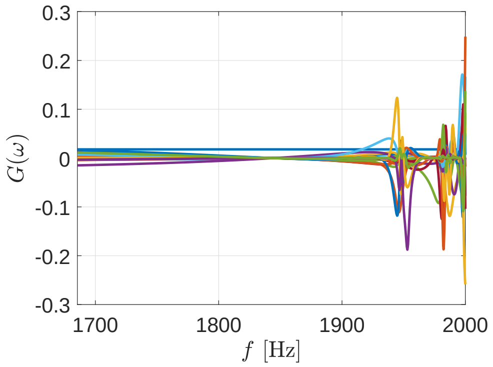

(g) Subdomain 7: [1685, 2000] Hz.

Figure 4.17: Full magnet problem; first 8 computed normalised parametric modes $G(\omega)$ for each frequency subdomain.

4.6.3 Validation of the PGD method

Once the PGD definition (4.4) is computed and store, the online PGD stage interpolates the solution fields for the desired set of parameters, in this case (r, z, ω). The goal of this section is to benchmark and validate the PGD implementation using the full order model as a reference solution.

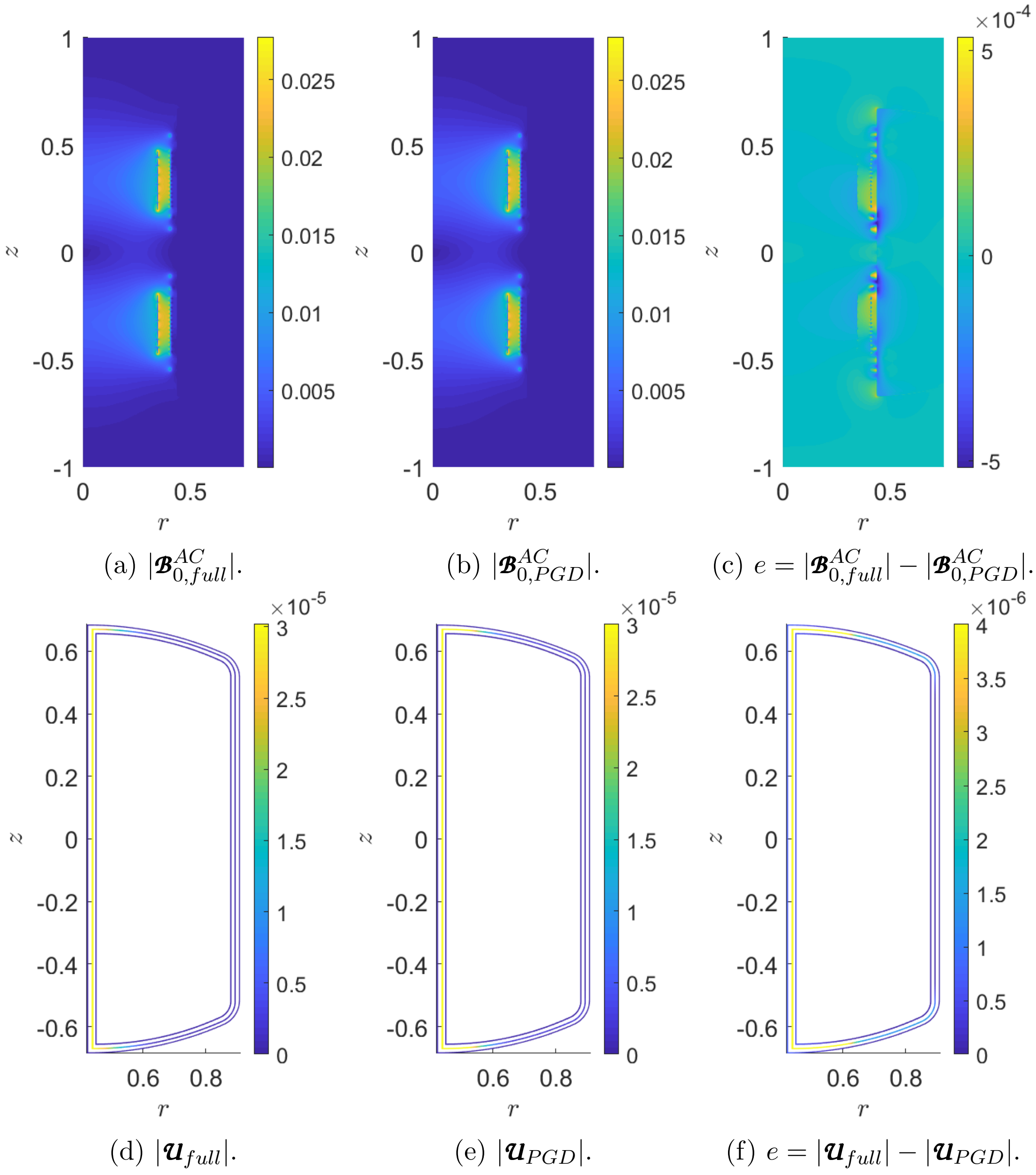

(a) $|\boldsymbol{\mathcal{B}}_{0,full}^{AC}|$. (b) $|\boldsymbol{\mathcal{B}}_{0,PGD}^{AC}|$. (c) $e = |\boldsymbol{\mathcal{B}}_{0,full}^{AC}| - |\boldsymbol{\mathcal{B}}_{0,PGD}^{AC}|$.

(d) $|\boldsymbol{\mathcal{U}}_{full}|$. (e) $|\boldsymbol{\mathcal{U}}_{PGD}|$. (f) $e = |\boldsymbol{\mathcal{U}}_{full}| - |\boldsymbol{\mathcal{U}}_{PGD}|$.

Figure 4.18: Full magnet problem; comparison between solution fields obtained using the full order model $(\cdot_{full})$ and the PGD approach $(\cdot_{PGD})$. Visualisation of $|\boldsymbol{\mathcal{B}}_0^{AC}|$ around the gradient coils and $|\boldsymbol{\mathcal{U}}|$ in the conducting shields for a frequency of 100 Hz.

The first study is to interpolate the vector potential and the displacement fields for a given value of the angular frequency ω, so it can be compared with the corresponding full order solution for the same ω. This study is presented in Figure 4.18, where it can be seen the PGD approximation and the full order model agree for both physics with errors of approximately 1-10%.

However, the main quantities of interest are the integrated dissipated power $P^0_{\Omega C}$ an the kinetic energy $E^k_{\Omega C}$ defined in (2.34). Therefore, the second study will be to exploit the fast online PGD stage in order to compute a value of the integrated quantities for several angular frequencies ω, being able to sweep over the entire global frequency range of interest.

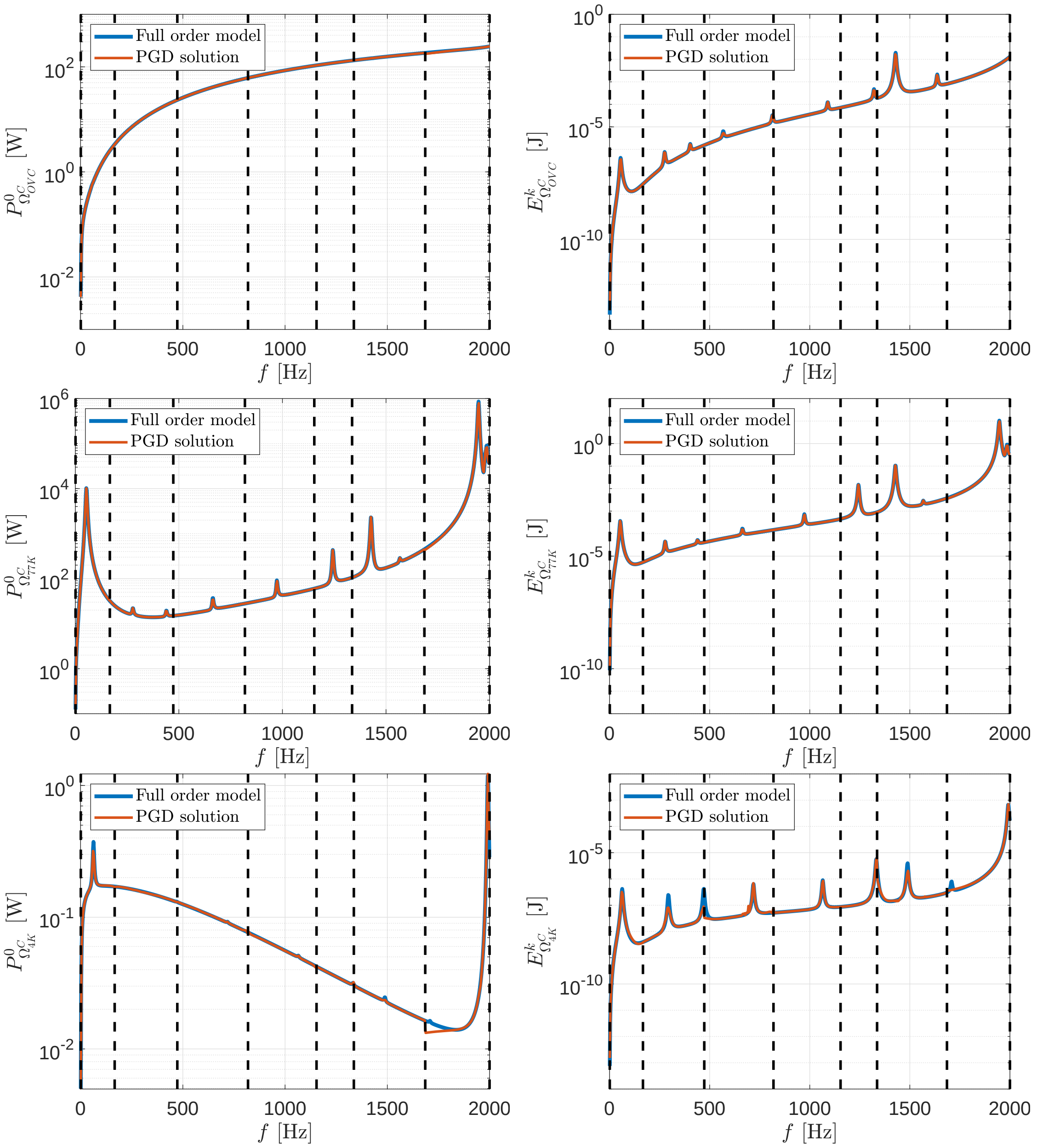

Figure 4.19: Full magnet problem; comparison between PGD approximation and full order model. Plot of dissipated power $P^0_{\Omega C}$ and kinetic energy $E^k_{\Omega C}$ in the three conducting shields OVC, 77K and 4K.

In Figure 4.19, both quantities, dissipated power and kinetic energy, are presented for each shield in the range $[1, 2000]$ Hz. These results demonstrate a complete agreement between PGD approximation and full order (reference) solution, being able to locate and capture all the resonant modes together with the solution between them. This fact suggests that the algorithm is robust since it can deal with different more demanding complex geometries.

4.7 Chapter summary

This chapter has presented a new Reduced Order Modelling Proper Generalised Decomposition (ROM-PGD) method to help speed up the MRI design phase, improving the optimisation workflow through a real-time, multiple-query, frequency-based enabled online stage. The work has focused on using the external exciting frequency as an additional parameter of the offline higher-dimensional parametric solution permitting frequency spectra for kinetic energy and dissipated power to be efficiently queried in the online stage. The ROM-PGD methodology has been derived for the coupled electro-magneto-mechanical problem of interest and a regularised-adaptive methodology has been introduced to account for the numerical singularities associated with the ill-conditioning of the discrete system in the vicinity of resonant modes. A key advantage of this approach is the fact that the major computational expense takes place during the offline stage, whilst the online stage can be resolved in real-time and through user-friendly app interfaces, such as that shown in Appendix E.

Consequently, this chapter has achieved the objectives "*To develop a frequency-based PGD formulation for coupled magneto-mechanical problems*", "*To propose a regularised-adaptive strategy in order to increase the PGD accuracy and robustness*" and "*To develop a graphical user interface for the online PGD stage that can be used in the industry environment*". The further consideration of optimisation parameters such as the magnetic conductivity, the strength of the static magnetic field or the thicknesses of the conducting shields constitute the following chapters of this thesis, in the search of a surrogate digital twin model which allows for real-time simulations, thus minimising human intervention.

Chapter 5

Staggered high-dimensional Proper Generalised Decomposition technique

5.1 Introduction

A novel frequency-based PGD technique has been presented in Chapter 4, see [88], in order to conduct real time evaluations of the performance of an MRI scanner when subjected to frequency dependent magnetic excitations. The aim of this chapter is to greatly enhance the flexibility of this PGD metamodel, by incorporating in addition to the already existing angular frequency ω, further parameters of interest into the query process, namely, the electrical conductivity γ and the strength of the static magnetic field B_0, computed as $B_0 = \max(\left|\boldsymbol{B}_0^{DC}|_{r=0}\right|)$. With this in mind, the solution domain Ω is expressed as the outer product of the spatial meridian (r, z) space Ω_p times the parametric domain Ω_q as $\Omega = \Omega_p \times \Omega_q$. Whilst in Chapter 4 the parametric domain exclusively contained the one-dimensional frequency domain $\Omega_q = \Omega_\omega$, in this chapter, the parametric domain is extended to further incorporate the electrical conductivity and the strength of the magnetic field as $\Omega_q = \Omega_\omega \times \Omega_\gamma \times \Omega_{B_0}$. Note that this chapter considers the staggered formulation presented in Section 2.5.2, to which the PGD will be applied. This will allow to compare both monolithic and staggered formulations and discuss possible advantages for the problem. Finally, this chapter also includes a comparison between the *a priori* PGD and the *a posteriori* POD methods, both benchmarked against the full order model.

The objectives discussed in this chapter are "*To extend the frequency-based PGD formulation to a higher-dimensional problem including now material parameters*", "*To exploit the staggered nature of the coupled problem at hand*" and "*To assess and compare the a priori PGD and the a posteriori POD methods against the full order model*". The formulation and results of this chapter are contained in the publication of the author of this thesis in [91].

5.2 High-dimensional parametric space

The conductivity of the embedded shields is a key parameter that is typically modified (in a continuous fashion) during the design stage of an MRI scanner. The approach followed in order to vary the conductivities of the mechanical components consists of introducing a scalar coefficient $\alpha_\gamma \in [0.5, 2]$ that scales the reference conductivities γ of all shields. In addition, the strength of the static magnetic field B_0, measured in Teslas [T], refers to the maximum value of the magnitude of the background static magnetic field $\boldsymbol{B}_0^{DC}$ along the $r = 0$ axis. This parameter is used to classify MRI scanners and indicate the overall strength of the equipment, with typical commercial values for B_0 currently at 1.5, 3 and 7 T. Therefore, a further scalar coefficient $\alpha_{B_0} \in [1, 7]$ is introduced in order to scale the strength of the static field $\boldsymbol{B}_0^{DC}$. Finally, the dependency of the solution field $\boldsymbol{\mathcal{Q}}$ upon the high-dimensional parametric space will be denoted as $\boldsymbol{\mathcal{Q}} = \boldsymbol{\mathcal{Q}}(r, z, \omega, \gamma, B_0)$.

Due to the staggered nature of the coupled governing differential equations summarised in (2.1), we advocate in this chapter a sequential solution procedure where the electromagnetic governing equations are solved first (in terms of the magnetic vector potential $\mathcal{A}_\phi$) followed by the solution of the mechanical governing equations (in terms of the displacement field $\boldsymbol{\mathcal{U}}$). This staggered solution procedure will be shown to greatly enhance the computational convergence (i.e. robustness and speed) of the PGD algorithm, especially when considering more than a single parameter of interest (as it was the case in Chapter 4).

As it was already shown in previous works [32, 33, 77, 88], numerical singularities in the vicinity of the conductors' resonant modes can arise when simulating the coupled magneto-mechanical problem. Due to the existence of these resonant phenomena, an automatic regularised-adaptive frequency PGD splitting technique has been introduced in Section 4.4 in order to accurately capture the location of the resonant modes. In [88], this splitting procedure was shown to be fundamental[1] in order to reconstruct, in real time, frequency response spectra for a series of (integrated) magnitudes of industrial interest (i.e. kinetic energy and dissipated power). Naturally, when employing a sequential PGD solution strategy, as will be the case in this work, different frequency (splitting) intervals can be considered when solving the electromagnetic (domain Ω_ω^A) and mechanical (domain Ω_ω^u) physics, separately. This is diagrammatically depicted in Figure 5.1 where, as an example, for a single frequency domain of interest in the electromagnetics problem, namely Ω_ω^A, three frequency intervals $\Omega_\omega^{u,1}$, $\Omega_\omega^{u,2}$ and $\Omega_\omega^{u,3}$ are used for the mechanical problem. This will always be the case, namely, the frequency range requires a higher level of discretisation (and possibly splitting) for the solution of the mechanical equations than for the solution of the electromagnetic equations (due to the presence of singularities in the former equations). This important consideration implies that non-matching parametric (frequency) meshes might be necessary when using the PGD algorithm in both physics separately. This will require the use of one-dimensional mortar integrals, see Section 5.4.2 and Appendix B for further details.

---

[1] As it is expected, these sharp changes in the kinetic energy and dissipated power can make extremely challenging the convergence of the PGD algorithm due to the ill-conditioning of the resulting PGD system in the proximity of these resonant modes.

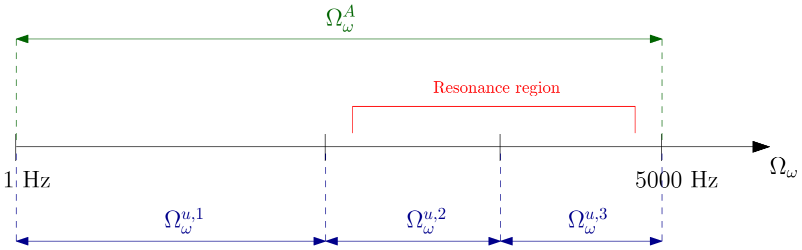

Figure 5.1: Different parametric domains for electromagnetics and mechanics due to adaptive splitting PGD technique.

5.3 Augmented weak formulation

Electromagnetics

The axisymmetric weak form of the electromagnetic problem is formulated in the high-dimensional space $\Omega_p \times \Omega_q^A$ (the upper index $(\cdot)^A$ is used to emphasise the electromagnetics parametric domain). Note that there is no dependency on B_0 in the electromagnetic weak formulation (2.23) and, thus, the electromagnetic parametric domain can be denoted as $\Omega_q^A = \Omega_\omega^A \times \Omega_\gamma^A$. The high-dimensional version of the full order weak form (2.23) can be written as: Find $\mathcal{A}_\phi(r,z,\omega,\gamma) \in \mathcal{X}(\mathcal{A}_{\phi,D})$ such that[2]

$$\mathcal{W}_K^A(\mathcal{A}_\phi, \delta\mathcal{A}_\phi) + \mathrm{i}\mathcal{W}_C^A(\mathcal{A}_\phi, \delta\mathcal{A}_\phi) = \mathcal{S}^A(\delta\mathcal{A}_\phi) \qquad \forall \delta\mathcal{A}_\phi \in \mathcal{X}(0), \tag{5.1}$$

with

$$\mathcal{W}_K^A(a,b) := \int_{\Omega_\gamma^A} \int_{\Omega_\omega^A} W_K^A(a,b)\,\mathrm{d}\omega\,\mathrm{d}\gamma, \tag{5.2a}$$

$$\mathcal{W}_C^A(a,b) := \int_{\Omega_\gamma^A} \alpha_\gamma \int_{\Omega_\omega^A} \omega W_C^A(a,b)\,\mathrm{d}\omega\,\mathrm{d}\gamma, \tag{5.2b}$$

$$\mathcal{S}^A(b) := \int_{\Omega_\gamma^A} \int_{\Omega_\omega^A} S^A(b)\,\mathrm{d}\omega\,\mathrm{d}\gamma, \tag{5.2c}$$

and

$$\mathcal{X}(\mathcal{A}_{\phi,D}) := \{\mathcal{A}_\phi : \mathcal{A}_\phi \in H^1(\Omega_p \times \Omega_\omega^A \times \Omega_\gamma^A), \mathcal{A}_\phi = \mathcal{A}_{\phi,D} \text{ on } \partial\Omega_{p,D} \times \Omega_\omega^A \times \Omega_\gamma^A\}. \tag{5.3}$$

---

[2] The formulation presented in this chapter is an extension of the previously developed frequency-based PGD formulation [88] in Chapter 4, where now the problem is integrated in a higher-dimensional space $\Omega_p \times \Omega_q$.

Mechanics

In the context of a typical MRI scanner configuration, it is often considered that the conducting shields are isolated from each other, see Figure 5.2. Therefore, when solving the mechanical governing equations, the shields can be solved individually (in parallel) and then proceed to assemble the mechanical response of the MRI system all together if needed. With this in mind, this section describes the underlying mechanical governing equations for a single conducting shielding component, formulated irrespective of the total number N^C of shielding components.

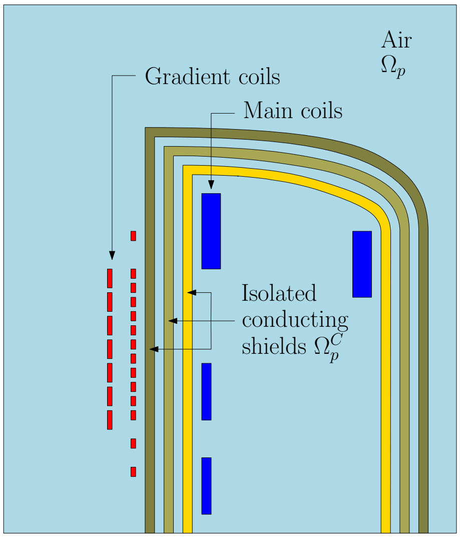

Figure 5.2: Typical axisymmetric MRI scanner geometry; presence of multiple ($N^C = 3$) isolated conducting components Ω_p^C embedded in a truncated non-conducting domain Ω_p.

The high-dimensional axisymmetric augmented weak form of the mechanical problem is formulated over a higher-dimensional space $\Omega_p^C \times \Omega_q^u$,[3] where $\Omega_q^u = \Omega_\omega^u \times \Omega_\gamma^u \times \Omega_{B_0}^u$ (the upper index $(\cdot)^u$ is used to emphasise the mechanical parametric domain) as: Find $\boldsymbol{\mathcal{U}}(r, z, \omega, \gamma, B_0) \in \mathcal{Y}(\boldsymbol{\mathcal{U}}_D)$ such that

$$\mathcal{W}_K^u(\boldsymbol{\mathcal{U}}, \delta\boldsymbol{\mathcal{U}}) + \mathrm{i}\mathcal{W}_C^u(\boldsymbol{\mathcal{U}}, \delta\boldsymbol{\mathcal{U}}) - \mathcal{W}_M^u(\boldsymbol{\mathcal{U}}, \delta\boldsymbol{\mathcal{U}}) = -\mathcal{S}^u(\mathcal{A}_\phi, \delta\boldsymbol{\mathcal{U}}) \qquad \forall \delta\boldsymbol{\mathcal{U}} \in \mathcal{Y}(\mathbf{0}), \quad (5.4)$$

with

$$\mathcal{W}_K^u(\boldsymbol{a}, \boldsymbol{b}) := \int_{\Omega_{B_0}^u} \int_{\Omega_\gamma^u} \int_{\Omega_\omega^u} W_K^u(\boldsymbol{a}, \boldsymbol{b}) \, \mathrm{d}\omega \, \mathrm{d}\gamma \, \mathrm{d}B_0, \qquad (5.5a)$$

$$\mathcal{W}_C^u(\boldsymbol{a}, \boldsymbol{b}) := \int_{\Omega_{B_0}^u} \int_{\Omega_\gamma^u} \int_{\Omega_\omega^u} \omega^2 W_C^u(\boldsymbol{a}, \boldsymbol{b}) \, \mathrm{d}\omega \, \mathrm{d}\gamma \, \mathrm{d}B_0, \qquad (5.5b)$$

$$\mathcal{W}_M^u(\boldsymbol{a}, \boldsymbol{b}) := \int_{\Omega_{B_0}^u} \int_{\Omega_\gamma^u} \int_{\Omega_\omega^u} \omega^2 W_M^u(\boldsymbol{a}, \boldsymbol{b}) \, \mathrm{d}\omega \, \mathrm{d}\gamma \, \mathrm{d}B_0, \qquad (5.5c)$$

---

[3] Only the conducting spatial domain Ω_p^C is considered for the mechanical problem, instead of the entire spatial domain Ω_p used for electromagnetics.

$$\mathcal{S}^u(a,\boldsymbol{b}) := \int_{\Omega^u_{B_0}} \alpha_{B_0} \int_{\Omega^u_\gamma} \int_{\Omega^u_\omega} W^{uA}_K(a,\boldsymbol{b}) \,\mathrm{d}\omega \,\mathrm{d}\gamma \,\mathrm{d}B_0, \tag{5.5d}$$

and

$$\mathcal{Y}(\boldsymbol{\mathcal{U}}_D) := \{\boldsymbol{\mathcal{U}} : \boldsymbol{\mathcal{U}} \in (H^1(\Omega^C_p \times \Omega^u_\omega \times \Omega^u_\gamma \times \Omega^u_{B_0}))^2, \boldsymbol{\mathcal{U}} = \boldsymbol{\mathcal{U}}_D \text{ on } \partial\Omega^C_{p,D} \times \Omega^u_\omega \times \Omega^u_\gamma \times \Omega^u_{B_0}\}. \tag{5.6}$$

Note that no direct dependency on the electric conductivity γ can be observed in any of the terms in (5.5). However, since the magnetic potential is γ-dependent, namely $\mathcal{A}_\phi = \mathcal{A}_\phi(r,z,\omega,\gamma)$, integration over Ω^u_γ is required in the above definitions in order to accommodate the right-hand side term $\mathcal{S}^u(\mathcal{A}_\phi, \delta\boldsymbol{\mathcal{U}})$ in (5.5d).

5.4 PGD for magneto-mechanical problems

This section contains the PGD formulation, see Chapter 3, particularised for the coupled magneto-mechanical problem of study, see Chapter 2. The electromagnetic PGD formulation is first presented followed by the PGD description for mechanics. In addition, the workflow of the PGD solver is presented together with the finite element discretisation of the system of equations obtained after applying the PGD method.

5.4.1 PGD formulation for electromagnetics

The PGD method is applied to the AC electromagnetic problem (5.1) by approximating the scalar potential field $\mathcal{A}_\phi$ with a separable expression. The general high-dimensional PGD definition for a vector field $\boldsymbol{\mathcal{Q}}$, see (3.4), is particularised for the electromagnetic scalar potential $\mathcal{A}_\phi$ as

$$\mathcal{A}_\phi(r,z,\omega,\gamma) \approx \mathcal{A}_\phi^{N_A}(r,z,\omega,\gamma) := \sum_{n=1}^{N_A} \beta^n_{\mathcal{A}_\phi} F^n_{\mathcal{A}_\phi}(r,z) G^n_{\mathcal{A}_\phi}(\omega) H^n_{\mathcal{A}_\phi}(\gamma), \tag{5.7}$$

where N_A is the total number of electromagnetic modes computed, the spatial modes $\boldsymbol{\mathcal{F}}^n(r,z)$ appearing in (3.4) reduce to $F^n_{\mathcal{A}_\phi}(r,z)$[4], the parametric modes are $\mathcal{G}^n_1(w_1) = G^n_{\mathcal{A}_\phi}(\omega)$ and $\mathcal{G}^n_2(w_2) = H^n_{\mathcal{A}_\phi}(\gamma)$ and the modal weight becomes $\beta^n = \beta^n_{\mathcal{A}_\phi}$. The n^{th} accumulated solution is then

$$\begin{aligned} \mathcal{A}^n_\phi(r,z,\omega,\gamma) &= \sum_{m=1}^{n-1} \beta^m_{\mathcal{A}_\phi} F^m_{\mathcal{A}_\phi}(r,z) G^m_{\mathcal{A}_\phi}(\omega) H^m_{\mathcal{A}_\phi}(\gamma) + f_{\mathcal{A}_\phi}(r,z) g_{\mathcal{A}_\phi}(\omega) h_{\mathcal{A}_\phi}(\gamma) \\ &= \mathcal{A}^{n-1}_\phi(r,z,\omega,\gamma) + f_{\mathcal{A}_\phi}(r,z) g_{\mathcal{A}_\phi}(\omega) h_{\mathcal{A}_\phi}(\gamma), \end{aligned} \tag{5.8}$$

where, as mentioned in Section 3.3, the uppercase and lowercase fonts indicate converged and non-converged quantities in the process of a fixed-point ADS algorithm.

---

[4] Note that the general separable expression for a vector field $\boldsymbol{q}$ (3.4) is reduced to a scalar field $\mathcal{A}_\phi$ and thus, the vectorial function $\boldsymbol{\mathcal{F}}^n(r,z)$ becomes the scalar function $F^n_{\mathcal{A}_\phi}(r,z)$.

A suitable (compatible) test function can be introduced as

$$\delta\mathcal{A}_\phi = \delta f_{\mathcal{A}_\phi} g_{\mathcal{A}_\phi} h_{\mathcal{A}_\phi} + f_{\mathcal{A}_\phi} \delta g_{\mathcal{A}_\phi} h_{\mathcal{A}_\phi} + f_{\mathcal{A}_\phi} g_{\mathcal{A}_\phi} \delta h_{\mathcal{A}_\phi}. \tag{5.9}$$

The two expressions (5.8) and (5.9) can be now substituted into the electromagnetic weak form (5.1), allowing the problem to be formulated as: Find $(f_{\mathcal{A}_\phi}, g_{\mathcal{A}_\phi}, h_{\mathcal{A}_\phi}) \in X(0) \times Z(\Omega_\omega^A) \times Z(\Omega_\gamma^A)$ such that

$$\begin{aligned} \mathcal{R}_{f_{\mathcal{A}_\phi}}(\delta f_{\mathcal{A}_\phi}; \mathcal{A}_\phi^{n-1}, f_{\mathcal{A}_\phi}, g_{\mathcal{A}_\phi}, h_{\mathcal{A}_\phi}) + \mathcal{R}_{g_{\mathcal{A}_\phi}}(\delta g_{\mathcal{A}_\phi}; \mathcal{A}_\phi^{n-1}, f_{\mathcal{A}_\phi}, g_{\mathcal{A}_\phi}, h_{\mathcal{A}_\phi}) \\ + \mathcal{R}_{h_{\mathcal{A}_\phi}}(\delta h_{\mathcal{A}_\phi}; \mathcal{A}_\phi^{n-1}, f_{\mathcal{A}_\phi}, g_{\mathcal{A}_\phi}, h_{\mathcal{A}_\phi}) = 0, \end{aligned} \tag{5.10}$$

$\forall(\delta f_{\mathcal{A}_\phi}, \delta g_{\mathcal{A}_\phi}, \delta h_{\mathcal{A}_\phi}) \in X(0) \times Z(\Omega_\omega^A) \times Z(\Omega_\gamma^A)$, where $Z(\Omega) = L^2(\Omega)$ and the three electromagnetic residual forms are defined as

$$\begin{aligned} \mathcal{R}_{f_{\mathcal{A}_\phi}}(\delta f_{\mathcal{A}_\phi}; \mathcal{A}_\phi^{n-1}, f_{\mathcal{A}_\phi}, g_{\mathcal{A}_\phi}, h_{\mathcal{A}_\phi}) := {} & \mathcal{W}_K^A(f_{\mathcal{A}_\phi} g_{\mathcal{A}_\phi} h_{\mathcal{A}_\phi}, \delta f_{\mathcal{A}_\phi} g_{\mathcal{A}_\phi} h_{\mathcal{A}_\phi}) \\ & + \mathrm{i}\mathcal{W}_C^A(f_{\mathcal{A}_\phi} g_{\mathcal{A}_\phi} h_{\mathcal{A}_\phi}, \delta f_{\mathcal{A}_\phi} g_{\mathcal{A}_\phi} h_{\mathcal{A}_\phi}) \\ & - \mathcal{S}^A(\delta f_{\mathcal{A}_\phi} g_{\mathcal{A}_\phi} h_{\mathcal{A}_\phi}) + \mathcal{W}_K^A(\mathcal{A}_\phi^{n-1}, \delta f_{\mathcal{A}_\phi} g_{\mathcal{A}_\phi} h_{\mathcal{A}_\phi}) \\ & + \mathrm{i}\mathcal{W}_C^A(\mathcal{A}_\phi^{n-1}, \delta f_{\mathcal{A}_\phi} g_{\mathcal{A}_\phi} h_{\mathcal{A}_\phi}), \end{aligned} \tag{5.11a}$$

$$\begin{aligned} \mathcal{R}_{g_{\mathcal{A}_\phi}}(\delta g_{\mathcal{A}_\phi}; \mathcal{A}_\phi^{n-1}, f_{\mathcal{A}_\phi}, g_{\mathcal{A}_\phi}, h_{\mathcal{A}_\phi}) := {} & \mathcal{W}_K^A(f_{\mathcal{A}_\phi} g_{\mathcal{A}_\phi} h_{\mathcal{A}_\phi}, f_{\mathcal{A}_\phi} \delta g_{\mathcal{A}_\phi} h_{\mathcal{A}_\phi}) \\ & + \mathrm{i}\mathcal{W}_C^A(f_{\mathcal{A}_\phi} g_{\mathcal{A}_\phi} h_{\mathcal{A}_\phi}, f_{\mathcal{A}_\phi} \delta g_{\mathcal{A}_\phi} h_{\mathcal{A}_\phi}) \\ & - \mathcal{S}^A(f_{\mathcal{A}_\phi} \delta g_{\mathcal{A}_\phi} h_{\mathcal{A}_\phi}) + \mathcal{W}_K^A(\mathcal{A}_\phi^{n-1}, f_{\mathcal{A}_\phi} \delta g_{\mathcal{A}_\phi} h_{\mathcal{A}_\phi}) \\ & + \mathrm{i}\mathcal{W}_C^A(\mathcal{A}_\phi^{n-1}, f_{\mathcal{A}_\phi} \delta g_{\mathcal{A}_\phi} h_{\mathcal{A}_\phi}), \end{aligned} \tag{5.11b}$$

$$\begin{aligned} \mathcal{R}_{h_{\mathcal{A}_\phi}}(\delta h_{\mathcal{A}_\phi}; \mathcal{A}_\phi^{n-1}, f_{\mathcal{A}_\phi}, g_{\mathcal{A}_\phi}, h_{\mathcal{A}_\phi}) := {} & \mathcal{W}_K^A(f_{\mathcal{A}_\phi} g_{\mathcal{A}_\phi} h_{\mathcal{A}_\phi}, f_{\mathcal{A}_\phi} g_{\mathcal{A}_\phi} \delta h_{\mathcal{A}_\phi}) \\ & + \mathrm{i}\mathcal{W}_C^A(f_{\mathcal{A}_\phi} g_{\mathcal{A}_\phi} h_{\mathcal{A}_\phi}, f_{\mathcal{A}_\phi} g_{\mathcal{A}_\phi} \delta h_{\mathcal{A}_\phi}) \\ & - \mathcal{S}^A(f_{\mathcal{A}_\phi} g_{\mathcal{A}_\phi} \delta h_{\mathcal{A}_\phi}) + \mathcal{W}_K^A(\mathcal{A}_\phi^{n-1}, f_{\mathcal{A}_\phi} g_{\mathcal{A}_\phi} \delta h_{\mathcal{A}_\phi}) \\ & + \mathrm{i}\mathcal{W}_C^A(\mathcal{A}_\phi^{n-1}, f_{\mathcal{A}_\phi} g_{\mathcal{A}_\phi} \delta h_{\mathcal{A}_\phi}). \end{aligned} \tag{5.11c}$$

Regarding the implementation of the electromagnetic problem (5.10), this can be formulated using the concept of directional derivatives [84], where the problem is solved by incrementally updating the solution fields $f_{\mathcal{A}_\phi}$, $g_{\mathcal{A}_\phi}$ and $h_{\mathcal{A}_\phi}$. As mentioned in Section 3.3, the solver exploits a fixed-point ADS in order to efficiently converge within every modal component of the PGD solution. The detailed formulation and its implementation is presented in the following sections.

5.4.2 PGD formulation for mechanics

In a similar manner to electromagnetics, the PGD methodology approximates the displacement field $\boldsymbol{u}$ using a separable representation. In this case, the generic high-dimensional PGD definition (3.4) becomes

$$\boldsymbol{\mathcal{U}}(r,z,\omega,\gamma,B_0) \approx \boldsymbol{\mathcal{U}}^{N_u}(r,z,\omega,\gamma,B_0) := \sum_{n=1}^{N_u} \beta^n_{\boldsymbol{u}} \boldsymbol{F}^n_{\boldsymbol{u}}(r,z) G^n_{\boldsymbol{u}}(\omega) H^n_{\boldsymbol{u}}(\gamma) L^n_{\boldsymbol{u}}(B_0), \tag{5.12}$$

where N_u is the number of mechanical modes computed and the terms appearing in the general PGD definition (3.4) become $\beta^n = \beta^n_{\boldsymbol{u}}$, $\boldsymbol{\mathcal{F}}^n(r,z) = \boldsymbol{F}^n_{\boldsymbol{u}}(r,z)$, $\mathcal{G}^n_1(w_1) = G^n_{\boldsymbol{u}}(\omega)$, $\mathcal{G}^n_2(w_2) = H^n_{\boldsymbol{u}}(\gamma)$ and $\mathcal{G}^n_3(w_3) = L^n_{\boldsymbol{u}}(B_0)$. Considering a particular modal component n, the accumulated solution field is written as

$$\begin{aligned} \boldsymbol{\mathcal{U}}^n(r,z,\omega,\gamma,B_0) &= \sum_{m=1}^{n-1} \beta^m_{\boldsymbol{u}} \boldsymbol{F}^m_{\boldsymbol{u}}(r,z) G^m_{\boldsymbol{u}}(\omega) H^m_{\boldsymbol{u}}(\gamma) L^m_{\boldsymbol{u}}(B_0) + \boldsymbol{f}_{\boldsymbol{u}}(r,z) g_{\boldsymbol{u}}(\omega) h_{\boldsymbol{u}}(\gamma) l_{\boldsymbol{u}}(B_0) \\ &= \boldsymbol{\mathcal{U}}^{n-1}(r,z,\omega,\gamma,B_0) + \boldsymbol{f}_{\boldsymbol{u}}(r,z) g_{\boldsymbol{u}}(\omega) h_{\boldsymbol{u}}(\gamma) l_{\boldsymbol{u}}(B_0), \end{aligned} \tag{5.13}$$

where a suitable (compatible) test function can be introduced as

$$\delta\boldsymbol{\mathcal{U}} = \delta\boldsymbol{f}_{\boldsymbol{u}} g_{\boldsymbol{u}} h_{\boldsymbol{u}} l_{\boldsymbol{u}} + \boldsymbol{f}_{\boldsymbol{u}} \delta g_{\boldsymbol{u}} h_{\boldsymbol{u}} l_{\boldsymbol{u}} + \boldsymbol{f}_{\boldsymbol{u}} g_{\boldsymbol{u}} \delta h_{\boldsymbol{u}} l_{\boldsymbol{u}} + \boldsymbol{f}_{\boldsymbol{u}} g_{\boldsymbol{u}} h_{\boldsymbol{u}} \delta l_{\boldsymbol{u}}. \tag{5.14}$$

These two expressions (5.13) and (5.14) can be substituted into the mechanical augmented weak form (5.4) together with the electromagnetic PGD definition (5.7), allowing the problem to be formulated as: Find $(\boldsymbol{f}_{\boldsymbol{u}}, g_{\boldsymbol{u}}, h_{\boldsymbol{u}}, l_{\boldsymbol{u}}) \in Y(\boldsymbol{0}) \times Z(\Omega^u_\omega) \times Z(\Omega^u_\gamma) \times Z(\Omega^u_{B_0})$ such that

$$\begin{aligned} &\mathcal{R}_{\boldsymbol{f}_{\boldsymbol{u}}}(\delta\boldsymbol{f}_{\boldsymbol{u}}; \boldsymbol{\mathcal{U}}^{n-1}, \boldsymbol{f}_{\boldsymbol{u}}, g_{\boldsymbol{u}}, h_{\boldsymbol{u}}, l_{\boldsymbol{u}}) + \mathcal{R}_{g_{\boldsymbol{u}}}(\delta g_{\boldsymbol{u}}; \boldsymbol{\mathcal{U}}^{n-1}, \boldsymbol{f}_{\boldsymbol{u}}, g_{\boldsymbol{u}}, h_{\boldsymbol{u}}, l_{\boldsymbol{u}}) \\ &+\mathcal{R}_{h_{\boldsymbol{u}}}(\delta h_{\boldsymbol{u}}; \boldsymbol{\mathcal{U}}^{n-1}, \boldsymbol{f}_{\boldsymbol{u}}, g_{\boldsymbol{u}}, h_{\boldsymbol{u}}, l_{\boldsymbol{u}}) + \mathcal{R}_{l_{\boldsymbol{u}}}(\delta l_{\boldsymbol{u}}; \boldsymbol{\mathcal{U}}^{n-1}, \boldsymbol{f}_{\boldsymbol{u}}, g_{\boldsymbol{u}}, h_{\boldsymbol{u}}, l_{\boldsymbol{u}}) = 0, \end{aligned} \tag{5.15}$$

$\forall(\delta\boldsymbol{f}_{\boldsymbol{u}}, \delta g_{\boldsymbol{u}}, \delta h_{\boldsymbol{u}}, \delta l_{\boldsymbol{u}}) \in Y(\boldsymbol{0}) \times Z(\Omega^u_\omega) \times Z(\Omega^u_\gamma) \times Z(\Omega^u_{B_0})$ and the four mechanical residual forms are defined as

$$\begin{aligned} \mathcal{R}_{\boldsymbol{f}_{\boldsymbol{u}}}(\delta\boldsymbol{f}_{\boldsymbol{u}}; \boldsymbol{\mathcal{U}}^{n-1}, \boldsymbol{f}_{\boldsymbol{u}}, g_{\boldsymbol{u}}, h_{\boldsymbol{u}}, l_{\boldsymbol{u}}) :&= \mathcal{W}^u_K(\boldsymbol{f}_{\boldsymbol{u}} g_{\boldsymbol{u}} h_{\boldsymbol{u}} l_{\boldsymbol{u}}, \delta\boldsymbol{f}_{\boldsymbol{u}} g_{\boldsymbol{u}} h_{\boldsymbol{u}} l_{\boldsymbol{u}}) \\ &+ \mathrm{i}\mathcal{W}^u_C(\boldsymbol{f}_{\boldsymbol{u}} g_{\boldsymbol{u}} h_{\boldsymbol{u}} l_{\boldsymbol{u}}, \delta\boldsymbol{f}_{\boldsymbol{u}} g_{\boldsymbol{u}} h_{\boldsymbol{u}} l_{\boldsymbol{u}}) \\ &- \mathcal{W}^u_M(\boldsymbol{f}_{\boldsymbol{u}} g_{\boldsymbol{u}} h_{\boldsymbol{u}} l_{\boldsymbol{u}}, \delta\boldsymbol{f}_{\boldsymbol{u}} g_{\boldsymbol{u}} h_{\boldsymbol{u}} l_{\boldsymbol{u}}) \\ &+ \mathcal{S}^u(\mathcal{A}^{N_A}_\phi, \delta\boldsymbol{f}_{\boldsymbol{u}} g_{\boldsymbol{u}} h_{\boldsymbol{u}} l_{\boldsymbol{u}}) + \mathcal{W}^u_K(\boldsymbol{\mathcal{U}}^{n-1}, \delta\boldsymbol{f}_{\boldsymbol{u}} g_{\boldsymbol{u}} h_{\boldsymbol{u}} l_{\boldsymbol{u}}) \\ &+ \mathrm{i}\mathcal{W}^u_C(\boldsymbol{\mathcal{U}}^{n-1}, \delta\boldsymbol{f}_{\boldsymbol{u}} g_{\boldsymbol{u}} h_{\boldsymbol{u}} l_{\boldsymbol{u}}) - \mathcal{W}^u_M(\boldsymbol{\mathcal{U}}^{n-1}, \delta\boldsymbol{f}_{\boldsymbol{u}} g_{\boldsymbol{u}} h_{\boldsymbol{u}} l_{\boldsymbol{u}}), \end{aligned} \tag{5.16a}$$

$$\begin{aligned} \mathcal{R}_{g_{\boldsymbol{u}}}(\delta g_{\boldsymbol{u}}; \boldsymbol{\mathcal{U}}^{n-1}, \boldsymbol{f}_{\boldsymbol{u}}, g_{\boldsymbol{u}}, h_{\boldsymbol{u}}, l_{\boldsymbol{u}}) :&= \mathcal{W}^u_K(\boldsymbol{f}_{\boldsymbol{u}} g_{\boldsymbol{u}} h_{\boldsymbol{u}} l_{\boldsymbol{u}}, \boldsymbol{f}_{\boldsymbol{u}} \delta g_{\boldsymbol{u}} h_{\boldsymbol{u}} l_{\boldsymbol{u}}) \\ &+ \mathrm{i}\mathcal{W}^u_C(\boldsymbol{f}_{\boldsymbol{u}} g_{\boldsymbol{u}} h_{\boldsymbol{u}} l_{\boldsymbol{u}}, \boldsymbol{f}_{\boldsymbol{u}} \delta g_{\boldsymbol{u}} h_{\boldsymbol{u}} l_{\boldsymbol{u}}) \\ &- \mathcal{W}^u_M(\boldsymbol{f}_{\boldsymbol{u}} g_{\boldsymbol{u}} h_{\boldsymbol{u}} l_{\boldsymbol{u}}, \boldsymbol{f}_{\boldsymbol{u}} \delta g_{\boldsymbol{u}} h_{\boldsymbol{u}} l_{\boldsymbol{u}}) \\ &+ \mathcal{S}^u(\mathcal{A}^{N_A}_\phi, \boldsymbol{f}_{\boldsymbol{u}} \delta g_{\boldsymbol{u}} h_{\boldsymbol{u}} l_{\boldsymbol{u}}) + \mathcal{W}^u_K(\boldsymbol{\mathcal{U}}^{n-1}, \boldsymbol{f}_{\boldsymbol{u}} \delta g_{\boldsymbol{u}} h_{\boldsymbol{u}} l_{\boldsymbol{u}}) \\ &+ \mathrm{i}\mathcal{W}^u_C(\boldsymbol{\mathcal{U}}^{n-1}, \boldsymbol{f}_{\boldsymbol{u}} \delta g_{\boldsymbol{u}} h_{\boldsymbol{u}} l_{\boldsymbol{u}}) - \mathcal{W}^u_M(\boldsymbol{\mathcal{U}}^{n-1}, \boldsymbol{f}_{\boldsymbol{u}} \delta g_{\boldsymbol{u}} h_{\boldsymbol{u}} l_{\boldsymbol{u}}), \end{aligned} \tag{5.16b}$$

$$\begin{aligned}\mathcal{R}_{h_{\boldsymbol{u}}}(\delta h_{\boldsymbol{u}}; \boldsymbol{\mathcal{U}}^{n-1}, \boldsymbol{f}_{\boldsymbol{u}}, g_{\boldsymbol{u}}, h_{\boldsymbol{u}}, l_{\boldsymbol{u}}) :=\ & \mathcal{W}_K^u(\boldsymbol{f}_{\boldsymbol{u}} g_{\boldsymbol{u}} h_{\boldsymbol{u}} l_{\boldsymbol{u}}, \boldsymbol{f}_{\boldsymbol{u}} g_{\boldsymbol{u}} \delta h_{\boldsymbol{u}} l_{\boldsymbol{u}}) \\ & + \mathrm{i}\mathcal{W}_C^u(\boldsymbol{f}_{\boldsymbol{u}} g_{\boldsymbol{u}} h_{\boldsymbol{u}} l_{\boldsymbol{u}}, \boldsymbol{f}_{\boldsymbol{u}} g_{\boldsymbol{u}} \delta h_{\boldsymbol{u}} l_{\boldsymbol{u}}) \\ & - \mathcal{W}_M^u(\boldsymbol{f}_{\boldsymbol{u}} g_{\boldsymbol{u}} h_{\boldsymbol{u}} l_{\boldsymbol{u}}, \boldsymbol{f}_{\boldsymbol{u}} g_{\boldsymbol{u}} \delta h_{\boldsymbol{u}} l_{\boldsymbol{u}}) \\ & + \mathcal{S}^u(\mathcal{A}_\phi^{N_A}, \boldsymbol{f}_{\boldsymbol{u}} g_{\boldsymbol{u}} \delta h_{\boldsymbol{u}} l_{\boldsymbol{u}}) + \mathcal{W}_K^u(\boldsymbol{\mathcal{U}}^{n-1}, \boldsymbol{f}_{\boldsymbol{u}} g_{\boldsymbol{u}} \delta h_{\boldsymbol{u}} l_{\boldsymbol{u}}) \\ & + \mathrm{i}\mathcal{W}_C^u(\boldsymbol{\mathcal{U}}^{n-1}, \boldsymbol{f}_{\boldsymbol{u}} g_{\boldsymbol{u}} \delta h_{\boldsymbol{u}} l_{\boldsymbol{u}}) - \mathcal{W}_M^u(\boldsymbol{\mathcal{U}}^{n-1}, \boldsymbol{f}_{\boldsymbol{u}} g_{\boldsymbol{u}} \delta h_{\boldsymbol{u}} l_{\boldsymbol{u}}),\end{aligned} \tag{5.16c}$$

$$\begin{aligned}\mathcal{R}_{l_{\boldsymbol{u}}}(\delta l_{\boldsymbol{u}}; \boldsymbol{\mathcal{U}}^{n-1}, \boldsymbol{f}_{\boldsymbol{u}}, g_{\boldsymbol{u}}, h_{\boldsymbol{u}}, l_{\boldsymbol{u}}) :=\ & \mathcal{W}_K^u(\boldsymbol{f}_{\boldsymbol{u}} g_{\boldsymbol{u}} h_{\boldsymbol{u}} l_{\boldsymbol{u}}, \boldsymbol{f}_{\boldsymbol{u}} g_{\boldsymbol{u}} h_{\boldsymbol{u}} \delta l_{\boldsymbol{u}}) \\ & + \mathrm{i}\mathcal{W}_C^u(\boldsymbol{f}_{\boldsymbol{u}} g_{\boldsymbol{u}} h_{\boldsymbol{u}} l_{\boldsymbol{u}}, \boldsymbol{f}_{\boldsymbol{u}} g_{\boldsymbol{u}} h_{\boldsymbol{u}} \delta l_{\boldsymbol{u}}) \\ & - \mathcal{W}_M^u(\boldsymbol{f}_{\boldsymbol{u}} g_{\boldsymbol{u}} h_{\boldsymbol{u}} l_{\boldsymbol{u}}, \boldsymbol{f}_{\boldsymbol{u}} g_{\boldsymbol{u}} h_{\boldsymbol{u}} \delta l_{\boldsymbol{u}}) \\ & + \mathcal{S}^u(\mathcal{A}_\phi^{N_A}, \boldsymbol{f}_{\boldsymbol{u}} g_{\boldsymbol{u}} h_{\boldsymbol{u}} \delta l_{\boldsymbol{u}}) + \mathcal{W}_K^u(\boldsymbol{\mathcal{U}}^{n-1}, \boldsymbol{f}_{\boldsymbol{u}} g_{\boldsymbol{u}} h_{\boldsymbol{u}} \delta l_{\boldsymbol{u}}) \\ & + \mathrm{i}\mathcal{W}_C^u(\boldsymbol{\mathcal{U}}^{n-1}, \boldsymbol{f}_{\boldsymbol{u}} g_{\boldsymbol{u}} h_{\boldsymbol{u}} \delta l_{\boldsymbol{u}}) - \mathcal{W}_M^u(\boldsymbol{\mathcal{U}}^{n-1}, \boldsymbol{f}_{\boldsymbol{u}} g_{\boldsymbol{u}} h_{\boldsymbol{u}} \delta l_{\boldsymbol{u}}).\end{aligned} \tag{5.16d}$$

The mechanical problem (5.15) is solved following an analogous procedure to that for electromagnetics, see (5.10), where further details can be found in the following sections. Note that in the case of the mechanical problem, input information arising from the electromagnetic problem is needed, see the right-hand side in (5.4), which leads to the introductions of so-called mortar integral due to the possibility of considering different levels of discretisation in the parametric domains, as shown in Section 5.2. The numerical treatment of these mortar integrals is discussed and formulated in Appendix B.

5.4.3 Staggered PGD solver

The PGD solver described above exploits the staggered nature of the coupled magneto-mechanical problem (2.1), by solving the coupled magneto-mechanical problem in a sequential manner, as the workflow describes in Figure 5.3 where, the high-dimensional AC electromagnetic problem (5.10) is solved first in order to obtain a separable representation for the scalar potential $\mathcal{A}_\phi^{N_A}$. Subsequently, the high-dimensional AC mechanical problem (5.15) is solved for each mechanical component, until the complete mechanical response $\boldsymbol{\mathcal{U}}^{N_u}$ is obtained. The offline stage of the PGD method ends when the separable expressions for both physics $\mathcal{A}_\phi^{N_A}$ and $\boldsymbol{\mathcal{U}}^{N_u}$ are obtained and stored for future online postprocessing.

5.4.4 Alternating direction scheme

Electromagnetics

The electromagnetic residuals defined in (5.11) can be expanded taking advantage of the separability of the terms, see (5.8). Hence, these residuals can be shown to

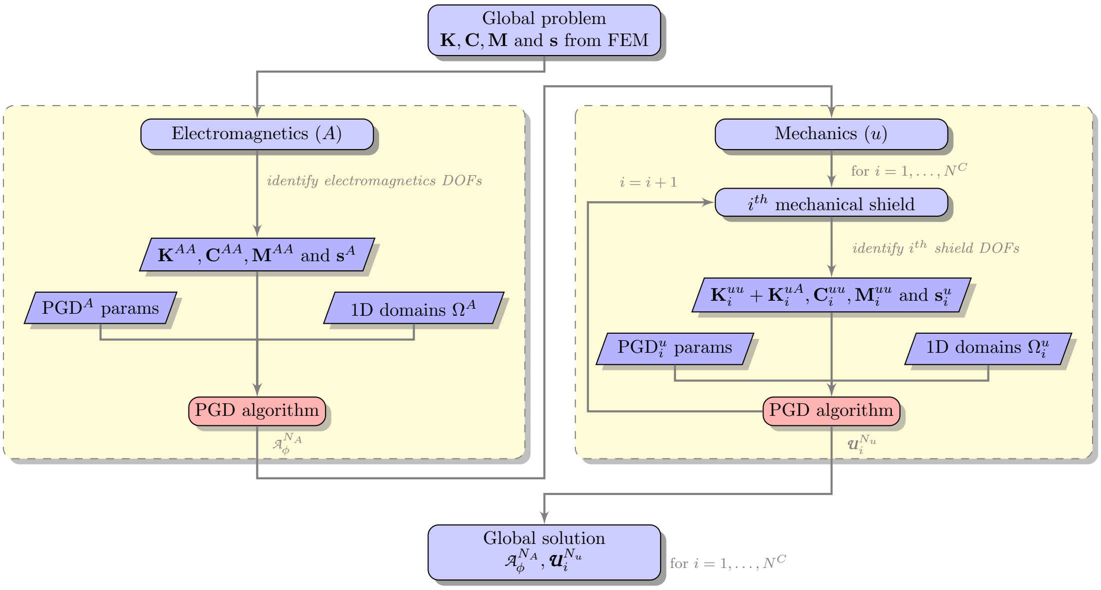
Global problem
$\mathbf{K}, \mathbf{C}, \mathbf{M}$ and $\mathbf{s}$ from FEM
Electromagnetics (A)
identify electromagnetics DOFs
$\mathbf{K}^{AA}, \mathbf{C}^{AA}, \mathbf{M}^{AA}$ and $\mathbf{s}^{A}$
PGD^A params
1D domains Ω^A
PGD algorithm
$\mathcal{A}_\phi^{N_A}$
Mechanics (u)
for $i = 1, \ldots, N^C$
$i = i + 1$
i^{th} mechanical shield
identify i^{th} shield DOFs
$\mathbf{K}_i^{uu} + \mathbf{K}_i^{uA}, \mathbf{C}_i^{uu}, \mathbf{M}_i^{uu}$ and $\mathbf{s}_i^{u}$
PGD$_i^u$ params
1D domains Ω_i^u
PGD algorithm
$\boldsymbol{u}_i^{N_u}$
Global solution
$\mathcal{A}_\phi^{N_A}, \boldsymbol{u}_i^{N_u}$
for $i = 1, \ldots, N^C$

Figure 5.3: Flow chart algorithm; description of the staggered PGD nature. The continuous and discrete formulations are detailed in Sections 5.4.4 and 5.4.5.

be

$$\begin{aligned}
\mathcal{R}_{f_{\mathcal{A}_\phi}}(\delta f_{\mathcal{A}_\phi}; \mathcal{A}_\phi^{n-1}, f_{\mathcal{A}_\phi}, g_{\mathcal{A}_\phi}, h_{\mathcal{A}_\phi}) = {} & W_K^A(f_{\mathcal{A}_\phi}, \delta f_{\mathcal{A}_\phi}) G_0^A(g_{\mathcal{A}_\phi}, g_{\mathcal{A}_\phi}) H_0^A(h_{\mathcal{A}_\phi}, h_{\mathcal{A}_\phi}) \\
& + \mathrm{i} W_C^A(f_{\mathcal{A}_\phi}, \delta f_{\mathcal{A}_\phi}) G_1^A(g_{\mathcal{A}_\phi}, g_{\mathcal{A}_\phi}) H_1^A(h_{\mathcal{A}_\phi}, h_{\mathcal{A}_\phi}) \\
& - S^A(\delta f_{\mathcal{A}_\phi}) G_0^A(1, g_{\mathcal{A}_\phi}) H_0^A(1, h_{\mathcal{A}_\phi}) \\
& + \sum_{m=1}^{n-1} \Big[W_K^A(F_{\mathcal{A}_\phi}^{[m]}, \delta f_{\mathcal{A}_\phi}) G_0^A(G_{\mathcal{A}_\phi}^{[m]}, g_{\mathcal{A}_\phi}) H_0^A(H_{\mathcal{A}_\phi}^{[m]}, h_{\mathcal{A}_\phi}) \\
& + \mathrm{i} W_C^A(F_{\mathcal{A}_\phi}^{[m]}, \delta f_{\mathcal{A}_\phi}) G_1^A(G_{\mathcal{A}_\phi}^{[m]}, g_{\mathcal{A}_\phi}) H_1^A(H_{\mathcal{A}_\phi}^{[m]}, h_{\mathcal{A}_\phi}) \Big],
\end{aligned} \tag{5.17a}$$

$$\begin{aligned}
\mathcal{R}_{g_{\mathcal{A}_\phi}}(\delta g_{\mathcal{A}_\phi}; \mathcal{A}_\phi^{n-1}, f_{\mathcal{A}_\phi}, g_{\mathcal{A}_\phi}, h_{\mathcal{A}_\phi}) = {} & W_K^A(f_{\mathcal{A}_\phi}, f_{\mathcal{A}_\phi}) G_0^A(g_{\mathcal{A}_\phi}, \delta g_{\mathcal{A}_\phi}) H_0^A(h_{\mathcal{A}_\phi}, h_{\mathcal{A}_\phi}) \\
& + \mathrm{i} W_C^A(f_{\mathcal{A}_\phi}, f_{\mathcal{A}_\phi}) G_1^A(g_{\mathcal{A}_\phi}, \delta g_{\mathcal{A}_\phi}) H_1^A(h_{\mathcal{A}_\phi}, h_{\mathcal{A}_\phi}) \\
& - S^A(f_{\mathcal{A}_\phi}) G_0^A(1, \delta g_{\mathcal{A}_\phi}) H_0^A(1, h_{\mathcal{A}_\phi}) \\
& + \sum_{m=1}^{n-1} \Big[W_K^A(F_{\mathcal{A}_\phi}^{[m]}, f_{\mathcal{A}_\phi}) G_0^A(G_{\mathcal{A}_\phi}^{[m]}, \delta g_{\mathcal{A}_\phi}) H_0^A(H_{\mathcal{A}_\phi}^{[m]}, h_{\mathcal{A}_\phi}) \\
& + \mathrm{i} W_C^A(F_{\mathcal{A}_\phi}^{[m]}, f_{\mathcal{A}_\phi}) G_1^A(G_{\mathcal{A}_\phi}^{[m]}, \delta g_{\mathcal{A}_\phi}) H_1^A(H_{\mathcal{A}_\phi}^{[m]}, h_{\mathcal{A}_\phi}) \Big],
\end{aligned} \tag{5.17b}$$

$$\begin{aligned}\mathcal{R}_{h_{\mathcal{A}_\phi}}(\delta h_{\mathcal{A}_\phi};\mathcal{A}_\phi^{n-1},f_{\mathcal{A}_\phi},g_{\mathcal{A}_\phi},h_{\mathcal{A}_\phi}) &= W_K^A(f_{\mathcal{A}_\phi},f_{\mathcal{A}_\phi})G_0^A(g_{\mathcal{A}_\phi},g_{\mathcal{A}_\phi})H_0^A(h_{\mathcal{A}_\phi},\delta h_{\mathcal{A}_\phi})\\ &+\mathrm{i}W_C^A(f_{\mathcal{A}_\phi},f_{\mathcal{A}_\phi})G_1^A(g_{\mathcal{A}_\phi},g_{\mathcal{A}_\phi})H_1^A(h_{\mathcal{A}_\phi},\delta h_{\mathcal{A}_\phi})\\ &-S^A(f_{\mathcal{A}_\phi})G_0^A(1,g_{\mathcal{A}_\phi})H_0^A(1,\delta h_{\mathcal{A}_\phi})\\ &+\sum_{m=1}^{n-1}\Big[W_K^A(F_{\mathcal{A}_\phi}^{[m]},f_{\mathcal{A}_\phi})G_0^A(G_{\mathcal{A}_\phi}^{[m]},g_{\mathcal{A}_\phi})H_0^A(H_{\mathcal{A}_\phi}^{[m]},\delta h_{\mathcal{A}_\phi})\\ &+\mathrm{i}W_C^A(F_{\mathcal{A}_\phi}^{[m]},f_{\mathcal{A}_\phi})G_1^A(G_{\mathcal{A}_\phi}^{[m]},g_{\mathcal{A}_\phi})H_1^A(H_{\mathcal{A}_\phi}^{[m]},\delta h_{\mathcal{A}_\phi})\Big],\end{aligned}\tag{5.17c}$$

where the terms $G_0^A, G_1^A, H_0^A, H_1^A$ associated with the parametric domain Ω_q are *generically* defined in terms of the fields b, c as

$$\begin{aligned}G_0^a(b,c) &:= \int_{\Omega_\omega^a} b\bar{c}\,\mathrm{d}\omega, \quad G_1^a(b,c) := \int_{\Omega_\omega^a} b\bar{c}\omega\,\mathrm{d}\omega,\\ H_0^a(b,c) &:= \int_{\Omega_\gamma^a} b\bar{c}\,\mathrm{d}\gamma, \quad H_1^a(b,c) := \int_{\Omega_\gamma^a} b\bar{c}\alpha_\gamma\,\mathrm{d}\gamma,\end{aligned}\tag{5.18}$$

where the upper index $(\cdot)^a$ defines the domain of integration (i.e. $(\cdot)^A$ for electromagnetics or $(\cdot)^u$ for mechanics). The high-dimensional electromagnetic problem (5.10) is solved for the solution fields increments as

$$f_{\mathcal{A}_\phi}^{[k+1]} := f_{\mathcal{A}_\phi}^{[k]} + \Delta f_{\mathcal{A}_\phi}, \quad g_{\mathcal{A}_\phi}^{[k+1]} := g_{\mathcal{A}_\phi}^{[k]} + \Delta g_{\mathcal{A}_\phi}, \quad h_{\mathcal{A}_\phi}^{[k+1]} := h_{\mathcal{A}_\phi}^{[k]} + \Delta h_{\mathcal{A}_\phi}, \tag{5.19}$$

where the concept of directional derivatives [84] is used to formulate the problem as: Find $(\Delta f_{\mathcal{A}_\phi}, \Delta g_{\mathcal{A}_\phi}, \Delta h_{\mathcal{A}_\phi}) \in X(0) \times Z(\Omega_\omega^A) \times Z(\Omega_\gamma^A)$ such that

$$D\mathcal{R}_{f_{\mathcal{A}_\phi}}(\delta f_{\mathcal{A}_\phi};\mathcal{A}_\phi^{n-1},f_{\mathcal{A}_\phi},g_{\mathcal{A}_\phi},h_{\mathcal{A}_\phi})[\Delta f_{\mathcal{A}_\phi}] = -\mathcal{R}_{f_{\mathcal{A}_\phi}}(\delta f_{\mathcal{A}_\phi};\mathcal{A}_\phi^{n-1},f_{\mathcal{A}_\phi},g_{\mathcal{A}_\phi},h_{\mathcal{A}_\phi}), \tag{5.20a}$$

$$D\mathcal{R}_{g_{\mathcal{A}_\phi}}(\delta g_{\mathcal{A}_\phi};\mathcal{A}_\phi^{n-1},f_{\mathcal{A}_\phi},g_{\mathcal{A}_\phi},h_{\mathcal{A}_\phi})[\Delta g_{\mathcal{A}_\phi}] = -\mathcal{R}_{g_{\mathcal{A}_\phi}}(\delta g_{\mathcal{A}_\phi};\mathcal{A}_\phi^{n-1},f_{\mathcal{A}_\phi},g_{\mathcal{A}_\phi},h_{\mathcal{A}_\phi}), \tag{5.20b}$$

$$D\mathcal{R}_{h_{\mathcal{A}_\phi}}(\delta h_{\mathcal{A}_\phi};\mathcal{A}_\phi^{n-1},f_{\mathcal{A}_\phi},g_{\mathcal{A}_\phi},h_{\mathcal{A}_\phi})[\Delta h_{\mathcal{A}_\phi}] = -\mathcal{R}_{h_{\mathcal{A}_\phi}}(\delta h_{\mathcal{A}_\phi};\mathcal{A}_\phi^{n-1},f_{\mathcal{A}_\phi},g_{\mathcal{A}_\phi},h_{\mathcal{A}_\phi}), \tag{5.20c}$$

$\forall(\delta f_{\mathcal{A}_\phi}, \delta g_{\mathcal{A}_\phi}, \delta h_{\mathcal{A}_\phi}) \in X(0) \times Z(\Omega_\omega^A) \times Z(\Omega_\gamma^A)$, where the directional derivatives are defined as

$$\begin{aligned}D\mathcal{R}_{f_{\mathcal{A}_\phi}}(\delta f_{\mathcal{A}_\phi};\mathcal{A}_\phi^{n-1},f_{\mathcal{A}_\phi},g_{\mathcal{A}_\phi},h_{\mathcal{A}_\phi})[\Delta f_{\mathcal{A}_\phi}] &= W_K^A(\Delta f_{\mathcal{A}_\phi},\delta f_{\mathcal{A}_\phi})G_0^A(g_{\mathcal{A}_\phi},g_{\mathcal{A}_\phi})H_0^A(h_{\mathcal{A}_\phi},h_{\mathcal{A}_\phi})\\ &+\mathrm{i}W_C^A(\Delta f_{\mathcal{A}_\phi},\delta f_{\mathcal{A}_\phi})G_1^A(g_{\mathcal{A}_\phi},g_{\mathcal{A}_\phi})H_1^A(h_{\mathcal{A}_\phi},h_{\mathcal{A}_\phi}),\end{aligned}\tag{5.21a}$$

$$\begin{aligned}D\mathcal{R}_{g_{\mathcal{A}_\phi}}(\delta g_{\mathcal{A}_\phi};\mathcal{A}_\phi^{n-1},f_{\mathcal{A}_\phi},g_{\mathcal{A}_\phi},h_{\mathcal{A}_\phi})[\Delta g_{\mathcal{A}_\phi}] &= W_K^A(f_{\mathcal{A}_\phi},f_{\mathcal{A}_\phi})G_0^A(\Delta g_{\mathcal{A}_\phi},\delta g_{\mathcal{A}_\phi})H_0^A(h_{\mathcal{A}_\phi},h_{\mathcal{A}_\phi})\\ &+\mathrm{i}W_C^A(f_{\mathcal{A}_\phi},f_{\mathcal{A}_\phi})G_1^A(\Delta g_{\mathcal{A}_\phi},\delta g_{\mathcal{A}_\phi})H_1^A(h_{\mathcal{A}_\phi},h_{\mathcal{A}_\phi}),\end{aligned}\tag{5.21b}$$

$$\begin{aligned}D\mathcal{R}_{h_{\mathcal{A}_\phi}}(\delta h_{\mathcal{A}_\phi};\mathcal{A}_\phi^{n-1},f_{\mathcal{A}_\phi},g_{\mathcal{A}_\phi},h_{\mathcal{A}_\phi})[\Delta h_{\mathcal{A}_\phi}] &= W_K^A(f_{\mathcal{A}_\phi},f_{\mathcal{A}_\phi})G_0^A(g_{\mathcal{A}_\phi},g_{\mathcal{A}_\phi})H_0^A(\Delta h_{\mathcal{A}_\phi},\delta h_{\mathcal{A}_\phi})\\ &+\mathrm{i}W_C^A(f_{\mathcal{A}_\phi},f_{\mathcal{A}_\phi})G_1^A(g_{\mathcal{A}_\phi},g_{\mathcal{A}_\phi})H_1^A(\Delta h_{\mathcal{A}_\phi},\delta h_{\mathcal{A}_\phi}).\end{aligned}\tag{5.21c}$$

Mechanics

The mechanical residual forms defined in (5.16) can be expanded by using the separability introduced in (5.13). The separated expression of the spatial two-dimensional residual $\mathcal{R}_{\boldsymbol{f}_{\boldsymbol{u}}}(\delta\boldsymbol{f}_{\boldsymbol{u}};\boldsymbol{\mathcal{U}}^{n-1},\boldsymbol{f}_{\boldsymbol{u}},g_{\boldsymbol{u}},h_{\boldsymbol{u}},l_{\boldsymbol{u}})$ and the three parametric one-dimensional residuals $\mathcal{R}_{g_{\boldsymbol{u}}}(\delta g_{\boldsymbol{u}};\boldsymbol{\mathcal{U}}^{n-1},\boldsymbol{f}_{\boldsymbol{u}},g_{\boldsymbol{u}},h_{\boldsymbol{u}},l_{\boldsymbol{u}})$, $\mathcal{R}_{h_{\boldsymbol{u}}}(\delta h_{\boldsymbol{u}};\boldsymbol{\mathcal{U}}^{n-1},\boldsymbol{f}_{\boldsymbol{u}},g_{\boldsymbol{u}},h_{\boldsymbol{u}},l_{\boldsymbol{u}})$ and $\mathcal{R}_{l_{\boldsymbol{u}}}(\delta l_{\boldsymbol{u}};\boldsymbol{\mathcal{U}}^{n-1},\boldsymbol{f}_{\boldsymbol{u}},g_{\boldsymbol{u}},h_{\boldsymbol{u}},l_{\boldsymbol{u}})$ are[5]

$$\begin{aligned}\mathcal{R}_{\boldsymbol{f}_{\boldsymbol{u}}} &= W_K^u(\boldsymbol{f}_{\boldsymbol{u}},\delta\boldsymbol{f}_{\boldsymbol{u}})G_0^u(g_{\boldsymbol{u}},g_{\boldsymbol{u}})H_0^u(h_{\boldsymbol{u}},h_{\boldsymbol{u}})L_0^u(l_{\boldsymbol{u}},l_{\boldsymbol{u}})\\
&+\mathrm{i}W_C^u(\boldsymbol{f}_{\boldsymbol{u}},\delta\boldsymbol{f}_{\boldsymbol{u}})G_2^u(g_{\boldsymbol{u}},g_{\boldsymbol{u}})H_0^u(h_{\boldsymbol{u}},h_{\boldsymbol{u}})L_0^u(l_{\boldsymbol{u}},l_{\boldsymbol{u}})\\
&-W_M^u(\boldsymbol{f}_{\boldsymbol{u}},\delta\boldsymbol{f}_{\boldsymbol{u}})G_2^u(g_{\boldsymbol{u}},g_{\boldsymbol{u}})H_0^u(h_{\boldsymbol{u}},h_{\boldsymbol{u}})L_0^u(l_{\boldsymbol{u}},l_{\boldsymbol{u}})\\
&+\sum_{m=1}^{N_A}\Big[S^u(F_{\mathcal{A}_\phi}^{[m]},\delta\boldsymbol{f}_{\boldsymbol{u}})G_0^u(G_{\mathcal{A}_\phi}^{[m]},g_{\boldsymbol{u}})H_0^u(H_{\mathcal{A}_\phi}^{[m]},h_{\boldsymbol{u}})L_1^u(L_{\mathcal{A}_\phi}^{[m]},l_{\boldsymbol{u}})\Big]\\
&+\sum_{m=1}^{n-1}\Big[W_K^u(\boldsymbol{F}_{\boldsymbol{u}}^{[m]},\delta\boldsymbol{f}_{\boldsymbol{u}})G_0^u(G_{\boldsymbol{u}}^{[m]},g_{\boldsymbol{u}})H_0^u(H_{\boldsymbol{u}}^{[m]},h_{\boldsymbol{u}})L_0^u(L_{\boldsymbol{u}}^{[m]},l_{\boldsymbol{u}})\\
&+\mathrm{i}W_K^u(\boldsymbol{F}_{\boldsymbol{u}}^{[m]},\delta\boldsymbol{f}_{\boldsymbol{u}})G_2^u(G_{\boldsymbol{u}}^{[m]},g_{\boldsymbol{u}})H_0^u(H_{\boldsymbol{u}}^{[m]},h_{\boldsymbol{u}})L_0^u(L_{\boldsymbol{u}}^{[m]},l_{\boldsymbol{u}})\\
&-W_K^u(\boldsymbol{F}_{\boldsymbol{u}}^{[m]},\delta\boldsymbol{f}_{\boldsymbol{u}})G_2^u(G_{\boldsymbol{u}}^{[m]},g_{\boldsymbol{u}})H_0^u(H_{\boldsymbol{u}}^{[m]},h_{\boldsymbol{u}})L_0^u(L_{\boldsymbol{u}}^{[m]},l_{\boldsymbol{u}})\Big],\end{aligned}\tag{5.22a}$$

$$\begin{aligned}\mathcal{R}_{g_{\boldsymbol{u}}} &= W_K^u(\boldsymbol{f}_{\boldsymbol{u}},\boldsymbol{f}_{\boldsymbol{u}})G_0^u(g_{\boldsymbol{u}},\delta g_{\boldsymbol{u}})H_0^u(h_{\boldsymbol{u}},h_{\boldsymbol{u}})L_0^u(l_{\boldsymbol{u}},l_{\boldsymbol{u}})\\
&+\mathrm{i}W_C^u(\boldsymbol{f}_{\boldsymbol{u}},\boldsymbol{f}_{\boldsymbol{u}})G_2^u(g_{\boldsymbol{u}},\delta g_{\boldsymbol{u}})H_0^u(h_{\boldsymbol{u}},h_{\boldsymbol{u}})L_0^u(l_{\boldsymbol{u}},l_{\boldsymbol{u}})\\
&-W_M^u(\boldsymbol{f}_{\boldsymbol{u}},\boldsymbol{f}_{\boldsymbol{u}})G_2^u(g_{\boldsymbol{u}},\delta g_{\boldsymbol{u}})H_0^u(h_{\boldsymbol{u}},h_{\boldsymbol{u}})L_0^u(l_{\boldsymbol{u}},l_{\boldsymbol{u}})\\
&+\sum_{m=1}^{N_A}\Big[S^u(F_{\mathcal{A}_\phi}^{[m]},\boldsymbol{f}_{\boldsymbol{u}})G_0^u(G_{\mathcal{A}_\phi}^{[m]},\delta g_{\boldsymbol{u}})H_0^u(H_{\mathcal{A}_\phi}^{[m]},h_{\boldsymbol{u}})L_1^u(L_{\mathcal{A}_\phi}^{[m]},l_{\boldsymbol{u}})\Big]\\
&+\sum_{m=1}^{n-1}\Big[W_K^u(\boldsymbol{F}_{\boldsymbol{u}}^{[m]},\boldsymbol{f}_{\boldsymbol{u}})G_0^u(G_{\boldsymbol{u}}^{[m]},\delta g_{\boldsymbol{u}})H_0^u(H_{\boldsymbol{u}}^{[m]},h_{\boldsymbol{u}})L_0^u(L_{\boldsymbol{u}}^{[m]},l_{\boldsymbol{u}})\\
&+\mathrm{i}W_K^u(\boldsymbol{F}_{\boldsymbol{u}}^{[m]},\boldsymbol{f}_{\boldsymbol{u}})G_2^u(G_{\boldsymbol{u}}^{[m]},\delta g_{\boldsymbol{u}})H_0^u(H_{\boldsymbol{u}}^{[m]},h_{\boldsymbol{u}})L_0^u(L_{\boldsymbol{u}}^{[m]},l_{\boldsymbol{u}})\\
&-W_K^u(\boldsymbol{F}_{\boldsymbol{u}}^{[m]},\boldsymbol{f}_{\boldsymbol{u}})G_2^u(G_{\boldsymbol{u}}^{[m]},\delta g_{\boldsymbol{u}})H_0^u(H_{\boldsymbol{u}}^{[m]},h_{\boldsymbol{u}})L_0^u(L_{\boldsymbol{u}}^{[m]},l_{\boldsymbol{u}})\Big],\end{aligned}\tag{5.22b}$$

$$\begin{aligned}\mathcal{R}_{h_{\boldsymbol{u}}} &= W_K^u(\boldsymbol{f}_{\boldsymbol{u}},\boldsymbol{f}_{\boldsymbol{u}})G_0^u(g_{\boldsymbol{u}},g_{\boldsymbol{u}})H_0^u(h_{\boldsymbol{u}},\delta h_{\boldsymbol{u}})L_0^u(l_{\boldsymbol{u}},l_{\boldsymbol{u}})\\
&+\mathrm{i}W_C^u(\boldsymbol{f}_{\boldsymbol{u}},\boldsymbol{f}_{\boldsymbol{u}})G_2^u(g_{\boldsymbol{u}},g_{\boldsymbol{u}})H_0^u(h_{\boldsymbol{u}},\delta h_{\boldsymbol{u}})L_0^u(l_{\boldsymbol{u}},l_{\boldsymbol{u}})\\
&-W_M^u(\boldsymbol{f}_{\boldsymbol{u}},\boldsymbol{f}_{\boldsymbol{u}})G_2^u(g_{\boldsymbol{u}},g_{\boldsymbol{u}})H_0^u(h_{\boldsymbol{u}},\delta h_{\boldsymbol{u}})L_0^u(l_{\boldsymbol{u}},l_{\boldsymbol{u}})\\
&+\sum_{m=1}^{N_A}\Big[S^u(F_{\mathcal{A}_\phi}^{[m]},\boldsymbol{f}_{\boldsymbol{u}})G_0^u(G_{\mathcal{A}_\phi}^{[m]},g_{\boldsymbol{u}})H_0^u(H_{\mathcal{A}_\phi}^{[m]},\delta h_{\boldsymbol{u}})L_1^u(L_{\mathcal{A}_\phi}^{[m]},l_{\boldsymbol{u}})\Big]\\
&+\sum_{m=1}^{n-1}\Big[W_K^u(\boldsymbol{F}_{\boldsymbol{u}}^{[m]},\boldsymbol{f}_{\boldsymbol{u}})G_0^u(G_{\boldsymbol{u}}^{[m]},g_{\boldsymbol{u}})H_0^u(H_{\boldsymbol{u}}^{[m]},\delta h_{\boldsymbol{u}})L_0^u(L_{\boldsymbol{u}}^{[m]},l_{\boldsymbol{u}})\\
&+\mathrm{i}W_K^u(\boldsymbol{F}_{\boldsymbol{u}}^{[m]},\boldsymbol{f}_{\boldsymbol{u}})G_2^u(G_{\boldsymbol{u}}^{[m]},g_{\boldsymbol{u}})H_0^u(H_{\boldsymbol{u}}^{[m]},\delta h_{\boldsymbol{u}})L_0^u(L_{\boldsymbol{u}}^{[m]},l_{\boldsymbol{u}})\\
&-W_K^u(\boldsymbol{F}_{\boldsymbol{u}}^{[m]},\boldsymbol{f}_{\boldsymbol{u}})G_2^u(G_{\boldsymbol{u}}^{[m]},g_{\boldsymbol{u}})H_0^u(H_{\boldsymbol{u}}^{[m]},\delta h_{\boldsymbol{u}})L_0^u(L_{\boldsymbol{u}}^{[m]},l_{\boldsymbol{u}})\Big],\end{aligned}\tag{5.22c}$$

---

[5] The explicit dependency of the residuals has been dropped for simplicity.

$$
\begin{aligned}
\mathcal{R}_{l_{\boldsymbol{u}}} &= W_K^u(\boldsymbol{f}_{\boldsymbol{u}}, \boldsymbol{f}_{\boldsymbol{u}}) G_0^u(g_{\boldsymbol{u}}, g_{\boldsymbol{u}}) H_0^u(h_{\boldsymbol{u}}, h_{\boldsymbol{u}}) L_0^u(l_{\boldsymbol{u}}, \delta l_{\boldsymbol{u}}) \\
&+ \mathrm{i} W_C^u(\boldsymbol{f}_{\boldsymbol{u}}, \boldsymbol{f}_{\boldsymbol{u}}) G_2^u(g_{\boldsymbol{u}}, g_{\boldsymbol{u}}) H_0^u(h_{\boldsymbol{u}}, h_{\boldsymbol{u}}) L_0^u(l_{\boldsymbol{u}}, \delta l_{\boldsymbol{u}}) \\
&- W_M^u(\boldsymbol{f}_{\boldsymbol{u}}, \boldsymbol{f}_{\boldsymbol{u}}) G_2^u(g_{\boldsymbol{u}}, g_{\boldsymbol{u}}) H_0^u(h_{\boldsymbol{u}}, h_{\boldsymbol{u}}) L_0^u(l_{\boldsymbol{u}}, \delta l_{\boldsymbol{u}}) \\
&+ \sum_{m=1}^{N_A} \left[S^u(F_{\mathcal{A}_\phi}^{[m]}, \boldsymbol{f}_{\boldsymbol{u}}) G_0^u(G_{\mathcal{A}_\phi}^{[m]}, g_{\boldsymbol{u}}) H_0^u(H_{\mathcal{A}_\phi}^{[m]}, h_{\boldsymbol{u}}) L_1^u(L_{\mathcal{A}_\phi}^{[m]}, \delta l_{\boldsymbol{u}}) \right] \\
&+ \sum_{m=1}^{n-1} \Big[W_K^u(\boldsymbol{F}_{\boldsymbol{u}}^{[m]}, \boldsymbol{f}_{\boldsymbol{u}}) G_0^u(G_{\boldsymbol{u}}^{[m]}, g_{\boldsymbol{u}}) H_0^u(H_{\boldsymbol{u}}^{[m]}, h_{\boldsymbol{u}}) L_0^u(L_{\boldsymbol{u}}^{[m]}, \delta l_{\boldsymbol{u}}) \\
&+ \mathrm{i} W_K^u(\boldsymbol{F}_{\boldsymbol{u}}^{[m]}, \boldsymbol{f}_{\boldsymbol{u}}) G_2^u(G_{\boldsymbol{u}}^{[m]}, g_{\boldsymbol{u}}) H_0^u(H_{\boldsymbol{u}}^{[m]}, h_{\boldsymbol{u}}) L_0^u(L_{\boldsymbol{u}}^{[m]}, \delta l_{\boldsymbol{u}}) \\
&- W_K^u(\boldsymbol{F}_{\boldsymbol{u}}^{[m]}, \boldsymbol{f}_{\boldsymbol{u}}) G_2^u(G_{\boldsymbol{u}}^{[m]}, g_{\boldsymbol{u}}) H_0^u(H_{\boldsymbol{u}}^{[m]}, h_{\boldsymbol{u}}) L_0^u(L_{\boldsymbol{u}}^{[m]}, \delta l_{\boldsymbol{u}}) \Big],
\end{aligned}
\tag{5.22d}
$$

where the terms related to the parametric domain Ω_q are defined following the same notation than in (5.18) as

$$
\begin{aligned}
&G_2^a(b, c) := \int_{\Omega_\omega^a} b \bar{c} \omega^2 \, \mathrm{d}\omega, \\
&L_0^a(b, c) := \int_{\Omega_{B_0}^a} b \bar{c} \, \mathrm{d}B_0, \quad L_1^a(b, c) := \int_{\Omega_{B_0}^a} b \bar{c} \alpha_{B_0} \, \mathrm{d}B_0.
\end{aligned}
\tag{5.23}
$$

The high-dimensional mechanical problem will be solved incrementally as

$$
\begin{aligned}
\boldsymbol{f}_{\boldsymbol{u}}^{[k+1]} &:= \boldsymbol{f}_{\boldsymbol{u}}^{[k]} + \Delta \boldsymbol{f}_{\boldsymbol{u}}, \quad g_{\boldsymbol{u}}^{[k+1]} := g_{\boldsymbol{u}}^{[k]} + \Delta g_{\boldsymbol{u}}, \\
h_{\boldsymbol{u}}^{[k+1]} &:= h_{\boldsymbol{u}}^{[k]} + \Delta h_{\boldsymbol{u}}, \quad l_{\boldsymbol{u}}^{[k+1]} := l_{\boldsymbol{u}}^{[k]} + \Delta l_{\boldsymbol{u}},
\end{aligned}
\tag{5.24}
$$

where the directional derivative definition [84] is used to formulate the problem as: Find
$(\Delta \boldsymbol{f}_{\boldsymbol{u}}, \Delta g_{\boldsymbol{u}}, \Delta h_{\boldsymbol{u}}, \Delta l_{\boldsymbol{u}}) \in Y(\boldsymbol{0}) \times Z(\Omega_\omega^u) \times Z(\Omega_\gamma^u) \times Z(\Omega_{B_0}^u)$ such that

$$
D\mathcal{R}_{\boldsymbol{f}_{\boldsymbol{u}}}(\delta \boldsymbol{f}_{\boldsymbol{u}}; \boldsymbol{\mathcal{U}}^{n-1}, \boldsymbol{f}_{\boldsymbol{u}}, g_{\boldsymbol{u}}, h_{\boldsymbol{u}}, l_{\boldsymbol{u}})[\Delta \boldsymbol{f}_{\boldsymbol{u}}] = -\mathcal{R}_{\boldsymbol{f}_{\boldsymbol{u}}}(\delta \boldsymbol{f}_{\boldsymbol{u}}; \boldsymbol{\mathcal{U}}^{n-1}, \boldsymbol{f}_{\boldsymbol{u}}, g_{\boldsymbol{u}}, h_{\boldsymbol{u}}, l_{\boldsymbol{u}}), \tag{5.25a}
$$

$$
D\mathcal{R}_{g_{\boldsymbol{u}}}(\delta g_{\boldsymbol{u}}; \boldsymbol{\mathcal{U}}^{n-1}, \boldsymbol{f}_{\boldsymbol{u}}, g_{\boldsymbol{u}}, h_{\boldsymbol{u}}, l_{\boldsymbol{u}})[\Delta g_{\boldsymbol{u}}] = -\mathcal{R}_{g_{\boldsymbol{u}}}(\delta g_{\boldsymbol{u}}; \boldsymbol{\mathcal{U}}^{n-1}, \boldsymbol{f}_{\boldsymbol{u}}, g_{\boldsymbol{u}}, h_{\boldsymbol{u}}, l_{\boldsymbol{u}}), \tag{5.25b}
$$

$$
D\mathcal{R}_{h_{\boldsymbol{u}}}(\delta h_{\boldsymbol{u}}; \boldsymbol{\mathcal{U}}^{n-1}, \boldsymbol{f}_{\boldsymbol{u}}, g_{\boldsymbol{u}}, h_{\boldsymbol{u}}, l_{\boldsymbol{u}})[\Delta h_{\boldsymbol{u}}] = -\mathcal{R}_{h_{\boldsymbol{u}}}(\delta h_{\boldsymbol{u}}; \boldsymbol{\mathcal{U}}^{n-1}, \boldsymbol{f}_{\boldsymbol{u}}, g_{\boldsymbol{u}}, h_{\boldsymbol{u}}, l_{\boldsymbol{u}}), \tag{5.25c}
$$

$$
D\mathcal{R}_{l_{\boldsymbol{u}}}(\delta l_{\boldsymbol{u}}; \boldsymbol{\mathcal{U}}^{n-1}, \boldsymbol{f}_{\boldsymbol{u}}, g_{\boldsymbol{u}}, h_{\boldsymbol{u}}, l_{\boldsymbol{u}})[\Delta l_{\boldsymbol{u}}] = -\mathcal{R}_{l_{\boldsymbol{u}}}(\delta l_{\boldsymbol{u}}; \boldsymbol{\mathcal{U}}^{n-1}, \boldsymbol{f}_{\boldsymbol{u}}, g_{\boldsymbol{u}}, h_{\boldsymbol{u}}, l_{\boldsymbol{u}}), \tag{5.25d}
$$

$\forall (\delta \boldsymbol{f}_{\boldsymbol{u}}, \delta g_{\boldsymbol{u}}, \delta h_{\boldsymbol{u}}, \delta l_{\boldsymbol{u}}) \in Y(\boldsymbol{0}) \times Z(\Omega_\omega^u) \times Z(\Omega_\gamma^u) \times Z(\Omega_{B_0}^u)$, where the directional derivatives are found to be

$$
\begin{aligned}
D\mathcal{R}_{\boldsymbol{f}_{\boldsymbol{u}}}(\delta \boldsymbol{f}_{\boldsymbol{u}}; \boldsymbol{\mathcal{U}}^{n-1}, \boldsymbol{f}_{\boldsymbol{u}}, g_{\boldsymbol{u}}, h_{\boldsymbol{u}}, l_{\boldsymbol{u}})[\Delta \boldsymbol{f}_{\boldsymbol{u}}] &= W_K^u(\boldsymbol{f}_{\boldsymbol{u}}, \delta \boldsymbol{f}_{\boldsymbol{u}}) G_0^u(g_{\boldsymbol{u}}, g_{\boldsymbol{u}}) H_0^u(h_{\boldsymbol{u}}, h_{\boldsymbol{u}}) L_0^u(l_{\boldsymbol{u}}, l_{\boldsymbol{u}}) \\
&+ \mathrm{i} W_C^u(\boldsymbol{f}_{\boldsymbol{u}}, \delta \boldsymbol{f}_{\boldsymbol{u}}) G_2^u(g_{\boldsymbol{u}}, g_{\boldsymbol{u}}) H_0^u(h_{\boldsymbol{u}}, h_{\boldsymbol{u}}) L_0^u(l_{\boldsymbol{u}}, l_{\boldsymbol{u}}) \\
&- W_M^u(\boldsymbol{f}_{\boldsymbol{u}}, \delta \boldsymbol{f}_{\boldsymbol{u}}) G_2^u(g_{\boldsymbol{u}}, g_{\boldsymbol{u}}) H_0^u(h_{\boldsymbol{u}}, h_{\boldsymbol{u}}) L_0^u(l_{\boldsymbol{u}}, l_{\boldsymbol{u}}),
\end{aligned}
\tag{5.26a}
$$

$$
\begin{aligned}
D\mathcal{R}_{g_{\boldsymbol{u}}}(\delta g_{\boldsymbol{u}}; \boldsymbol{\mathcal{U}}^{n-1}, \boldsymbol{f}_{\boldsymbol{u}}, g_{\boldsymbol{u}}, h_{\boldsymbol{u}}, l_{\boldsymbol{u}})[\Delta g_{\boldsymbol{u}}] &= W_K^u(\boldsymbol{f}_{\boldsymbol{u}}, \boldsymbol{f}_{\boldsymbol{u}}) G_0^u(g_{\boldsymbol{u}}, \delta g_{\boldsymbol{u}}) H_0^u(h_{\boldsymbol{u}}, h_{\boldsymbol{u}}) L_0^u(l_{\boldsymbol{u}}, l_{\boldsymbol{u}}) \\
&+ \mathrm{i} W_C^u(\boldsymbol{f}_{\boldsymbol{u}}, \boldsymbol{f}_{\boldsymbol{u}}) G_2^u(g_{\boldsymbol{u}}, \delta g_{\boldsymbol{u}}) H_0^u(h_{\boldsymbol{u}}, h_{\boldsymbol{u}}) L_0^u(l_{\boldsymbol{u}}, l_{\boldsymbol{u}}) \\
&- W_M^u(\boldsymbol{f}_{\boldsymbol{u}}, \boldsymbol{f}_{\boldsymbol{u}}) G_2^u(g_{\boldsymbol{u}}, \delta g_{\boldsymbol{u}}) H_0^u(h_{\boldsymbol{u}}, h_{\boldsymbol{u}}) L_0^u(l_{\boldsymbol{u}}, l_{\boldsymbol{u}}),
\end{aligned}
\tag{5.26b}
$$

$$\begin{aligned} D\mathcal{R}_{h_{\boldsymbol{u}}}(\delta h_{\boldsymbol{u}}; \boldsymbol{\mathcal{U}}^{n-1}, \boldsymbol{f}_{\boldsymbol{u}}, g_{\boldsymbol{u}}, h_{\boldsymbol{u}}, l_{\boldsymbol{u}})[\Delta h_{\boldsymbol{u}}] &= W_K^u(\boldsymbol{f}_{\boldsymbol{u}}, \boldsymbol{f}_{\boldsymbol{u}}) G_0^u(g_{\boldsymbol{u}}, g_{\boldsymbol{u}}) H_0^u(h_{\boldsymbol{u}}, \delta h_{\boldsymbol{u}}) L_0^u(l_{\boldsymbol{u}}, l_{\boldsymbol{u}}) \\ &+ \mathrm{i} W_C^u(\boldsymbol{f}_{\boldsymbol{u}}, \boldsymbol{f}_{\boldsymbol{u}}) G_2^u(g_{\boldsymbol{u}}, g_{\boldsymbol{u}}) H_0^u(h_{\boldsymbol{u}}, \delta h_{\boldsymbol{u}}) L_0^u(l_{\boldsymbol{u}}, l_{\boldsymbol{u}}) \\ &- W_M^u(\boldsymbol{f}_{\boldsymbol{u}}, \boldsymbol{f}_{\boldsymbol{u}}) G_2^u(g_{\boldsymbol{u}}, g_{\boldsymbol{u}}) H_0^u(h_{\boldsymbol{u}}, \delta h_{\boldsymbol{u}}) L_0^u(l_{\boldsymbol{u}}, l_{\boldsymbol{u}}), \end{aligned} \tag{5.26c}$$

$$\begin{aligned} D\mathcal{R}_{l_{\boldsymbol{u}}}(\delta l_{\boldsymbol{u}}; \boldsymbol{\mathcal{U}}^{n-1}, \boldsymbol{f}_{\boldsymbol{u}}, g_{\boldsymbol{u}}, h_{\boldsymbol{u}}, l_{\boldsymbol{u}})[\Delta l_{\boldsymbol{u}}] &= W_K^u(\boldsymbol{f}_{\boldsymbol{u}}, \boldsymbol{f}_{\boldsymbol{u}}) G_0^u(g_{\boldsymbol{u}}, g_{\boldsymbol{u}}) H_0^u(h_{\boldsymbol{u}}, h_{\boldsymbol{u}}) L_0^u(l_{\boldsymbol{u}}, \delta l_{\boldsymbol{u}}) \\ &+ \mathrm{i} W_C^u(\boldsymbol{f}_{\boldsymbol{u}}, \boldsymbol{f}_{\boldsymbol{u}}) G_2^u(g_{\boldsymbol{u}}, g_{\boldsymbol{u}}) H_0^u(h_{\boldsymbol{u}}, h_{\boldsymbol{u}}) L_0^u(l_{\boldsymbol{u}}, \delta l_{\boldsymbol{u}}) \\ &- W_M^u(\boldsymbol{f}_{\boldsymbol{u}}, \boldsymbol{f}_{\boldsymbol{u}}) G_2^u(g_{\boldsymbol{u}}, g_{\boldsymbol{u}}) H_0^u(h_{\boldsymbol{u}}, h_{\boldsymbol{u}}) L_0^u(l_{\boldsymbol{u}}, \delta l_{\boldsymbol{u}}). \end{aligned} \tag{5.26d}$$

5.4.5 Finite element discretisation

A finite element discretisation, see Section 2.6, of the described formulation has to be performed in order to obtain the separable PGD expression. Following the same procedure than in previous sections, the discretisation of the problem is structured in two different sections for electromagnetics and mechanics.

Electromagnetics

The standard Galerkin FEM discretisation [28] is carried out in order to numerically solve the described electromagnetic problem. The global discretised version of (5.20) is obtained by the standard assembling procedure [28] as

$$\left(g_0^A h_0^A \mathbf{K}^A + \mathrm{i} g_1^A h_1^A \mathbf{C}^A\right) \Delta \mathbf{f}_{\mathcal{A}_\phi} = -\mathbf{R}_{f_{\mathcal{A}_\phi}}(f_{\mathcal{A}_\phi}, g_{\mathcal{A}_\phi}, h_{\mathcal{A}_\phi}), \tag{5.27a}$$

$$\left(k^A h_0^A \mathbf{G}_0^A + \mathrm{i} c^A h_1^A \mathbf{G}_1^A\right) \Delta \mathbf{g}_{\mathcal{A}_\phi} = -\mathbf{R}_{g_{\mathcal{A}_\phi}}(f_{\mathcal{A}_\phi}, g_{\mathcal{A}_\phi}, h_{\mathcal{A}_\phi}), \tag{5.27b}$$

$$\left(k^A g_0^A \mathbf{H}_0^A + \mathrm{i} c^A g_1^A \mathbf{H}_1^A\right) \Delta \mathbf{h}_{\mathcal{A}_\phi} = -\mathbf{R}_{h_{\mathcal{A}_\phi}}(f_{\mathcal{A}_\phi}, g_{\mathcal{A}_\phi}, h_{\mathcal{A}_\phi}), \tag{5.27c}$$

where the Roman (non-italic) font denotes a certain discretised quantity. The discretised version of the residuals is

$$\begin{aligned} \mathbf{R}_{f_{\mathcal{A}_\phi}}(f_{\mathcal{A}_\phi}, g_{\mathcal{A}_\phi}, h_{\mathcal{A}_\phi}) &= \left(g_0^A h_0^A \mathbf{K}^A + \mathrm{i} g_1^A h_1^A \mathbf{C}^A\right) \mathbf{f}_{\mathcal{A}_\phi} - g_0^{A,s} h_0^{A,s} \mathbf{s}^A \\ &+ \sum_{m=1}^{n-1} \left[g_0^{A,[m]} h_0^{A,[m]} \mathbf{K}^A + \mathrm{i} g_1^{A,[m]} h_1^{A,[m]} \mathbf{C}^A\right] \mathbf{F}_{\mathcal{A}_\phi}^{[m]}, \end{aligned} \tag{5.28a}$$

$$\begin{aligned} \mathbf{R}_{g_{\mathcal{A}_\phi}}(f_{\mathcal{A}_\phi}, g_{\mathcal{A}_\phi}, h_{\mathcal{A}_\phi}) &= \left(k^A h_0^A \mathbf{G}_0^A + \mathrm{i} c^A h_1^A \mathbf{G}_1^A\right) \mathbf{g}_{\mathcal{A}_\phi} - s^A h_0^{A,s} \mathbf{g}_0^{A,s} \\ &+ \sum_{m=1}^{n-1} \left[k^{A,[m]} h_0^{A,[m]} \mathbf{G}_0^A + \mathrm{i} c^{A,[m]} h_1^{A,[m]} \mathbf{G}_1^A\right] \mathbf{G}_{\mathcal{A}_\phi}^{[m]}, \end{aligned} \tag{5.28b}$$

$$\begin{aligned} \mathbf{R}_{h_{\mathcal{A}_\phi}}(f_{\mathcal{A}_\phi}, g_{\mathcal{A}_\phi}, h_{\mathcal{A}_\phi}) &= \left(k^A g_0^A \mathbf{H}_0^A + \mathrm{i} c^A g_1^A \mathbf{H}_1^A\right) \mathbf{h}_{\mathcal{A}_\phi} - s^A g_0^{A,s} \mathbf{h}_0^{A,s} \\ &+ \sum_{m=1}^{n-1} \left[k^{A,[m]} g_0^{A,[m]} \mathbf{H}_0^{AA} + \mathrm{i} c^{A,[m]} g_1^{A,[m]} \mathbf{H}_1^A\right] \mathbf{H}_{\mathcal{A}_\phi}^{[m]}, \end{aligned} \tag{5.28c}$$

and where the scalar quantities are defined as

$$
\begin{aligned}
g_0^A &:= G_0^A(g_{\mathcal{A}_\phi}, g_{\mathcal{A}_\phi}), & h_0^A &:= H_0^A(h_{\mathcal{A}_\phi}, h_{\mathcal{A}_\phi}), & k^A &:= W_K^A(f_{\mathcal{A}_\phi}, f_{\mathcal{A}_\phi}),\\
g_1^A &:= G_1^A(g_{\mathcal{A}_\phi}, g_{\mathcal{A}_\phi}), & h_1^A &:= H_1^A(h_{\mathcal{A}_\phi}, h_{\mathcal{A}_\phi}), & c^A &:= W_C^A(f_{\mathcal{A}_\phi}, f_{\mathcal{A}_\phi}),\\
g_0^{A,s} &:= G_0^A(1, g_{\mathcal{A}_\phi}), & h_0^{A,s} &:= H_0^A(1, h_{\mathcal{A}_\phi}), & s^A &:= S^A(1, f_{\mathcal{A}_\phi}),\\
g_0^{A,[m]} &:= G_0^A(G_{\mathcal{A}_\phi}^{[m]}, g_{\mathcal{A}_\phi}), & h_0^{A,[m]} &:= H_0^A(H_{\mathcal{A}_\phi}^{[m]}, h_{\mathcal{A}_\phi}), & k^{A,[m]} &:= W_K^A(F_{\mathcal{A}_\phi}^{[m]}, f_{\mathcal{A}_\phi}),\\
g_1^{A,[m]} &:= G_1^A(G_{\mathcal{A}_\phi}^{[m]}, g_{\mathcal{A}_\phi}), & h_1^{A,[m]} &:= H_1^A(H_{\mathcal{A}_\phi}^{[m]}, h_{\mathcal{A}_\phi}), & c^{A,[m]} &:= W_C^A(F_{\mathcal{A}_\phi}^{[m]}, f_{\mathcal{A}_\phi}).
\end{aligned}
\tag{5.29}
$$

Mechanics

The standard Galerkin FEM discretisation process [28] is used in order to obtain the discrete solution of the mechanical problem. Thus, equations (5.25) are expressed in their discretised version as

$$
\left(g_0^u h_0^u l_0^u \mathbf{K}^u + \mathrm{i} g_2^u h_0^u l_0^u \mathbf{C}^u - g_2^u h_0^u l_0^u \mathbf{M}^u\right) \Delta \mathbf{f}_{\boldsymbol{u}} = -\mathbf{R}_{\boldsymbol{f_u}}(\boldsymbol{f_u}, g_{\boldsymbol{u}}, h_{\boldsymbol{u}}, l_{\boldsymbol{u}}), \tag{5.30a}
$$

$$
\left(k^u h_0^u l_0^u \mathbf{G}_0^u + \mathrm{i} c^u h_0^u l_0^u \mathbf{G}_2^u - m^u h_0^u l_0^u \mathbf{G}_2^u\right) \Delta \mathbf{g}_{\boldsymbol{u}} = -\mathbf{R}_{g_{\boldsymbol{u}}}(\boldsymbol{f_u}, g_{\boldsymbol{u}}, h_{\boldsymbol{u}}, l_{\boldsymbol{u}}), \tag{5.30b}
$$

$$
\left(k^u g_0^u l_0^u \mathbf{H}_0^u + \mathrm{i} c^u g_2^u l_0^u \mathbf{H}_0^u - m^u g_2^u l_0^u \mathbf{H}_0^u\right) \Delta \mathbf{h}_{\boldsymbol{u}} = -\mathbf{R}_{h_{\boldsymbol{u}}}(\boldsymbol{f_u}, g_{\boldsymbol{u}}, h_{\boldsymbol{u}}, l_{\boldsymbol{u}}), \tag{5.30c}
$$

$$
\left(k^u g_0^u h_0^u \mathbf{L}_0^u + \mathrm{i} c^u g_2^u h_0^u \mathbf{L}_0^u - m^u g_2^u h_0^u \mathbf{L}_0^u\right) \Delta \mathbf{l}_{\boldsymbol{u}} = -\mathbf{R}_{l_{\boldsymbol{u}}}(\boldsymbol{f_u}, g_{\boldsymbol{u}}, h_{\boldsymbol{u}}, l_{\boldsymbol{u}}), \tag{5.30d}
$$

with

$$
\begin{aligned}
\mathbf{R}_{\boldsymbol{f_u}}(\boldsymbol{f_u}, g_{\boldsymbol{u}}, h_{\boldsymbol{u}}, l_{\boldsymbol{u}}) = {} & \left(g_0^u h_0^u l_0^u \mathbf{K}^u + \mathrm{i} g_2^u h_0^u l_0^u \mathbf{C}^u - g_2^u h_0^u l_0^u \mathbf{M}^u\right) \mathbf{f}_{\boldsymbol{u}}\\
& + \sum_{m=1}^{N_A} \left[g_{0,s}^{u,[m]} h_{0,s}^{u,[m]} l_{1,s}^{u,[m]} \mathbf{K}^{uA}\right] \mathbf{F}_{\mathcal{A}_\phi}^{[m]}\\
& + \sum_{m=1}^{n-1} \left[g_0^{u,[m]} h_0^{u,[m]} l_0^{u,[m]} \mathbf{K}^u + \mathrm{i} g_2^{u,[m]} h_0^{u,[m]} l_0^{u,[m]} \mathbf{C}^u\right.\\
& \left. - g_2^{u,[m]} h_0^{u,[m]} l_0^{u,[m]} \mathbf{M}^u\right] \mathbf{F}_{\boldsymbol{u}}^{[m]},
\end{aligned}
\tag{5.31a}
$$

$$
\begin{aligned}
\mathbf{R}_{g_{\boldsymbol{u}}}(\boldsymbol{f_u}, g_{\boldsymbol{u}}, h_{\boldsymbol{u}}, l_{\boldsymbol{u}}) = {} & \left(k^u h_0^u l_0^u \mathbf{G}_0^u + \mathrm{i} c^u h_0^u l_0^u \mathbf{G}_2^u - m^u h_0^u l_0^u \mathbf{G}_2^u\right) \mathbf{g}_{\boldsymbol{u}}\\
& + \sum_{m=1}^{N_A} \left[k_s^{u,[m]} h_{0,s}^{u,[m]} l_{1,s}^{u,[m]} \mathbf{G}_0^u\right] \mathbf{G}_{\mathcal{A}_\phi}^{[m]}\\
& + \sum_{m=1}^{n-1} \left[k^{u,[m]} h_0^{u,[m]} l_0^{u,[m]} \mathbf{G}_0^u + \mathrm{i} c^{u,[m]} h_0^{u,[m]} l_0^{u,[m]} \mathbf{G}_2^u\right.\\
& \left. - m^{u,[m]} h_0^{u,[m]} l_0^{u,[m]} \mathbf{G}_2^u\right] \mathbf{G}_{\boldsymbol{u}}^{[m]},
\end{aligned}
\tag{5.31b}
$$

$$
\begin{aligned}
\mathbf{R}_{h_{\boldsymbol{u}}}(\boldsymbol{f}_{\boldsymbol{u}}, g_{\boldsymbol{u}}, h_{\boldsymbol{u}}, l_{\boldsymbol{u}}) = {} & \left(k^u g_0^u l_0^u \mathbf{H}_0^u + \mathrm{i}c^u g_2^u l_0^u \mathbf{H}_0^u - m^u g_2^u l_0^u \mathbf{H}_0^u\right)\mathbf{h}_{\boldsymbol{u}} \\
& + \sum_{m=1}^{N_A} \left[k_s^{u,[m]} g_{0,s}^{u,[m]} l_{1,s}^{u,[m]} \mathbf{H}_0^u\right] \mathbf{H}_{\mathcal{A}_\phi}^{[m]} \\
& + \sum_{m=1}^{n-1} \Big[k^{u,[m]} g_0^{u,[m]} l_0^{u,[m]} \mathbf{H}_0^u + \mathrm{i}c^{u,[m]} g_2^{u,[m]} l_0^{u,[m]} \mathbf{H}_0^u \\
& - m^{u,[m]} g_2^{u,[m]} l_0^{u,[m]} \mathbf{H}_0^u\Big] \mathbf{H}_{\boldsymbol{u}}^{[m]},
\end{aligned}
\tag{5.31c}
$$

$$
\begin{aligned}
\mathbf{R}_{l_{\boldsymbol{u}}}(\boldsymbol{f}_{\boldsymbol{u}}, g_{\boldsymbol{u}}, h_{\boldsymbol{u}}, l_{\boldsymbol{u}}) = {} & \left(k^u g_0^u h_0^u \mathbf{L}_0^u + \mathrm{i}c^u g_2^u h_0^u \mathbf{L}_0^u - m^u g_2^u h_0^u \mathbf{L}_0^u\right)\mathbf{l}_{\boldsymbol{u}} \\
& + \sum_{m=1}^{N_A} \left[k_s^{u,[m]} g_{0,s}^{u,[m]} h_{0,s}^{u,[m]} \mathbf{L}_1^u\right] \mathbf{L}_{\mathcal{A}_\phi}^{[m]} \\
& + \sum_{m=1}^{n-1} \Big[k^{u,[m]} g_0^{u,[m]} h_0^{u,[m]} \mathbf{L}_0^u + \mathrm{i}c^{u,[m]} g_2^{u,[m]} h_0^{u,[m]} \mathbf{L}_0^u \\
& - m^{u,[m]} g_2^{u,[m]} h_0^{u,[m]} \mathbf{L}_0^u\Big] \mathbf{L}_{\boldsymbol{u}}^{[m]},
\end{aligned}
\tag{5.31d}
$$

and where the scalar quantities are defined as

$$
\begin{aligned}
g_0^u &:= G_0^u(g_{\boldsymbol{u}}, g_{\boldsymbol{u}}), \\
g_2^u &:= G_2^u(g_{\boldsymbol{u}}, g_{\boldsymbol{u}}), \\
g_0^{u,[m]} &:= G_0^u(G_{\boldsymbol{u}}^{[m]}, g_{\boldsymbol{u}}), \\
g_2^{u,[m]} &:= G_2^u(G_{\boldsymbol{u}}^{[m]}, g_{\boldsymbol{u}}), \\
g_{0,s}^{u,[m]} &:= G_0^u(G_{\mathcal{A}_\phi}^{[m]}, g_{\boldsymbol{u}}),
\end{aligned}
\qquad
\begin{aligned}
h_0^u &:= H_0^u(h_{\boldsymbol{u}}, h_{\boldsymbol{u}}), \\
h_0^{u,[m]} &:= H_0^u(H_{\boldsymbol{u}}^{[m]}, h_{\boldsymbol{u}}), \\
h_{0,s}^{u,[m]} &:= H_0^u(H_{\mathcal{A}_\phi}^{[m]}, h_{\boldsymbol{u}}), \\
l_0^u &:= L_0^u(l_{\boldsymbol{u}}, l_{\boldsymbol{u}}), \\
l_1^u &:= L_1^u(l_{\boldsymbol{u}}, l_{\boldsymbol{u}}), \\
l_0^{u,[m]} &:= L_0^u(L_{\boldsymbol{u}}^{[m]}, l_{\boldsymbol{u}}), \\
l_1^{u,[m]} &:= L_1^u(L_{\boldsymbol{u}}^{[m]}, l_{\boldsymbol{u}}), \\
l_{1,s}^{u,[m]} &:= L_1^u(L_{\mathcal{A}_\phi}^{[m]}, l_{\boldsymbol{u}}),
\end{aligned}
\qquad
\begin{aligned}
k^u &:= W_K^u(\boldsymbol{f}_{\boldsymbol{u}}, \boldsymbol{f}_{\boldsymbol{u}}), \\
c^u &:= W_C^u(\boldsymbol{f}_{\boldsymbol{u}}, \boldsymbol{f}_{\boldsymbol{u}}), \\
m^u &:= W_M^u(\boldsymbol{f}_{\boldsymbol{u}}, \boldsymbol{f}_{\boldsymbol{u}}), \\
k^{u,[m]} &:= W_K^u(\boldsymbol{F}_{\boldsymbol{u}}^{[m]}, \boldsymbol{f}_{\boldsymbol{u}}), \\
c^{u,[m]} &:= W_C^u(\boldsymbol{F}_{\boldsymbol{u}}^{[m]}, \boldsymbol{f}_{\boldsymbol{u}}), \\
m^{u,[m]} &:= W_M^u(\boldsymbol{F}_{\boldsymbol{u}}^{[m]}, \boldsymbol{f}_{\boldsymbol{u}}), \\
k_s^{u,[m]} &:= S^u(F_{\mathcal{A}_\phi}^{[m]}, \boldsymbol{f}_{\boldsymbol{u}}),
\end{aligned}
\tag{5.32}
$$

Note that the integration of the parametric quantities $G_0^u(G_{\mathcal{A}_\phi}^{[m]}, g_{\boldsymbol{u}})$, $H_0^u(H_{\mathcal{A}_\phi}^{[m]}, h_{\boldsymbol{u}})$ and $L_1^u(L_{\mathcal{A}_\phi}^{[m]}, l_{\boldsymbol{u}})$ involves the use of one-dimensional mortar integrals which are detailed in Appendix B.

5.5 Staggered versus monolithic PGD techniques

This Chapter follows the PGD methodology, detailed in Chapter 3, applied to a staggered coupled magneto-mechanical problem. However, a different strategy has been followed in Chapter 4, where the PGD technique has been implemented simultaneously to both physics in a monolithic manner. This section will compare the approaches focusing on the advantages of exploiting the staggered nature of the magneto-mechanical problem (2.1) by comparing it with the monolithic approach.

The convergence of the PGD methodology is often measured by the contribution of the last computed mode [21]. This means that, if the last computed mode has a weight that is small enough, this particular mode will not be as important when compared to the previously accumulated ones and, therefore, the Greedy algorithm can be safely stopped. The so-called error norms used to quantify this modal contribution are defined in (4.15). These error norms give an overall idea of the efficiency of the PGD algorithm and, thus, they are useful in order to compare the previously published monolithic approach [88] against the new staggered PGD approach, see Figure 5.4.

For the electromagnetic equations (Figure 5.4 left), two convergence curves are presented, monolithic PGD e^A_{mono} and staggered PGD e^A_{stag}. It is clear that the staggered PGD approach converges considerably faster and to a lower modal contribution. As for the mechanics equations (Figure 5.4 right), one convergence curve is displayed for the monolithic PGD e^u_{mono} model and three additional curves for the staggered approach e^u_{stag}, namely, one per shield ($e^{u,OVC}_{stag}$, $e^{u,77K}_{stag}$ and $e^{u,4K}_{stag}$). Note that in this case the total number of modes is actually the same for both approaches, 60 modes for the monolithic PGD approach and $20 \cdot 3 = 60$ for the staggered PGD approach. However, recall that for the staggered PGD approach, the time required for the computation of each mode is lower as a result of considering every shield individually (in parallel). Moreover, the error norms converge to a lower modal contribution. All in all, from these results it can be concluded that the staggered PGD methodology offers a very competitive alternative in terms of accuracy, robustness and computational time.

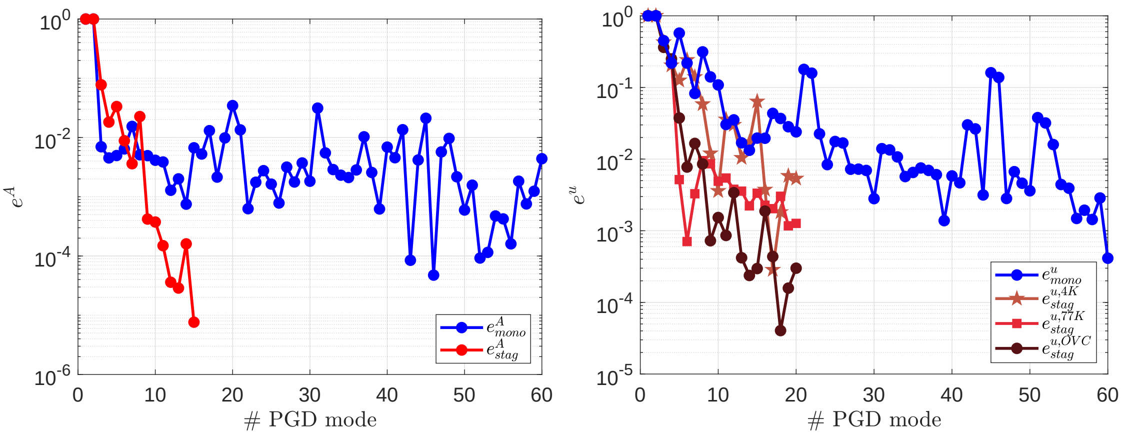

Figure 5.4: Test magnet problem; Last mode contribution for electromagnetics e^A and mechanics e^u. Comparison between monolithic PGD e_{mono} and staggered PGD e_{stag} approaches. Both PGD algorithms only depending on space (r, z) and frequency ω with no splitting in the frequency domain.

An additional benefit of the staggered PGD approach that must be emphasised is the flexibility of the PGD algorithm, enabling to set different control parameters for electromagnetics and mechanics and allowing the automatic split of the frequency domain only for the mechanics. This flexibility permits the use of different convergence criteria for the PGD, concentrating the computational effort where it is truly needed.

5.5.1 Staggered adaptive frequency splitting

The automatic adaptive frequency splitting [88] for the monolithic PGD approach has been presented in Section 4.4, where the PGD algorithm is used to identify the excited resonant modes and split the frequency domain accordingly. The monolithic PGD algorithm was very sensitive to the frequency subdomain, where each subinterval had to contain a few natural frequencies as centred as possible. However, with the staggered PGD approach presented in this chapter, the algorithm becomes more robust and it is possible to apply a simpler splitting procedure based on the location of the smallest and largest eigenvalues of the mechanical problem contained within the frequency range of interest.

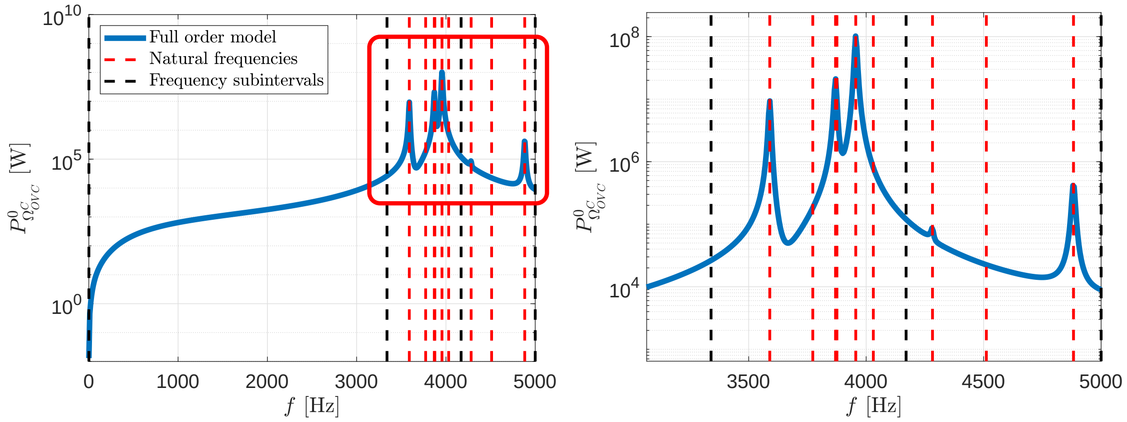

Figure 5.5: Test magnet problem; natural frequencies (red) obtained from eigenvalue analysis and frequency subdomains (black) defined through frequency splitting. Right figure shows a zoomed view in the resonance region (red rectangle). Full order model results (blue) shown for a mesh of 2.9K triangular elements using a polynomial order $p = 4$.

As displayed in Figure 5.5, a complete eigenvalue analysis of the problem is too generic and does not actually provide reliable information about the truly excited resonant frequencies. Instead, frequencies with high multiplicity and non-excited resonance frequencies may be obtained. For the implementation of the staggered PGD algorithm, the first and last eigenvalues inside the frequency range of interest are computed, which will define the resonance region of our problem. Once this region is located, uniform splitting is performed using a user-defined tolerance tol_{ω}^{split} that sets the maximum size of the frequency subdomains in the resonance area. The above eigenvalue analysis is not a computational burden as a result of (i) the consideration of each individual conducting shield one at a time, see Section 5.3, and (ii) the need to extract only the maximum and minimum values within the frequency range of interest.

The main advantage of this simpler automatic adaptive frequency splitting is its computational efficiency, where the cost of computing two eigenvalues of a small (single shield) mechanical system is radically smaller than the computation of few

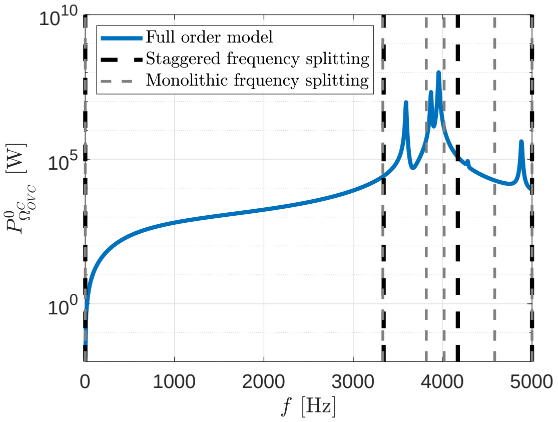

Figure 5.6: Test magnet problem; comparison between staggered (black dashed lines) and monolithic (grey dashed lines) frequency splitting algorithms. Full order model results (blue) shown for a mesh of 2.9K triangular elements using a polynomial order $p = 4$.

PGD solutions for the entire coupled problem. Moreover, the new eigenvalue-based frequency splitting results in a lower overall number of frequency subdomains and thus, a smaller number of times that the PGD algorithm has to be executed. This fact is graphically shown in Figure 5.6, where the total number of frequency subdomains has been decreased from five to three. Also it is interesting to see from the figure that both splitting algorithms detect the exact same resonance region (between 3300 and 5000 Hz approximately) and hence, the first frequency subdomain is practically the same for both. On the other hand, it is clearly seen in the resonance area that the staggered splitting consists in a uniform refinement (defined by the tolerance) while the monolithic splitting tries to capture fewer picks as centred as possible for each subdomain. Note that the monolithic frequency splitting is the one presented in Figure 4.4.

5.6 Test magnet problem

The first problem considered in order to validate and assess the staggered high-dimensional PGD algorithm is the test magnet geometry described in Section 2.8.1. For this problem, two ROM techniques, PGD and EM-POD, will be compared against the full order model, focusing on the computational advantages of each method.

5.6.1 ROM techniques on the electromagnetic problem

The Electro-Magnetic Proper Orthogonal Decomposition method (EM-POD) was developed in [49], where the electromagnetic problem is approximated with the EM-POD solution while the mechanical equations are solved using the full order model. The details of the EM-POD formulation are presented in Appendix A.

The reason for only approximating the electromagnetic equations is that no benefit would be obtained by using the POD algorithm for mechanics, as a similar number of snapshots to that of a full order model was needed in order to accurately capture the location of the resonance (mechanical) singularities. Therefore, this section only considers the uncoupled electromagnetic equations to compare both PGD and EM-POD strategies against the full order model. PGD and EM-POD are presented in Chapter 3 and Appendix A, respectively, and they are implemented herein for the electromagnetic problem of the test magnet geometry, in order to approximate the scalar magnetic potential field $\mathcal{A}_\phi = \mathcal{A}_\phi(r, z, \omega, \gamma)$ dependent upon the spatial domain (r, z) and two extra parameters, namely, the angular frequency ω and the electric conductivity γ.

Regarding PGD, see Figure 3.1, the user-defined parameters are presented in Table 5.1, where due to the sequential nature of the solution process, some of these PGD input parameters use the superscript $(\cdot^A)$ or $(\cdot^u)$ to denote whether they refer to the electromagnetic or mechanical problems, respectively. Note that these parameters have been already defined for Table 4.1 in Section 4.4, where the only difference is that, for the staggered high-dimensional PGD method, only one PGD algorithm is executed, whereas the monolithic PGD technique needed first a global and then a refined PGD algorithm run. Moreover, the new high-dimensional parametric space considers not only the angular frequency ω but also the electric conductivities γ and the strength of the static field B_0.

Table 5.1: Electromagnetic test magnet problem; user-defined parameters for the staggered high-dimensional PGD method.

PGD parameters				Parametric domains		Spatial domain		
I_N^A	tol_N^A	I_{FP}	tol_{FP}	h_ω	h_γ	h_{Ω_p}	p	ξ
40	10^{-4}	10	10^{-2}	$2 \cdot 10^{-5}$	$6 \cdot 10^{-3}$	$5 \cdot 10^{-3}$	4	10^{-3}

Regarding EM-POD, see Figure A.1 in Appendix A, the algorithm is initiated given a series of snapshots computed using the electromagnetic full order model, which in this case consists of a combination of 23 frequencies f^{snap} and 3 scaling of the electric conductivity α_γ^{snap} that make up a total of 69 snapshots ($N_s = 69$). Note that an optimum frequency sampling for this problem requires a non-evenly spaced (in frequency) set of snapshots, clustered near the low frequency region. Indeed (this will be shown subsequently) the electromagnetic problem varies more rapidly in the low frequency range and, thus, this *a priori* knowledge of the problem at hand can be used to optimise the number and location of snapshots needed. The TSVD is applied on the set of stored snapshots and truncated after 20 modes ($M = 20$). In addition, the mesh size h_{Ω_p}, the polynomial order p and the damping ratio ξ are also required. This information regarding the EM-POD set-up is summarised in Table 5.2.

PGD and EM-POD, see Figure 3.1 and A.1, respectively, are then run and com-

Table 5.2: Electromagnetic test magnet problem; user-defined parameters for the EM-POD method. Quantity $f^{snap} = [f_{min} : \Delta f : f_{max}]$ defined through minimum f_{min} and maximum f_{max} frequencies and spacing Δf.

EM-POD parameters				Snapshots		
f^{snap} [Hz]	α_γ^{snap}	N_s	M	h_{Ω_p}	p	ξ
$[10 : 80 : 1000, 1400 : 400 : 5000]$	$[0.5, 1.25, 2]$	69	20	$5 \cdot 10^{-3}$	4	10^{-3}

pared against the full order (reference) solution. Figure 5.7a shows three different cases, each one consisting of a frequency sweep, for three different values of the scaling of the electric conductivity α_γ. The agreement between the different techniques is clearly observed and, hence, the implementation of PGD and EM-POD is validated. Moreover, the error introduced by either of the ROM techniques is negligible and, crucially, controllable by the various tolerance values used in the analyses. As noted above, the scalar magnetic potential field is smooth throughout the entire frequency spectrum but with a sharp gradient observable in the low frequency range.

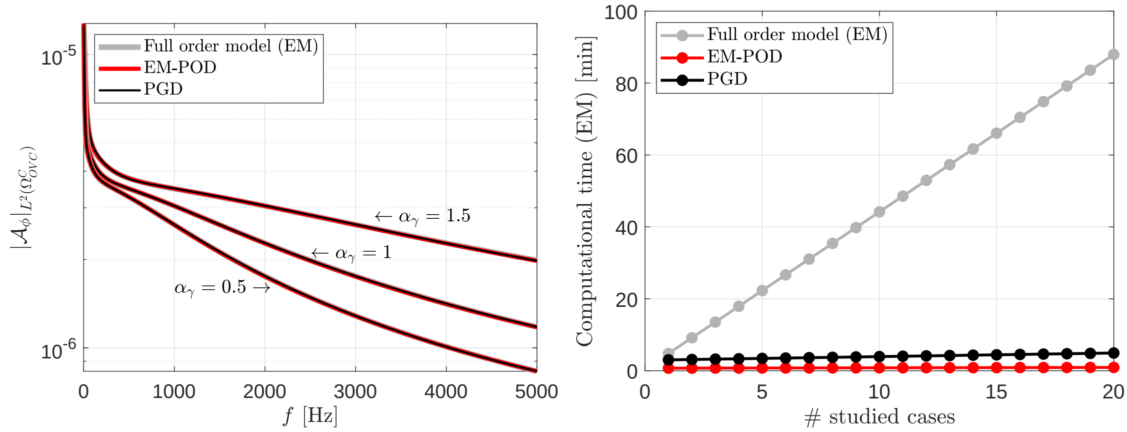

(a) Three different cases ($\alpha_\gamma = 0.5$, $\alpha_\gamma = 1$ and $\alpha_\gamma = 1.5$). Plot of the L^2 norm of the scalar potential field in the OVC conducting shield $|\mathcal{A}_\phi|_{L^2(\Omega^C_{OVC})}$.

(b) Total computational time required for each method to solve 20 studied cases (different parameter combinations).

Figure 5.7: Electromagnetic test magnet problem; comparison between PGD and EM-POD approximations against the reference full order model.

In addition, Figure 5.7b presents the computational time that the three methods (full order, EM-POD and PGD) require in order to complete the analysis of 20 different parametric cases. The full order model shows a clearly defined linear computational time cost, as each new case study implies the solution of an identical problem yet with a different parametric combination. However, the trend of the two ROM techniques is almost constant in cost due to the fact that the online costs of both methods are almost negligible compared to the offline costs. Note that, for this particular case, the time required for both ROM methods is comparable, being the PGD slightly more expensive (with the extra advantage that an explicit parametric solution field is obtained). Moreover, it has to be stressed that the number of snapshots used in the EM-POD method has been drastically minimised using the *a priori* knowledge of the solution, whereas the PGD technique does not require at all any previous knowledge of the problem.

For the PGD method, the offline calculations consist in obtaining and assimilating all terms appearing in the separable representation (5.7) and the online stage consists of a simple interpolation of the previously computed high-order parametric solution, that can be straightforwardly carried out in real time. As for the EM-POD method, the offline stage requires the computation of the snapshots, the TSVD and the non-parameter dependent assembly process (if the problem allows for an affine decomposition [49]). In the online stage, the parameter dependent assembly process is carried out in order to solve the reduced system of equations (size $M \times M$) that yields the electromagnetic response of the problem. Note that in this particular problem, the affine decomposition is possible, see (2.23), and thus, the online cost is still relatively small compared to the offline one. Note that this study has been performed with a smaller number of cases and then it has been extrapolated to 20 cases.

5.6.2 Coupled magneto-mechanical problem

After comparing both ROM techniques with the full order solution (for the electromagnetic problem), the more challenging fully coupled magneto-mechanical problem is now considered, where singularities in the solution field arise due to resonance. Regarding EM-POD, see flow chart in Figure A.1, it combines the use of POD for the electromagnetic equations (with excellent accuracy with respect to the full order model as shown in Figure 5.7a) and a full order model for the mechanical equations. As a result, the EM-POD method does not introduce additional errors with respect to the full order model when solving the mechanical problem, although the mechanical solutions will not be exactly the same due to the fact that the mechanical source term is based on an approximated electromagnetic solution $\mathcal{A}_\phi^{POD}$. However, important savings with respect to a complete full order solve are gained as the size of the electromagnetic problem (solved using POD) is generally orders of magnitude larger than that of the mechanical one (which is solved using the full order model).

The staggered PGD algorithm, see Figure 3.1, has been applied to the test magnet problem using the user-defined parameters in Table 5.3 in order to obtain (offline) the magnetic potential and the displacement field for the two physics considered.

Frequency splitting

The electromagnetic problem presented in Section 5.6.1 does not require the use of the frequency splitting algorithm due to the absence of numerical singularities in the electromagnetic equations. Since the PGD algorithm is executed once for electro-

Table 5.3: Test magnet problem; user-defined parameters for the staggered high-dimensional PGD method.

PGD parameters						Parametric domains				Spatial domain		
I_N^A	I_N^u	tol_N^A	tol_N^u	I_{FP}	tol_{FP}	h_ω	tol_ω^{split}	h_γ	h_{B_0}	h_{Ω_p}	p	ξ
40	60	10^{-4}	10^{-5}	10	10^{-2}	$2 \cdot 10^{-5}$	20%	$6 \cdot 10^{-3}$	$8 \cdot 10^{-3}$	$5 \cdot 10^{-3}$	4	10^{-3}

magnetics and once for each mechanical component, see Section 5.3, the staggered adaptive frequency splitting described in Section 5.5.1 is applied to each of the three radiation shields; OVC, 77K and 4K.

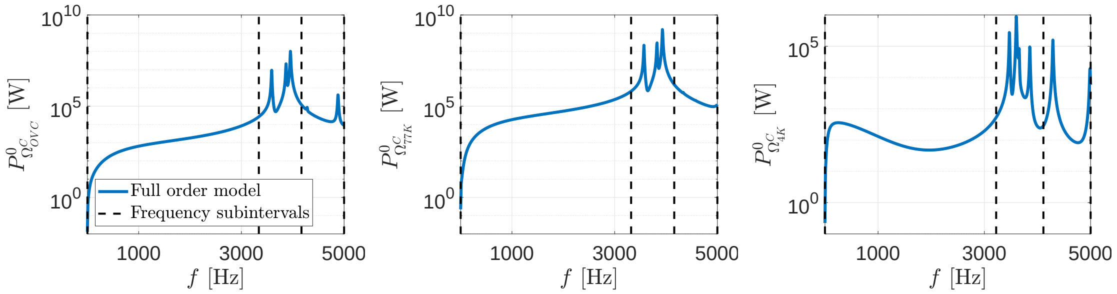

(a) OVC shield. (b) 77K shield. (c) 4K shield.

Figure 5.8: Test magnet problem; frequency subdomains resulting from staggered frequency splitting algorithm. Plotting the full order model solution (dissipated power) for $B_0 = 7$ T and $\alpha_\gamma = 1.5$.

The outputs of the staggered frequency splitting are presented in Figure 5.8, where the full order model solution is shown in terms of the dissipated power for each of the three shields, together with the resulting frequency subdomains. Note that since the eigenvalues of each mechanical component are slightly different, the frequency subdomains will be very similar but not identical. For this particular geometry, the resulting frequency subdomains are $f_1^{OVC} = [1, 3339]$, $f_2^{OVC} = [3339, 4169]$ and $f_3^{OVC} = [4169, 5000]$ Hz for the OVC shield, $f_1^{77K} = [1, 3320]$, $f_2^{77K} = [3320, 4160]$ and $f_3^{77K} = [4160, 5000]$ Hz for the 77K shield and $f_1^{4K} = [1, 3222]$, $f_2^{4K} = [3222, 4111]$ and $f_3^{4K} = [4111, 5000]$ Hz for the 4K shield, where the subscripts $(\cdot_1)$, $(\cdot_2)$ and $(\cdot_3)$ denote the first, second and third frequency subdomains.

PGD algorithm convergence

This section shows the convergence of both iterative procedures Greedy algorithm and fixed-point ADS, see Section 3.6, in order to study the process followed to obtain the offline PGD solution.

Regarding the Greedy algorithm, the quantity measured in order to determine whether the algorithm can be safely stopped is the mode amplitude (4.15). As mentioned before, the staggered PGD algorithm is used once for electromagnetics and several times for each mechanical radiation shield, depending on the number of frequency subdomains generated by the frequency splitting algorithm. Therefore, for this particular test magnet problem, four mode amplitudes are presented in Figure 5.9; $e^n_{EM,N}$ for electromagnetics and $e^n_{OVC,N}$, $e^n_{77K,N}$ and $e^n_{4K,N}$ for each radiation shield. The electromagnetic problem, see Figure 5.9a, has been found to converge with 33 PGD modes when setting a tolerance $tol^A_N = 10^{-4}$, which is almost twice as fast when compared to the PGD behaviour for mechanics.

The mechanical equations are solved for each shield and for each frequency subdomain, running a total of 9 times (3 shields times 3 frequency subdomain per shield) the PGD algorithm. Figures 5.9b-5.9d show the mechanical mode amplitudes for each frequency subdomain, where all subdomains reach the maximum number of modes allowed ($I^u_N = 60$). It has been found that the mechanical problem is often reaching the maximum number of modes and thus, this will often be the parameter controlling the quality and accuracy of the offline PGD solution. In addition, it is interesting to see how no significant differences are observed between shields in the same frequency subdomain. Instead, the first frequency subdomain in Figure 5.9b clearly reaches a lower mode amplitude with a less oscillatory trend when compared to the second and third frequency subdomains in Figures 5.9c and 5.9d.

The computation of each PGD mode requires the use of a fixed-point ADS algorithm that computes the converged modal quantities, see Figure 3.1. Figure 5.10 shows the FP-ADS convergence for electromagnetics and for the three frequency subdomains in the OVC shield. The overall behaviour of the ADS algorithm agrees with the one observed for the monolithic frequency-based PGD algorithm in Figure 4.14, where some modes reach the desired convergence whilst the others are stopped using the maximum number of ADS iterations I_{FP}. As mentioned in Section 4.5.1, the PGD algorithm has been found to be more efficient [42] when allowing only few ADS iterations I_{FP} and increasing the total number of computed modes I^A_N and I^u_N. Note that Figure 5.10 only contains the convergence of the OVC shield due to the fact that a very similar behaviour was observed in the other two radiation shields and hence, the other two shields are not included in the figure.

Modes visualisation

The electromagnetic solution variable, the scalar potential $\mathcal{A}_\phi = \mathcal{A}_\phi(r, z, \omega, \gamma)$, is approximated by three separable functions; the spatial modes $F_{\mathcal{A}_\phi}(r, z)$ and the scalar parametric functions $G_{\mathcal{A}_\phi}(\omega)$ and $H_{\mathcal{A}_\phi}(\gamma)$, see (5.7). These quantities are obtained after executing the PGD algorithm for the electromagnetic equations. First, the spatial electromagnetic modes are shown in Figure 5.11, which are smooth functions defined in the two-dimensional spatial domain Ω_p. Note that, as expected, the modes computed are completely different to the ones obtained with the monolithic frequency-based PGD technique for the same test magnet geometry, see Figure 4.7, due to the fact that a different approximation of $\mathcal{A}_\phi = \mathcal{A}_\phi(r, z, \omega, \gamma)$ is chosen for both cases. However, note that they follow the same main idea, they represent

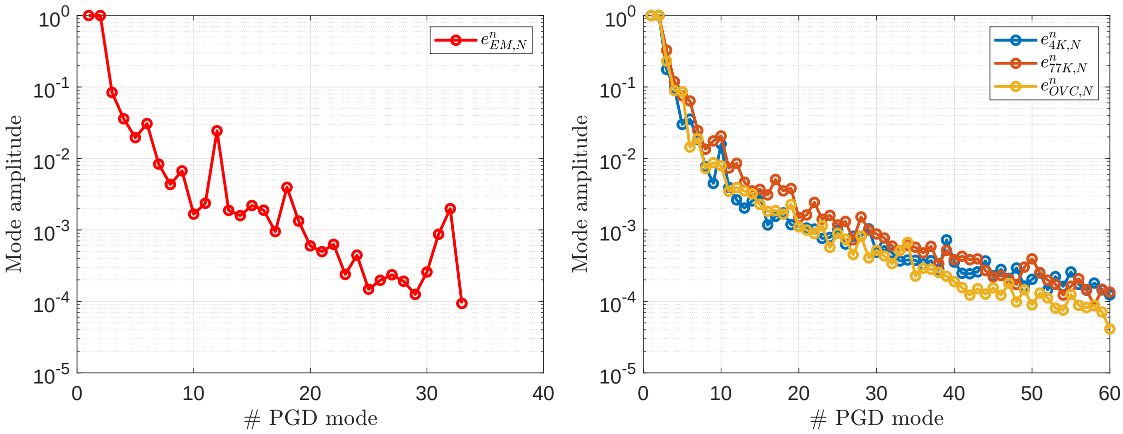

(a) Electromagnetics.

(b) Mechanics (1^{st} frequency subdomain).

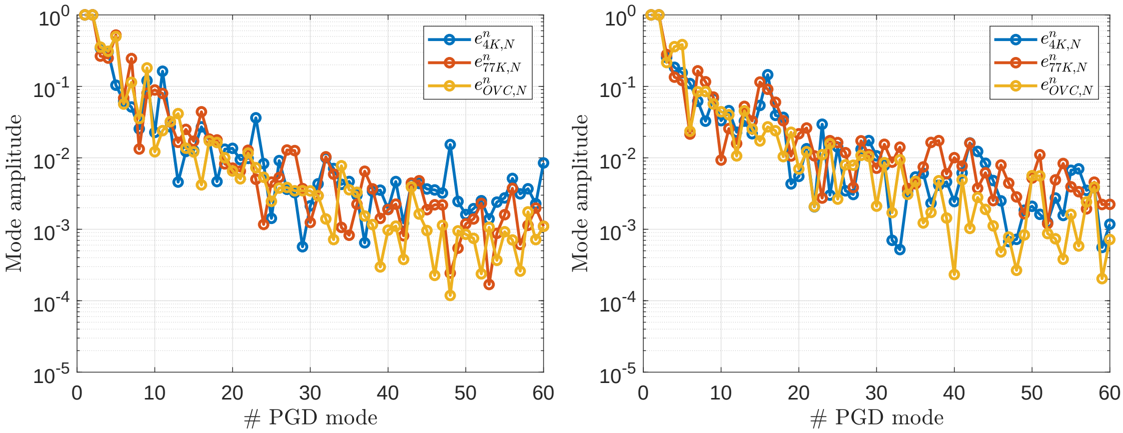

(c) Mechanics (2^{nd} frequency subdomain).

(d) Mechanics (3^{rd} frequency subdomain).

Figure 5.9: Test magnet problem; Greedy algorithm convergence for electromagnetics and for the three (mechanical) frequency subdomains.

the variations of the electromagnetic solution in Ω_p, where the main changes are located in the vicinity of the AC coils. Moreover, similarly to what is discussed in Figure 4.7, the computed modes do not follow a particular order, where low and high frequency modes and changes of sign are alternated during the computation of these modes through the ADS algorithm. Note that in this case, the staggered high-dimensional PGD technique does not require a frequency splitting in electromagnetics and thus, the modes shown in Figure 5.11 are valid for the entire range of the two one-dimensional parametric modes; the frequency $f \in [1, 5000]$ Hz and the dimensionless conductivity scaling factor $\alpha_\gamma \in [0.5, 2]$.

The one-dimensional parametric modes associated to electromagnetics are shown in Figure 5.12. Regarding the parametric electromagnetic modes $G_{\mathcal{A}_\phi}(\omega)$, a rapid change is observed in the low frequency region, as discussed in Section 5.6.1, and no resonance phenomenon is observed. In addition, the parametric modes associated with the conductivities $H_{\mathcal{A}_\phi}(\gamma)$ are smooth nonlinear functions. The absence of resonance and the smooth behaviour of the solution enable the electromagnetic equations to be easily represented by any ROM method and hence, all the computa-

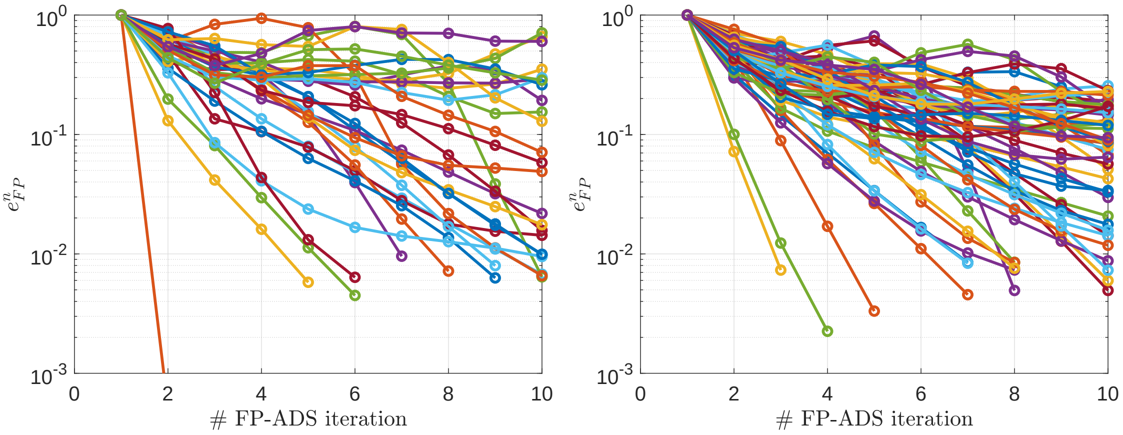

(a) Electromagnetics. (b) OVC shield (1^{st} frequency subdomain).

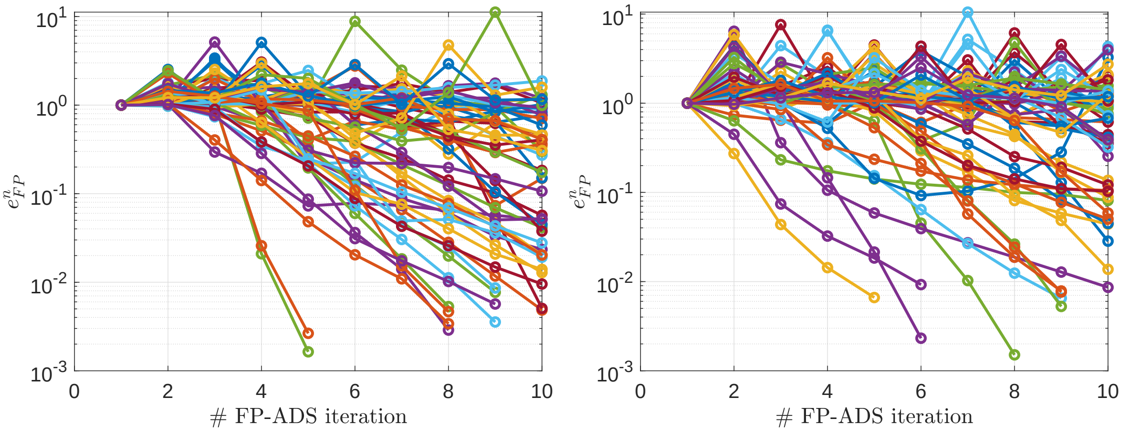

(c) OVC shield (2^{nd} frequency subdomain). (d) OVC shield (3^{rd} frequency subdomain).

Figure 5.10: Test magnet problem; convergence of the fixed-point ADS algorithm for each of the six frequency subdomains of the OVC shield.

tional effort and numerical strategies such as numerical regularisation and frequency splitting will feature when solving the mechanical equations.

The displacement field $\boldsymbol{\mathcal{U}} = \boldsymbol{\mathcal{U}}(r, z, \omega, \gamma, B_0)$ is approximated using a spatial function $\boldsymbol{F}_{\boldsymbol{\mathcal{U}}}(r, z)$ and three scalar parametric functions $G_{\boldsymbol{\mathcal{U}}}(\omega)$, $H_{\boldsymbol{\mathcal{U}}}(\gamma)$ and $L_{\boldsymbol{\mathcal{U}}}(B_0)$, see (5.12). These four quantities are obtained as outputs of the PGD algorithm when applied to the mechanical problem and they are stored ready to be used when a new case (parameter combination) is queried. The spatial modes $\boldsymbol{F}_{\boldsymbol{\mathcal{U}}} = [F_{\mathcal{U}_r}, F_{\mathcal{U}_z}]^T$ are visualised by computing its magnitude $F_{\boldsymbol{\mathcal{U}}} = \sqrt{F^2_{\mathcal{U}_r} + F^2_{\mathcal{U}_z}}$ as presented in Figure 5.13. Since the staggered high-dimensional PGD strategy consists of several runs of the PGD algorithm (once per shield and per frequency subdomain), the computed magnitude $F_{\boldsymbol{\mathcal{U}}}$ for a specific frequency subdomain is obtained as a union of the mechanical modes of each shield, $F_{\boldsymbol{\mathcal{U}}} = F^{OVC}_{\boldsymbol{\mathcal{U}}} \cup F^{77K}_{\boldsymbol{\mathcal{U}}} \cup F^{4K}_{\boldsymbol{\mathcal{U}}}$. Therefore, the spatial mechanical modes $F_{\boldsymbol{\mathcal{U}}}$ presented in Figure 5.13 are representing all three shields (OVC, 77K and 4K) in the entire range of frequencies $f \in [1, 5000]$ Hz and conductivity scaling $\alpha_\gamma \in [0.5, 2]$ but only within the first frequency subinterval. As discussed in Section 5.6.2, the frequency subdomains will be very similar yet not

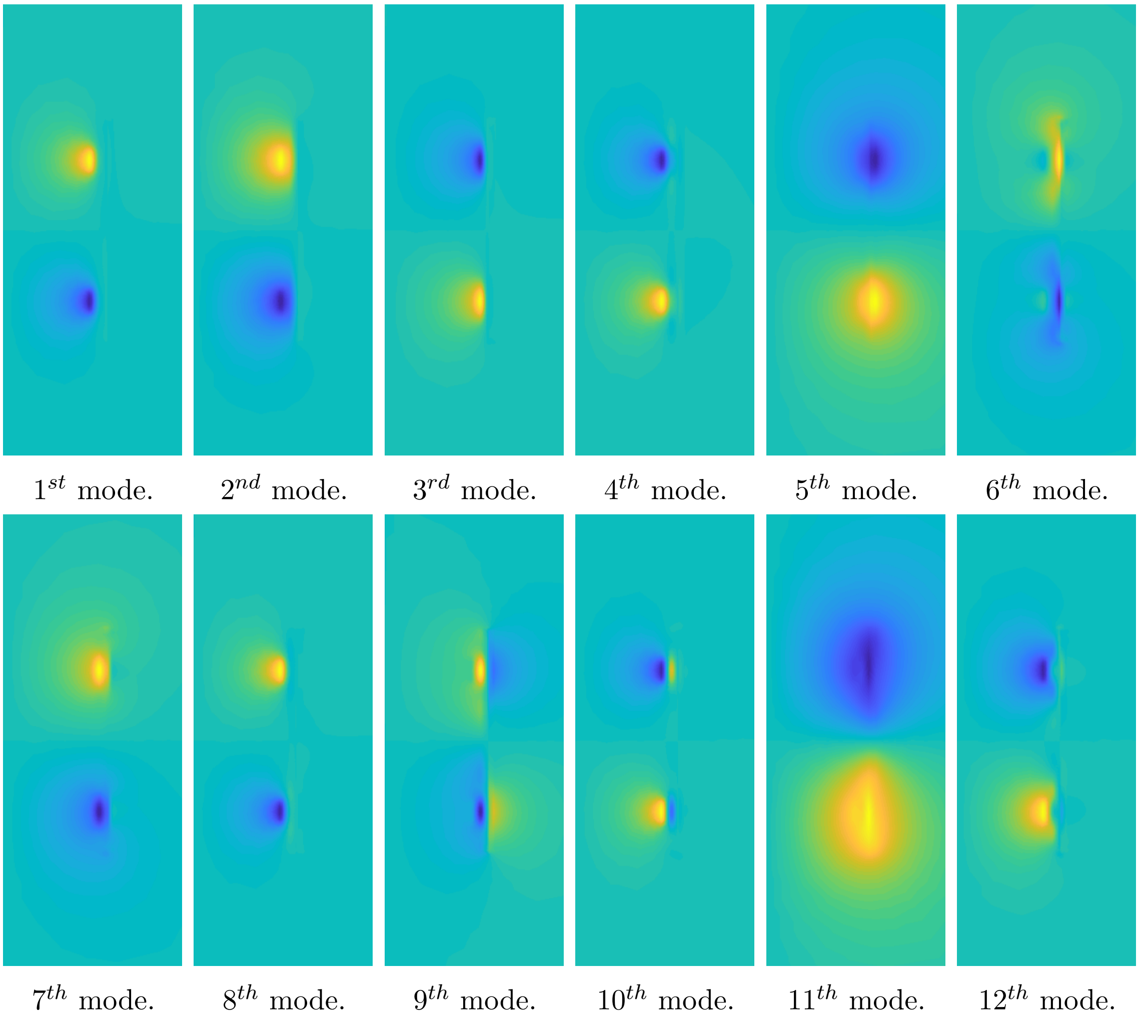
1^{st} mode. 2^{nd} mode. 3^{rd} mode. 4^{th} mode. 5^{th} mode. 6^{th} mode.

7^{th} mode. 8^{th} mode. 9^{th} mode. 10^{th} mode. 11^{th} mode. 12^{th} mode.

Figure 5.11: Test magnet problem; first 12 computed electromagnetic spatial modes $F_{\mathcal{A}_\phi}(r, z)$. All modes have been L^2 normalised. Same colour scale for all subfigures.

identical for all three shields, see Figure 5.8. Figure 5.13 has been generated as $F_{\boldsymbol{u}} = F_{\boldsymbol{u}}^{OVC} \cup F_{\boldsymbol{u}}^{77K} \cup F_{\boldsymbol{u}}^{4K}$ for visualisation purposes.

The one-dimensional mechanical parametric modes $G_{\boldsymbol{u}}(\omega)$, $H_{\boldsymbol{u}}(\gamma)$ and $L_{\boldsymbol{u}}(B_0)$ of the OVC shield (denoted with the upper index OVC) are presented in Figure 5.14. Each column corresponds to one parametric mode whilst each row is related to the first, second and third frequency subintervals, represented with the upper index 1, 2 and 3, respectively. Note that all modes presented have been L^2 normalised as described in Section 3.5. Regarding the modes associated with the angular frequency $G_{\boldsymbol{u}}^{OVC}(\omega)$, it is clear that they behave in the same way than in the monolithic frequency-based PGD method, see Figure 4.9,[6] where a non-smooth behaviour is obtained in order to represent the sharp changes on frequency in the solution field. Differently to the frequency-based PGD technique, now $G_{\boldsymbol{u}}^{OVC}(\omega)$ only represents the solution in the OVC shield and hence, less resonant singularities have to be

---

[6] The upper index OVC and the subindex $\boldsymbol{u}$ were not required for the monolithic frequency-based PGD method since the PGD algorithm was executed only once.

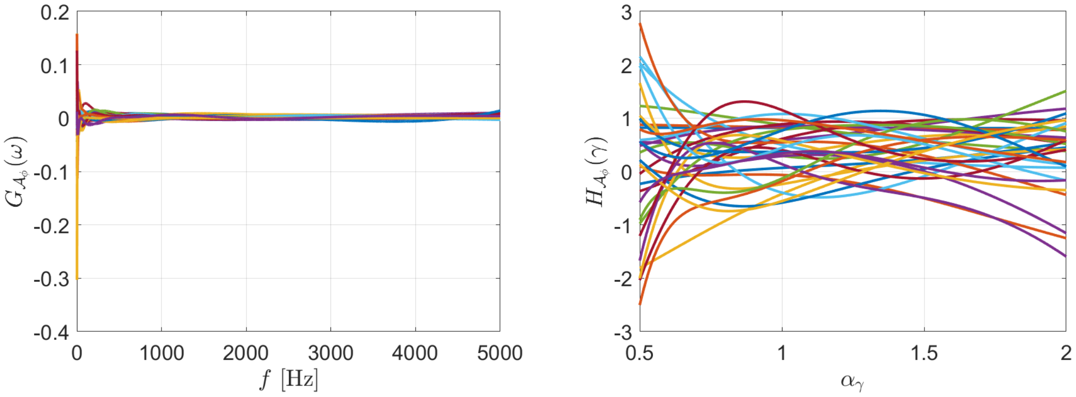

Figure 5.12: Test magnet problem; visualisation of the one-dimensional parametric electromagnetic modes $G_{\mathcal{A}_\phi}(\omega)$ and $H_{\mathcal{A}_\phi}(\gamma)$ for the entire range of the one-dimensional parametric domains; frequency $f \in [1, 5000]$ Hz and dimensionless conductivity scaling factor $\alpha_\gamma \in [0.5, 2]$. All modes have been L^2 normalised.

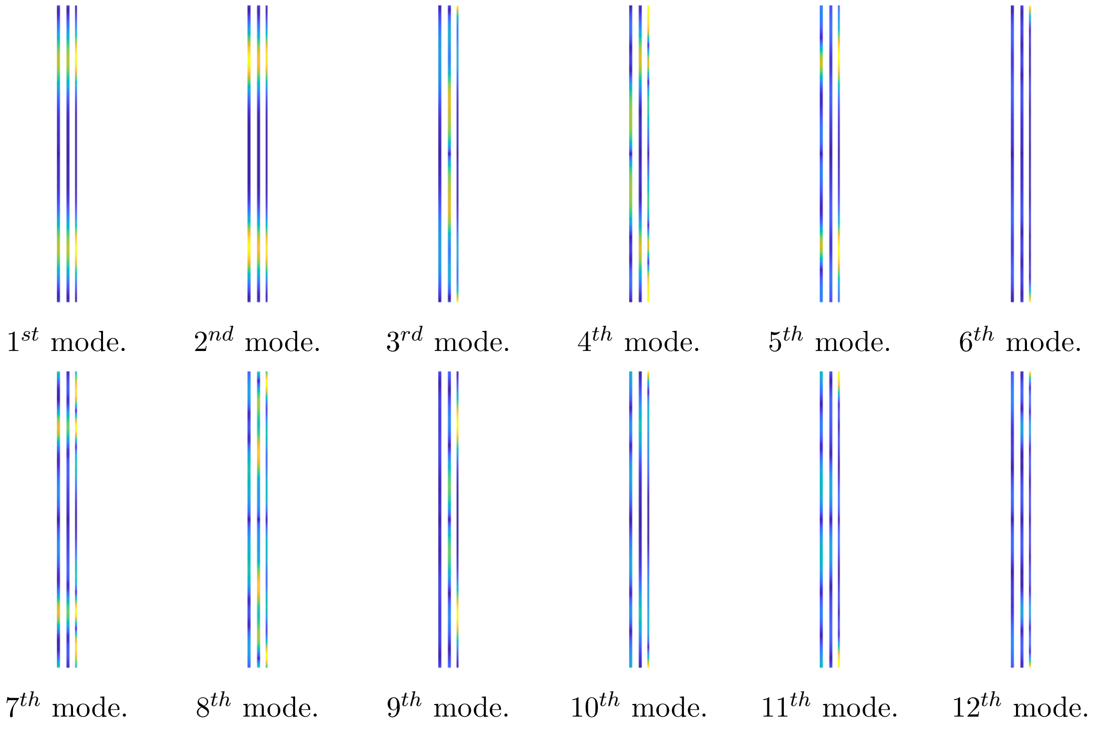
1^{st} mode. 2^{nd} mode. 3^{rd} mode. 4^{th} mode. 5^{th} mode. 6^{th} mode.

7^{th} mode. 8^{th} mode. 9^{th} mode. 10^{th} mode. 11^{th} mode. 12^{th} mode.

Figure 5.13: Test magnet problem; first 12 computed mechanical spatial modes $F_{\boldsymbol{u}}(r, z)$ for the first frequency subdomain. All modes have been L^2 normalised. Same colour scale for all subfigures.

captured. This fact helps the PGD algorithm to converge faster and it is one of the main causes of the increased efficiency and accuracy of the novel staggered high-dimensional PGD technique.

On the other hand, the parametric modes $H_{\boldsymbol{u}}^{OVC}(\gamma)$ and $L_{\boldsymbol{u}}^{OVC}(B_0)$ are presented in the second and third columns, respectively, where no splitting is performed in

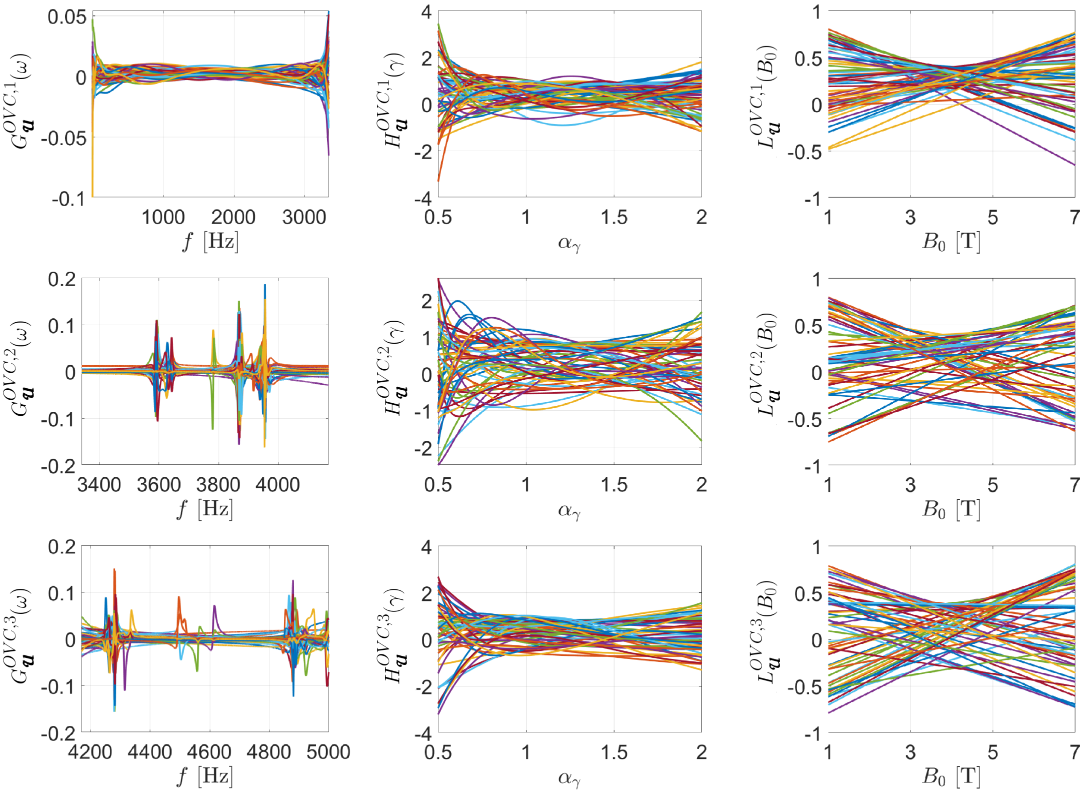

Figure 5.14: Test magnet problem; visualisation of the three one-dimensional parametric mechanical modes $G_{\boldsymbol{u}}(\omega)$, $H_{\boldsymbol{u}}(\gamma)$ and $L_{\boldsymbol{u}}(B_0)$ of the OVC shield for the three frequency subdomains. All modes have been L^2 normalised.

these one-dimensional domains (γ and B_0) and thus, the horizontal axis remains constant for all frequency subdomains. Both parametric modes are found to be smooth functions and it is interesting to realise how the change of the displacement field in terms of γ is nonlinear whereas the solution behaves linearly on B_0 as expected.

Validation of the PGD method

Now that the PGD approximations of both the scalar potential $\mathcal{A}_\phi$, see (5.7) and the displacement field $\boldsymbol{\mathcal{U}}$, see (5.12) are computed and stored, only a simple interpolation is required in the online PGD stage in order to study a certain parameter combination or case, see Section 3.7. With this, the solution fields are obtained for a particular case of study and the complex physical behaviour of the MRI scanner can be assessed by the engineers in charge of the design stage.

More importantly in the context of MRI scanner design, these solution fields $\mathcal{A}_\phi$ and $\boldsymbol{\mathcal{U}}$ can be post-processed in order to compute the integrated quantities (2.34), namely, the dissipated or Ohmic power $P^0_{\Omega^C}$ and the kinetic energy $E^k_{\Omega^C}$, which are the key quantities used in the early design stage of MRI scanners. Note that an efficient computation of these integrated quantities is described in Appendix C. The results for these two quantities are presented in Figure 5.15, where $P^0_{\Omega^C}$ (left) and $E^k_{\Omega^C}$ (right) are shown for each of the three conducting shields. A series of curves are displayed in each figure, where the black solid lines on the background denote the full order model solution[7] for different sets of parameters B_0 and α_γ. The coloured lines lying on top refer to the different PGD solutions for the equivalent sets of parameters used in the full order model. Note that the specific sets of parameters used are presented in the figure legend. These results show that the PGD approximation is able to accurately reproduce the behaviour of the full order model, splitting the frequency range only where it is required and accurately capturing all the singularities of the response. These results clearly demonstrate the validity of the reported staggered PGD model.

Figure 5.16 shows the comparison in terms of the total computational time required by the staggered PGD model and the full order model. First, the total time is shown in Figure 5.16a, where a clear time reduction is observed between the full order model and the PGD approach even if just a few cases (parameter combinations) are required. Moreover, the online PGD cost is no longer negligible as it was when only considering the electromagnetic problem, see Figure 5.7b. The reason is that the online cost now includes the computation of the integrated quantities (2.34). Figure 5.16b shows the time reduction in percentage obtained for the PGD technique using the full order method as a reference, where a great reduction of approximately 85% is obtained when studying, for instance, 20 different cases. PGD is based on the general idea of maximising the computational effort during the offline stage in order to reduce as much as possible online computing tasks. In particular, the online stage reduces to a mere interpolation process that can be easily conducted in real time and displayed via user-friendly application tool (the reader is referred to [88] for an example of an online PGD application tool).

5.7 Full magnet problem

The full magnet problem, presented in Section 2.8.2, represents a more realistic MRI scanner configuration of great interest to industry. A similar comparison (full order versus EM-POD and PGD) to that presented in Figure 5.7 was repeated for this more challenging geometry, but as the conclusions were the same they have not been repeated. Instead, the coupled magneto-mechanical problem is considered and the user-defined parameters in order to compute the PGD offline solution for the full magnet geometry are presented in Table 5.4. The parameters related to the parametric and spatial domains are almost identical to the ones employed for the test magnet problem (see Table 5.3). However, there are substantial changes in the PGD parameters used, mainly in the computation of the offline electromagnetic problem. As expected, the increased complexity of this problem in comparison to the test magnet problem leads to a greater number of PGD modes in order to

---

[7] Identical results are obtained when using the EM-POD combined with a mechanical full order solution.

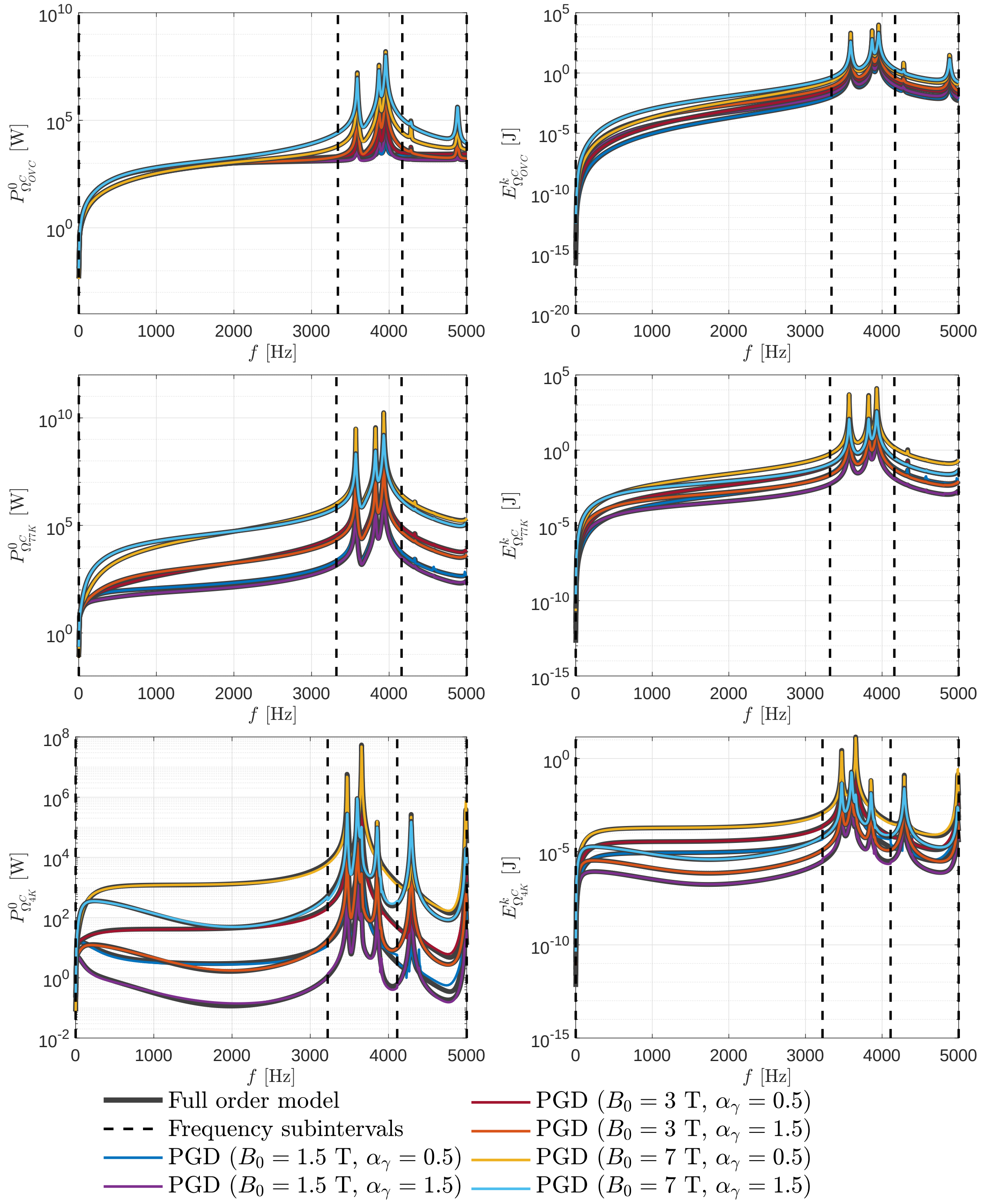

Figure 5.15: Test magnet problem; comparison between PGD solution and full order model. Plot of the dissipated power $P^0_{\Omega^C}$ and kinetic energy $E^k_{\Omega^C}$ in the three conducting shields OVC, 77K and 4K for six different cases.

obtain an accurate offline solution. As for the offline mechanical problem, the total maximum number of modes per frequency subinterval and per shield I^u_N has also been increased with respect to the test magnet problem.

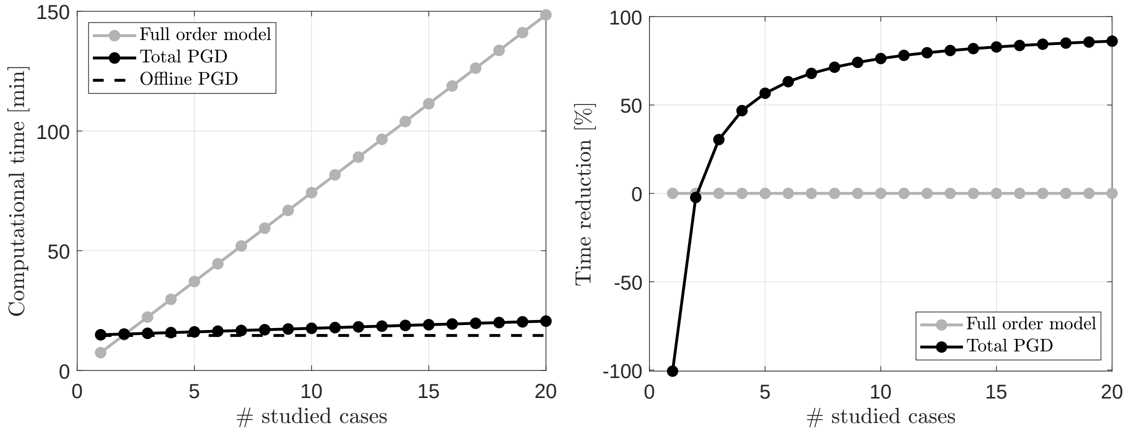

(a) Total time (solid line) and offline time (dashed line) for the three methods.

(b) Time reduction (%) obtained for each method.

Figure 5.16: Test magnet problem; study of the computational time taken by the full order model and both offline and online stages of the PGD technique. 700 frequencies have been sampled for each case of study.

Table 5.4: Full magnet problem; user-defined PGD parameters for the staggered high-dimensional PGD method.

PGD parameters						Parametric domains				Spatial domain		
I_N^A	I_N^u	tol_N^A	tol_N^u	I_{FP}	tol_{FP}	h_ω	tol_ω^{split}	h_γ	h_{B_0}	h_{Ω_p}	p	ξ
60	40	10^{-6}	10^{-5}	10	10^{-2}	$2 \cdot 10^{-5}$	20%	$6 \cdot 10^{-3}$	$8 \cdot 10^{-3}$	$7 \cdot 10^{-3}$	4	10^{-3}

5.7.1 Frequency splitting

The same staggered frequency splitting algorithm described in Section 5.5.1 is applied to the full magnet geometry in order to split the frequency domain where mechanical resonant singularities appear. The resulting frequency subdomains are presented in Figure 5.17, where a total of six subdomains have been generated. Note that this geometry features resonance even in the low frequency region and, thus, the frequency splitting algorithm has created six subdomains throughout the entire frequency range of interest $f \in [1, 2000]$ Hz. Similar to the test magnet geometry, see Figure 5.8, the eigenvalues associated to each shield are different and therefore, the splitting will be slightly different for each mechanical component. The exact frequency subdomains are $f_1^{OVC} = [1, 354]$, $f_2^{OVC} = [354, 707]$, $f_3^{OVC} = [707, 1060]$, $f_4^{OVC} = [1060, 1412]$, $f_5^{OVC} = [1412, 1706]$ and $f_6^{OVC} = [1706, 2000]$ Hz for the OVC shield, $f_1^{77K} = [1, 382]$, $f_2^{77K} = [382, 763]$, $f_3^{77K} = [763, 1144]$, $f_4^{77K} = [1144, 1526]$, $f_5^{77K} = [1526, 1763]$ and $f_6^{77K} = [1763, 2000]$ Hz for the 77K shield and $f_1^{4K} = [1, 396]$, $f_2^{4K} = [396, 791]$, $f_3^{4K} = [791, 1186]$, $f_4^{4K} = [1186, 1581]$, $f_5^{4K} = [1581, 1790]$ and $f_6^{4K} = [1790, 2000]$ Hz for the 4K shield.

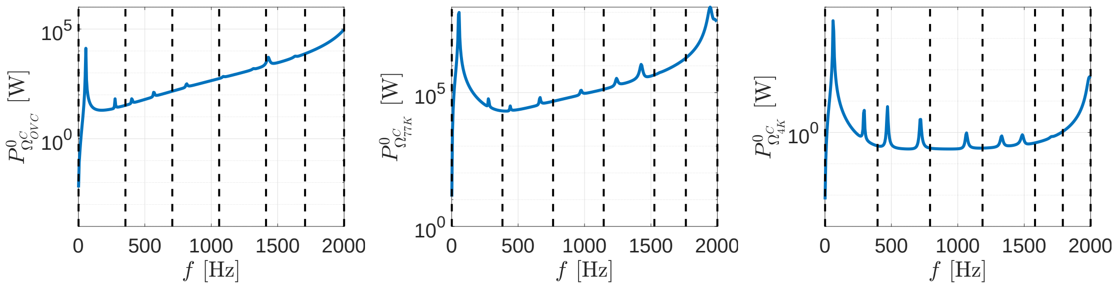

(a) OVC shield. (b) 77K shield. (c) 4K shield.

Figure 5.17: Full magnet problem; frequency subdomains resulting from staggered frequency splitting algorithm. Plotting the full order model solution (dissipated power) for $B_0 = 7$ T and $\alpha_\gamma = 1.5$.

5.7.2 PGD algorithm convergence

The convergence criteria described in Section 3.6 is applied to the full magnet problem in order to stop the two iterative algorithms appearing in the PGD method; the Greedy algorithm and the fixed-point ADS. The staggered PGD method requires only one PGD solution for electromagnetics and, thus, Figure 5.18 shows the convergence of the Greedy algorithm when applied to electromagnetics. Since the electromagnetic solution is known to be smooth, the Greedy algorithm reaches amplitudes of almost 10^{-6} when allowing a maximum of 60 PGD modes.

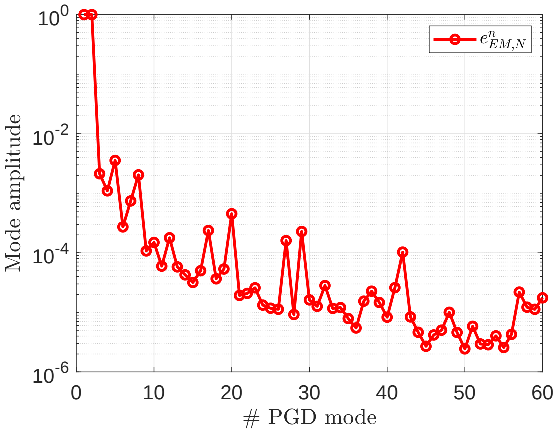

Figure 5.18: Full magnet problem; electromagnetic Greedy algorithm convergence.

As mentioned throughout this thesis, the mechanical equations need to be solved for smaller frequency ranges in order to preserve the PGD accuracy. Consequently, the staggered frequency splitting is applied to automatically generate six frequency subdomains, see Section 5.7.1, and hence, Figure 5.19 presents the Greedy algorithm convergence in all three conducting components (OVC, 77K and 4K radiation shields) for the six different frequency subintervals. Similarly to the test magnet geometry, see Figure 5.9, these results show a similar behaviour for all three shields. However, this more challenging geometry features resonance in the entire

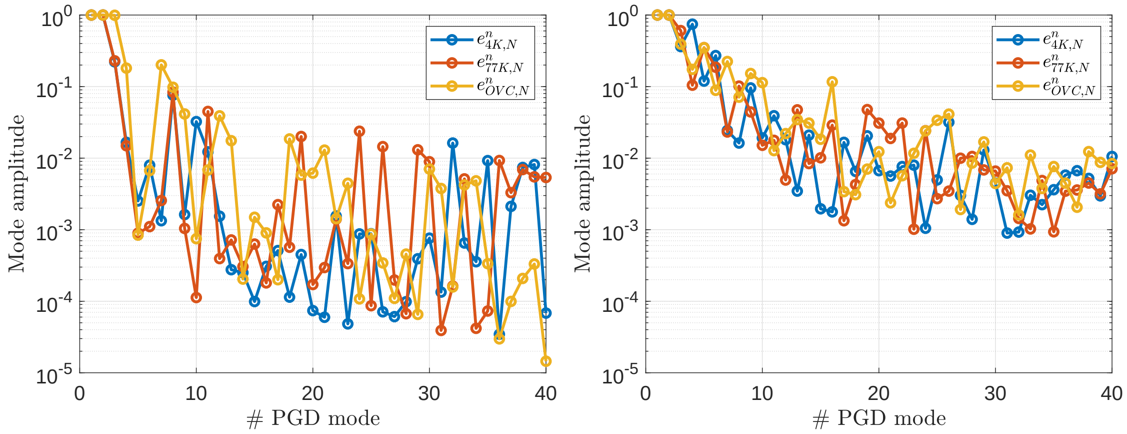

(a) 1^{st} frequency subdomain. (b) 2^{nd} frequency subdomain.

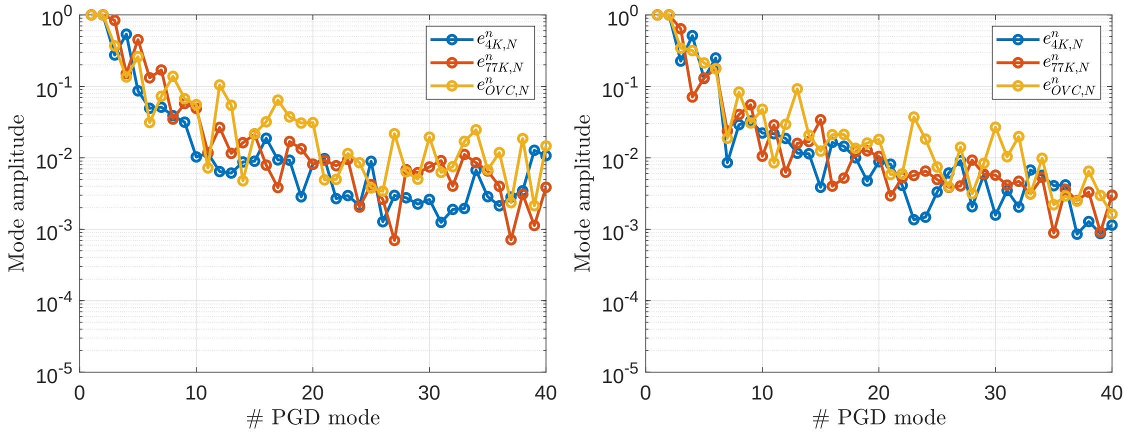

(c) 3^{rd} frequency subdomain. (d) 4^{th} frequency subdomain.

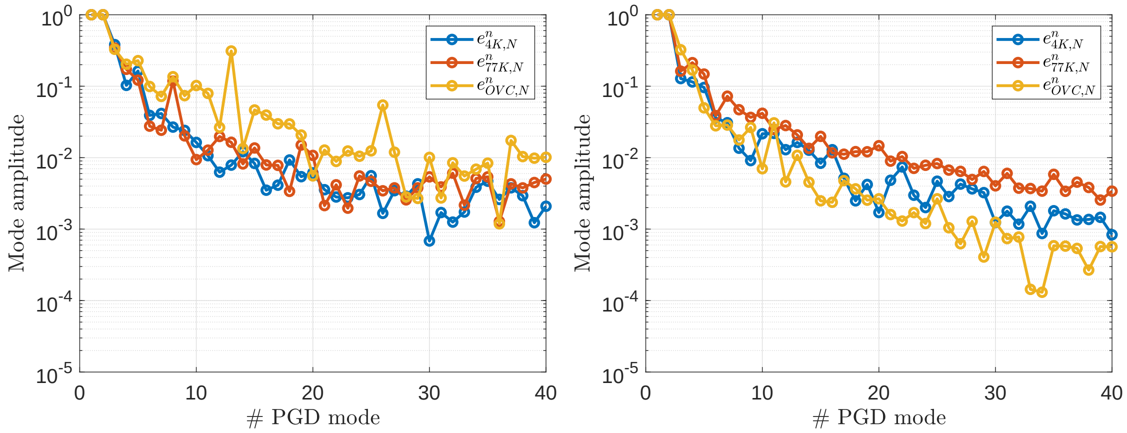

(e) 5^{th} frequency subdomain. (f) 6^{th} frequency subdomain.

Figure 5.19: Full magnet problem; mechanical Greedy algorithm convergence for the six frequency subdomains.

frequency spectrum and, hence, all six frequency subdomains reach a similar tolerance allowing a maximum of 40 PGD modes per subdomain.

The second iterative procedure required for the computation of each PGD mode is the ADS algorithm, which computes the converged modal quantities, see Section

5.4.4. The stopping criteria in Section 3.6 is then applied to determine weather a certain mode has already converged. Since the staggered PGD technique solves the two physics consecutively, the electromagnetic convergence of the ADS algorithm is first shown in Figure 5.20. The results show a fairly steady behaviour that converges almost linearly.

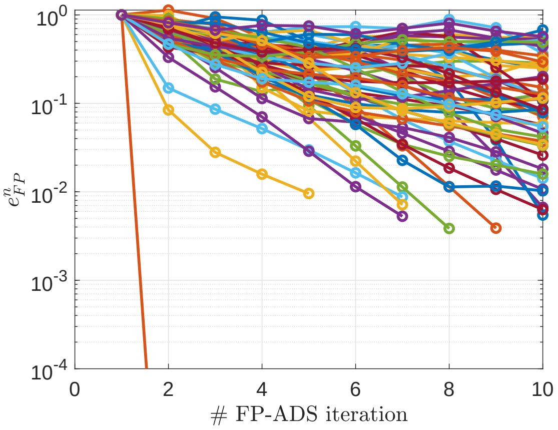

Figure 5.20: Full magnet problem; electromagnetic convergence of the fixed-point ADS algorithm.

The mechanical FP-ADS convergence is presented in Figure 5.21, where only the convergence of the OVC shield is shown due to the fact that a similar behaviour was observed for all three shields. Differently to the electromagnetic case, the mechanical convergence is visibly oscillating more because of the resonant singularities appearing in the mechanical equations. Note that the same idea of reducing the maximum number of FP-ADS iterations while increasing the maximum number of PGD modes [42] is applied in this case to speed up the overall PGD algorithm.

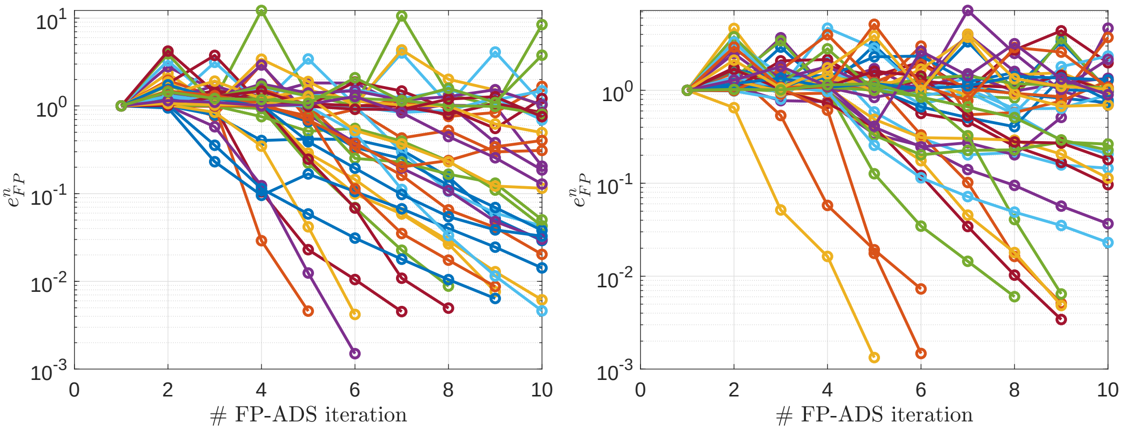

(a) OVC shield (1^{st} frequency subdomain). (b) OVC shield (2^{nd} frequency subdomain).

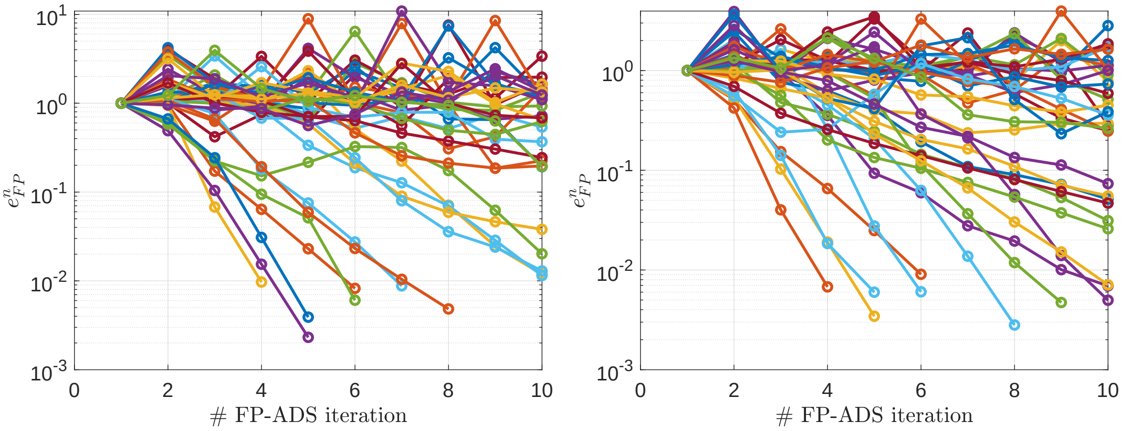

(c) OVC shield (3^{rd} frequency subdomain). (d) OVC shield (4^{th} frequency subdomain).

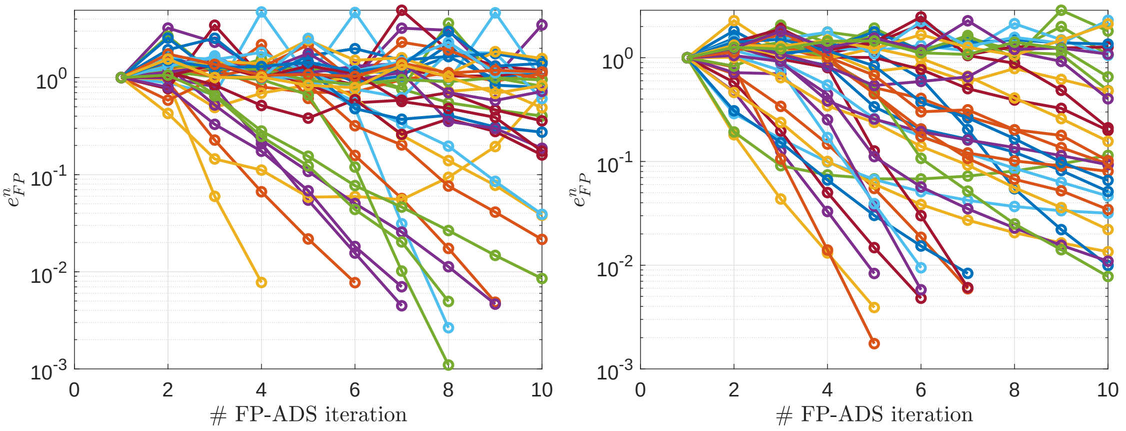

(e) OVC shield (5^{th} frequency subdomain). (f) OVC shield (6^{th} frequency subdomain).

Figure 5.21: Full magnet problem; mechanical convergence of the fixed-point ADS algorithm for each of the six frequency subdomains of the OVC shield.

5.7.3 Modes visualisation

At this point, all the required PGD modes have been computed and the high-dimensional expressions of the solution variables for electromagnetics, see (5.7), and mechanics, see (5.12), are hence obtained. This section presents first the spatial electromagnetic modes $F_{\mathcal{A}_\phi}(r,z)$ in Figure 5.22. The results are consistent with the ones studied for different geometries and different PGD methods, which represent the variations in the scalar potential variable in the vicinity of the AC coils. Note that all modes are L^2 normalised as described in Section 3.5. It is important to realise that the electromagnetic problem is indeed more challenging for this geometry than for the test magnet geometry, see Figure 5.11. The main reason of this increased difficulty seems to be determined by the more realistic coils considered in the full magnet geometry and therefore, more PGD modes are required for the electromagnetic problem.

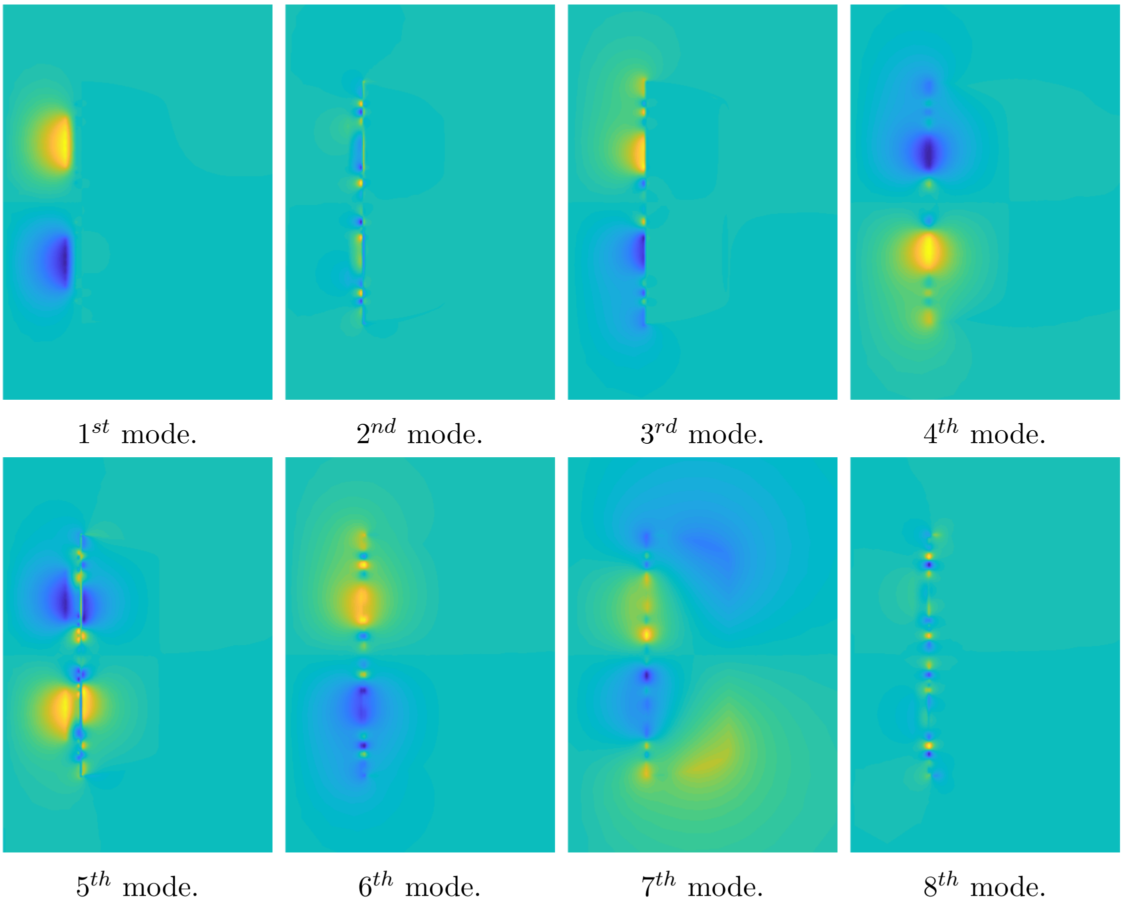
1^{st} mode. 2^{nd} mode. 3^{rd} mode. 4^{th} mode.

5^{th} mode. 6^{th} mode. 7^{th} mode. 8^{th} mode.

Figure 5.22: Full magnet problem; first 8 computed electromagnetic spatial modes $F_{\mathcal{A}_\phi}(r,z)$ for the entire range of the one-dimensional parametric domains; frequency $f \in [1, 2000]$ Hz. All modes have been L^2 normalised. Same colour scale for all subfigures.

The two parametric modes that are involved in the electromagnetics solution are associated with the frequency domain $G_{\mathcal{A}_\phi}(\omega)$ and the conductivity scaling domain

$H_{\mathcal{A}_\phi}(\gamma)$, see Figure 5.23. The results for these two parametric modes are significantly different; the frequency modes $G_{\mathcal{A}_\phi}(\omega)$ present sharp changes in the low frequency region whilst the conductivity scaling modes $H_{\mathcal{A}_\phi}(\gamma)$ are smooth in the entire range $\alpha_\gamma = [0.5, 2]$.

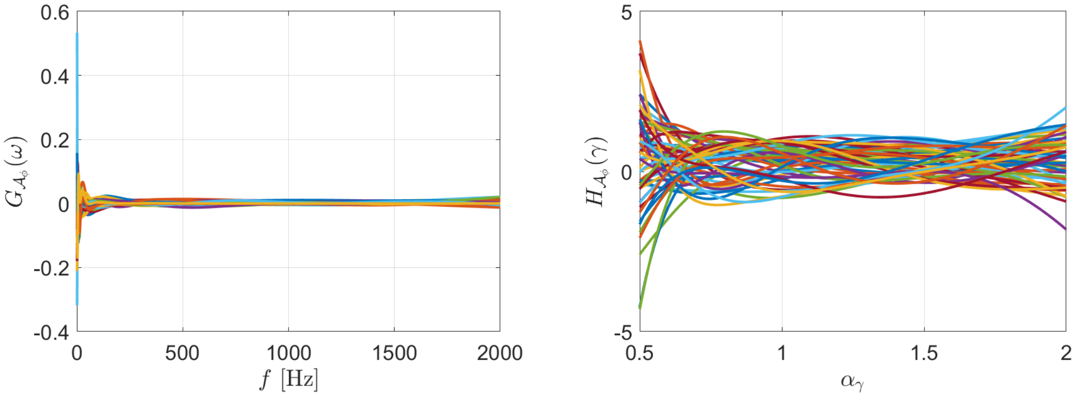

Figure 5.23: Full magnet problem; visualisation of the one-dimensional parametric electromagnetic modes $G_{\mathcal{A}_\phi}(\omega)$ and $H_{\mathcal{A}_\phi}(\gamma)$ for the entire range of the one-dimensional parametric domains; frequency $f \in [1, 2000]$ Hz and dimensionless conductivity scaling factor $\alpha_\gamma \in [0.5, 2]$. All modes have been L^2 normalised.

The mechanical equations are modelled using one spatial vectorial function $\boldsymbol{F}_{\boldsymbol{u}}(r, z)$ and three parametric scalar functions $G_{\boldsymbol{u}}(\omega)$, $H_{\boldsymbol{u}}(\gamma)$ and $L_{\boldsymbol{u}}(B_0)$, see (5.12). Regarding the spatial modes, Figure 5.24 shows the magnitude $F_{\boldsymbol{u}} = \sqrt{F^2_{\mathcal{U}_r} + F^2_{\mathcal{U}_z}}$ of the first eight computed modes. From these results it can be observed how different modes represent the variations of the displacement field in different parts of each conducting shield. Similarly to Section 5.6.2, the PGD modes are computed for each shield consecutively because of the staggered nature of the PGD technique. Therefore, the results shown in Figure 5.24 correspond to the union of the PGD modes computed per each shield, that is $F_{\boldsymbol{u}} = F^{OVC}_{\boldsymbol{u}} \cup F^{77K}_{\boldsymbol{u}} \cup F^{4K}_{\boldsymbol{u}}$. Moreover, since the frequency splitting is required in order to obtain a good PGD approximation, these modes correspond to the first frequency subdomain, which is slightly different for each shield as shown in Figure 5.17.

The modes representing the one-dimensional parametric spaces Ω_ω, Ω_γ and Ω_{B_0} are $G_{\boldsymbol{u}}(\omega)$, $H_{\boldsymbol{u}}(\gamma)$ and $L_{\boldsymbol{u}}(B_0)$, respectively, and they are presented in Figure 5.25 only for the OVC shield. As expected, they behave in the same way than for the test magnet geometry, see Figure 5.14. The frequency modes $G_{\boldsymbol{u}}(\omega)$ are non-smooth functions that are required to represent the resonance effect that now features in the entire frequency range of interest. Instead, $H_{\boldsymbol{u}}(\gamma)$ is a smooth nonlinear function on α_γ and $L_{\boldsymbol{u}}(B_0)$ behaves linearly with respect to the strength of the static magnetic field B_0. Note that this more challenging geometry requires the use of six different automatically generated frequency subdomains (each of the rows in the figure) in order to obtained an accurate representation of the solution fields.

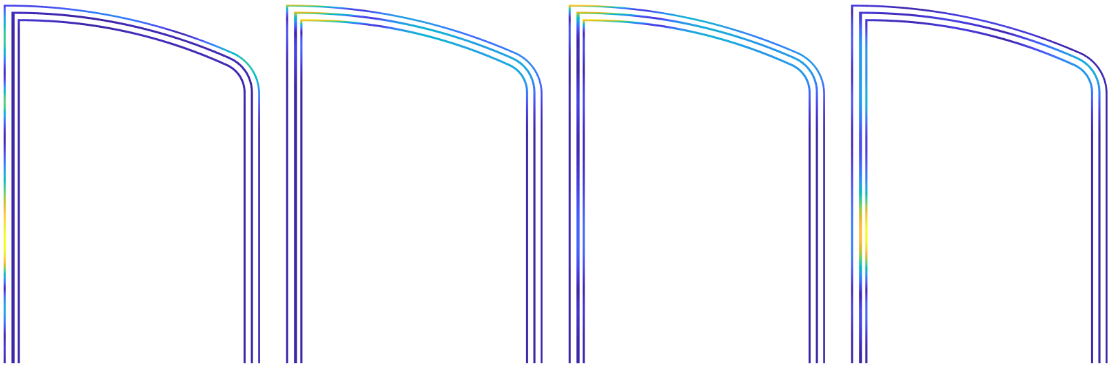

1^{st} mode. 2^{nd} mode. 3^{rd} mode. 4^{th} mode.

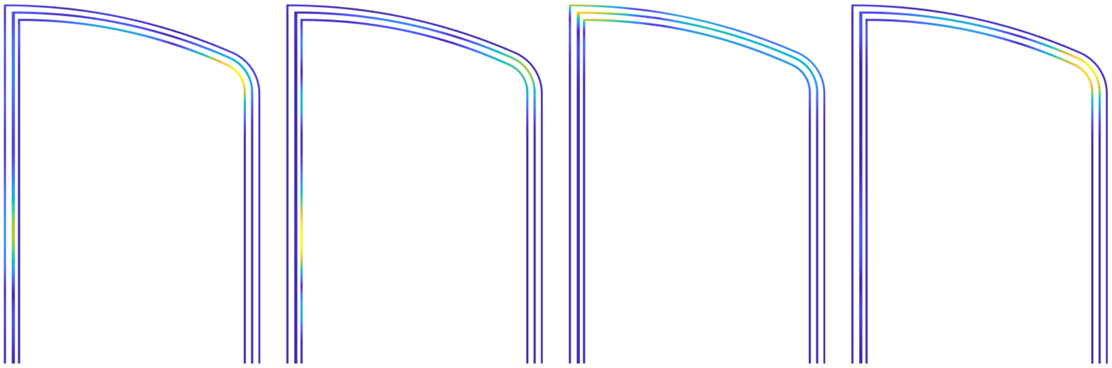

5^{th} mode. 6^{th} mode. 7^{th} mode. 8^{th} mode.

Figure 5.24: Full magnet problem; first 8 computed mechanical spatial modes $F_{\boldsymbol{u}}(r,z)$ for the first frequency subdomain. All modes have been L^2 normalised. Same colour scale for all subfigures.

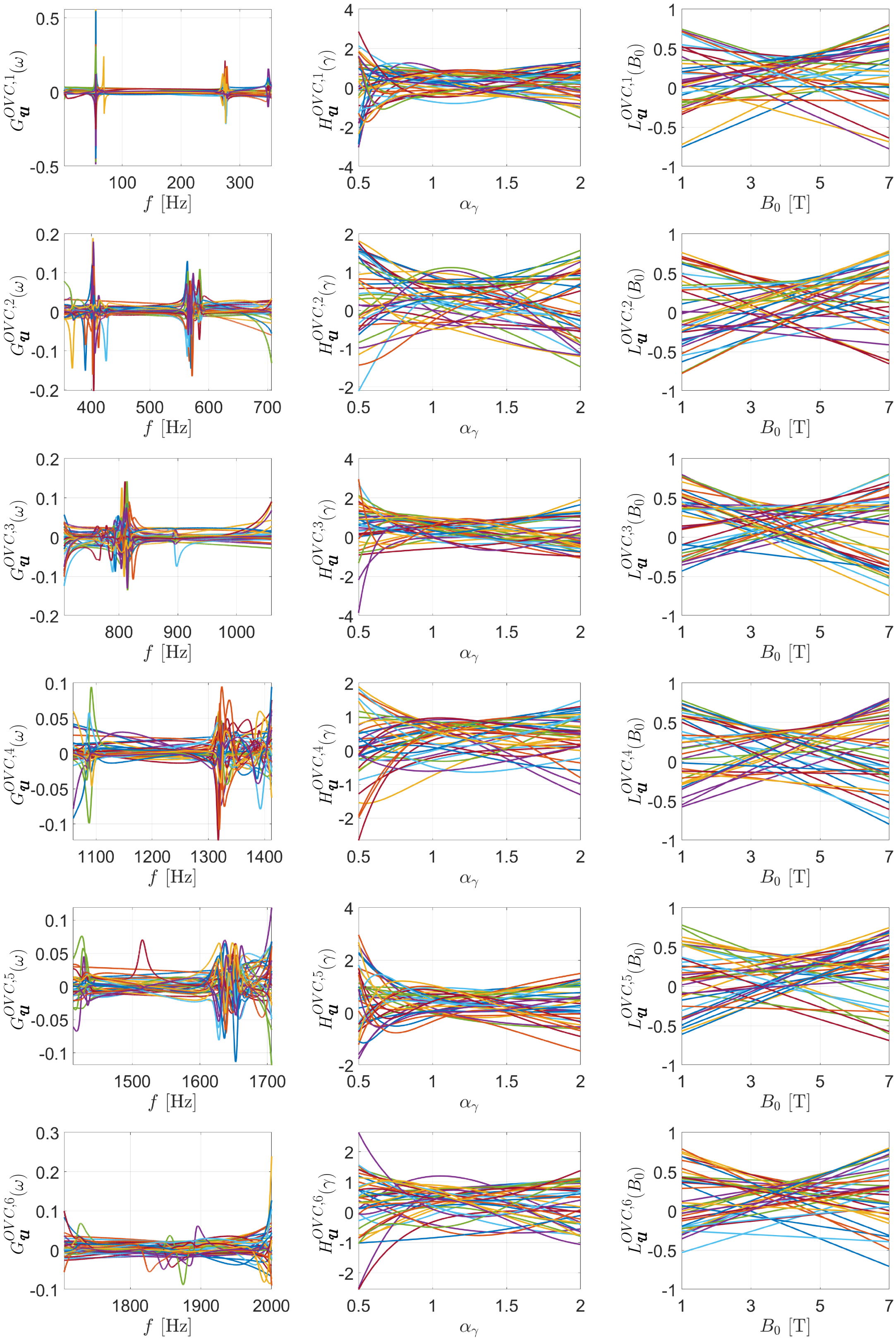

Figure 5.25: Full magnet problem; visualisation of the three one-dimensional parametric mechanical modes $G_{\boldsymbol{u}}(\omega)$, $H_{\boldsymbol{u}}(\gamma)$ and $L_{\boldsymbol{u}}(B_0)$ of the OVC shield for the six frequency subdomains. All modes have been L^2 normalised.

5.7.4 Validation of the PGD method

To demonstrate the validity and accuracy of the computed offline PGD solution, the post-processed quantities of interest, dissipated power $P^0_{\Omega^C}$ and kinetic energy $E^k_{\Omega^C}$ (2.34), are presented in Figure 5.26 for the entire coupled magneto-mechanical problem. Similarly to the test magnet problem, the full order model is denoted with a black solid line for all the different cases, whilst the PGD solution is plotted with coloured lines that can be associated with different combinations of parameters (B_0, γ) in the legend. From Figure 5.26, it can be concluded that the PGD approximation is able to accurately replicate the full order solution and locate all the resonance singularities for this complex simulation.

The computational time required to compute the different cases appearing in Figure 5.26 has been used to generate Figure 5.27, where the full order model and the PGD method are compared considering up to 20 cases (different parameter combinations). These results show a more costly PGD method with respect to the full order model than for the test magnet geometry, see Figure 5.16. However, it is clearly seen how with just 6 cases the PGD approach is already cheaper than the full order model. Moreover, massive savings can be achieved if more cases need to be studied, reaching approximately a 70% reduction.

Although integrated quantities, such as dissipated power $P^0_{\Omega^C}$ and kinetic energy $E^k_{\Omega^C}$ (2.34), are important quantities of interest for industry, they are not the only quantities required for design. Other field quantities such as the magnetic field, displacements, stresses and eddy current distributions are also taken into account as part of the design process. It is here where an additional advantage of the PGD methodology can be exploited, by pre-computing explicit separable expressions of the solution fields which can be then queried in real time. Figure 5.28 shows the eddy current distribution $\boldsymbol{J}^0$ inside the conductors, computed as $\boldsymbol{J}^0 = \gamma \boldsymbol{\mathcal{E}}^{AC}$, for $B_0 = 1.5$ T, $\gamma = 1$ and different values of the frequency of excitation f. A typical phenomenon can be observed in this Figure; the skin depth effect. For low frequencies (100 Hz) see how the eddy current field is constant across the shield's thickness. However, in the high-frequency region (2000 and 4000 Hz) the skin depth effect becomes more dominant, modifying the eddy current distribution within the radiation shields by concentrating the eddy currents in the interfaces of the shields. The fact that sharp changes are observed in a small part of the shields' thickness makes the problem more demanding from the computational point of view, requiring the careful combination of high fidelity space-time discretisations and reduced order computational models.

5.7.5 Sensitivity maps

Once the offline PGD solution has been stored, the online PGD stage can be applied at any time in order to obtain fast evaluations for the different parameters considered in the offline stage. It is interesting to demonstrate a further capability of the PGD methodology, related to its ability to efficiently conduct online multiple-queries (in

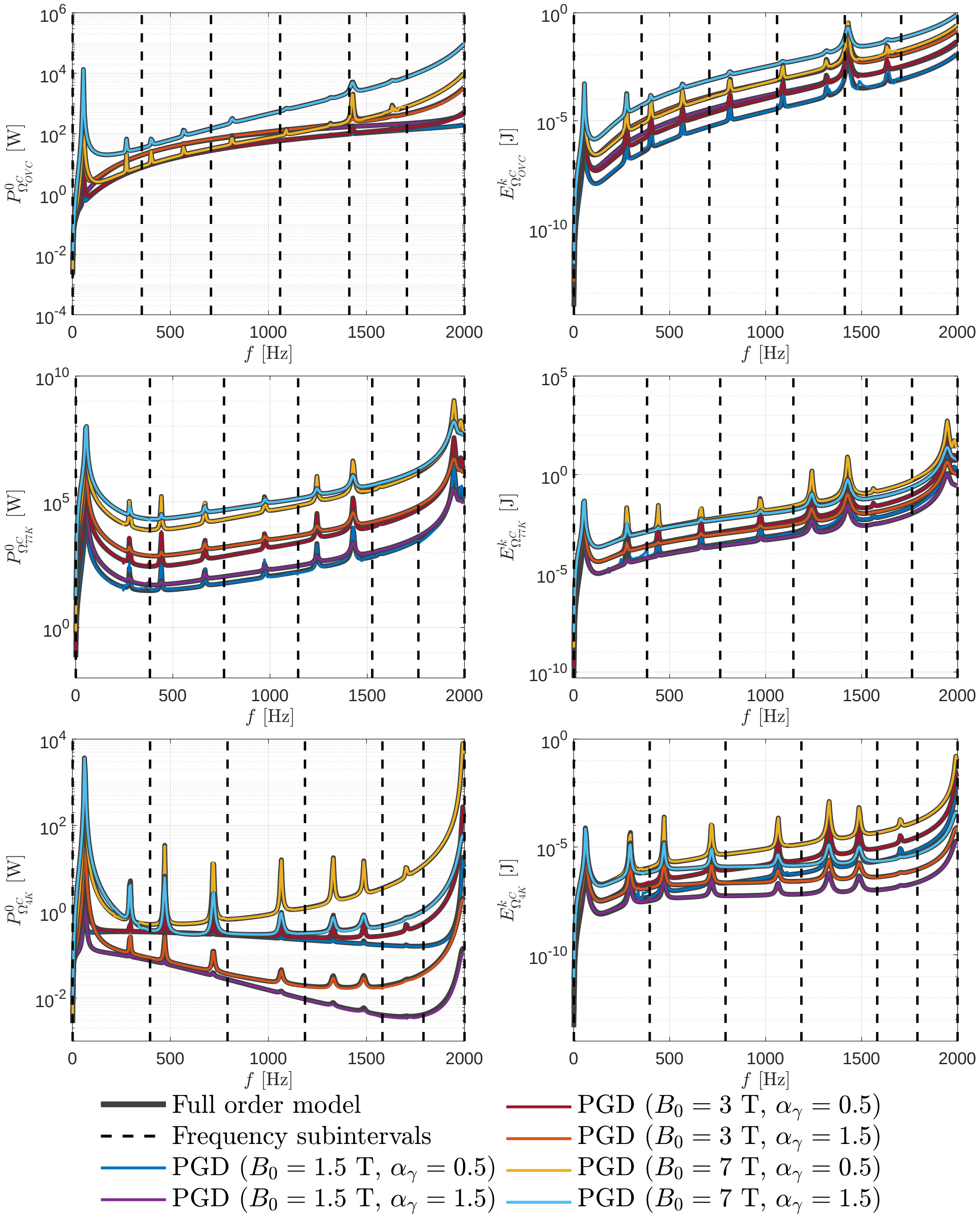

Figure 5.26: Full magnet problem; comparison between PGD solution and full order model. Plot of the dissipated power $P^0_{\Omega^C}$ and kinetic energy $E^k_{\Omega^C}$ in the three conducting shields OVC, 77K and 4K for six different cases.

real time) to the high-dimensional parametric offline solution. As an example, it is possible to compute and plot output sensitivity maps or response surfaces (for a given quantity of interest) when arbitrarily varying the set of input parameters used in the construction of the PGD offline solution. Figure 5.29 shows three different response surfaces of the post-processed output power in the OVC shield $P^0_{\Omega^C_{OVC}}$ for

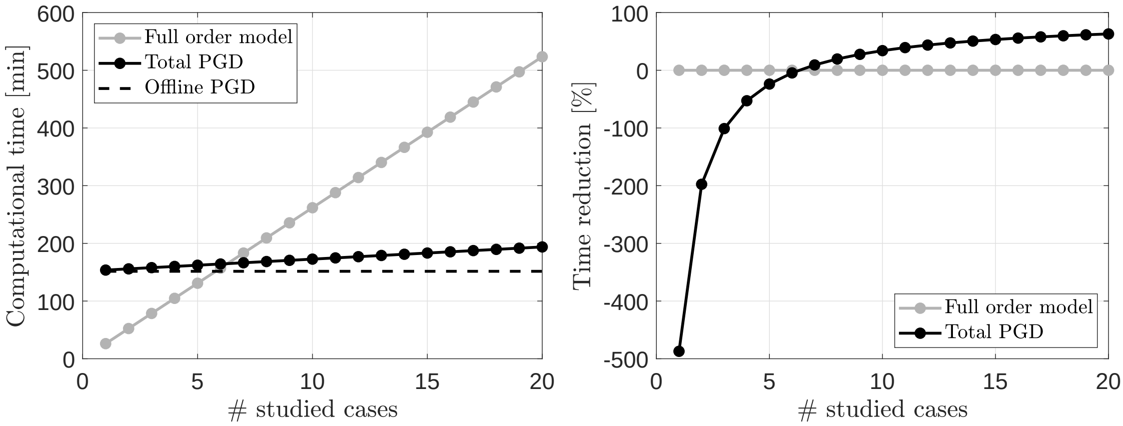

(a) Total time (solid line) and offline time (dashed line) for the full order model and staggered PGD approaches.

(b) Time reduction (%) obtained with the PGD method.

Figure 5.27: Full magnet problem; study of the computational time taken by the full order model and the staggered PGD approach. 400 frequencies have been sampled for each case of study.

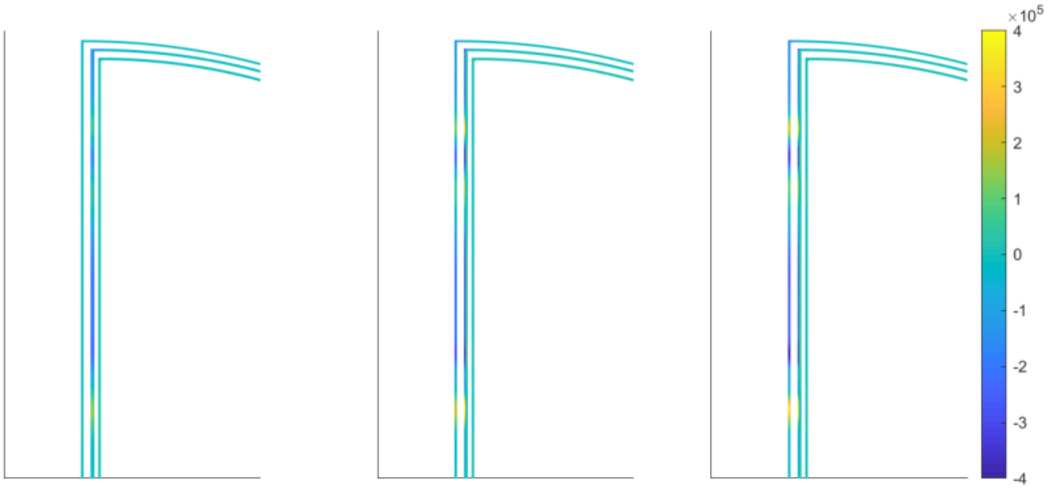

(a) $f = 100$ Hz.

(b) $f = 2000$ Hz.

(c) $f = 4000$ Hz.

Figure 5.28: Full magnet problem; Eddy current distribution within the radiation (conducting) shields for different frequencies f, $B_0 = 1.5$ T and $\gamma = 1$.

different combinations of frequency f [Hz], strength of static magnetic field B_0 [T] and dimensionless scaling of electric conductivity α_γ. Note that, although it is technically possible to compute these sensitivity maps with the full order model, the computational time required would be extremely high since a large number of sample points (2000 in this case) can be typically needed in order to display the surface with an acceptable level of resolution. The formulation used to compute these sensitivity maps within the PGD framework is presented in Appendix D.

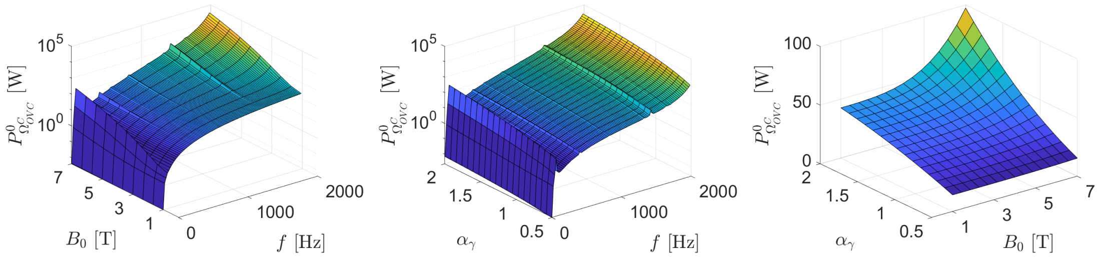

(a) f/B_0 plot for $\alpha_\gamma = 1.5$. (b) f/α_γ plot for $B_0 = 5$ T. (c) B_0/α_γ plot for $f = 500$ Hz.

Figure 5.29: Full magnet problem; response surfaces of the output power in the OVC shield $P^0_{\Omega^C_{OVC}}$ for different values of f, B_0 and α_γ.

5.8 Chapter summary

This chapter has presented a new Reduced Order Modelling (ROM) Proper Generalised Decomposition (PGD) method for use in the design phase of new MRI scanner configurations. The methodology builds upon previous work developed by the authors in [88] where a PGD-frequency based methodology was developed and it is here enhanced by considering two further material parameters as part of the high-dimensional parametric PGD offline solution, namely, the electrical conductivity and the strength of the static magnetic field. This aligns with the objective "*To extend the frequency-based PGD formulation to a higher-dimensional problem including now material parameters*". The new (reduced order) PGD methodology has been validated against a reference (full order) solution in terms of accuracy and computational time, where it has been clearly shown how the PGD method can drastically optimise the multiple-query online stage without sacrificing accuracy. Moreover, the staggered nature of the underlying magneto-mechanical problem has been exploited in this chapter, in order to obtain a sequential PGD algorithm that has been proven to be both efficient and robust, which aligns with the objective of the thesis "*To exploit the staggered nature of the coupled problem at hand*".

The *a priori* PGD algorithm has also been compared in terms of the electromagnetic output against an alternative *a posteriori* ROM method specifically designed for this problem, the electromagnetic Proper Orthogonal Decomposition (EM-POD) method, achieving the thesis objective "*To assess and compare the a priori PGD and the a posteriori POD methods against the full order model*". This study concludes that a massive time reduction can be obtained in the electromagnetic problem with both ROM approaches. When considering the entire coupled magneto-mechanical problem, the EM-POD strategy developed in [49] is still able to greatly reduce the computational cost of the problem at the expense of increasing the calculations done in the online POD stage. On the other hand, the staggered PGD presented in this chapter is able to simulate the entire coupled magneto-mechanical problem, obtaining an explicit expression of the solution fields, conserving the real-time attractiveness during the online PGD stage and allowing to output sensitivity maps.

The next chapter of this thesis will focus on extending the PGD formulation to include geometrical changes, for instance the thickness of the conducting shields, as extra parameters of the PGD offline solution, in the search of a computational metamodel which allows for real time simulations, thus minimising human intervention.

Chapter 6

Integration of geometric parameters into the PGD methodology

6.1 Introduction

The previous chapters of this thesis have described the development of a PGD methodology for an MRI problem based on a Lagrangian coupled magneto-mechanical FEM formulation. In Chapter 4, the frequency of excitation was treated as a parameter of the higher-dimensional parametric offline PGD solution, namely $\Omega_q = \Omega_\omega$. Subsequently, in Chapter 5, the PGD formulation has been extended to a higher-dimensional parametric domain $\Omega_q = \Omega_\omega \times \Omega_\gamma \times \Omega_{B_0}$ including the electric conductivity γ and the strength of the static magnetic field B_0. Building upon the developments of Chapter 5, the current chapter focuses on incorporating possible geometric variations in the developed PGD computational framework.

During the design stage of an MRI scanner, Siemens Healthineers is specially interested in the assessment of different shields' thicknesses for any novel MRI configuration. Typically, this is the first geometric parameter that is studied in the design stage, seeking to find the most optimum thickness for the various conducting components before proceeding to other parametric design studies (e.g. variable γ and B_0). Consequently, a generic scalar parameter h will be used to define the thickness of all three mechanical components[1], OVC, 77K and 4K radiation shields.

The consideration of geometrically parametrised problems via a PGD computational formulation has been recently studied in [70,75,92–94], using slightly different approaches albeit with the same underpinning idea: inclusion of geometric parameters in the PGD separable definition so that the resulting offline parametrised solution fields account implicitly for geometrical changes. In the context of this thesis, the use of an axisymmetric assumption has resulted into relatively complex expressions of the differential operators[2], namely divergence, curl and gradient operators, and has demanded a scaling of the solution fields using the r-coordinate (to avoid singularities near the bore axis), see Section 2.5. These two considerations lead to a cumbersome formulation of the PGD technique when attempting to incorporate the thickness h as an extra parameter of the offline PGD solution. Consequently, an alternative approach which balances efficiency, accuracy and industrial demand, is advocated in this chapter.

---

[1] The formulation can potentially be extended to a set of parameters (for instance h_{OVC}, h_{77K} and h_{4K}) defining the thickness of each shield separately.

The proposed strategy can be broken down into the following steps. First, the computation a series of high-dimensional PGD solutions for a series of discrete values of $h \in \Omega_h$, where Ω_h defines the parametric thickness domain of interest for the end user, which in this case Siemens Healthineers has proposed as $\Omega_h = [1, 5]$ mm. Secondly, the coefficients of a high-order snapshot data tensor are efficiently computed via the online PGD stage, generating a point cloud for a certain integrated quantity of interest [3]. Thirdly, the high-order data tensor is then separated by means of a collocation PGD-projection approach developed in [42, 48], aiming to obtain a separable expression of the offline solution into the various spatial, material and geometric parametric modes.

With this aim, a study on the sensitivity of the selected quantity of interest to the variation of the shields' thickness h will be presented, highlighting several numerical difficulties that will be addressed in the following sections. A moving mesh technique, developed in [95] and exploited in this chapter, will be briefly described in order to create comparable (connectivity wise) FE meshes for different geometries (variations of h). Finally, the collocation PGD-projection will be briefly introduced and a set of numerical results will be presented in order to assess the performance of the presented approach against the full order model.

6.2 Problems of interest

The aim of this section is the study of the influence of the shields' thickness on the solution of the coupled MRI problem. The two main problems considered are the test magnet problem and the full magnet problem, defined in Section 2.8.

Figure 6.1 presents the three configurations to be analysed; first the test magnet problem, see Figure 6.1a, which is identical to the one presented in Section 2.8. Secondly, a new configuration proposed by Siemens Healthineers, which is called the test magnet 2 problem, see Figure 6.1b, where the geometry coincides with that of the test magnet, but the Dirichlet boundary conditions are now applied to the top edge of each shield, allowing for larger displacements (worst case scenario) than in the previous case, where the shields where fixed in the middle section of the shield span. Finally, the last problem is the most challenging full magnet configuration, see Figure 6.1c, which is also detailed in Section 2.8.

---

[2] These operators are considerably simpler when expressed in a 3D Cartesian setting.

[3] As motivated throughout this thesis, integrated quantities such as the dissipated power, are the quantities of utmost interest to the MRI industry.

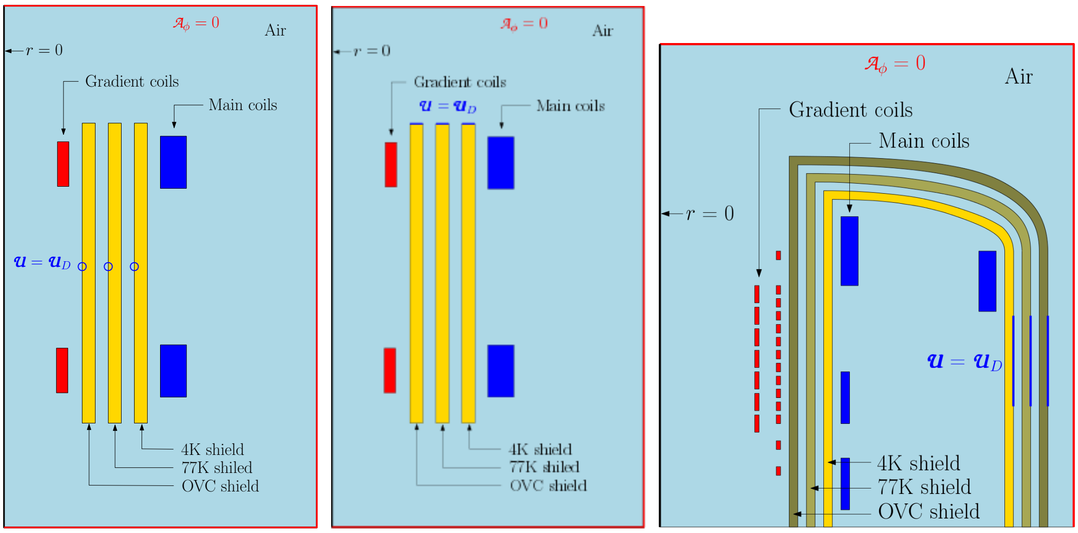

(a) Test magnet (b) Test magnet 2 (c) Full magnet

Figure 6.1: Description of the three MRI configurations considered. Two different Dirichlet boundary conditions are set for the test magnet geometry.

6.2.1 Visualisation of the solution for several geometries

The three MRI configurations presented in Figure 6.1 will now be studied for different values of the shields' thickness h. To do so, a frequency sweep will be carried out for each value of h and the response spectra will be compared and discussed, analysing how the solution changes as a function of h.

The numerical solution for the different values of h and frequency sweep, will be obtained by taking advantage of the staggered PGD formulation presented in Chapter 5. However, to start with, only the frequency will be considered as a parametric variation (with γ and B_0 fixed). Consequently, the separable expressions of the approximated solution fields will be defined as

$$\mathcal{A}_\phi^h(r,z,\omega) \approx \mathcal{A}_\phi^{N_A,h}(r,z,\omega) := \sum_{n=1}^{N_A} \beta_{\mathcal{A}_\phi}^{n,h} F_{\mathcal{A}_\phi}^{n,h}(r,z) G_{\mathcal{A}_\phi}^{n,h}(\omega), \tag{6.1a}$$

$$\boldsymbol{\mathcal{U}}^h(r,z,\omega) \approx \boldsymbol{\mathcal{U}}^{N_u,h}(r,z,\omega) := \sum_{n=1}^{N_u} \beta_{\boldsymbol{\mathcal{U}}}^{n,h} \boldsymbol{F}_{\boldsymbol{\mathcal{U}}}^{n,h}(r,z) G_{\boldsymbol{\mathcal{U}}}^{n,h}(\omega), \tag{6.1b}$$

where the superscript $(^h)$ is used to indicate that a particular PGD solution corresponds to a specific value of the thickness h. The user-defined parameters regarding the computation of the above separable expressions are stated in Table 6.1, which have been selected using the validated high-dimensional PGD method described in Section 5.6.2. Note that the only difference with respect to the parameters in the aforementioned section is that now a reduced value of the damping coefficient ξ is used to permit a better visualisation of the resonance frequencies.

Table 6.1: Test magnet problem; user-defined parameters for the staggered frequency-based PGD method.

PGD parameters						Parametric domain		Spatial domain		
I_N^A	I_N^u	tol_N^A	tol_N^u	I_{FP}	tol_{FP}	h_ω	tol_ω^{split}	h_{Ω_p}	p	ξ
40	60	10^{-4}	10^{-5}	10	10^{-2}	$2 \cdot 10^{-5}$	20%	$5 \cdot 10^{-3}$	4	10^{-4}

The frequency sweeps for the three MRI configurations are shown in Figure 6.2, where each subfigure contains five sweeps, one for each value of $h = [1, 2, 3, 4, 5]$ mm. The left column presents a 3D view of the entire frequency and thickness ranges whilst the right column shows a zoomed view of the area where the resonance effect develops. Moreover, black dashed lines have been plotted for a better visualisation of the evolution of the resonance frequencies with the thickness h. These results show that the location of resonant modes vary in the frequency domain for different values of the thickness and more importantly, that bifurcation may also occur. These two facts become important when trying to obtain a frequency sweep for a new (not sampled) thickness, as it will be discussed later on. Moreover, these results also suggest that the lower modes are less sensitive to variations of h, whereas high frequency modes behave in a very non-linear manner. Note that this conclusion is not problem dependent, since it is observed in all three configurations.

6.3 Characteristic polynomial

The location of the numerical singularities shown in the previous section are given by the eigenvalues of the mechanical problem. Hence, the aim of this section is to study, discuss and justify the behaviour observed in Section 6.2.1. To this point, the thesis has presented how the mechanical problem (2.25) can be solved either with the full order model approach, see Chapter 2, or within a PGD framework, see Chapters 4 and 5. Both strategies lead to a discretised system of equations consisting of a stiffness, damping and mass matrices with a forcing vector (see (2.33) for the discretised mechanical problem using the full order model and (5.30a) for the discretised system of equations that is solved within the PGD framework).

In order to understand the change of location of the singularities associated with resonance and the bifurcation phenomenon observed in the previous section, an illustrative problem has been designed, reducing the complexity of the problem but maintaining its essence. Therefore, the weak formulation to be considered in this section is presented as: Find $\boldsymbol{u}(r, z) \in Y(\boldsymbol{u}_D)$ such that[4]

$$W_K^{u,h}(\boldsymbol{u}, \delta\boldsymbol{u}) - \omega^2 W_M^{u,h}(\boldsymbol{u}, \delta\boldsymbol{u}) = -S^{u,h}(\mathcal{A}_\phi, \delta\boldsymbol{u}) \quad \forall \delta\boldsymbol{u} \in Y(\mathbf{0}), \tag{6.2}$$

where, the dependency of the compact forms on h is explicitly written (see upper

---

[4] Note that the damping term has been neglected for simplicity.

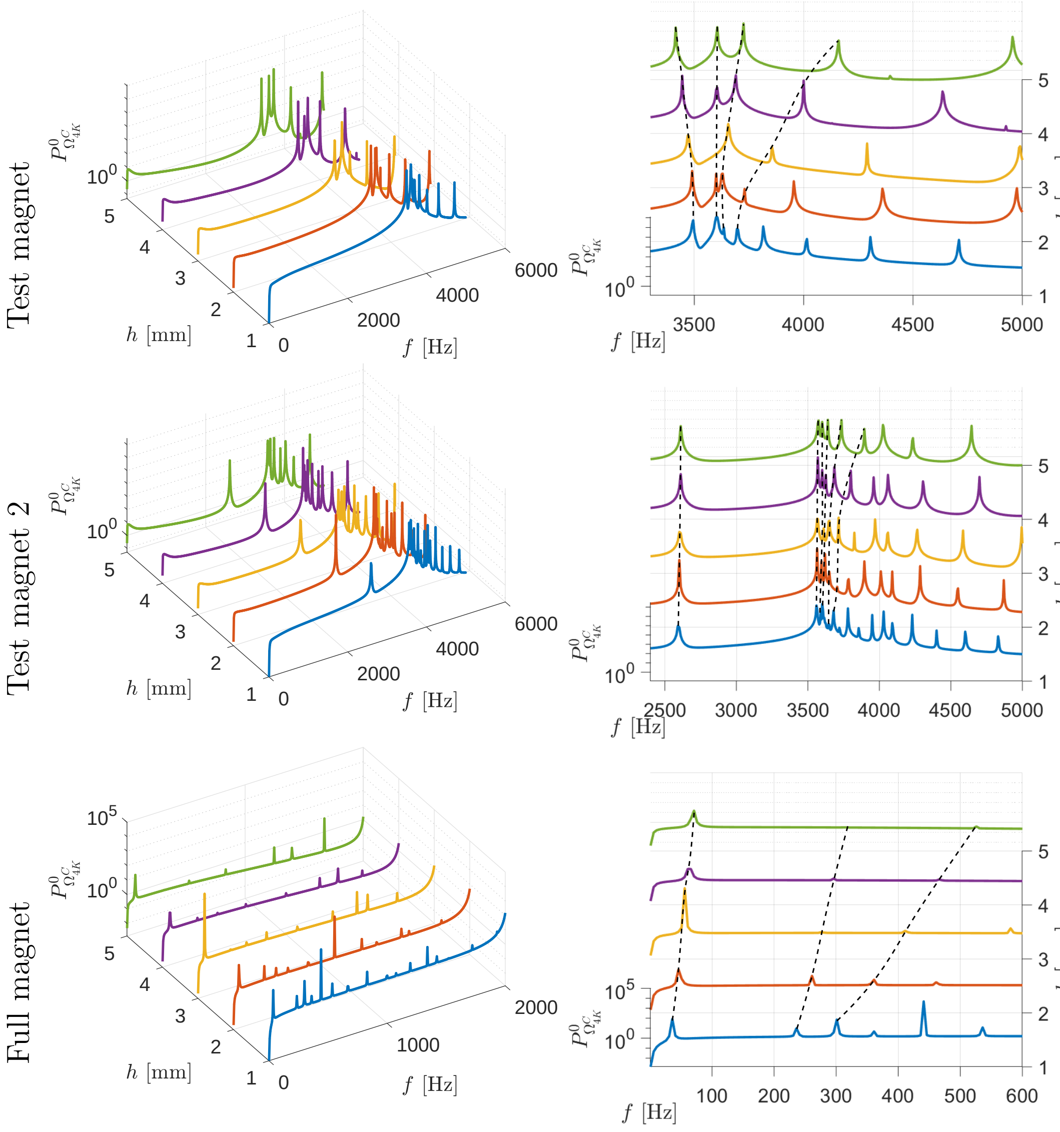

3D visualisation of the frequency sweeps Zoom in the resonance area

Figure 6.2: Frequency sweep for three different MRI configurations computing the dissipated power $P^0_{\Omega^C_{4K}}$ from the precomputed PGD offline solution for five different geometries.

index h). This expression can be spatially discretised, see Section 2.6, in order to obtain the following algebraic system of equations

$$\big(\mathbf{K}_{uu}(h) - \omega^2\mathbf{M}_{uu}(h)\big)\boldsymbol{\mathcal{U}} = \mathbf{s}_u, \tag{6.3}$$

where the dependency on the shields' thickness h is explicitly written for both matrices $\mathbf{K}_{uu}(h)$ and $\mathbf{M}_{uu}(h)$. Since the goal of this section is to understand how the eigenvalues of a certain system of equations evolve depending on h, the representation of the characteristic polynomial $P(\lambda, h)$ is a good way to illustrate its schematic response. The characteristic polynomial contains the eigenvalues $\lambda = \omega^2$ as roots and these are given by the following equation

$$P(\lambda, h) = P(\omega^2, h) = \det[\mathbf{K}_{uu}(h) - \omega^2\mathbf{M}_{uu}(h)] = 0, \tag{6.4}$$

where there will be N_{rank} (not necessarily distinct) eigenvalues, with N_{rank} being the rank of $\mathbf{K}_{uu}(h)$ and $\mathbf{M}_{uu}(h)$. Different eigenvalues and thus, characteristic polynomials, will be obtained for each geometry h considered. Figure 6.3 shows three polynomials associated with three different geometries of this artificial problem. As mentioned before, this is not the actual system of equations of the coupled magneto-mechanic problem. However, this study illustrates that there are cases in which for different geometric values of h the multiplicity of a certain root may vary. For this particular example, $P(\lambda, h_1)$ has three roots with multiplicity one whereas a slight change in the geometry h could potentially result in $P(\lambda, h_2)$, observing only two roots with one of them having a root of multiplicity equal to two. Again, further changes in the geometry may shift the characteristic polynomial as in $P(\lambda, h_3)$, where only one root is observed in the range considered. Therefore, this schematic problem shows that slight changes in h may indeed change the location of the singularities (eigenvalues) but also its degree of multiplicity, which explains the bifurcations observed in Section 6.2.1.

After this illustrative example, another study that can be performed is the monitoring of the smaller and larger eigenvalues within the frequency range of interest, which are ordered such that $0 < \lambda_1 \leq \lambda_2 \leq \ldots \leq \lambda_{N_{rank}-1} \leq \lambda_{N_{rank}}$. Figure 6.4 presents then the evolution of the three smallest (λ_1,λ_2,λ_3) and largest ($\lambda_{N_{rank}-2}$,$\lambda_{N_{rank}-1}$,$\lambda_{N_{rank}}$) eigenvalues obtained for the test magnet geometry when solving the actual system of equations at hand (2.33). These results display the same idea observed in Figure 6.2, namely, the low frequency eigenvalues are fairly constant regardless of the value of h. On the other hand, it is clear from this figure that high frequency eigenvalues are very sensitive to geometrical changes and they behave in a very non-linear manner. Finally, it can also be observed how bifurcations may occur, as previously discussed in Figure 6.3.

6.4 Mesh deformation through linear elasticity

The main goal of this chapter is the use of the PGD methodology in order to obtain fast (real-time) computations of integrated quantities of interest for different geomet-

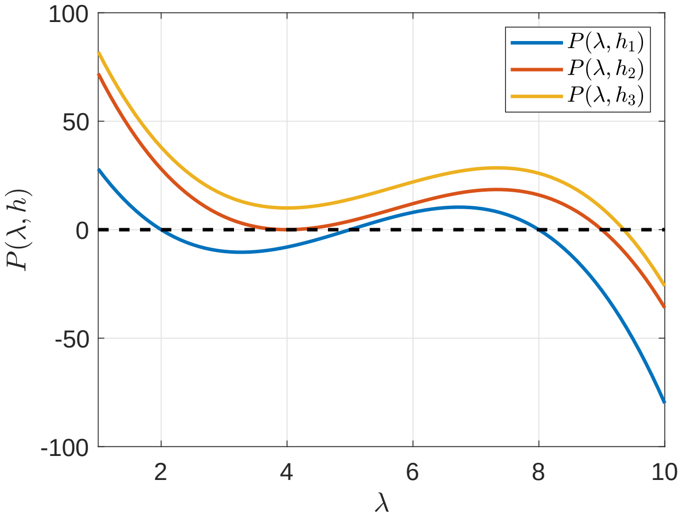

Figure 6.3: Visualisation of three characteristic polynomials for three different geometries of an illustrative problem.

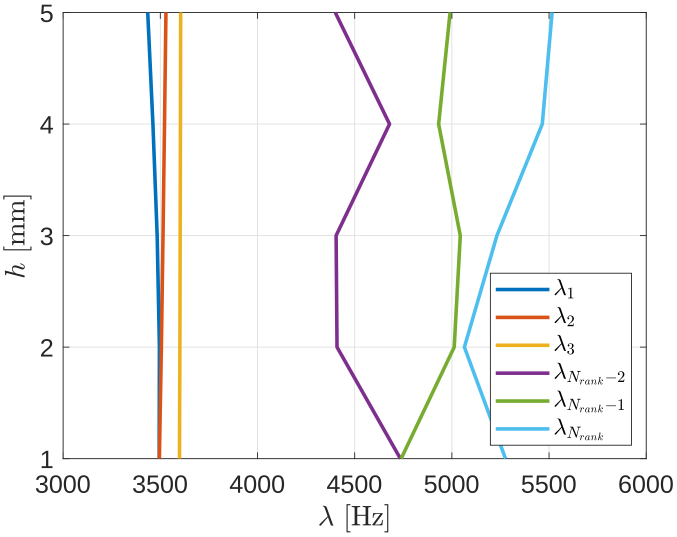

Figure 6.4: Test magnet problem; tracking of the three smallest and biggest eigenvalues for five different geometries within the frequency range of interest.

ries, where the geometric parameter of interest is the shields' thickness h. The mesh generation process used in the numerical simulations previously presented generates a mesh dependent upon the input geometry and therefore, it can potentially create a different mesh connectivity when modifying h. This is no longer acceptable since the precomputed offline PGD solutions, for different sampled geometries, will be used in order to interpolate a new one. Hence, this section presents a method that deforms a certain reference mesh by solving a linear elastic problem with Dirichlet boundary conditions, obtaining comparable meshes for geometries with different thicknesses.

This meshing method was presented in [95] (and extended in [83]) and consists in generating a reference mesh representing a pseudo-elastic material, which is deformed to a spatial configuration compliant with some pre-imposed Dirichlet boundary conditions. Once the Dirichlet boundary conditions necessary to deform the reference mesh to the desired geometrical configuration, a linear elastic problem is solved, obtaining the displacement field of all nodes and thus, the deformed mesh. Although this method is used here in a 2D setting, it was originally developed to generate arbitrary order curved meshes for 3D finite element analysis, see [83, 95].

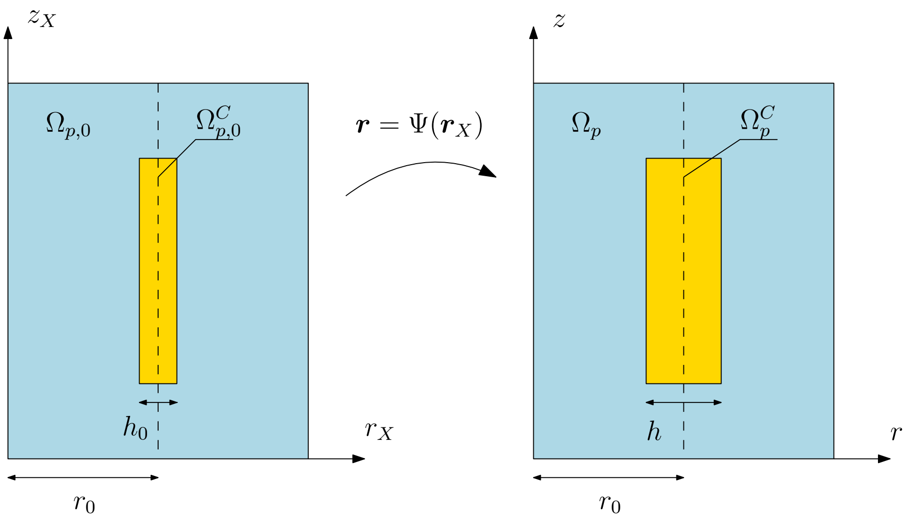

Figure 6.5: Reference (r_X, z_X) axisymmetric MRI shield that is mapped through $\Psi(\boldsymbol{r}_X)$ to the actual deformed (r, z) domain.

In our case, the required Dirichlet boundary conditions are computed depending on the new shields' thickness h. This is straightforward for the test magnet geometry due to the fact that the mapping can be explicitly obtained as shown in Figure 6.5. From this figure it can be seen that only the conducting components are deformed from a reference domain $\Omega^C_{p,0}$ to the spatial domain Ω^C_p as

$$\begin{aligned} \Omega^C_{p,0} &\longrightarrow \Omega^C_p \\ (r_X, \phi_X, z_X) &\longmapsto (r, \phi, z) = \Psi(r_X, \phi_X, z_X) \end{aligned} \tag{6.5}$$

with

$$\begin{aligned} r &= r_0 + \alpha_h (r_X - r_0), \\ \phi &= \phi_X, \\ z &= z_X, \end{aligned} \tag{6.6}$$

where α_h is defined as $\alpha_h := h/h_0$. On the other hand, the Dirichlet boundary conditions in the non-conducting subdomains are set equal to zero to ensure that only the conducting shields are deformed. Once all Dirichlet boundary conditions are set, the mesh deformation algorithm is used to create comparable meshes for different values of h as presented in Figure 6.6, where only the nodes in the vicinity of the shields have experienced significant displacements. Note that the non-conducting components, namely main and gradient coils, should not be deformed at all and

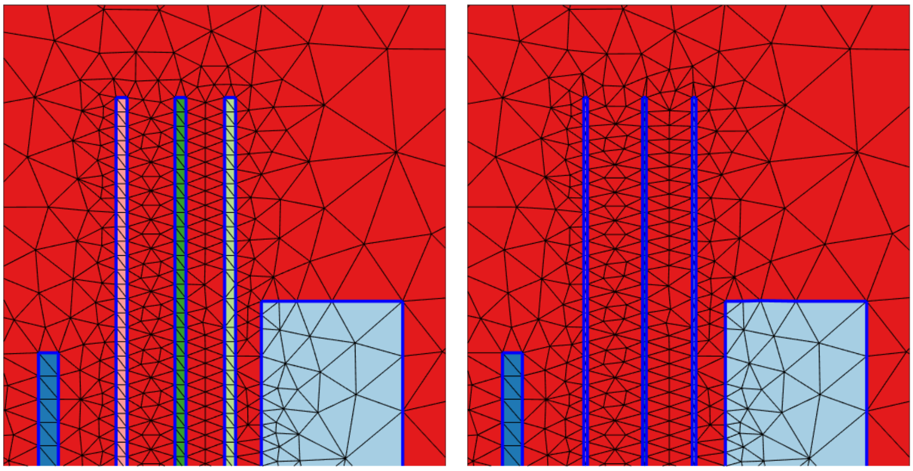

Figure 6.6: Mesh deformation of the test magnet problem; reference mesh with $h_0 = 3$ mm (left) and deformed mesh with $h = 1$ mm (right).

hence, the Dirichlet boundary conditions in these nodes have been all set equal to zero.

However, an explicit mapping such as (6.6) cannot be obtained for the full magnet geometry, see Figure 6.1c. Instead, an alternative approach will be now presented in order to obtain the required Dirichlet boundary conditions for an arbitrary MRI configuration. Note that this fact is key in the industrial context since several geometries, often with no closed-form mappings from a given referential configuration, are tested in the design stage.

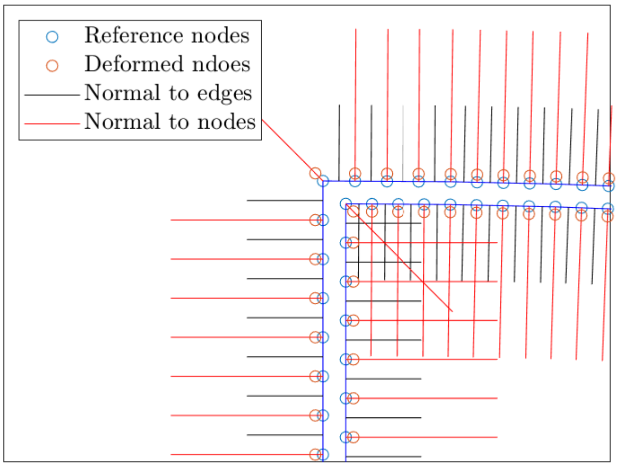

Figure 6.7: Mesh deformation of the full magnet problem; process of computing the required Dirichlet boundary conditions to deform mesh using linear elastic solver.

The alternative approach to obtain the Dirichlet boundary conditions consists first in computing the outward normal vector of each edge $\boldsymbol{n}^e$ in a conducting boundary from the reference mesh information as shown in Figure 6.7. After that, the normal at each node $\boldsymbol{n}^n$ is computed as

$$\boldsymbol{n}^n = \frac{\boldsymbol{n}^e + \boldsymbol{n}^{e+1}}{||\boldsymbol{n}^e + \boldsymbol{n}^{e+1}||} \tag{6.7}$$

where the edges e and $e+1$ share the node n, see Figure 6.7. Finally, the displacement field that has to be applied to each node in a smooth region $\boldsymbol{\mathcal{U}}^n$ and to each node in a sharp corner $\boldsymbol{\mathcal{U}}_c^n$ is computed using the normal to each node and the new h as

$$\boldsymbol{\mathcal{U}}^n = \frac{h - h_0}{2}\boldsymbol{n}^n, \quad \boldsymbol{\mathcal{U}}_c^n = \frac{h - h_0}{\sqrt{2}}\boldsymbol{n}^n, \tag{6.8}$$

which is the displacement field applied as Dirichlet boundary conditions in order to ensure that nodes are placed in the correct location, see red nodes in Figure 6.7, for the new geometry. The result of applying this method is presented in Figure 6.8, where the reference mesh ($h_0 = 3$ mm) is deformed for a new thickness $h = 5$ mm.

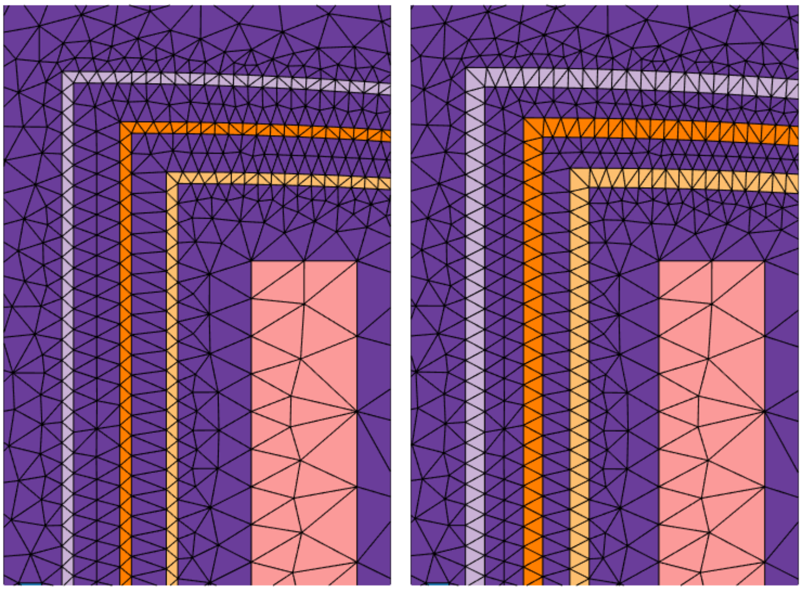

Figure 6.8: Mesh deformation of the full magnet problem; reference mesh with $h_0 = 3$ mm (left) and deformed mesh with $h = 5$ mm (right).

6.5 Higher-order PGD-projection technique

A high-order snapshot data tensor is generated by computing the value of the dissipated power $P^0_{\Omega^C}$ for several frequencies ω within the range of interest and for each sampled geometry, that is $P^0_{\Omega^C} = P^0_{\Omega^C}(\omega, h)$, where now the dependency on ω and h

is explicitly emphasised. Therefore, the tensor[5] $\boldsymbol{V}(P^0_{\Omega^C};\omega,h)$ is represented as

$$\boldsymbol{V}(P^0_{\Omega^C};\omega,h) = \begin{bmatrix} P^0_{\Omega^C}(\omega_1,h_1) & \cdots & P^0_{\Omega^C}(\omega_1,h_{N_h}) \\ \vdots & \ddots & \vdots \\ P^0_{\Omega^C}(\omega_{N_\omega},h_1) & \cdots & P^0_{\Omega^C}(\omega_{N_\omega},h_{N_h}) \end{bmatrix} \tag{6.9}$$

where N_ω is the total number of frequencies contained in the sweep and N_h the number of sampled geometries. Note that although $\boldsymbol{V}$ is indeed a second order tensor, it will increase its order when adding more parameters such as the conductivity γ and the strength of the static magnetic field B_0, namely $\boldsymbol{V}(P^0_{\Omega^C};\omega,\gamma,B_0,h)$.

This high-order tensor $\boldsymbol{V}$ can now be separated using the high-order PGD-projection algorithm presented in [42,48]. This algorithm is based on a least squares approximation and it returns a separable expression of the high-order data tensor. The aim is then to obtain an expression for $P^0_{\Omega^C}(\omega,h)$ as[6]

$$P^0_{\Omega^C}(\omega,h) \approx P^{0,N_V}_{\Omega^C}(\omega,h) := \sum_{n=1}^{N_V} G^n(\omega)T^n(h), \tag{6.10}$$

where $G^n(\omega)$ and $T^n(h)$ are the unknowns of the following minimisation problem

$$\min_{G^n,T^n} \Pi(G^1,\dots,G^{N_V};T^1,\dots,T^{N_V}) \quad \text{for } n=1,\dots,N_V, \tag{6.11}$$

with the functional $\Pi(G^1,\dots,G^{N_V};T^1,\dots,T^{N_V})$ defined as

$$\Pi(G^1,\dots,G^{N_V};T^1,\dots,T^{N_V}) := \frac{1}{2}\int_{\Omega_\omega}\int_{\Omega_h}\left[P^{0,N_V}_{\Omega^C}(\omega,h) - P^0_{\Omega^C}(\omega,h)\right]^2 \mathrm{d}\omega\,\mathrm{d}h, \tag{6.12}$$

in which both dimensions (space and frequency domains) are integrated. For more details about this approach the reader is referred to [42]. A slightly different approach is the one presented in [48], where the parametric space, in this case the frequency and thickness domains, are solved using a collocation method and hence, the functional $\Pi(G^1,\dots,G^{N_V};T^1,\dots,T^{N_V})$ that has to be minimised is

$$\Pi_{col}(G^1,\dots,G^{N_V};T^1,\dots,T^{N_V}) := \frac{1}{2}\sum_{i=1}^{N_\omega}\sum_{j=1}^{N_h}\left[P^{0,N_V}_{\Omega^C}(\omega_i,h_j) - P^0_{\Omega^C}(\omega_i,h_j)\right]^2 \Delta\omega_i\Delta h_j, \tag{6.13}$$

where $\Delta\omega_i$ and Δh_j are the integration weights corresponding to the frequency and thickness domains, respectively. The solution of the minimisation problem (6.11) involves the same machinery than in the PGD technique, see Chapter 3, where a Greedy algorithm is used to enrich the separable expression by modal addition.

---

[5] Note that only the tensor coefficients are displayed in (6.9). The representation of the actual tensor would require the basis corresponding to the two parametric domains Ω_ω and Ω_h.

[6] Note that the modal weights or amplitudes β^n are included in the parametric modes $G^n(\omega)$ and $T^n(h)$.

The collocation PGD-projection (6.13) is the approach followed in this thesis and consequently, the n^{th} accumulated functional is

$$\begin{aligned}\Pi^{n}_{col}(P^{0,n-1}_{\Omega^C}, G^n, T^n) = \frac{1}{2}\sum_{i=1}^{N_\omega}\sum_{j=1}^{N_h}\Big[G^n(\omega_i)T^n(h_j) + P^{0,n-1}_{\Omega^C}(\omega_i, h_j) \\ - P^{0}_{\Omega^C}(\omega_i, h_j)\Big]^2 \Delta\omega_i \Delta h_j,\end{aligned} \tag{6.14}$$

For the computation of each mode, a fixed point ADS is performed to compute converged values of $G^n(\omega)$ and $T^n(h)$ as

$$D\Pi_{col}(P^{0,n-1}_{\Omega^C}, G^n, T^n)[\delta G^n] = 0, \tag{6.15a}$$

$$D\Pi_{col}(P^{0,n-1}_{\Omega^C}, G^n, T^n)[\delta T^n] = 0, \tag{6.15b}$$

where the directional derivatives are computed as

$$\begin{aligned}D\Pi_{col}(P^{0,n-1}_{\Omega^C}, G^n, T^n)[\delta G^n] = \sum_{i=1}^{N_\omega}\sum_{j=1}^{N_h}\Big(G^n(\omega_i)T^n(h_j) + \sum_{m=1}^{n-1} G^m(\omega_i)T^m(h_j) \\ - P^{0}_{\Omega^C}(\omega_i, h_j)\Big)\big(\delta G^n(\omega_i)T^n(h_j)\big)\Delta\omega_i \Delta h_j,\end{aligned} \tag{6.16a}$$

$$\begin{aligned}D\Pi_{col}(P^{0,n-1}_{\Omega^C}, G^n, T^n)[\delta T^n] = \sum_{i=1}^{N_\omega}\sum_{j=1}^{N_h}\Big(G^n(\omega_i)T^n(h_j) + \sum_{m=1}^{n-1} G^m(\omega_i)T^m(h_j) \\ - P^{0}_{\Omega^C}(\omega_i, h_j)\Big)\big(G^n(\omega_i)\delta T^n(h_j)\big)\Delta\omega_i \Delta h_j,\end{aligned} \tag{6.16b}$$

from the functional definition (6.13).

6.6 Incorporation of thickness variations into the frequency-based PGD method

The collocation PGD-projection technique presented in Section 6.5 is now used in order to approximate the integrated quantities for an arbitrary h from the precomputed PGD solutions for a number N_h of sampled geometries. Note that, as a first attempt, the PGD formulation considered is the staggered frequency-based PGD formulation, which is obtained by restricting the parametric domain Ω_q to only the frequency domain of the high-dimensional electromagnetic and mechanic PGD formulations (5.7) and (5.12), respectively. Consequently, the solution fields $\mathcal{A}_\phi$ and $\boldsymbol{\mathcal{U}}$ are approximated in this section using the PGD framework as

$$\mathcal{A}^{h_i}_\phi(r,z,\omega) \approx \mathcal{A}^{N_A,h_i}_\phi(r,z,\omega) := \sum_{n=1}^{N_A} \beta^{n,h_i}_{\mathcal{A}_\phi} F^{n,h_i}_{\mathcal{A}_\phi}(r,z) G^{n,h_i}_{\mathcal{A}_\phi}(\omega), \tag{6.17a}$$

$$\boldsymbol{\mathcal{U}}^{h_i}(r,z,\omega) \approx \boldsymbol{\mathcal{U}}^{N_u,h_i}(r,z,\omega) := \sum_{n=1}^{N_u} \beta^{n,h_i}_{\boldsymbol{\mathcal{U}}} \boldsymbol{F}^{n,h_i}_{\boldsymbol{\mathcal{U}}}(r,z) G^{n,h_i}_{\boldsymbol{\mathcal{U}}}(\omega), \tag{6.17b}$$

for $i = 1, \dots, N_h$, where the dependency on a particular sampled geometry h_i is explicitly stated for each term. Each of the N_h PGD solutions are computed using the user-defined parameters presented in Table 6.2. In addition, since the PGD definitions (6.17) only considered frequency in the parametric domain, the other two parametric domains Ω_γ and Ω_{B_0} have been condensed into two constant values $\alpha_\gamma = 1$ and $B_0 = 1.5$ T.

Table 6.2: User-defined parameters used to compute the frequency-based PGD solutions for N_h sampled geometries. Three different MRI configurations considered, see Figure 6.1.

PGD parameters						Parametric domain		Spatial domain		
I_N^A	I_N^u	tol_N^A	tol_N^u	I_{FP}	tol_{FP}	h_ω	tol_ω^{split}	h_{Ω_p}	p	ξ
40	60	10^{-4}	10^{-5}	10	10^{-2}	$2 \cdot 10^{-5}$	20%	$5 \cdot 10^{-3}$	2	$5 \cdot 10^{-3}$

A first integrated quantity of interest used in this section is the L^2 norm of the displacement field in the 4K shield $|\boldsymbol{u}|_{L^2(\Omega^C_{4K})}$, as it has been observed that is the most challenging one of the three shields under consideration.

Table 6.3: User-defined parameters for the PGD-projection algorithm used to separate the high-order tensor coefficients.

Parameter	Value
I_N^V	80
I_{FP}^V	50
tol^V	10^{-8}

The strategy consists of first computing frequency sweeps in terms of displacements $|\boldsymbol{u}|_{L^2(\Omega^C_{4K})}(\omega, h)$ for each of the N_h sampled geometries. Subsequently, the high-order data tensor $\boldsymbol{V}(|\boldsymbol{u}|_{L^2(\Omega^C_{4K})}; \omega, h)$ can be constructed and separated as described in Section 6.5, obtaining a separable expression of the selected integrated quantity. Note that, although in Section 6.5 the formulation was presented for the dissipated power, the procedure remains identical for any integrated quantity. The PGD-projection algorithm requires three user-defined parameters that are presented in Table 6.3, where, following the same notation than in Chapters 4 and 5, I_N^V denotes the maximum number of Greedy algorithm iterations, I_{FP}^V is the maximum number of FP-ADS iterations within a mode and tol^V is the tolerance for both Greedy and ADS algorithms. The selection of the parameters presented in Table 6.3 ensures the convergence of the PGD-projection algorithm, which has been optimised in order to project all directions in a very efficient manner [42, 48]. The separable expression of $|\boldsymbol{u}|_{L^2(\Omega^C_{4K})}(\omega, h)$ provided by the PGD-projection is

$$|\boldsymbol{u}|_{L^2(\Omega^C_{4K})}(\omega, h) \approx |\boldsymbol{u}|^{N_V}_{L^2(\Omega^C_{4K})}(\omega, h) := \sum_{n=1}^{N_V} G^n(\omega) T^n(h), \tag{6.18}$$

which allows to generate an approximated frequency sweep for any h within the range considered. Again, notice that the modal weights are included in the parametric modes $G^n(\omega)$ and $T^n(h)$.

Table 6.4: Sampled points in Ω_h for different resolutions N_h. Quantity $h^{snap} = [h_{min} : \Delta h : h_{max}]$ defined through minimum h_{min} and maximum h_{max} thicknesses and spacing Δh.

N_h	h^{snap} [mm]
3	[1:2:5]
5	[1:1:5]
9	[1:0.5:5]
17	[1:0.25:5]

Figure 6.9 presents the first results for the test magnet problem when approximating a new geometry ($h = 1.6$ mm) from the N_h precomputed PGD solutions, where the selected values of N_h and its corresponding sampled points h^{snap} are presented in Table 6.4. Different values of N_h have been considered in order to study the effect of refining the number of sampled points in the thickness domain Ω_h. In this figure, the PGD-projection technique is compared to the linear interpolation approach and to the reference full order model solution, obtained by computing the direct problem for $h = 1.6$ mm, $\alpha_\gamma = 1$ and $B_0 = 1.5$ T. Note that the difference between PGD-projection and interpolation solutions are undistinguishable on this scale, which is the expected outcome since the interpolation is performed using the high-order tensor coefficients before applying the PGD-projection technique to separate it. Thus, the information contained in the separated expression (6.18) is the same than in the high-order tensor $\boldsymbol{V}(|\boldsymbol{\mathcal{U}}|_{L^2(\Omega^C_{4K})}; \omega, h)$,[7] resulting in an identical approximation (on the figure scale) with both interpolation and PGD-projection.

From the results in Figure 6.9, it can be observed how both approaches, PGD-projection and interpolation, become more accurate when increasing N_h, although no significant improvements are observed beyond $N_h = 9$. Hence, it can be concluded that, for this particular geometry, the smooth region is extremely well captured, as are the first few resonant modes. This region, which contains up to the first more dominant resonant modes, has been highlighted in the figure as the critical range for industry because the low frequency modes are known to be the more dominant ones [10]. As discussed in Sections 6.2.1 and 6.3, the highly non-linear behaviour of the high-frequency modes for small changes on the shields' thickness implies that any ROM technique will lack of accuracy within the high-frequency region. Moreover, the industrial interest when considering different shields' thickness is to determine the more dominant modes (located in the low-frequency region), whilst the entire frequency spectrum is later considered in further parametric studies where no changes in the geometry occur. The advocated approach has been shown to accurately represent the critical range for industry and, thus, it is of great interest for Siemens Healthineers.

---

[7] Provided that convergence is reached in the iterative process involved in the PGD-projection algorithm.

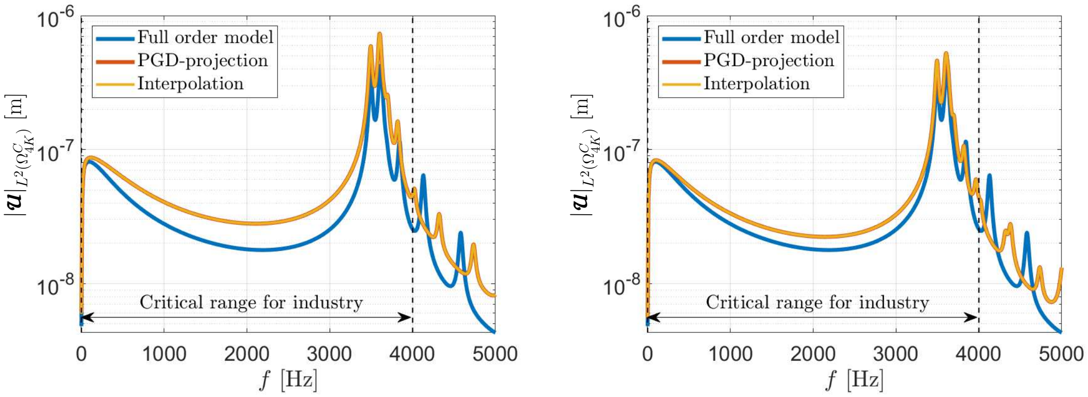

(a) $N_h = 3$ (b) $N_h = 5$

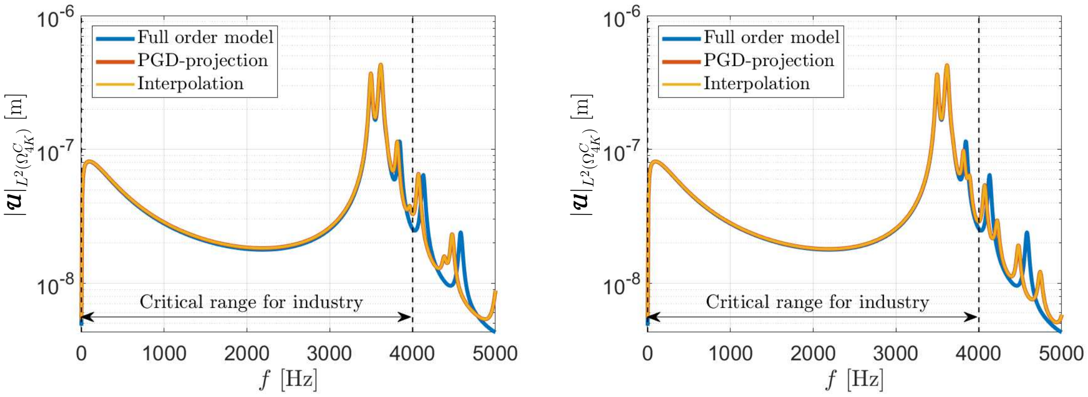

(c) $N_h = 9$ (d) $N_h = 17$

Figure 6.9: Test magnet problem; Approximation of the frequency sweep for a new geometry $h = 1.6$ mm using stored PGD solutions (6.17) for N_h sampled geometries with $\alpha_\gamma = 1$ and $B_0 = 1.5$ T. Plotting the L^2 norm of the displacement field $|\boldsymbol{u}|_{L^2(\Omega^C_{4K})}$ in the 4K shield.

However, robustness is key in industry and, thus, Siemens Healthineers proposed to validate these conclusions through two further problems: the test magnet 2 and the full magnet configurations, see Figure 6.1. These results are shown in Figure 6.10, where, based on the previous results, only the $N_h = 9$ sampling in Ω_h is considered. Again, the PGD-projection and interpolation approaches give identical results as expected, which are benchmarked against the reference full order model for $h = 1.6$ mm, $\alpha_\gamma = 1$ and $B_0 = 1.5$ T. More importantly, the same idea is observed for these two MRI configurations; a good level of accuracy is obtained for the smooth region and for the low frequency modes. Note that lower frequency modes are observed in the full magnet configuration and hence, the critical range for industry is significantly smaller for this problem. These results indicate that the conclusions of this section are applicable to the three industrially relevant configurations presented and consequently, the next step will be to consider the full high-dimensional staggered PGD, including the full parametric domain $\Omega_q = \Omega_\omega \times \Omega_\gamma \times \Omega_{B_0}$.

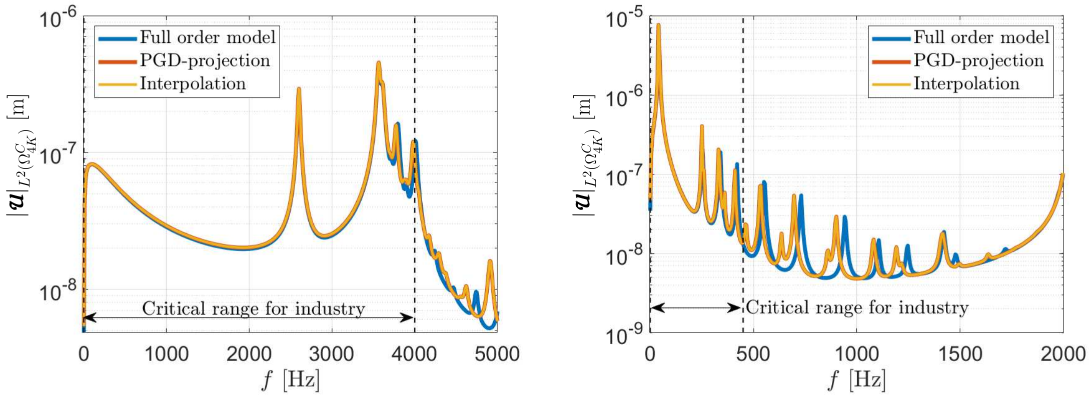

(a) Test magnet 2 (b) Full magnet

Figure 6.10: Approximation of the frequency sweep for a new geometry $h = 1.6$ mm, computing the L^2 norm of the displacement field $|\boldsymbol{u}|_{L^2(\Omega^C_{4K})}$ from the precomputed offline PGD solutions (6.17) for $N_h = 9$ with $\alpha_\gamma = 1$ and $B_0 = 1.5$ T. Displaying two different MRI configurations (test magnet 2 and full magnet).

6.7 Incorporation of thickness variations into the high-dimensional PGD method

The PGD-projection strategy has been observed to accurately represent the solution of the coupled magneto-mechanical problem within the critical range for industry, which includes the smooth frequency region together with the first few resonant modes. The results presented in Section 6.6 were obtained from the precomputed frequency-based PGD solutions for different thicknesses (6.17) and, hence, the main goal of this section is to extend the PGD-projection approach to the high-dimensional PGD formulation, see Chapter 5, and to consider the dissipated power (2.34), the most relevant integrated quantity during the design stage of MRI scanners. Section 6.6 has discussed why both PGD-projection and interpolation methods give the same results and, thus, this section will only consider the PGD-projection. The PGD-projection approach allows to decompose the high-order data tensor in several modes, which can be easily stored even in portable devices. On the other hand, the interpolation method would require the storage of the entire high-order data tensor and, consequently, this could potentially limit the use of portable devices due to memory requirements. Moreover, since section 6.6 has only considered the frequency in the parametric domain, the SVD technique could be used to decompose the high-order data tensor. However, this section considers a more general case with more than one variable in the parametric domain and, hence, the SVD is no longer applicable and its high-order version (the HOSVD) is known to loose the optimality of the standard SVD [48].

Following the same procedure than before, one PGD solution will be computed for each sampled thickness h_i as

$$\mathcal{A}_\phi^{h_i}(r,z,\omega) \approx \mathcal{A}_\phi^{N_A,h_i}(r,z,\omega) := \sum_{n=1}^{N_A} \beta_{\mathcal{A}_\phi}^{n,h_i} F_{\mathcal{A}_\phi}^{n}(r,z) G_{\mathcal{A}_\phi}^{n,h_i}(\omega) H_{\mathcal{A}_\phi}^{n,h_i}(\gamma), \tag{6.19a}$$

$$\boldsymbol{\mathcal{U}}^{h_i}(r,z,\omega) \approx \boldsymbol{\mathcal{U}}^{N_u,h_i}(r,z,\omega) := \sum_{n=1}^{N_u} \beta_{\boldsymbol{u}}^{n,h_i} \boldsymbol{F}_{\boldsymbol{u}}^{n,h_i}(r,z) G_{\boldsymbol{u}}^{n,h_i}(\omega) H_{\boldsymbol{u}}^{n,h_i}(\gamma) L_{\boldsymbol{u}}^{n,h_i}(B_0), \tag{6.19b}$$

for $i = 1, \ldots, N_h$. These PGD formulation was presented in Chapter 5 and consequently, the user-defined PGD parameters used were presented in Table 5.3 for the test magnet and test magnet 2 problems[8] and in Table 5.4 for the full magnet configuration. From the separable expressions in (6.19), the coefficients of the high-order tensor $\boldsymbol{V}(P^0_{\Omega^C_{4K}}; \omega, \gamma, B_0, h)$ can be efficiently computed with the fast online PGD stage, particularising each high-dimensional PGD solution for several values of ω, α_γ and B_0. Note that this high-order tensor is the extended version of (6.9), where the parametric domains Ω_γ and Ω_{B_0} are also included. The generation of these high-order tensor coefficients are obtained with the sampling defined in Table 6.5. Note that the frequency domain Ω_ω will vary depending on the problem, where the frequency sampling is [1:10:3000, 3005:5:5000] Hz for the test magnet and test magnet 2 problems, whilst for the full magnet configuration is [1:5:2000] Hz.

Table 6.5: Sampled points in the parametric domains for the generation of the high-order tensor coefficients

Parametric domain	Sampled points	Units
Ω_γ	[0.5:0.2:1.5]	-
Ω_{B_0}	[1:0.3:7]	T
Ω_h	[1:0.5:5]	mm

The PGD-projection algorithm is now used to obtain a separable expression of the dissipated power as

$$P^0_{\Omega^C_{4K}}(\omega,\gamma,B_0,h) \approx P^{0,N_V}_{\Omega^C_{4K}}(\omega,\gamma,B_0,h) := \sum_{n=1}^{N_V} G^n(\omega) H^n(\gamma) L^n(B_0) T^n(h), \tag{6.20}$$

where the modal weights or amplitudes are included in the parametric functions. As presented in Section 6.5, the collocation PGD-projection consists in the minimisation problem

$$\min_{G^n,H^n,L^n,T^n} \Pi(G^1,\ldots,G^{N_V}; H^1,\ldots,H^{N_V}; L^1,\ldots,L^{N_V}; T^1,\ldots,T^{N_V}), \tag{6.21}$$

---

[8] Note that the same parameters are used for both the test magnet and test magnet 2 problems due to the fact that is the exact same geometry with different Dirichlet boundary conditions.

for $n = 1, \ldots, N_V$, where now the unknowns are the set of parametric scalar functions $G^n(\omega)$, $H^n(\gamma)$, $L^n(B_0)$ and $T^n(h)$. Consequently, the functional using the collocation method is defined in the higher-dimensional space as

$$\Pi_{col}(G^1, \ldots, G^{N_V}; H^1, \ldots, H^{N_V}; L^1, \ldots, L^{N_V}; T^1, \ldots, T^{N_V}) :=$$
$$\frac{1}{2} \sum_{i=1}^{N_\omega} \sum_{j=1}^{N_\gamma} \sum_{k=1}^{N_{B_0}} \sum_{l=1}^{N_h} \left[P^{0,N_V}_{\Omega^C}(\omega_i, \gamma_j, B_{0,k}, h_l) - P^0_{\Omega^C}(\omega_i, \gamma_j, B_{0,k}, h_l) \right]^2 \Delta\omega_i \Delta\gamma_j \Delta B_{0,k} \Delta h_l. \tag{6.22}$$

The process in order to compute the separable expression for the dissipated power (6.20) remains identical to what has been presented in Section 6.5 but now extended to the higher-dimensional space. Moreover, the user-defined parameters for the PGD-projection algorithm are presented in Table 6.6, where the allowed maximum number of iterations of both the Greedy and ADS algorithms has been substantially increased due to the higher-dimensional space considered. However, the increase in computational cost is relatively small since the algorithm has been highly optimised for this purpose.

Table 6.6: User-defined parameters for the PGD-projection algorithm used to separate the high-order tensor coefficients.

Parameter	Value
I_N^V	600
I_{FP}^V	100
tol^V	10^{-8}

Once the separable expression for the dissipated power (6.20) is obtained, multiple-query evaluations can be performed in real-time. Similarly to the study presented in Section 6.6, the PGD-projection approach will be validated and assessed in terms of accuracy in the higher-dimensional space $\Omega_\omega \times \Omega_\gamma \times \Omega_{B_0} \times \Omega_h$ using the three MRI configurations shown in Figure 6.1. Figure 6.11 shows a comparison between the approximated PGD-projection solution (coloured curves) and the full order model (black curves on the background) for different not-sampled parameter combinations of (ω, γ, B_0, h). The three subfigures show the dissipated power in the three radiation shields (OVC, 77K and 4K). From the presented results, it is clear that a very good agreement is achieved within the critical range for industry, whereas some discrepancies are observed between the PGD-projection approximation and the full order (reference) solution as expected. In addition of the great accuracy achieved in the critical range for industry, the PGD-projection approach is also capable of accurately representing the mean trend of the solution within the high-frequency region. Note that all results shown in figures within this section have also been computed using the interpolation approach, obtaining the same results as discussed in Section 6.6.

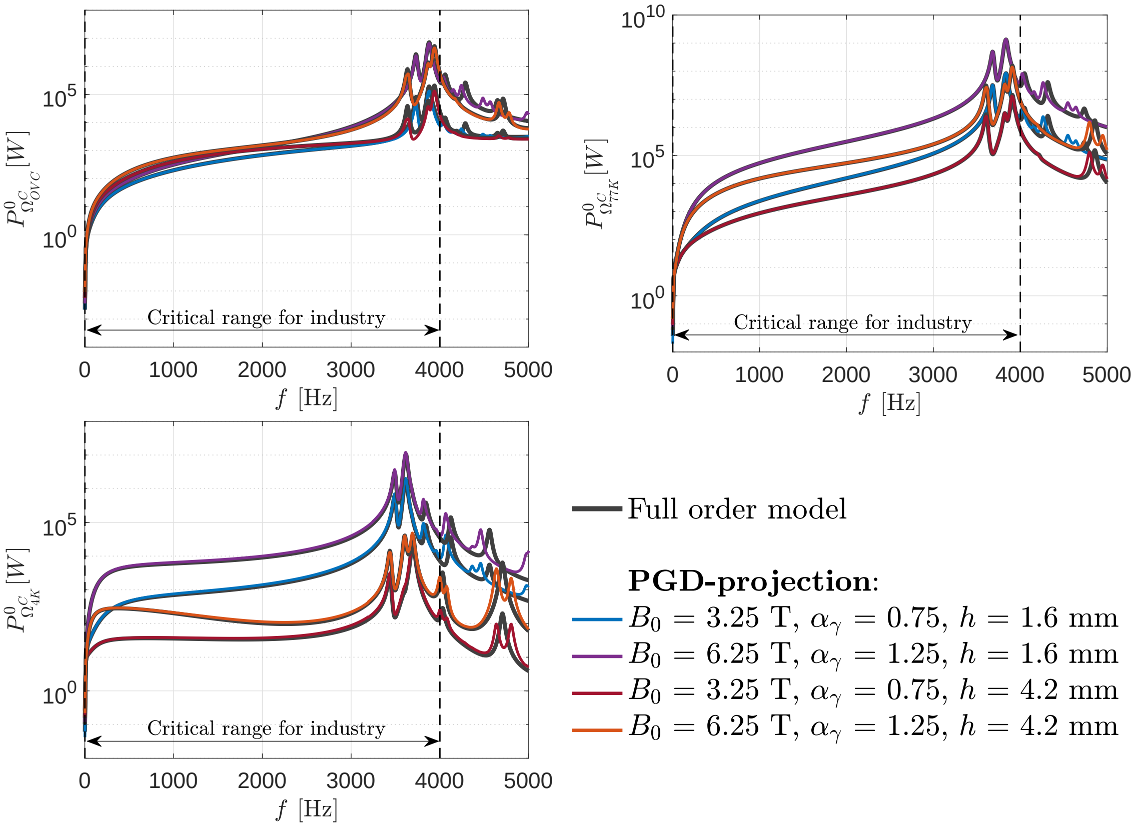

Figure 6.11: Test magnet problem; collocation PGD-projection approximation for different values of B_0, α_γ and h benchmarked against the full order model for the same parameter combination. Plotting the dissipated power for the three radiation shields (OVC, 77K and 4K).

Figure 6.12 shows the same study with the same parameter combinations but now considering the test magnet 2 geometry, where only the top edge of each shield is fixed and, thus, lower frequency modes appear. Again, a very good agreement is observed in the dissipated power for all three conducting shields within the critical range for industry, accurately capturing the smooth solution and the first more dominant resonant modes.

Finally, the results for the more challenging full magnet MRI configuration are presented in Figure 6.13. Similarly to the two other geometries, the dissipated power is evaluated in the three conducting components for different parameter combinations. It is interesting to see how the overall trend of the solution is well captured throughout the entire frequency spectrum and the singularities associated with resonant effects are very well captured within the critical range for industry. From the results in Figures 6.11, 6.12 and 6.13 it can be concluded that the PGD-projection is able to accurately resolve the solution of the MRI coupled magneto-mechanical problem for the first low resonant modes. As stated before, the low frequency modes are the more dominant ones, which constitute the critical range for industry. In addition, the consideration of three different MRI configurations suggest that the conclusions

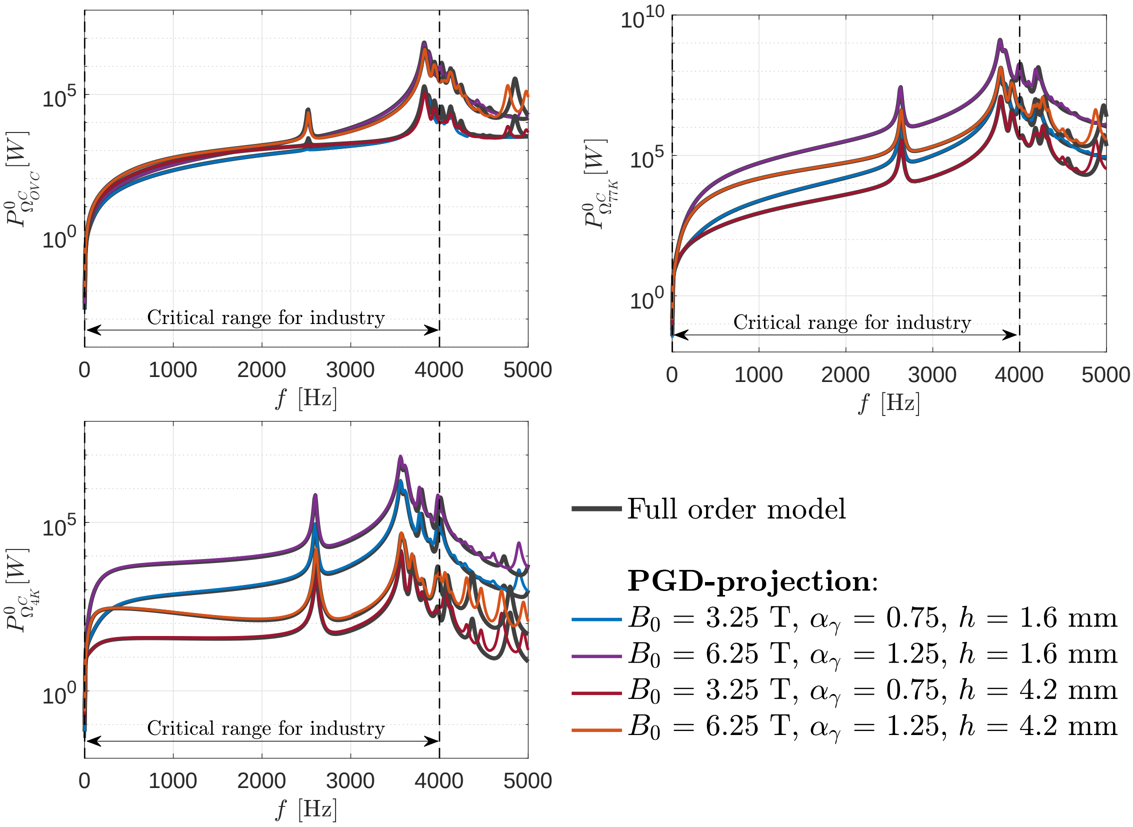

Figure 6.12: Test magnet 2 problem; collocation PGD-projection approximation for different values of B_0, α_γ and h benchmarked against the full order model for the same parameter combination. Plotting the dissipated power for the three radiation shields (OVC, 77K and 4K).

extracted from these results are applicable to the problems considered during the MRI design stage and that the PGD-projection approach is robust enough to be used in an industrial context.

6.8 Chapter summary

This chapter has presented an alternative approach in order to incorporate geometry changes into the PGD computational framework for coupled magneto-mechanical problems developed in previous chapters of this thesis. First, it has been studied how the solution evolves when considering different values of the shields' thickness. From this study it has been concluded that the high-frequency resonant modes behave in a highly non-linear manner, where small changes in h may change the location of the singularities associated with resonance and, more importantly, they can experience bifurcations. Consequently, any ROM technique will suffer when trying to approximate a numerical solution with such a non-linear behaviour.

Other techniques are based on incorporating directly geometrical parameters in the PGD formulation, although the axisymmetric description of the mathematical

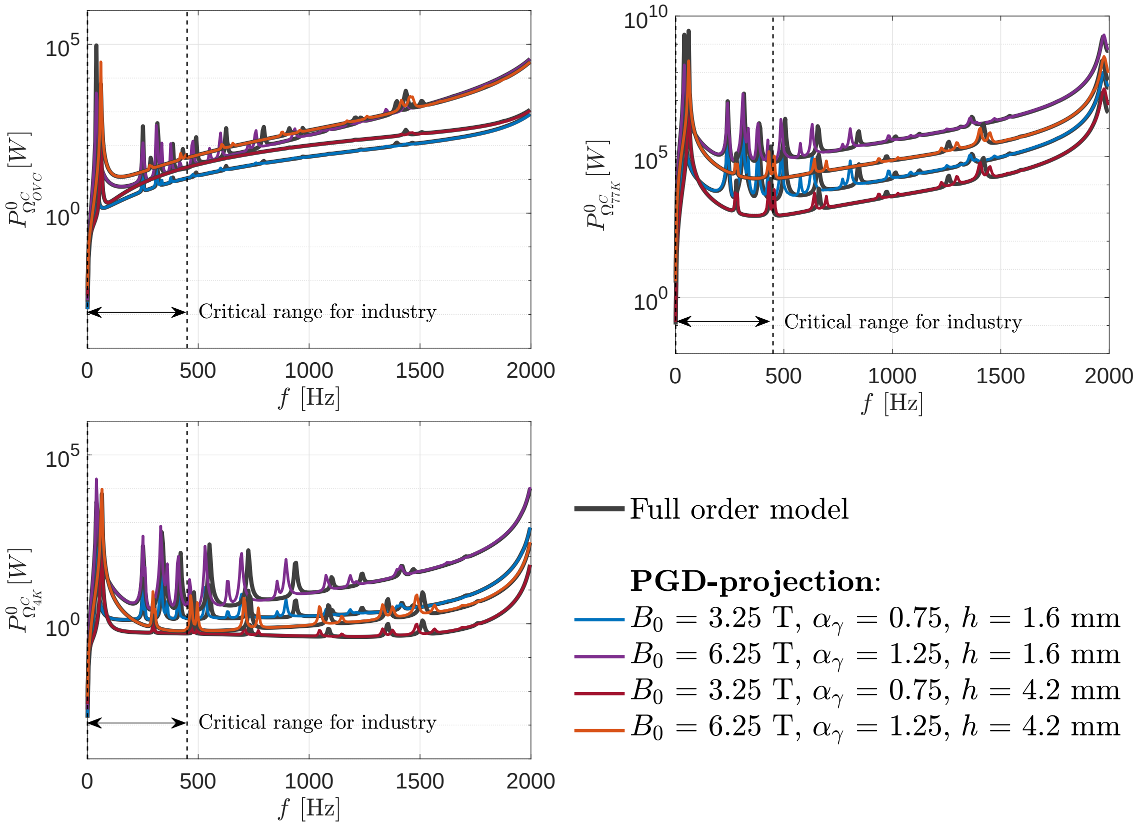

Figure 6.13: Full magnet problem; collocation PGD-projection approximation for different values of B_0, α_γ and h benchmarked against the full order model for the same parameter combination. Plotting the dissipated power for the three radiation shields (OVC, 77K and 4K).

operators and the scaling of the fields lead to a cumbersome formulation for this particular problem. Instead, the PGD-projection technique represents a good compromise in terms of efficiency and accuracy, obtaining separable expressions of the relevant integrated quantities for industry and allowing for real-time multiple-query input/output evaluations of several material and geometric parameters.

Chapter 7

Concluding remarks

7.1 Conclusions

The need for computational simulations in the context of MRI scanner design as well as the industry requirements and needs have been stated in Chapter 1. The recently introduced Reduced Order Modelling (ROM) techniques are a sensible approach to reduce the large number of numerical simulations required for the various design iterations during the manufacturing workflow. As such, the main goal of this thesis has been the development of a robust PGD computational framework for coupled magneto-mechanical problems, working towards the optimisation of the design stage of MRI scanners. This end goal has been achieved through the objectives described in Section 1.4, which have been addressed throughout the chapters of this thesis. As a summary, the conclusions of each chapter are presented in this section.

- ***Chapter 2: Full order model.*** This chapter started with a brief presentation of the full order model, consisting in a coupled magneto-mechanical problem developed in [32,33,36] which has become the starting point of the thesis. The fully non-linear coupled system has been presented and then a series of assumptions have been applied in order to derive the linearised time-harmonic problem in an axisymmetric setting. This chapter also contains a description of two industrially relevant MRI configurations of great interest in the MRI community, together with a set of numerical simulations that have helped to understand the numerical difficulties and challenges specific to the problem under consideration. This chapter has addressed the objective "*To develop a coupled magneto-mechanical formulation in a Lagrangian setting from an existing axisymmetric finite element framework*".

- ***Chapter 3: General PGD formulation.*** This chapter presented a detailed description of a generic PGD computational framework for the problem at hand which considers the axisymmetric two-dimensional (r, z) space Ω_p and a generic d-dimensional parametric space $\Omega_q = \Omega_{w_1} \times \cdots \times \Omega_{w_d}$ as the domains within which the high-dimensional parametric solution is sought for. Some technical aspects of the PGD technique have been also discussed, such as the incorporation of non-homogeneous Dirichlet boundary conditions, the scaling of the PGD modes and the two convergence criteria used for the iterative algorithms involved in the offline stage. The online PGD stage, which consists in a fast evaluation of the precomputed high-dimensional parametric solution, is also described in this chapter.

- ***Chapter 4: Monolithic frequency-based PGD technique.*** The PGD formulation presented in Chapter 3 is applied to the coupled MRI magneto-mechanical problem described in Chapter 2. This general PGD framework has been particularised for the high-dimensional space $\Omega_p \times \Omega_q$, where the parametric space only accounts for variations of the external exciting frequency $\Omega_q = \Omega_\omega$. This allows frequency spectra for kinetic energy and dissipated power to be efficiently queried in the online stage, which is a study of great interest to industry to help speed up the design phase of the next generation of MRI scanners (>7 T). Moreover, a regularised-adaptive strategy is proposed in order to circumvent the numerical singularities associated with the resonance phenomenon, resulting in an increased robustness and accuracy of the PGD approximation. Finally, a user-friendly app has been presented in Appendix E to show the potential of the PGD method in the online stage, enabling real-time simulations for non-expert users. The addressed objectives within this chapter are "*To develop a frequency-based PGD formulation for coupled magneto-mechanical problems*", "*To propose a regularised-adaptive strategy in order to increase the PGD accuracy and robustness*" and "*To develop a graphical user interface for the online PGD stage that can be used in the industry environment*".

- ***Chapter 5: Staggered high-dimensional PGD technique.*** This chapter presented an extension of the frequency-based PGD approach presented in Chapter 4 to a higher parametric domain $\Omega_q = \Omega_\omega \times \Omega_\gamma \times \Omega_{B_0}$, incorporating the electrical conductivity of the conducting components γ and the strength of the static magnetic field B_0. From the presented results, it has been observed that the high-dimensional PGD technique can drastically optimise the multiple-query online stage without sacrificing accuracy. In addition, the staggered nature of the underlying magneto-mechanical problem has been exploited and it has been concluded that this approach has led to a more efficient and robust algorithm. This chapter also contains a comparison in terms of the electromagnetic output between the developed *a prori* PGD method and an *a posteriori* POD method, see [49]. This study concludes that a massive time reduction can be obtained with both ROM methods, although only the PGD technique is able to find an explicit expression of the solution field of the entire magneto-mechanical problem. This chapter addresses the objectives "*To extend the frequency-based PGD formulation to a higher-dimensional problem including now material parameters*", "*To exploit the staggered nature of the* *coupled problem at hand*" and "*To assess and compare the a priori PGD and the a posteriori POD methods against the full order model*".

- ***Chapter 6: Integration of geometric parameters into the PGD methodology.*** This chapter studied the effect that altering the thickness of the radiation shields has in the integrated quantities of interest (i.e. kinetic energy and dissipated power) used in the design stage of MRI scanners. It has been shown that high-frequency modes may experience a highly non-linear behaviour (i.e. bifurcation) and, thus, the challenges of any ROM technique when attempting their capturing have been motivated. A collocation PGD-projection strategy has been presented in order to account for parametric variations of the shields' thickness without having to include it directly into the PGD formulation. This approach has been found to be very efficient from the industrial standpoint, capturing the overall trend of the response spectra together with the first few resonant modes very accurately. This region of interest has been named the critical range for industry, since low frequency modes are the most dominant ones and, thus, the most critical to be found in the design stage. The proposed PGD-projection technique allows then for real-time multiple-query input/output evaluations of several material parameters and thickness variations, addressing the last objective of the thesis "*To include geometrical changes in the computational domain within the developed PGD framework*".

7.2 Further work

The research carried out during this project opens the door to other lines of research that would be of interest to the scientific community and, hence, this section provides advice on the specific topics that could be studied next. Since this is a project in close collaboration with Siemens Healthineers, the industrial point of view has always been taken into account and, consequently, the suggested future work will include both "further research developments" and "transfer to industry developments".

7.2.1 Further research developments

From the academic research point of view, several topics of interest can be identified after the research carried out in this thesis. These are listed below.

- Implement the PGD formulation for coupled magneto-mechanical problems in a **3D setting**. The axisymmetric assumption is used by Siemens Healthineers in order to reduce the computational cost during the design stage. However, 3D solvers for this coupled problem have been developed, see [77], and thus, the PGD technique could be tested in non axisymmetrical MRI configurations. This would allow for more realistic solutions by considering non-axisymmetric gradient coil effects.

- Further studies on **including geometry** changes within the PGD framework. As motivated in Section 6.1, introducing geometrical parameters in the axisymmetric coupled magneto-mechanical equations leads to a very cumbersome formulation due to the axisymmetric description of the mathematical operators and the scaling of the solution fields. However, further research could aim to find simplifications and geometrical approximations, for instance, the consideration of very thin conducting components. On the other hand, the presented PGD-projection approach could also be further studied, for instance, by using a canonic basis together with the PGD-projection algorithm, avoiding the generation of the high-order data tensor. Moreover, other integrated quantities of interest could be also assessed.

- Study the viability of **Machine Learning techniques and Neural Networks algorithms** [96] as an alternative/complement to ROM in order to obtain fast approximations of the solution fields of the coupled magneto-mechanical presented. In [97], the accuracy of the POD technique is enhanced by making use of neural network in order to interpolate the POD coefficients. Also, data-driven approaches within Machine Learning [98] use numerical data in order to train the model (unsupervised training). Consequently, PGD could potentially optimise the training cost of Machine Learning algorithms by exploiting the speed of evaluations in the online PGD stage.

- Consideration of **thermal effects**. As mentioned in Chapter 1, the thermal energy transfer from the coils to the helium vessel (4K radiation shield) plays an important role during the design stage, aiming to minimise helium boil-off [16]. Also, a thermo-magneto-mechanical formulation [99] would allow for the modelling of quenching in conducting components [100].

- Addition of **acoustics** in the magneto-mechanical formulation. Acoustics effects were considered for this problem in [10, 32, 33]. Consequently, it would be interesting to introduce this third physics (in a staggered manner) into the PGD formulation to model the acoustic field generated in a MRI scanner in a parametric formulation.

- **Uncertainty** quantification. Techniques to estimate the uncertainty of a finite element based output require a large number of finite element solutions [101] and hence, fast PGD evaluations in the online stage could be used to optimise this purpose.

- Bounding **error estimators**. Techniques to estimate both global error and error on outputs of interest have been used in the PGD context [102] and, thus, a suggested line of research is to study the incorporation of existing or novel error estimation techniques within the developed PGD framework.

7.2.2 Transfer to industry developments

Research developments accomplished throughout this thesis are relevant for the industrial partner of this project, Siemens Healthineers. However, further work is required in order to ensure that the developed PGD methodology can be safely transferred into an industrial context. Specifically,

- Consider a more realistic MRI configuration where each conducting component has different material and geometric parameters. This is an extension of the developed PGD formulation, which only considers single scalars α_γ and h in order to modify the conductivity and the thickness of all three radiation shields, respectively.
- Code optimisation. The developed Matlab code should be translated into a more efficient programming language and several functions and routines could be optimised through the use of encapsulating object-oriented programming. Moreover, PGD compression techniques [42,48] could be used within the Greedy algorithm in order to compress the amount of information contained in the computed PGD modes and speed up the calculations.
- Implementation of the developed PGD formulation in a robust and well-maintained platform. Most companies use either commercial or open-source software and hence, the implementation of a fully tested PGD package in their preferred platform is a must.

Appendices

Appendix A

Electromagnetic-Proper Orthogonal Decomposition (EM-POD) methodology

This appendix presents an alternative to the PGD technique described in this thesis, an *a posteriori* ROM technique which, by also exploiting the staggered nature of the underlying coupled equations, combines the POD method for electromagnetics and the full order model for mechanics (referred to as EM-POD hereafter)[1]. The methodology, in addition to be used for benchmarking purposes, will help draw some meaningful conclusions in terms of computational effort when comparing it against the staggered PGD method. Whilst in [49], this EM-POD methodology was applied to three-dimensional configurations, this is here suitably adapted to account for axisymmetric configurations.

The fundamental idea behind the EM-POD methodology relies on the application of the POD method to the electromagnetic problem in order to obtain an approximation $\mathcal{A}_\phi^{POD}(r,z,\omega,\gamma)$ to $\mathcal{A}_\phi(r,z,\omega,\gamma)$ and then use this as an input source to the mechanical full order problem to compute $\boldsymbol{\mathcal{U}}(r,z,\omega,\gamma,B_0)$.[2] Before that, the problem is first discretised in space using a typical FEM expansion as

$$\mathcal{A}_\phi(r,z,\omega,\gamma) \approx \sum_{i=1}^{Q_A} N_i(r,z)\mathcal{A}_i(\omega,\gamma), \qquad \boldsymbol{\mathcal{U}}(r,z,\omega,\gamma,B_0) \approx \sum_{i=1}^{Q_u} N_i(r,z)\boldsymbol{\mathcal{U}}_i(\omega,\gamma,B_0), \tag{A.1}$$

where Q_A and Q_u are the number of electromagnetic and mechanical degrees of freedom, respectively, and N_i denote typical hierarchic H^1 conforming basis functions, which can be rewritten in matrix notation as

$$\mathcal{A}_\phi(r,z,\omega,\gamma) \approx \mathbf{N}^{\mathrm{A}}(r,z)\boldsymbol{\mathcal{A}}_\phi(\omega,\gamma), \quad \boldsymbol{\mathcal{U}}(r,z,\omega,\gamma,B_0) \approx \mathbf{N}^{\mathrm{u}}(r,z)\boldsymbol{\mathcal{U}}(\omega,\gamma,B_0), \tag{A.2}$$

---

[1] Note that this methodology was recently developed in [49] under the name "combined POD-full order model" approach.

[2] For a more generic description of the POD method applied to an arbitrary number of parameters, namely $\mathcal{A}_\phi(r,z,w_1,\dots,w_d)$ and $\boldsymbol{\mathcal{U}}(r,z,w_1,\dots,w_d)$, the reader is referred to [49].

where the discrete vectors of coefficients $\boldsymbol{\mathcal{A}}_\phi(\omega,\gamma)$, $\boldsymbol{\mathcal{U}}(\omega,\gamma,B_0)$ have been already presented and the matrices $\mathbf{N}^{\mathrm{A}}(r,z)$ and $\mathbf{N}^{\mathrm{u}}(r,z)$ are defined as

$$\mathbf{N}^{\mathrm{A}}(r,z) := \left[N_1 \dots N_{Q_A}\right], \tag{A.3a}$$

$$\mathbf{N}^{\mathrm{u}}(r,z) := \left[\mathbf{n}_1^{\mathrm{u}} \dots \mathbf{n}_{Q_u}^{\mathrm{u}}\right] = \begin{bmatrix} N_1 & 0 & \dots & N_{Q_u} & 0 \\ 0 & N_1 & \dots & 0 & N_{Q_u} \end{bmatrix}. \tag{A.3b}$$

At this point, POD is applied to approximate $\boldsymbol{\mathcal{A}}_\phi(\omega,\gamma)$, which is carried out by means of the method of snapshots [46, 50]. First, the vector $\mathbf{w}$ is defined as $\mathbf{w} := (\mathbf{w}_1 \dots \mathbf{w}_{N_s})$, which contains N_s parameter sets (combinations of different parameter values ω and γ). Then, a matrix of N_s snapshots[3] $\mathbf{D} \in \mathbb{C}^{Q_A \times N_s}$ is built as

$$\mathbf{D} := \left[\boldsymbol{\mathcal{A}}_\phi(\mathbf{w}_1) \dots \boldsymbol{\mathcal{A}}_\phi(\mathbf{w}_{N_s})\right], \tag{A.4}$$

where $\boldsymbol{\mathcal{A}}_\phi(\mathbf{w}_j)$ is a single snapshot obtained for the parameter set $\mathbf{w}_j$. Then, a TSVD [103, 104] is applied in order to obtain a low rank approximation to the snapshot matrix as

$$\mathbf{D} \approx \mathbf{D}^M := \sum_{k=1}^{M} \mathbf{h}_k \sigma_k \overline{\mathbf{g}}_k^T = \mathbf{H}^M \boldsymbol{\Sigma}^M \left(\overline{\mathbf{G}}^M\right)^T, \tag{A.5}$$

where $\mathbf{H}^M = [\mathbf{h}_1 \dots \mathbf{h}_M] \in \mathbb{C}^{Q_A \times M}$ is a matrix containing the first M left singular vectors of $\mathbf{D}$, $\mathbf{G}^M = [\mathbf{g}_1 \dots \mathbf{g}_M] \in \mathbb{C}^{N_s \times M}$ is the matrix of right singular vectors and $\boldsymbol{\Sigma}^M = \mathrm{diag}(\sigma_1 \dots \sigma_M) \in \mathbb{R}^{M \times M}$ is a diagonal matrix containing the first M singular values, which are sorted in decreasing order. Note that the choice here is to consider the physical space (r,z) and the parametric space (ω,γ) as the two dimensions that have to be separated, so the TSVD can be applied. Otherwise, the high-order version of the TSVD (High-Order Singular Value Decomposition HOSVD [21,105]) would be required to separate more than two dimensions, loosing the known optimality of the TSVD [48]. The snapshot calculation and the TSVD constitute the so-called offline stage of the POD algorithm as presented in the left box in Figure A.1, where the EM-POD algorithm is summarised using a flow chart. In this particular problem, the affine decomposition structure of the electromagnetic problem (2.23) is used to perform most of the assembly (the non-parameter dependent assembly) as part of the offline stage[4], resulting in a much faster online POD stage.

Subsequently, at the online stage, either interpolation based POD (PODI) [51, 106, 107] or projection based POD (PODP or POD-Galerkin) [108–110] can be considered in order to obtain $\boldsymbol{\mathcal{A}}_\phi(\omega,\gamma)$ for any ω and γ. In this case, we explore the use of PODP and $\boldsymbol{\mathcal{A}}_\phi(\omega,\gamma)$ is approximated as a linear combination of above left singular vectors as

$$\boldsymbol{\mathcal{A}}_\phi(\omega,\gamma) \approx \boldsymbol{\mathcal{A}}_\phi^{\mathrm{POD}}(\omega,\gamma) := \sum_{k=1}^{M} \mathbf{h}_k \mathrm{g}_k^{\mathrm{P}}(\omega,\gamma) = \mathbf{H}^M \mathbf{g}^P(\omega,\gamma), \tag{A.6}$$

---

[3] Typically, the snapshots are obtained after solving the so-called full order model.

[4] In most problems, the matrix assembly has to be carried out within the online stage making this POD stage less computationally efficient.

where $\mathbf{h}_k$ represents the k-th column of the $\mathbf{H}^M$ matrix and the parametric mode vector $\mathbf{g}^P(\omega, \gamma)$ $\big($of coefficients $\mathrm{g}_k^{\mathrm{P}}(\omega, \gamma)\big)$ is yet unknown and must be computed for each ω and γ. The computation of the unknown vector $\mathbf{g}^P(\omega, \gamma)$ is obtained from the solution of the weak form (2.23) by using a Galerkin approximation with $(A.2)_a$ and (A.6). This leads to the solution of a reduced system of size $M \times M$ as shown in Figure A.1. This must be applied N_o times to obtain the solution for all the parameters sets of interest $(\omega_1, \gamma_1), \ldots, (\omega_{N_o}, \gamma_{N_o})$.

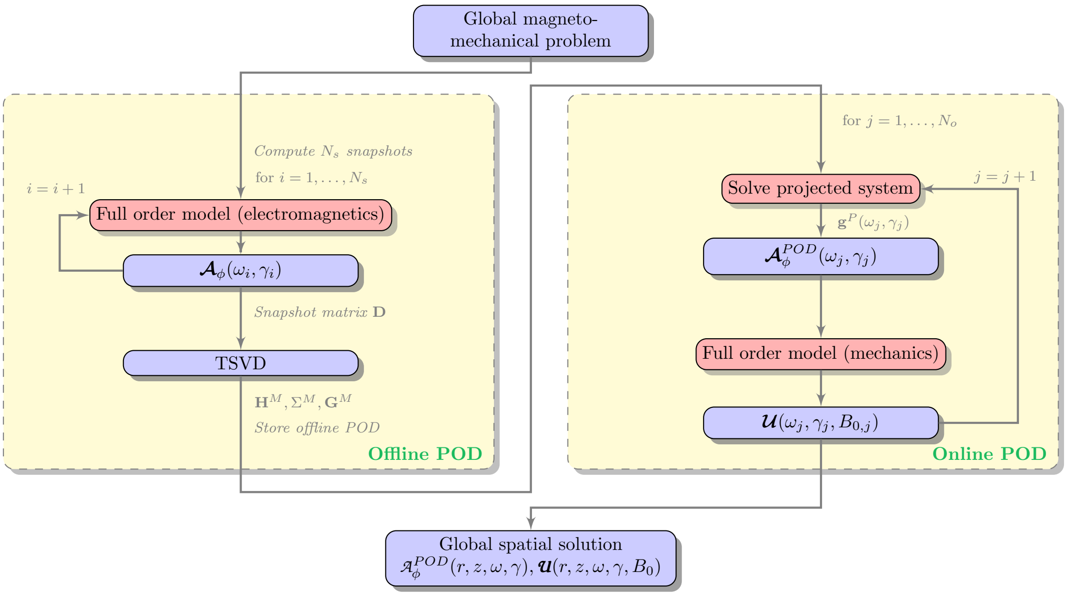
Global magneto-mechanical problem
Compute N_s snapshots
for $i = 1, \ldots, N_s$
$i = i + 1$
Full order model (electromagnetics)
$\boldsymbol{\mathcal{A}}_\phi(\omega_i, \gamma_i)$
Snapshot matrix $\mathbf{D}$
TSVD
$\mathbf{H}^M, \Sigma^M, \mathbf{G}^M$
Store offline POD
Offline POD
for $j = 1, \ldots, N_o$
Solve projected system
$j = j + 1$
$\mathbf{g}^P(\omega_j, \gamma_j)$
$\boldsymbol{\mathcal{A}}_\phi^{POD}(\omega_j, \gamma_j)$
Full order model (mechanics)
$\boldsymbol{\mathcal{U}}(\omega_j, \gamma_j, B_{0,j})$
Online POD
Global spatial solution
$\mathcal{A}_\phi^{POD}(r, z, \omega, \gamma), \boldsymbol{\mathcal{U}}(r, z, \omega, \gamma, B_0)$

Figure A.1: Flow chart algorithm; description of the EM-POD technique.

Once the solution $\mathcal{A}_\phi^{POD}(r, z, \omega, \gamma)$ is obtained, this is used as a source term for the mechanical full order solver [49]. The online stage is graphically presented in the right box of Figure A.1. For further details about the EM-POD technique and its performance in the context of three-dimensional configurations, the reader is referred to [49].

Appendix B

One-dimensional mortar integral treatment

Some of the terms featuring in (5.31) require the computation of an integral that can potentially involve different non-matching one-dimensional meshes. In the context of friction and contact-impact problems [111–113], this type of integrals are known as mortar integrals and this appendix provides a detailed explanation of the implementation for the one-dimensional case used in this thesis, see Chapter 5. As an example, let us consider the evaluation of $g_0^{uA,[m]}$. As it appears in (5.32), the definition of this coefficient is

$$g_{0,s}^{u,[m]} := G_0^u(G_{\mathcal{A}_\phi}^{[m]}, g_{\boldsymbol{u}}) = \bar{\mathbf{g}}_{\boldsymbol{u}}^T \mathbf{G}_0^u \mathbf{G}_{\mathcal{A}_\phi}^{[m]}, \tag{B.1}$$

where the product $\bar{\mathbf{g}}_{\boldsymbol{u}}^T \mathbf{G}_0^u \mathbf{G}_{\mathcal{A}_\phi}^{[m]}$ may require the assembly of a rectangular mass type matrix, allowing the use of different meshes with different number of degrees of freedom for both electromagnetics and mechanics fields. Note that for the case where the electromagnetic parametric mesh coincides with the mechanical one, then $\mathbf{G}_0^u = \mathbf{G}_0^A$ which coincides with the standard one-dimensional consistent mass matrix for both physics. In general,

$$G_0^u(G_{\mathcal{A}_\phi}^{[m]}, g_{\boldsymbol{u}}) = \int_{\Omega_\omega^u} G_{\mathcal{A}_\phi}^{[m]}(\omega) \bar{g}_{\boldsymbol{u}}(\omega) \, \mathrm{d}\omega, \tag{B.2}$$

where the two integrands are discretised as

$$g_{\boldsymbol{u}} = \sum_{a=1}^{Q_\omega^u} N_{\boldsymbol{u}}^a g_{\boldsymbol{u}}^a, \quad G_{\mathcal{A}_\phi}^{[m]} = \sum_{b=1}^{Q_\omega^A} N_{\mathcal{A}_\phi}^b G_{\mathcal{A}_\phi}^{b,[m]}, \tag{B.3}$$

with Q_ω^u and Q_ω^A being the total number of degrees of freedom of the frequency domain for mechanics and electromagnetics, respectively. The integral can then be written as

$$G_0^u(G_{\mathcal{A}_\phi}^{[m]}, g_{\boldsymbol{u}}) = \sum_{a=1}^{Q_\omega^u} \sum_{b=1}^{Q_\omega^A} \bar{g}_{\boldsymbol{u}}^a \underbrace{\int_{\Omega_\omega^{u,(e)}} N_{\boldsymbol{u}}^a N_{\mathcal{A}_\phi}^b \, \mathrm{d}\omega}_{=m_{ab}} \; G_{\mathcal{A}_\phi}^{b,[m]}, \tag{B.4}$$

and, thus, a particular ab entry of $\mathbf{G}_0^{u,(e)}$ is computed using a Gaussian quadrature as

$$m_{ab} = \sum_{i=1}^{Q_{gp}} N_{\boldsymbol{u}}^a(\zeta_i) N_{\mathcal{A}_\phi}^b(\zeta_i) J_i w_i, \tag{B.5}$$

where ζ_i, J_i and w_i are the position of the Gauss points, the Jacobian and weights of the Gauss points, respectively, which are all related to the mechanical frequency domain since the integral is over Ω_ω^u. The computation of this term require careful consideration in the case of non-matching meshes in the parametric domain (for the electromagnetics and mechanical physics), see Figure B.1. For the simple one-dimensional case, the necessary steps are summarised in Algorithm 1.

Algorithm 1 One-dimensional mortar integral computation

```
for e = 1 : $N_{el}$ do                                          ▷ Loop on elements
    for i = 1 : $N_{gp}$ do                                       ▷ Loop on Gauss points
        Evaluate $N_{\boldsymbol{u}}^a(\zeta_i)$ in $\Omega_\omega^u$ (standard in FEM)
        Locate $\zeta_i$ in $\Omega_\omega^A$. Find position and element in $\Omega_\omega^A$
        Evaluate $N_{\mathcal{A}_\phi}^b(\zeta_i)$ in $\Omega_\omega^A$ (not standard in FEM since $\zeta_i$ is not a Gauss point in $\Omega_\omega^A$)
        Compute entry $m_{ab}$ of elemental matrix $\mathbf{G}_0^{u,(e)}$
    end for
    Assemble elemental contribution to global matrix $\mathbf{G}_0^u$
end for
```

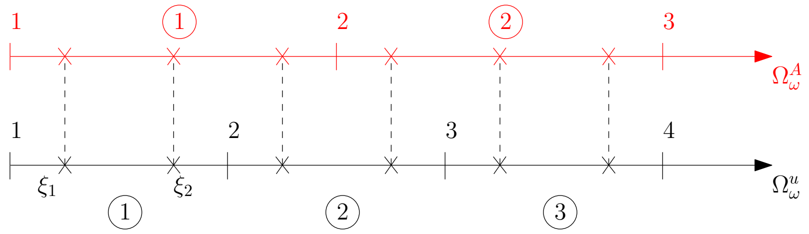

Figure B.1: Representation of two non-matching one-dimensional meshes.

Using Figure B.1 as an example of two different one-dimensional meshes, the three elemental matrices in Ω_ω^u have the following structure

$$\mathbf{G}_0^{u,(1)} = \begin{bmatrix} m_{11} & m_{12} \\ m_{21} & m_{22} \end{bmatrix}, \quad \mathbf{G}_0^{u,(2)} = \begin{bmatrix} m_{21} & m_{22} & 0 \\ 0 & m_{32} & m_{33} \end{bmatrix}, \quad \mathbf{G}_0^{u,(3)} = \begin{bmatrix} m_{32} & m_{33} \\ m_{42} & m_{43} \end{bmatrix}, \tag{B.6}$$

which are assembled in the global matrix as

$$\mathbf{G}_0^u = \begin{bmatrix} m_{11} & m_{12} & 0 \\ m_{21} & m_{22} & 0 \\ 0 & m_{32} & m_{33} \\ 0 & m_{42} & m_{43} \end{bmatrix}. \tag{B.7}$$

Appendix C

Efficient computation of integrated quantities

The computation of the integrated quantities stated in (2.34) can be optimised by incorporating some of the calculations into the offline stage of the PGD technique. The aim of this appendix is to briefly formulate these computations in order to reduce the computational effort in the online stage.

C.1 Integration of the output power

As an example, this section presents how to efficiently compute the dissipated power. Other integrated quantities, such as the kinetic energy and the L^2 norm of a certain field, are computed following an analogous procedure.

Following the general notation used in Chapter 3, the dissipated power (2.34) is computed in the axisymmetric setting as

$$P^0_{\Omega^C_p}(w_1, \dots, w_d) = \gamma\pi \int_{\Omega^C_p} |\boldsymbol{\mathfrak{E}}^{AC}|^2 r \,\mathrm{d}\Omega, \tag{C.1}$$

where now the integration is performed over the axisymmetric conducting component Ω^C_p. The parameter dependency is explicitly written only in the left side of the equal sign for the sake of clarity. Note that since only one shield is considered at a time, the shield conductivity γ can be understood as a constant outside the integral. By using the expression of the electric field intensity

$$\boldsymbol{\mathfrak{E}}^{AC}(r, z, w_1, \dots, w_d) = \mathrm{i}\omega(\boldsymbol{B}^{DC}_0 \times \boldsymbol{\mathfrak{U}}^{AC} - \boldsymbol{\mathfrak{A}}^{AC}), \tag{C.2}$$

the dissipated power can be written as

$$P^0_{\Omega^C_p}(w_1, \dots, w_d) = \gamma\pi\omega^2 \int_{\Omega^C_p} |\boldsymbol{B}^{DC}_0 \times \boldsymbol{\mathfrak{U}}^{AC} - \boldsymbol{\mathfrak{A}}^{AC}|^2 r \,\mathrm{d}\Omega. \tag{C.3}$$

The solution fields are sought within an axisymmetric framework, see Section

2.5, and thus, the quantities $\boldsymbol{\mathcal{A}}^{AC}$ and $\boldsymbol{\mathcal{U}}^{AC}$ can be expressed as

$$\boldsymbol{\mathcal{A}}^{AC}(r,z,w_1,\dots,w_d) = \begin{bmatrix} 0 \\ r\mathcal{A}_\phi \\ 0 \end{bmatrix}, \quad \boldsymbol{\mathcal{U}}^{AC}(r,z,w_1,\dots,w_d) = \begin{bmatrix} r\,\mathcal{U}_r \\ 0 \\ \mathcal{U}_z \end{bmatrix}, \tag{C.4}$$

where both terms $\boldsymbol{B}_0^{DC} \times \boldsymbol{\mathcal{U}}^{AC}$ and $\boldsymbol{\mathcal{A}}^{AC}$ have only one non-zero component. Consequently, equation (C.3) may be rewritten as

$$\begin{aligned} P^0_{\Omega_p^C}(w_1,\dots,w_d) &= \gamma\pi\omega^2 \int_{\Omega_p^C} |B_{0,r}^{DC}\,\mathcal{U}_z - rB_{0,z}^{DC}\,\mathcal{U}_r - r\mathcal{A}_\phi|^2 r \,\mathrm{d}\Omega \\ &= P_1 - P_2 - P_3 - P_4 + P_5 + P_6 - P_7 + P_8 + P_9, \end{aligned} \tag{C.5}$$

with

$$P_1(w_1,\dots,w_d) := \gamma\pi\omega^2 {B_{0,r}^{DC}}^2 \int_{\Omega_p^C} \mathcal{U}_z \overline{\mathcal{U}}_z r \,\mathrm{d}\Omega, \tag{C.6a}$$

$$P_2(w_1,\dots,w_d) := \gamma\pi\omega^2 {B_{0,z}^{DC}}^2 \int_{\Omega_p^C} \overline{\mathcal{U}}_r r^2 \,\mathrm{d}\Omega, \tag{C.6b}$$

$$P_3(w_1,\dots,w_d) := \gamma\pi\omega^2 B_{0,r}^{DC} \int_{\Omega_p^C} \mathcal{U}_z \overline{\mathcal{A}}_\phi r^2 \,\mathrm{d}\Omega, \tag{C.6c}$$

$$P_4(w_1,\dots,w_d) := \gamma\pi\omega^2 {B_{0,z}^{DC}}^2 \int_{\Omega_p^C} \mathcal{U}_r \overline{\mathcal{U}}_z r^2 \,\mathrm{d}\Omega, \tag{C.6d}$$

$$P_5(w_1,\dots,w_d) := \gamma\pi\omega^2 {B_{0,z}^{DC}}^2 \int_{\Omega_p^C} \mathcal{U}_r \overline{\mathcal{U}}_r r^3 \,\mathrm{d}\Omega, \tag{C.6e}$$

$$P_6(w_1,\dots,w_d) := \gamma\pi\omega^2 B_{0,z}^{DC} \int_{\Omega_p^C} \mathcal{U}_r \overline{\mathcal{A}}_\phi r^3 \,\mathrm{d}\Omega, \tag{C.6f}$$

$$P_7(w_1,\dots,w_d) := \gamma\pi\omega^2 B_{0,r}^{DC} \int_{\Omega_p^C} \mathcal{A}_\phi \overline{\mathcal{U}}_z r^2 \,\mathrm{d}\Omega, \tag{C.6g}$$

$$P_8(w_1,\dots,w_d) := \gamma\pi\omega^2 B_{0,z}^{DC} \int_{\Omega_p^C} \mathcal{A}_\phi \overline{\mathcal{U}}_r r^3 \,\mathrm{d}\Omega, \tag{C.6h}$$

$$P_9(w_1,\dots,w_d) := \gamma\pi\omega^2 \int_{\Omega_p^C} \mathcal{A}_\phi \overline{\mathcal{A}}_\phi r^3 \,\mathrm{d}\Omega. \tag{C.6i}$$

At this point, the only quantities that are needed in order to compute the dissipated power $P^0_{\Omega_p^C}(w_1,\dots,w_d)$ are the scalar potential $\mathcal{A}_\phi$ and both components of the displacement field $\mathcal{U}_r$ and $\mathcal{U}_z$. These solution fields can be directly obtained for a certain parameter combination $(w_1,\dots,w_d)$ with the full order model. On the other hand, a more general approach is to use the PGD method in order to obtain the explicit separable expression of each quantity as

$$\mathcal{A}_\phi(r,z,w_1,\dots,w_d) \approx \mathcal{A}_\phi^{N_A}(r,z,w_1,\dots,w_d) := \sum_{n=1}^{N_A} F^n_{\mathcal{A}_\phi}(r,z) \prod_{i=1}^{d} G^n_{\mathcal{A}_\phi,i}(w_i), \tag{C.7a}$$

$$\mathcal{U}_r(r,z,w_1,\dots,w_d) \approx \mathcal{U}_r^{N_u}(r,z,w_1,\dots,w_d) := \sum_{n=1}^{N_u} F^n_{\mathcal{U}_r}(r,z) \prod_{i=1}^{d} G^n_{\boldsymbol{\mathcal{U}},i}(w_i), \tag{C.7b}$$

$$\mathcal{U}_z(r,z,w_1,\dots,w_d) \approx \mathcal{U}_z^{N_u}(r,z,w_1,\dots,w_d) := \sum_{n=1}^{N_u} F^n_{\mathcal{U}_z}(r,z)\prod_{i=1}^{d} G^n_{\boldsymbol{\mathcal{U}},i}(w_i), \tag{C.7c}$$

Note that in Chapter 5 it has been shown how a staggered approach is beneficial in terms of accuracy and robustness of the algorithm and, therefore, the PGD definition (C.7) has been presented using the notation in Chapter 3 but separating both physics. Moreover, in order to write the expression for $\mathcal{U}_r$ and $\mathcal{U}_z$ the definition of the vectorial function $\boldsymbol{F}^n_{\boldsymbol{\mathcal{U}}} = [F^n_{\mathcal{U}_r}, F^n_{\mathcal{U}_z}]^T$ has been used, whereas the d parametric domains use a single scalar function $G^n_{\boldsymbol{\mathcal{U}},i}$ for each dimension $i = 1,\dots,d$.

C.1.1 Full order model approach

Although the main focus of this thesis is the use of the PGD method in the context of MRI scanner design, this section describes how the full order model approach can also benefit from precomputing certain terms in order to speed up the calculation of the integrated quantities of interest (2.34).

After running the full order model, the solution fields $\mathcal{A}_\phi$, $\mathcal{U}_r$ and $\mathcal{U}_z$ are obtained for a certain combination of parameters $(w_1,\dots,w_d)$. Hence, the dissipated power $P^0_{\Omega^C_p}$ in (C.5) does not depend on the parameters $(w_1,\dots,w_d)$ anymore. Since all six terms are derived following the same procedure, only one term will be expanded as an example. For instance, the third term P_3 can be written as

$$P_3 = \gamma\pi\omega^2 B^{DC}_{0,r}\int_{\Omega^C_p} \mathcal{U}_z\overline{\mathcal{A}}_\phi r^2 \,\mathrm{d}\Omega, \tag{C.8}$$

and is discretised following the standard FEM procedure, see Section 2.6, in order to obtain

$$P_3 = 2\gamma\pi\omega^2 B^{DC}_{0,r}\sum_{a=1}^{n_{dof}(\mathcal{U}_z)}\sum_{b=1}^{n_{dof}(\mathcal{U}_z)} \overline{\mathcal{A}}^a_\phi \int_{\Omega^C_p} N^a N^b r^2\,\mathrm{d}\Omega\,\mathcal{U}^b_z, \tag{C.9}$$

where $n_{dof}(\mathcal{U}_z)$ restricts the total number of degrees of freedom n_{dof} to only the ones corresponding to the z-mechanical degrees of freedom. Once the assembly process is completed, this expression can be written as

$$P_3 = 2\gamma\pi\omega^2 B^{DC}_{0,r}\overline{\boldsymbol{\mathcal{A}}}^T_{\phi(\mathcal{U}_z)}\mathbf{M}_3\boldsymbol{\mathcal{U}}_z, \tag{C.10}$$

where following the same notation than before, $\overline{\boldsymbol{\mathcal{A}}}^T_{\phi(\mathcal{U}_z)}$ denotes the transposed of the complex conjugate of the nodal values restricted to the z-mechanical degrees of freedom. Moreover, $\mathbf{M}_3$ symbolises a type of mass matrix. Notice that for every term P_i for $i = 1,\dots,6$ featuring in (C.6), a different mass type matrix $\mathbf{M}$ is obtained.

It is clear from (C.10) that the mass type matrices for each term in (C.5), namely $\mathbf{M}_i$ for $i = 1,\dots,6$, can be assembled and stored during the finite element assembly process. Consequently, if the integration of the dissipated power is required, the only operation that will be performed is a simple post- and pre-multiplication of these matrices times its corresponding solution vectors, obtaining a massive time reduction when compared to integrating the entire term (C.1) as a postprocess.

C.1.2 PGD approach

A more interesting approach in the context of this thesis is to obtain the explicit separable expressions (C.7) using the PGD methodology proposed in Chapter 5. This section considers however a lower parametric dimensional space $\Omega_p = \Omega_\omega$ consisting only in the frequency domain instead of the general d-dimensional space $\Omega_p = w_1 \times \cdots \times w_d$. The PGD definition (C.7) is then reduced to

$$\mathcal{A}_\phi(r,z,\omega) \approx \mathcal{A}_\phi^{N_A}(r,z,\omega) := \sum_{n=1}^{N_A} F^n_{\mathcal{A}_\phi}(r,z) G^n_{\mathcal{A}_\phi}(\omega), \tag{C.11a}$$

$$\mathcal{U}_r(r,z,\omega) \approx \mathcal{U}_r^{N_u}(r,z,\omega) := \sum_{n=1}^{N_u} F^n_{\mathcal{U}_r}(r,z) G^n_{\boldsymbol{\mathcal{U}}}(\omega), \tag{C.11b}$$

$$\mathcal{U}_z(r,z,\omega) \approx \mathcal{U}_z^{N_u}(r,z,\omega) := \sum_{n=1}^{N_u} F^n_{\mathcal{U}_z}(r,z) G^n_{\boldsymbol{\mathcal{U}}}(\omega). \tag{C.11c}$$

Following the same reasoning than in Section C.1.1 only the third term $P_3(\omega)$ appearing in (C.5) will be derived as an example, so both approaches (full order model and PGD) can be compared and discussed. Note that, differently from the full order model approach, the PGD considers the frequency as a parametric space and this is denoted explicitly in $P_3 = P_3(\omega)$. Having said that, the PGD definitions (C.11) can be substituted into the definition of $P_3(\omega)$ (C.6c) to obtain

$$P_3(\omega) = 2\gamma\pi\omega^2 B^{DC}_{0,r} \int_{\Omega_p^C} \left(\sum_{n=1}^{N_u} F^n_{\mathcal{U}_z} G^n_{\boldsymbol{\mathcal{U}}} \right) \left(\sum_{m=1}^{N_A} \overline{F}^m_{\mathcal{A}_\phi} \overline{G}^m_{\mathcal{A}_\phi} \right) r^2 \, \mathrm{d}\Omega, \tag{C.12}$$

where the terms that do not depend on space can be taken out from the integral as

$$P_3(\omega) = 2\gamma\pi\omega^2 B^{DC}_{0,r} \sum_{n=1}^{N_u} \sum_{m=1}^{N_A} G^n_{\boldsymbol{\mathcal{U}}} \overline{G}^m_{\mathcal{A}_\phi} \int_{\Omega_p^C} F^n_{\mathcal{U}_z} \overline{F}^m_{\mathcal{A}_\phi} r^2 \, \mathrm{d}\Omega. \tag{C.13}$$

The only two terms remaining in the integral are treated in the same way than in (C.8) for the full order model case. After the finite element discretisation, see Section 2.6, this integral can be written as

$$\int_{\Omega_p^C} F^n_{\mathcal{U}_z} \overline{F}^m_{\mathcal{A}_\phi} r^2 \, \mathrm{d}\Omega = \sum_{a=1}^{n_{dof(\mathcal{U}_z)}} \sum_{b=1}^{n_{dof(\mathcal{U}_z)}} \overline{F}^{m,a}_{\mathcal{A}_\phi} \int_{\Omega_p^C} N^a N^b r^2 \, \mathrm{d}\Omega F^{n,b}_{\mathcal{U}_z}, \tag{C.14}$$

and once assembled, it reads

$$\int_{\Omega_p^C} F^n_{\mathcal{U}_z} \overline{F}^m_{\mathcal{A}_\phi} r^2 \, \mathrm{d}\Omega = \overline{\mathbf{F}}^{m,T}_{\mathcal{A}_\phi(\mathcal{U}_z)} \mathbf{M}_3 \mathbf{F}^n_{\mathcal{U}_z}. \tag{C.15}$$

Then, the final expression of (C.13) is

$$P_3(\omega) = 2\gamma\pi\omega^2 B^{DC}_{0,r} \sum_{n=1}^{N_u} \sum_{m=1}^{N_A} G^n_{\boldsymbol{\mathcal{U}}} \overline{G}^m_{\mathcal{A}_\phi} \overline{\mathbf{F}}^{m,T}_{\mathcal{A}_\phi(\mathcal{U}_z)} \mathbf{M}_3 \mathbf{F}^n_{\mathcal{U}_z}, \tag{C.16}$$

where the same notation than in Section C.1.1 has been used here in order to restrict the electromagnetic degrees of freedom to a smaller set that only contains the z-mechanical degrees of freedom. By comparing the two final expressions obtained with both approaches, (C.10) and (C.16), it is clear that the PGD method allows for directly computing values of $P_3(\omega)$ and thus, $P^0_{\Omega_p^C}(\omega)$ when adding all terms, for several values of ω, optimising the frequency sweeps that are required in the design stage of MRI scanners.

Appendix D

Sensitivity maps

The sensitivity maps or response surfaces shown in Section 5.7.5 are another PGD feature that can be easily obtained as a postprocess of the precomputed offline PGD solution. These type of surfaces contain information on how a certain field, in this case the integrated quantities, evolve when changing a certain parameter and thus, they are a great tool in the design stage of any product or system.

The computation of these surfaces can be done by directly computing the differences between values in a point cloud, obtained from evaluating the precomputed high-dimensional PGD solution a large number of times. However, a more elegant approach is to formulate how the dissipated power (2.34) changes in terms of, for instance, the strength of the static magnetic field B_0. Note that this section considers the high-dimensional PGD formulation, see Chapter 5, and this is emphasised by explicitly writing the dependency of the dissipated power $P^0_{\Omega^C} = P^0_{\Omega^C}(\omega, \gamma, B_0)$. Then, the derivative of $P^0_{\Omega^C}$ with respect to B_0 is computed as[1]

$$\frac{\partial P^0_{\Omega^C}(\omega, \gamma, B_0)}{\partial B_0} = \gamma \int_{\Omega^C} 2\mathrm{Re} \left(\boldsymbol{\mathcal{E}}^{AC} \cdot \frac{\partial \overline{\boldsymbol{\mathcal{E}}}^{AC}}{\partial B_0} \right) \mathrm{d}\Omega, \tag{D.1}$$

where the electric conductivity γ has been taken out from the integral since it is constant within each conducting component. The electric field intensity $\boldsymbol{\mathcal{E}}^{AC}(r, z, \omega, \gamma, B_0)$ is defined in the high-dimensional space $\Omega_p \times \Omega_q$ as

$$\boldsymbol{\mathcal{E}}^{AC}(r, z, \omega, \gamma, B_0) = \mathrm{i}\omega \big(\alpha_{B_0} \boldsymbol{B}_0^{DC} \times \boldsymbol{\mathcal{U}}^{AC} - \boldsymbol{\mathcal{A}}^{AC} \big), \tag{D.2}$$

where the scalar coefficient α_{B_0} appears due to the fact that the static problem is set such that it generates a magnetic field of strength $B_0 = 1$ T, and hence, the coefficient α_{B_0} scales this magnetic field to the actual required strength, as detailed in Chapter 5. Having said that, the partial of $\boldsymbol{\mathcal{E}}^{AC}(r, z, \omega, \gamma, B_0)$ with respect to B_0 is

$$\frac{\partial \overline{\boldsymbol{\mathcal{E}}}^{AC}(r, z, \omega, \gamma, B_0)}{\partial B_0} = -\mathrm{i}\omega \left(\boldsymbol{B}_0^{DC} \times \overline{\boldsymbol{\mathcal{U}}}^{AC} + \alpha_{B_0} \boldsymbol{B}_0^{DC} \times \frac{\partial \overline{\boldsymbol{\mathcal{U}}}^{AC}}{\partial B_0} \right), \tag{D.3}$$

---

[1] Note that $\frac{\partial |z|^2}{\partial x} = z \frac{\partial \overline{z}}{\partial x} + \frac{\partial z}{\partial x} \overline{z} = 2\mathrm{Re} \left(z \frac{\partial \overline{z}}{\partial x} \right)$.

which can be substituted into (D.1) to obtain the following expression

$$\frac{\partial P^0_{\Omega^C}(\omega,\gamma,B_0)}{\partial B_0} = -P^{B_0}_1 - P^{B_0}_2 + P^{B_0}_3, \tag{D.4}$$

where

$$P^{B_0}_1(\omega,\gamma,B_0) := 2\gamma\omega^2 \int_{\Omega^C} \mathrm{Re}\left(\boldsymbol{\mathcal{A}}^{AC}\cdot\left(\boldsymbol{B}^{DC}_0 \times \overline{\boldsymbol{\mathcal{U}}}^{AC}\right)\right)\,\mathrm{d}\Omega, \tag{D.5a}$$

$$\begin{aligned} P^{B_0}_2(\omega,\gamma,B_0) := 2\gamma\omega^2\alpha_{B_0}\Bigg[& \int_{\Omega^C} \mathrm{Re}\left(\boldsymbol{\mathcal{A}}^{AC}\cdot\left(\boldsymbol{B}^{DC}_0 \times \frac{\partial\overline{\boldsymbol{\mathcal{U}}}^{AC}}{\partial B_0}\right)\right)\,\mathrm{d}\Omega \\ & - \int_{\Omega^C} \mathrm{Re}\left(\left(\boldsymbol{B}^{DC}_0 \times \boldsymbol{\mathcal{U}}^{AC}\right)\cdot\left(\boldsymbol{B}^{DC}_0 \times \overline{\boldsymbol{\mathcal{U}}}^{AC}\right)\right)\,\mathrm{d}\Omega\Bigg], \end{aligned} \tag{D.5b}$$

$$P^{B_0}_3(\omega,\gamma,B_0) := 2\gamma\omega^2\alpha^2_{B_0} \int_{\Omega^C} \mathrm{Re}\left(\left(\boldsymbol{B}^{DC}_0 \times \boldsymbol{\mathcal{U}}^{AC}\right)\cdot\left(\boldsymbol{B}^{DC}_0 \times \frac{\partial\overline{\boldsymbol{\mathcal{U}}}^{AC}_D}{\partial B_0}\right)\right)\,\mathrm{d}\Omega. \tag{D.5c}$$

The only two unknowns in the above equation are the vector potential $\boldsymbol{\mathcal{A}}^{AC}(r,z,\omega,\gamma)$ and the derivative of the displacement field $\boldsymbol{\mathcal{U}}^{AC}(r,z,\omega,\gamma,B_0)$ with respect to B_0, which will be obtained from evaluating the offline PGD solution as detailed in Section 3.7. Hence, since an axisymmetric formulation is used, the vector potential will be approximated using the standard electromagnetic PGD definition as

$$\boldsymbol{\mathcal{A}}^{AC} = \begin{bmatrix} 0 \\ r\mathcal{A}_\phi \\ 0 \end{bmatrix}, \quad \mathcal{A}_\phi(r,z,\omega,\gamma) \approx \mathcal{A}^{N_A}_\phi(r,z,\omega,\gamma) := \sum_{n=1}^{N_A} \beta^n F^n_{\mathcal{A}_\phi}(r,z) G^n_{\mathcal{A}_\phi}(\omega) H^n_{\mathcal{A}_\phi}(\gamma). \tag{D.6}$$

On the other hand, the derivative of displacement field with respect to B_0

$$\frac{\partial\boldsymbol{\mathcal{U}}^{AC}}{\partial B_0} = \begin{bmatrix} r\frac{\partial\mathcal{U}_r}{\partial B_0} \\ 0 \\ \frac{\partial\mathcal{U}_z}{\partial B_0} \end{bmatrix}, \tag{D.7}$$

is described with only two components $\frac{\partial\mathcal{U}_r}{\partial B_0}$ and $\frac{\partial\mathcal{U}_z}{\partial B_0}$. In the same way that the displacement field is written as $\boldsymbol{\mathcal{U}} = [\mathcal{U}_r, \mathcal{U}_z]^T$, omitting the zero component, its derivative with respect to B_0 can also be written as $\frac{\partial\boldsymbol{\mathcal{U}}}{\partial B_0} = [r\frac{\partial\mathcal{U}_z}{\partial B_0}, \frac{\partial\mathcal{U}_z}{\partial B_0}]^T$, which is approximated using the mechanical PGD definition as

$$\frac{\partial\boldsymbol{\mathcal{U}}(r,z,\omega,\gamma,B_0)}{\partial B_0} \approx \frac{\partial\boldsymbol{\mathcal{U}}^{N_u}(r,z,\omega,\gamma,B_0)}{\partial B_0} := \sum_{n=1}^{N_u} \beta^n \boldsymbol{F}^n_{\boldsymbol{\mathcal{U}}}(r,z) G^n_{\boldsymbol{\mathcal{U}}}(\omega) H^n_{\boldsymbol{\mathcal{U}}}(\gamma) \frac{\partial L^n_{\boldsymbol{\mathcal{U}}}(B_0)}{\partial B_0}, \tag{D.8}$$

where only the term depending on B_0 has to be derived thanks to the separable approximation provided by the PGD technique. Note that the evaluation of this term is simple since it only involves the derivatives of the linear one-dimensional shape functions with respect to B_0. Once all terms are computed, the derivative $\frac{\partial P^0_{\Omega^C}(\omega,\gamma,B_0)}{\partial B_0}$ can be evaluated for several values of (ω,γ) in order to create the sensitivity map of $P^0_{\Omega^C}(\omega,\gamma,B_0)$ with respect to B_0.

The procedure is similar when computing a response surface for other parameters. For example, if the electrical conductivity γ is considered, the derivative of $P^0_{\Omega^C}$ with respect to γ reads

$$\begin{aligned}\frac{\partial P^0_{\Omega^C}(\omega,\gamma,B_0)}{\partial\gamma} &= \frac{1}{2}\int_{\Omega^C}\frac{\partial}{\partial\gamma}(\gamma\boldsymbol{\mathcal{E}}^{AC}\cdot\overline{\boldsymbol{\mathcal{E}}}^{AC})\,\mathrm{d}\Omega = \\ &= \frac{1}{2}\int_{\Omega^C}|\boldsymbol{\mathcal{E}}^{AC}|^2\,\mathrm{d}\Omega + 2\gamma\int_{\Omega^C}\mathrm{Re}\left(\boldsymbol{\mathcal{E}}^{AC}\cdot\frac{\partial\overline{\boldsymbol{\mathcal{E}}}^{AC}}{\partial\gamma}\right)\mathrm{d}\Omega.\end{aligned} \tag{D.9}$$

Note that the first term in (D.9) is almost identical to the original expression of the dissipated power but without γ and hence, it will not be derived. However, the second term features the derivative of $\boldsymbol{\mathcal{E}}^{AC}(r,z\omega,\gamma,B_0)$ with respect to γ, which is expressed as

$$\frac{\partial\overline{\boldsymbol{\mathcal{E}}}^{AC}(r,z\omega,\gamma,B_0)}{\partial\gamma} = -\mathrm{i}\omega\left(\alpha_{B_0}\boldsymbol{B}_0^{DC}\times\frac{\partial\overline{\boldsymbol{\mathcal{U}}}^{AC}}{\partial\gamma} - \frac{\partial\overline{\boldsymbol{\mathcal{A}}}^{AC}}{\partial\gamma}\right). \tag{D.10}$$

Consequently, the second term in (D.9) is expanded as

$$2\gamma\int_{\Omega^C}\mathrm{Re}\left(\boldsymbol{\mathcal{E}}^{AC}\cdot\frac{\partial\overline{\boldsymbol{\mathcal{E}}}^{AC}}{\partial\gamma}\right)\mathrm{d}\Omega = P_1^\gamma - P_2^\gamma + P_3^\gamma, \tag{D.11}$$

with

$$P_1^\gamma(\omega,\gamma,B_0) := 2\gamma\omega^2\int_{\Omega^C}\mathrm{Re}\left(\boldsymbol{\mathcal{A}}^{AC}\cdot\frac{\partial\overline{\boldsymbol{\mathcal{A}}}^{AC}}{\partial\gamma}\right)\mathrm{d}\Omega, \tag{D.12a}$$

$$\begin{aligned}P_2^\gamma(\omega,\gamma,B_0) := 2\gamma\omega^2\alpha_{B_0}\Bigg[&\int_{\Omega^C}\mathrm{Re}\left((\boldsymbol{B}_0^{DC}\times\boldsymbol{\mathcal{U}}^{AC})\cdot\frac{\partial\overline{\boldsymbol{\mathcal{A}}}^{AC}}{\partial\gamma}\right)\mathrm{d}\Omega \\ &+\int_{\Omega^C}\mathrm{Re}\left(\boldsymbol{\mathcal{A}}^{AC}\cdot\left(\overline{\boldsymbol{B}}_0^{DC}\times\frac{\partial\overline{\boldsymbol{\mathcal{U}}}^{AC}}{\partial\gamma}\right)\right)\mathrm{d}\Omega\Bigg],\end{aligned} \tag{D.12b}$$

$$P_3^\gamma(\omega,\gamma,B_0) := 2\gamma\omega^2\alpha_{B_0}^2\int_{\Omega^C}\mathrm{Re}\left((\boldsymbol{B}_0^{DC}\times\boldsymbol{\mathcal{U}}^{AC})\cdot\left(\overline{\boldsymbol{B}}_0^{DC}\times\frac{\partial\overline{\boldsymbol{\mathcal{U}}}^{AC}}{\partial\gamma}\right)\right)\mathrm{d}\Omega. \tag{D.12c}$$

where three terms have to be evaluated, namely $\boldsymbol{\mathcal{A}}^{AC}$, $\frac{\partial\boldsymbol{\mathcal{A}}^{AC}}{\partial\gamma}$ and $\frac{\partial\boldsymbol{\mathcal{U}}^{AC}}{\partial\gamma}$. The case for $\boldsymbol{\mathcal{A}}^{AC}$ has been already mentioned in (D.6). Regarding the two derivatives with respect to γ, $\frac{\partial\boldsymbol{\mathcal{A}}^{AC}}{\partial\gamma} = [0, r\frac{\partial\mathcal{A}_\phi}{\partial\gamma}, 0]$ and $\frac{\partial\boldsymbol{\mathcal{U}}^{AC}}{\partial\gamma} = [r\frac{\partial\mathcal{U}_r}{\partial\gamma}, 0, \frac{\partial\mathcal{U}_z}{\partial\gamma}]$, the non-zero coefficients $\mathcal{A}_\phi$ and $\frac{\partial\boldsymbol{\mathcal{U}}}{\partial\gamma} = [r\frac{\partial\mathcal{U}_r}{\partial\gamma}, \frac{\partial\mathcal{U}_z}{\partial\gamma}]$ are approximated as

$$\frac{\partial\mathcal{A}_\phi(r,z,\omega,\gamma)}{\partial\gamma} \approx \frac{\partial\mathcal{A}_\phi^{N_A}(r,z,\omega,\gamma)}{\partial\gamma} := \sum_{n=1}^{N_A}\beta^n F^n_{\mathcal{A}_\phi}(r,z)G^n_{\mathcal{A}_\phi}(\omega)\frac{\partial H^n_{\mathcal{A}_\phi}}{\partial\gamma}(\gamma) \tag{D.13a}$$

$$\frac{\partial \boldsymbol{\mathcal{U}}(r,z,\omega,\gamma,B_0)}{\partial \gamma} \approx \frac{\partial \boldsymbol{\mathcal{U}}^{N_u}(r,z,\omega,\gamma,B_0)}{\partial \gamma} := \sum_{n=1}^{N_u} \beta^n \boldsymbol{F}^n_{\boldsymbol{\mathcal{U}}}(r,z) G^n_{\boldsymbol{\mathcal{U}}}(\omega) \frac{\partial H^n_{\boldsymbol{\mathcal{U}}}}{\partial \gamma}(\gamma) L^n_{\boldsymbol{\mathcal{U}}}(B_0). \tag{D.13b}$$

Similarly than in the previous case, the evaluation of these two derivatives only involves the computation of one-dimensional linear shape functions and then, the sensitivity of $P^0_{\Omega^C}$ with respect to γ can be plotted by evaluating (D.9) several times.

Appendix E

GUI for the online PGD stage and code description

E.1 GUI for the online PGD stage

A general PGD formulation has been presented in Chapter 3 and it has been particularised for magneto-mechanical problems in Chapters 4 and 5, following a monolithic and staggered approaches, respectively. As mentioned in these chapters, the computations in order to obtain the high-order parametric solution constitute the offline stage. On the other hand, the online stage, see Section 3.7, allows for very fast input/output evaluations of the precomputed high-order parametric solution. Since the computational cost of the online stage is minimum, this operation can be performed even in portable devices and therefore, a Graphical User Interface (GUI) is presented in this appendix in order to visualise and show the benefits of the PGD technique in an industrial environment.

With this aim, a simple Matlab [114] application has been designed to create a user-friendly interface that particularises the high-dimensional parametric solution computed in the offline PGD stage as presented in Figure 3.2 in a flow chart format. Note that this GUI was developed for the monolithic frequency-based PGD method presented in Chapter 4, although it can be extended to the staggered high-dimensional, see Chapter 5. This online PGD app is presented in Figure E.1 where four different tabs are displayed. The first one presents the application and its developers. The second one loads a particular precomputed PGD offline solution which is defined with the following parameters: polynomial order, frequency range, PGD tolerance and the parametric mesh size[1]. The third tab displays the plot of a particular field of interest. Moreover, this tab also offers numerical quantities, namely dissipated power and kinetic energy, computed on the fly that are industrially relevant. Note that here is where the PGD technique can be exploited at its greatest, obtaining solutions in real time for any desired frequency. Moreover, other

---

[1] Since the parametric domain for the frequency-based PGD method is $\Omega_p = \Omega_\omega$, the parametric mesh size refers to Ω_ω.

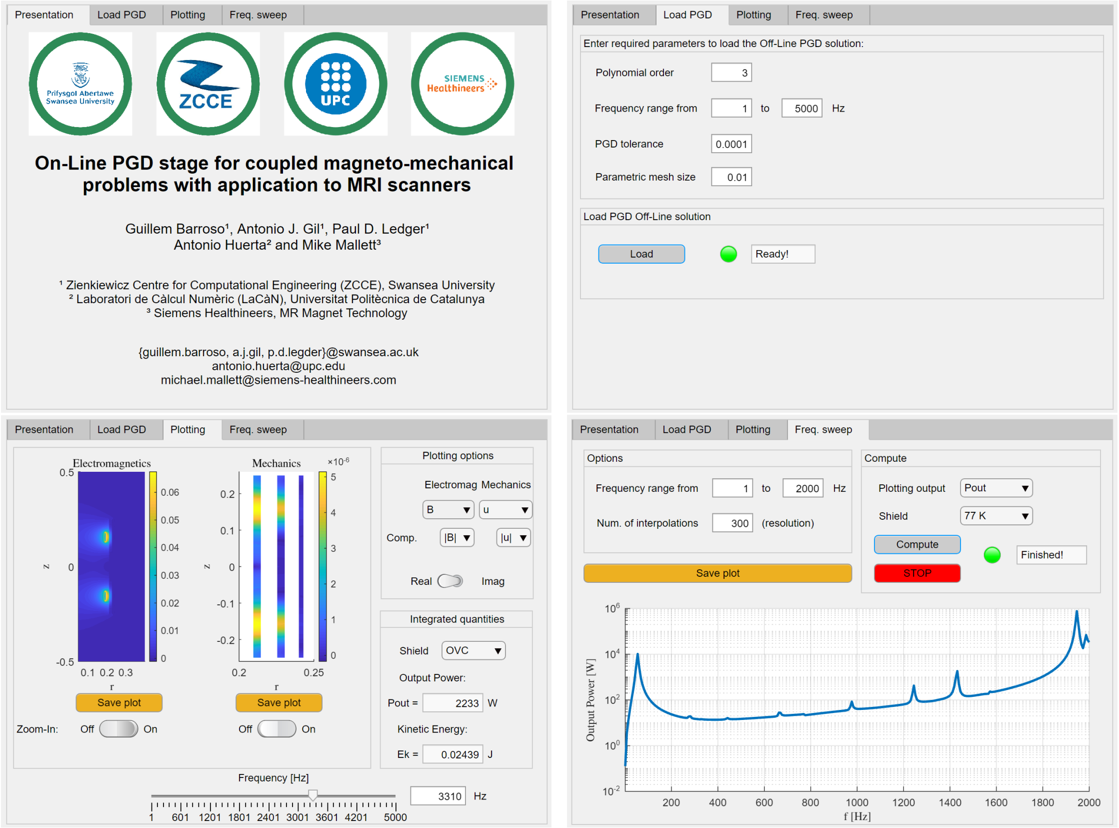
Presentation
Load PGD
Plotting
Freq. sweep
Prifysgol Abertawe Swansea University
ZCCE
UPC
SIEMENS Healthineers
Load
Electromagnetics
Mechanics
×10-6
z
r
Save plot
Zoom-In:
Off
On
Plotting options
Electromag
Mechanics
Real
Imag
Integrated quantities
Frequency [Hz]
1
601
1201
1801
2401
3001
3601
4201
5000
Options
Compute
STOP
Output Power [W]
f [Hz]
200
400
600
800
1000
1200
1400
1600
1800
2000

On-Line PGD stage for coupled magneto-mechanical problems with application to MRI scanners

Guillem Barroso¹, Antonio J. Gil¹, Paul D. Ledger¹
Antonio Huerta² and Mike Mallett³

¹ Zienkiewicz Centre for Computational Engineering (ZCCE), Swansea University
² Laboratori de Càlcul Numèric (LaCàN), Universitat Politècnica de Catalunya
³ Siemens Healthineers, MR Magnet Technology

{guillem.barroso, a.j.gil, p.d.legder}@swansea.ac.uk
antonio.huerta@upc.edu
michael.mallett@siemens-healthineers.com

Enter required parameters to load the Off-Line PGD solution:
Polynomial order 3
Frequency range from 1 to 5000 Hz
PGD tolerance 0.0001
Parametric mesh size 0.01
Load PGD Off-Line solution
● Ready!

B ▼ u ▼
Comp. |B| ▼ |u| ▼
Shield OVC ▼
Output Power:
Pout = 2233 W
Kinetic Energy:
Ek = 0.02439 J
3310 Hz

Frequency range from 1 to 2000 Hz
Num. of interpolations 300 (resolution)
Plotting output Pout ▼
Shield 77 K ▼
● Finished!

Figure E.1: On-line PGD application for coupled magneto-mechanical problems with application to MRI scanners. Visualisation of the four tabs; Presentation, Loading PGD, Plotting and Frequency sweep.

useful options have been added such that a zoom-in to the conducting shields and a plotting button that creates and saves a figure with the displayed image. The last tab offers the possibility to perform a frequency sweep in a range of interest and plot a specific quantity of interest in one of the conducting components of the problem. The entire interface is based on sliders, numerical boxes, switches and lamps that make the app very user-friendly.

E.2 Code description

The script `main.m` is the file that interacts with the entire coupled magneto-mechanical finite element code, in which the staggered PGD technique developed in [91] has been implemented. The aim of this user manual is to generally describe the workflow of the code and to indicate which options are available for a third user. First, the main script (`main.m`) is used to either solve the coupled magneto-mechanical problem presented in [91] using the full order model approach or to generate the explicit high dimensional PGD solution for a certain range of frequencies and material parameters.

E.2.1 Code structure

The aim of the code was originally to compute the coupled magneto-mechanical problem first presented in [32,33,36] using the full order model approach. Then, the staggered PGD technique was implemented as described in [91] in order to incorporate the angular frequency of excitation ω, the conductivity γ and the strength of the magnetic field B_0 as extra parameters in the high-dimensional PGD solution. The general structure of the code is defined as follows

1. Definition of the user-defined PGD parameters.
2. Selection of the geometry and spatial discretisation.
3. Mesh generation of the considered geometry.
4. Reference element-related calculations.
5. Numbering of the problem unknowns for the different physics.
6. Solution of the static (DC) problem.
7. Precomputation of certain quantities used later for postprocessing the solution variables and obtain the integrated quantities of interest.
8. Solution of the transient (AC) problem using either
    - Full order model approach for given values of ω,γ and B_0.
    - PGD technique considering ω,γ and B_0 as parameters. In this case, the online PGD stage is also applied in order to evaluate the precomputed high-dimensional solution for specific values of ω,γ and B_0.
9. Postprocessing of the solution fields $\mathcal{A}_\phi$ and $\boldsymbol{\mathcal{U}}$; plotting options, calculation of integrated quantities, generation of Paraview files and error calculation.

E.2.2 PGD user-defined parameters

The first step required in `main.m` is to define the PGD user-defined parameters as shown in Figure E.2, where the first section named PGD options contains the following three options

- `PGDsolver`: 1 → run PGD solver, 0 → run full order model.
- `freqSplit`: 1 → automatically split frequency domain in order to obtain and accurate PGD solution in the entire frequency range of interest, 0 → do not split the frequency domain.
- `Rg_dirac`: 1 → use dirac delta functions for the 1D frequency domain, 0 → use standard linear test functions.

Note that the recommended settings when running the staggered PGD solver are the ones displayed in Figure E.2, where the frequency splitting is activated to obtain an accurate PGD solution and standard linear shape functions are used to interpolate the frequency subdomain. The advantages of activating the option `Rg_dirac` are discussed in [88], although the staggered algorithm performs better when it is set to 0.

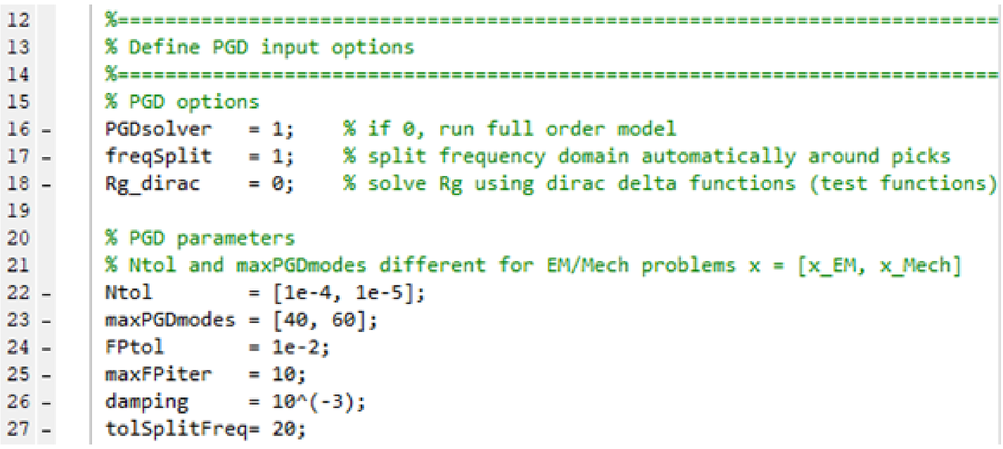

```
%==========================================================================
% Define PGD input options
%==========================================================================
% PGD options
PGDsolver   = 1;    % if 0, run full order model
freqSplit   = 1;    % split frequency domain automatically around picks
Rg_dirac    = 0;    % solve Rg using dirac delta functions (test functions)

% PGD parameters
% Ntol and maxPGDmodes different for EM/Mech problems x = [x_EM, x_Mech]
Ntol        = [1e-4, 1e-5];
maxPGDmodes = [40, 60];
FPtol       = 1e-2;
maxFPiter   = 10;
damping     = 10^(-3);
tolSplitFreq= 20;
```

Figure E.2: Definition of the PGD input options.

The second block of options correspond to the parameters that determine the behaviour of the iterative procedures involved in the offline PGD solution computation; the Greedy algorithm and the fixed-point Alternating Direction Scheme (ADS). These parameters are described as

- `Ntol`: Tolerance criteria to stop the Greedy algorithm. Measures the relative modal amplitude of the last computed mode.
- `maxPGDmodes`: Maximum number of PGD modes allowed in the Greedy algorithm.
- `FPtol`: Tolerance criteria to stop the fixed-point ADS.
- `maxFPiter`: Maximum number of iterations of the fixed-point ADS within one mode.
- `damping`: Rayleigh damping coefficient that controls the amount of numerical regularisation introduced.
- `tolSplitFreq`: Tolerance of the frequency splitting algorithm (in %) to control the maximum size of the frequency subdomains generated.

The values appearing in Figure E.2 correspond to the values for a particular geometry, namely the test magnet problem. This setting was used to generate the results for this geometry and can be found in [91] together with a different setting for the full magnet problem. Note that the different geometries will be discussed later in this manual.

E.2.3 Online PGD parameters

As mentioned in Section E.2.1, the online PGD stage is required in the code in order to evaluate the previously computed PGD offline solution for given values of ω,γ and B_0, see step 8. These parameters are presented in Figure E.3 and are defined as

- `B0`: value of the strength of the static magnetic field.
- `gamma`: value of the scaling factor of the conductivities of all mechanical components.
- `freq`: Frequency $f = 2\pi\omega$ (in Hz) of excitation of the AC problem.

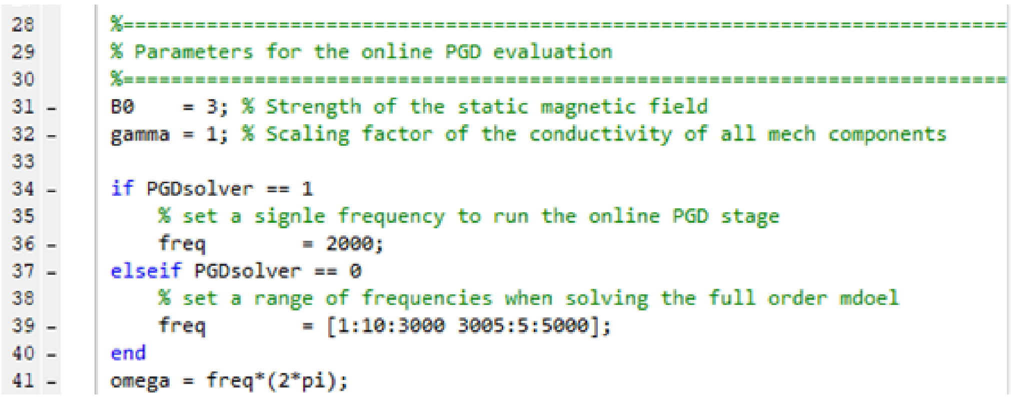

```
%==========================================================================
% Parameters for the online PGD evaluation
%==========================================================================
B0    = 3; % Strength of the static magnetic field
gamma = 1; % Scaling factor of the conductivity of all mech components

if PGDsolver == 1
    % set a signle frequency to run the online PGD stage
    freq        = 2000;
elseif PGDsolver == 0
    % set a range of frequencies when solving the full order mdoel
    freq        = [1:10:3000 3005:5:5000];
end
omega = freq*(2*pi);
```

Figure E.3: Specification of the online PGD parameters to evaluate the previously stored offline PGD solution.

When using the full order model approach (`PGDsolver = 0`), the variable `freq` can be specified as a single scalar value or as a set of frequencies which will be computed sequentially. Instead, then using the PGD technique (`PGDsolver = 1`) only the scalar case can be considered. The frequency sweeps using the PGD technique are done in the `onlinePGDstage.m` script, which exploits the real-time evaluations of the offline PGD solution and it is discussed later in the manual.

E.2.4 One-dimensional parametric domains

The PGD technique, as formulated in [91] involves solving three one-dimensional problems for each of the extra parameters considered, namely f, γ and B_0 and thus, the parameters that are required are

- `freqRange`: Global frequency range of interest (Hz) considered in the PGD algorithm.
- `sizeMesh`: Element size of the 1D frequency domain. The code allows to specify different element sizes depending on the physic considered, electromagnetics or mechanics.

- `gammaRange`: Range of interest of the conductivity scaling considered in the PGD algorithm. Note that no units are introduced here since it is a scaling of all conductivities.
- `gammaSizeMesh`: Element size of the 1D γ-domain.
- `B0Range`: Range of interest of B_0 (T) considered in the PGD algorithm.
- `B0SizeMesh`: Element size of the 1D B_0-domain.

and they have to be introduced in the code as shown in Figure E.4. The frequency domain has been implemented in a more flexible way in which different meshes can be used for the two physics considered. As discussed in [88, 91] the electromagnetic problem does not require a fine mesh since the solution fields are smooth, whilst the mechanical problem features resonance. Similarly than before, these values where used in [91] to compute the offline PGD solution of the test magnet geometry.

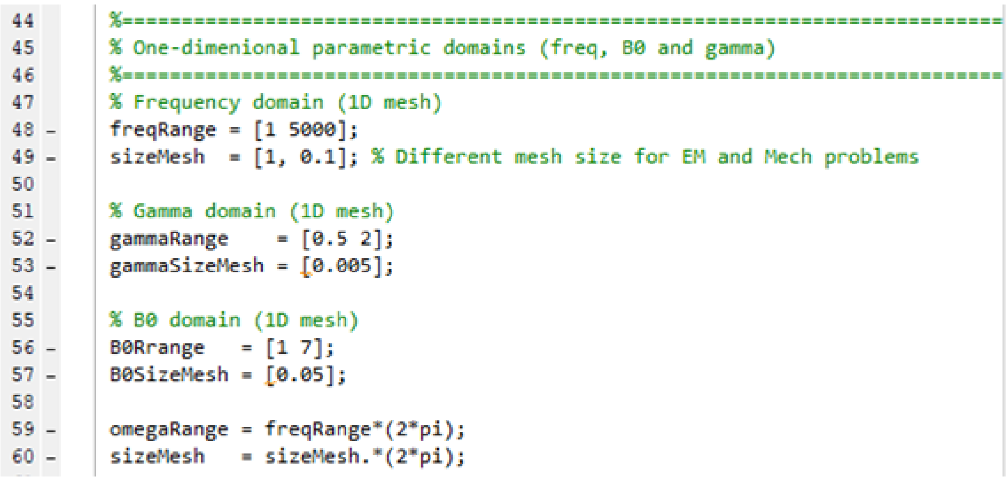

```
%==========================================================================
% One-dimenional parametric domains (freq, B0 and gamma)
%==========================================================================
% Frequency domain (1D mesh)
freqRange = [1 5000];
sizeMesh  = [1, 0.1]; % Different mesh size for EM and Mech problems

% Gamma domain (1D mesh)
gammaRange    = [0.5 2];
gammaSizeMesh = [0.005];

% B0 domain (1D mesh)
B0Rrange   = [1 7];
B0SizeMesh = [0.05];

omegaRange = freqRange*(2*pi);
sizeMesh   = sizeMesh.*(2*pi);
```

Figure E.4: Information related to the one-dimensional parametric domains considered in the PGD technique.

E.2.5 Spatial discretisation

The spatial discretisation is introduced in the same way for both the full order model approach and the PGD technique. The three parameters that control the discretisation of the spacial 2D domain are

- `h`: Element size of the 2D finite elements in the non-conducting region.
- `hCond`: Element size of the 2D finite elements in the conducting region.
- `order`: Polynomial order of interpolation.

Since, in the context of MRI scanners, the conducting components tend to be thin radiation shields, the element size is introduced separately for both conducting and non-conducting domains. The values presented in Figure E.5 have been used for all the geometries considered.

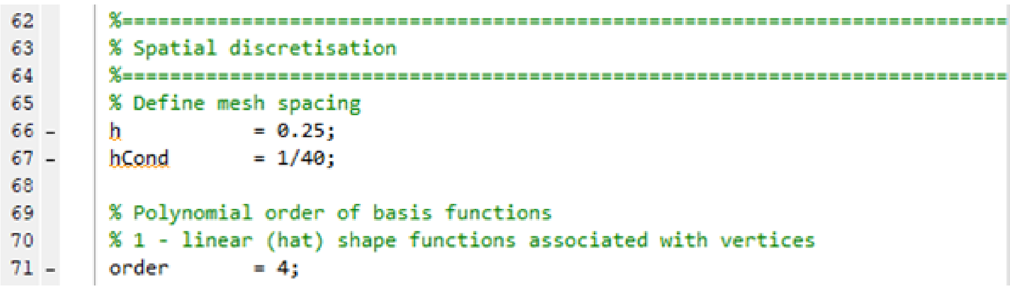

```
%==========================================================================
% Spatial discretisation
%==========================================================================
% Define mesh spacing
h           = 0.25;
hCond       = 1/40;

% Polynomial order of basis functions
% 1 - linear (hat) shape functions associated with vertices
order       = 4;
```

Figure E.5: Spatial discretisation of the 2D (r, z) domain for both full order and PGD approaches.

E.2.6 Geometry definition

The geometry is defined through a problem file script which contains all the information regarding geometry, boundary conditions, material parameters and current sources applied to the problem. The three geometries considered in [88, 91] are

- Magneto-mechanical test problem (`problem = 1`): conducting mechanical shell in alternating uniform field.
- Test magnet problem (`problem = 'Toy'`): simplified MRI scanner configuration with three radiation shields (OVC, 77K and 4K).
- Full magnet problem (`problem = 'Full'`): more realistic MRI scanner configuration where the radiation shields (OVC, 77K and 4K) are closed cylindrical shells.

The code requires the problem file input as presented in Figure E.6, where the variable `problem` is used to call different problem files, all contained in the `problemFiles` folder.

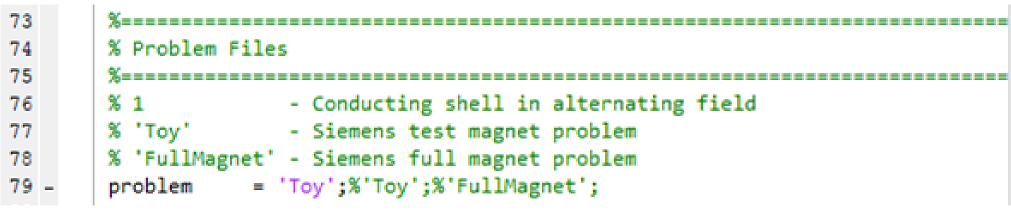

```
%==========================================================================
% Problem Files
%==========================================================================
% 1            - Conducting shell in alternating field
% 'Toy'        - Siemens test magnet problem
% 'FullMagnet' - Siemens full magnet problem
problem     = 'Toy';%'Toy';%'FullMagnet';
```

Figure E.6: Problem file definition in the code.

The three geometries are briefly presented in Figure E.7, where it is clearly seen how each geometry is increasingly the complexity of the problem, being the full magnet problem the more challenging one considered.

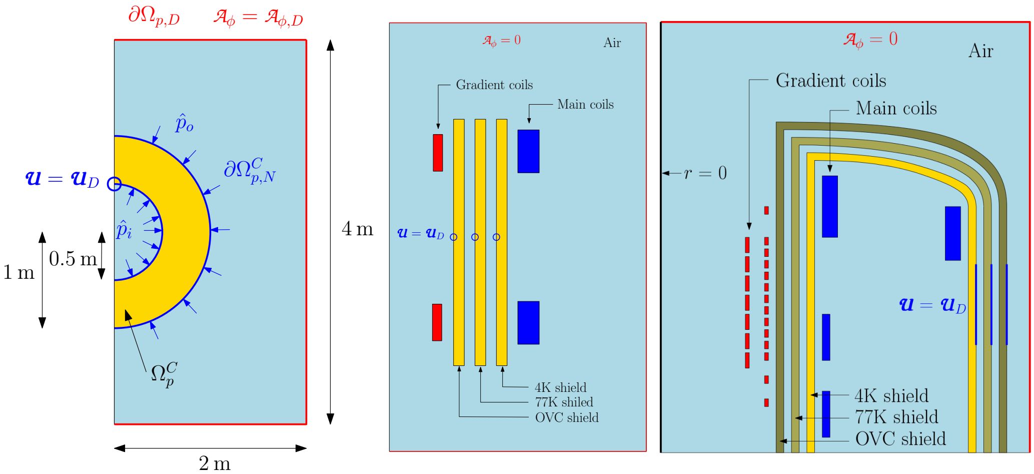
$\partial\Omega_{p,D}$
$\mathcal{A}_\phi = \mathcal{A}_{\phi,D}$
$\hat{p}_o$
$\boldsymbol{u} = \boldsymbol{u}_D$
$\partial\Omega^C_{p,N}$
$\hat{p}_i$
0.5 m
1 m
4 m
Ω^C_p
2 m
$\mathcal{A}_\phi = 0$
Air
Gradient coils
Main coils
$\boldsymbol{u} = \boldsymbol{u}_D$
4K shield
77K shiled
OVC shield
$\mathcal{A}_\phi = 0$
Air
Gradient coils
Main coils
$r = 0$
$\boldsymbol{u} = \boldsymbol{u}_D$
4K shield
77K shield
OVC shield

(a) Magneto-mechanical test problem.

(b) Test magnet geometry.

(c) Full magnet geometry.

Figure E.7: Problem files included in the code and tested with both full order model and PGD approaches.

If a third-user requires the simulation this coupled magneto-mechanical problem for a different geometry, the only change required would be to write a similar script to the ones in the `problemFile` folder with the same inputs and outputs.

E.2.7 Full order model options

Since this user manual focuses on the use of the staggered PGD technique, the full order model options will not be fully discussed. All options are presented in code format in Figure E.8, where three different groups can be found; solver flags, pre-processing flags and post-processing flags. The PGD technique has been implemented and tested for the flags presented in Figure E.8.

The only flags that should be modified are the post-processing flags, which are interesting in terms of results visualisation. The different options available are

- `fieldCalc`: Compute integrated quantities such as dissipated power and kinetic energy.
- `plotsOn`: Activates the generation of contour plots. More plotting options available in the `PostProcessing_v2.m` script.
- `linePlotOn`: Generates line plots in the $r = 0$ axis.
- `plotMeshOn`: Creates figures with the mesh generated for the specified geometry.
- `plotBounOn`: Creates figures with the specified boundary conditions of the problem.

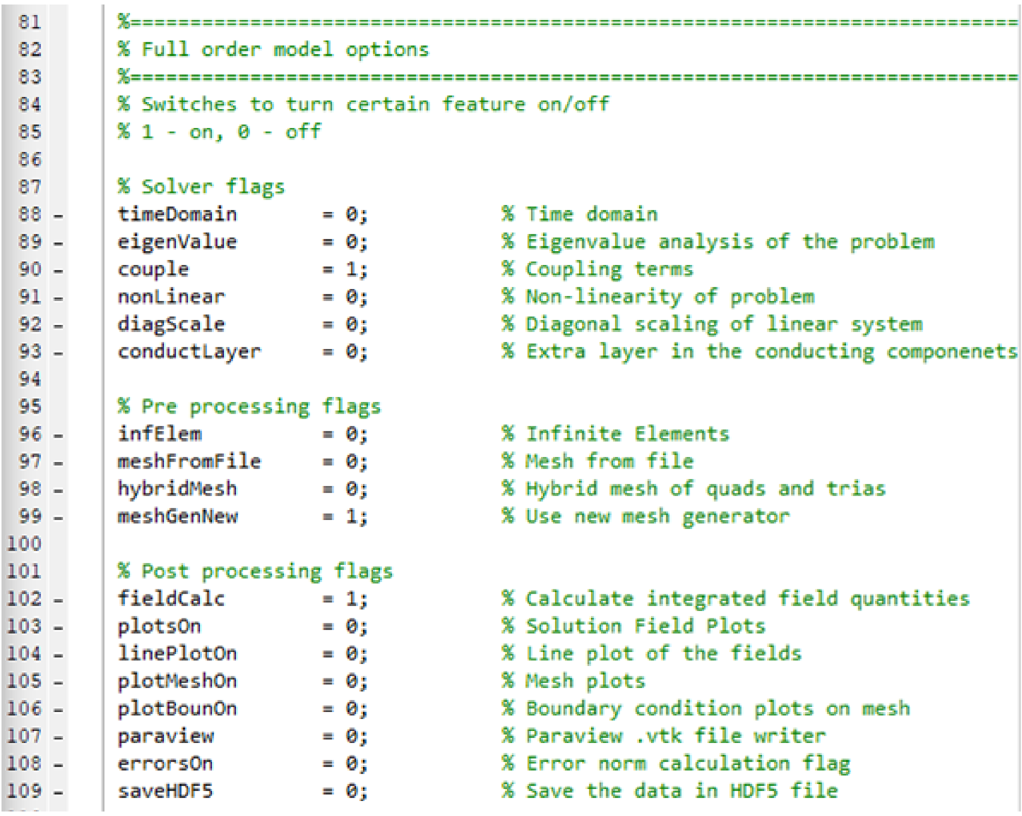

```
%===========================================================================
% Full order model options
%===========================================================================
% Switches to turn certain feature on/off
% 1 - on, 0 - off

% Solver flags
timeDomain       = 0;          % Time domain
eigenValue       = 0;          % Eigenvalue analysis of the problem
couple           = 1;          % Coupling terms
nonLinear        = 0;          % Non-linearity of problem
diagScale        = 0;          % Diagonal scaling of linear system
conductLayer     = 0;          % Extra layer in the conducting componenets

% Pre processing flags
infElem          = 0;          % Infinite Elements
meshFromFile     = 0;          % Mesh from file
hybridMesh       = 0;          % Hybrid mesh of quads and trias
meshGenNew       = 1;          % Use new mesh generator

% Post processing flags
fieldCalc        = 1;          % Calculate integrated field quantities
plotsOn          = 0;          % Solution Field Plots
linePlotOn       = 0;          % Line plot of the fields
plotMeshOn       = 0;          % Mesh plots
plotBounOn       = 0;          % Boundary condition plots on mesh
paraview         = 0;          % Paraview .vtk file writer
errorsOn         = 0;          % Error norm calculation flag
saveHDF5         = 0;          % Save the data in HDF5 file
```

Figure E.8: Switches (0 or 1 values) to activate certain features regarding the full order model.

- `paraview`: Generates files that can be read using Paraview for visualisation purposes.

- `errorsOn`: Computes error with respect to exact solution (only available when `problem = 1`, where the exact solution is known).

- `saveHDF5`: Stores outputs in HDF5 files. Files are stored in `.mat` format if this option is not activated.

E.2.8 Code output

The output when running `main.m` with the settings previously presented are a set of structures shown in Figure E.9. Each substructure contains different information as follows

- `Mesh`: Information about the spatial discretisation (mesh) of the two-dimensional space.

- `freq`: Frequency or range of frequencies of excitation of the problem. Note that, as mention in Section E.2.3, `freq` will be always scalar when running the PGD technique.

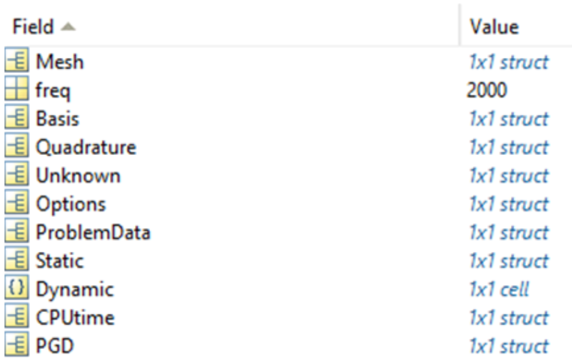

Field	Value
Mesh	1x1 struct
freq	2000
Basis	1x1 struct
Quadrature	1x1 struct
Unknown	1x1 struct
Options	1x1 struct
ProblemData	1x1 struct
Static	1x1 struct
Dynamic	1x1 cell
CPUtime	1x1 struct
PGD	1x1 struct

Figure E.9: Output of the `main.m` script when running the staggered PGD technique.

- `Basis`: Interpolation basis using hierarchical shape functions with the defined polynomial of interpolation `order`.
- `Quadrature`: Numerical quadrature used for integration of the terms appearing in the weak formulation.
- `Unknown`: Numbering of the unknown of the problem.
- `Options`: Contains all the options defined by the user.
- `ProblemData`: Information about the problem geometry and boundary conditions defined in the problem file, see Section E.2.6.
- `Static`: Contains the solution of the static (DC) magneto-mechanical problem.
- `Dynamic`: Cell structure with the solution of all transient (AC) magneto-mechanical problems solved, one for each frequency as specified in `freq`. Again, when running the PGD approach this cell will have only one entry with the online evaluation of the offline PGD solution for the parameters defined in Section E.2.3.
- `CPUtime`: Computational time required to preprocess and solve the DC and AC problems.
- `PGD`: Contains all the information related to the offline high-dimensional PGD solution. This structure can be used in `onlinePGDstage.m` in order to evaluate the stored offline solution.

E.2.9 Online PGD stage

Once all the offline calculations are stored in the `main.m` output, the online PGD stage can be performed in order to evaluate in real-time the high-dimensional offline PGD solution. The main script for this is `onlinePGDstage.m`, in which several options have been implemented and shown in Figure E.10. These switches (0 or 1 values) are defined as

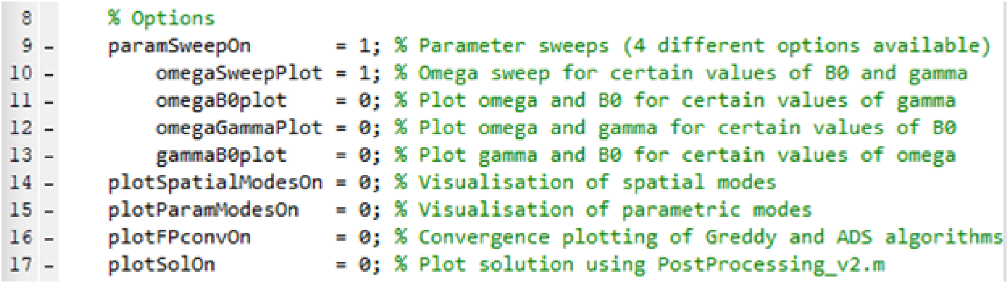

```
% Options
paramSweepOn        = 1; % Parameter sweeps (4 different options available)
    omegaSweepPlot = 1; % Omega sweep for certain values of B0 and gamma
    omegaB0plot    = 0; % Plot omega and B0 for certain values of gamma
    omegaGammaPlot = 0; % Plot omega and gamma for certain values of B0
    gammaB0plot    = 0; % Plot gamma and B0 for certain values of omega
plotSpatialModesOn = 0; % Visualisation of spatial modes
plotParamModesOn   = 0; % Visualisation of parametric modes
plotFPconvOn       = 0; % Convergence plotting of Greddy and ADS algorithms
plotSolOn          = 0; % Plot solution using PostProcessing_v2.m
```

Figure E.10: Switches (0 or 1 values) to activate certain features in `onlinePGDstage.m`.

- `paramSweepOn`: Turns on the parametric sweep options. Four different options have been implemented; `omegaSweepPlot`, `omegaB0plot`, `omegaGammaPlot` and `gammaB0plot`.
  - `omegaSweepPlot`: Frequency sweeps for different combinations of γ and B_0.
  - `omegaB0plot`: Response surface ω/B_0 for certain values of γ.
  - `omegaGammaPlot`: Response surface ω/γ for certain values of B_0.
  - `gammaB0plot`: Response surface γ/B_0 for certain values of ω.
- `plotSpatialModesOn`: Plots the spatial modes computed in the offline PGD stage.
- `plotParamModesOn`: Plots the parametric modes computed in the offline PGD stage.
- `plotFPconvOn`: Plots the convergence of both Greedy and ADS algorithms.
- `plotSolOn`: Evaluation of the offline PGD solution for certain values of ω, γ and B_0 and plotting using `PostProcessing_v2.m`.

References

[1] L. Clarke, R. Velthuizen, M. Camacho, J. Heine, M. Vaidyanathan, L. Hall, R. Thatcher, and M. Silbiger, "MRI segmentation: methods and applications," *Magnetic Resonance Imaging*, vol. 13, no. 3, pp. 343–368, 1995.

[2] S. J. Matzat, J. van Tiel, G. E. Gold, and E. H. Oei, "Quantitative MRI techniques of cartilage composition," *Quantitative Imaging in Medicine and Surgery*, vol. 3, no. 3, p. 162, 2013.

[3] A. Savnik, H. Malmskov, H. S. Thomsen, L. B. Graff, H. Nielsen, B. Danneskiold-Samsøe, J. Boesen, and H. Bliddal, "MRI of the wrist and finger joints in inflammatory joint diseases at 1-year interval: MRI features to predict bone erosions," *European Radiology*, vol. 12, no. 5, pp. 1203–1210, 2002.

[4] P. Kozlowski, S. D. Chang, E. C. Jones, K. W. Berean, H. Chen, and S. L. Goldenberg, "Combined diffusion-weighted and dynamic contrast-enhanced MRI for prostate cancer diagnosis: Correlation with biopsy and histopathology," *Journal of Magnetic Resonance Imaging: An Official Journal of the International Society for Magnetic Resonance in Medicine*, vol. 24, no. 1, pp. 108–113, 2006.

[5] J. A. Pope, *Medical Physics: Imaging*. Heinemann, Portsmouth, United States, 1999.

[6] R. Aarnink and J. Overweg, "Magnetic resonance imaging, a success story for superconductivity," *Europhysics News*, vol. 43, no. 4, pp. 26–29, 2012.

[7] W. R. Hendee and E. R. Ritenour, *Medical Imaging Physics*. John Wiley & Sons, New Jersey, United States, 2003.

[8] J. M. Theysohn, S. Maderwald, O. Kraff, C. Moenninghoff, M. E. Ladd, and S. C. Ladd, "Subjective acceptance of 7 Tesla MRI for human imaging," *Magnetic Resonance Materials in Physics, Biology and Medicine*, vol. 21, no. 1-2, p. 63, 2008.

[9] "Siemens Healthineers web page." `https://www.siemens-healthineers.com/en-uk/`, 2019. Accessed: 11/11/2019.

[10] S. Bagwell, *A Numerical Multi-Physics Approach to Understanding MRI Scanners and their Complex Behaviour*. PhD thesis, Swansea University, UK, 2018.

[11] G. H. Glover and J. M. Pauly, "Projection reconstruction techniques for reduction of motion effects in MRI," *Magnetic Resonance in Medicine*, vol. 28, no. 2, pp. 275–289, 1992.

[12] I. D. Vagner, B. I. Lembrikov, and P. R. Wyder, *Electrodynamics of Magnetoactive Media*, vol. 135. Springer Science & Business Media, Berlin, Germany, 2013.

[13] T. G. Reese, O. Heid, R. Weisskoff, and V. Wedeen, "Reduction of eddy-current-induced distortion in diffusion MRI using a twice-refocused spin echo," *Magnetic Resonance in Medicine: An Official Journal of the International Society for Magnetic Resonance in Medicine*, vol. 49, no. 1, pp. 177–182, 2003.

[14] W. R. Smythe, *Static and Dynamic Electricity*. New York: McGraw-Hill Watanabe M, Taoka T, Ohta S, Anazawa N and Kat S, 1974.

[15] J. L. Meriam and L. G. Kraige, *Engineering Mechanics: Dynamics*, vol. 2. John Wiley & Sons, 2012.

[16] E. T. Laskaris, B. Dorri, and R. A. Ackermann, "Cryogen-cooled open MRI superconductive magnet," Oct. 8 1996. US Patent 5,563,566.

[17] W. Mao, M. B. Smith, and C. M. Collins, "Exploring the limits of RF shimming for high-field MRI of the human head," *Magnetic Resonance in Medicine: An Official Journal of the International Society for Magnetic Resonance in Medicine*, vol. 56, no. 4, pp. 918–922, 2006.

[18] T. C. Cosmus and M. Parizh, "Advances in whole-body MRI magnets," *IEEE Transactions on Applied Superconductivity*, vol. 21, no. 3, pp. 2104–2109, 2011.

[19] "Siemens Healthineers. Magnetic resonance imaging." `https://www.healthcare.siemens.co.uk/news/smt-7t.html`, 2019. Accessed: 27/03/2019.

[20] D. Amsallem and C. Farhat, "Interpolation method for adapting reduced-order models and application to aeroelasticity," *AIAA Journal*, vol. 46, no. 7, pp. 1803–1813, 2008.

[21] F. Chinesta, R. Keunings, and A. Leygue, *The Proper Generalized Decomposition for Advanced Numerical Simulations: A Primer*. Springer Science & Business Media, Berlin, Germany, 2013.

[22] G. Rozza, D. B. P. Huynh, and A. T. Patera, "Reduced basis approximation and a posteriori error estimation for affinely parametrized elliptic coercive partial differential equations," *Archives of Computational Methods in Engineering*, 2008.

[23] P. D. Ledger, J. Peraire, K. Morgan, O. Hassan, and N. Weatherill, "Adaptive *hp* finite element computations of the scattering width output of Max-

well's equations.," *International Journal for Numerical Methods in Fluids*, vol. 43, pp. 953–978, 2003.

[24] A. Buffa, H. Ammari, and J.-C. Nédélec, "A justification of eddy currents model for the Maxwell equations," *SIAM Journal on Applied Mathematics*, vol. 60, no. 5, pp. 1805–1823, 2000.

[25] A. A. Rodríguez and A. Valli, *Eddy Current Approximation of Maxwell Equations: Theory, Algorithms and Applications*, vol. 4. Springer Science & Business Media, Berlin, Germany, 2010.

[26] S. Kurz, J. Fetzer, G. Lehner, and W. M. Rucker, "A novel formulation for 3D eddy current problems with moving bodies using a Lagrangian description and BEM-FEM coupling," *IEEE Transactions on Magnetics*, vol. 34, no. 5, pp. 3068–3073, 1998.

[27] P. D. Ledger and S. Zaglmayr, "*hp*-Finite element simulation of three-dimensional eddy current problems on multiply connected domains," *Computer Methods in Applied Mechanics and Engineering*, vol. 199, no. 49, pp. 3386–3401, 2010.

[28] T. J. R. Hughes, *The Finite Element Method: Linear Static and Dynamic Finite Element Analysis.* Courier Corporation, Massachusetts, United States, 2012.

[29] M. J. Graves and D. G. Mitchell, "Body MRI artifacts in clinical practice: a physicist's and radiologist's perspective," *Journal of Magnetic Resonance Imaging*, vol. 38, no. 2, pp. 269–287, 2013.

[30] K. Krupa and M. Bekiesińska-Figatowska, "Artifacts in magnetic resonance imaging," *Polish Journal of Radiology*, vol. 80, p. 93, 2015.

[31] C. Lalanne, *Mechanical Vibration and Shock Analysis, Fatigue Damage*, vol. 4. John Wiley & Sons, 2010.

[32] S. Bagwell, P. D. Ledger, A. J. Gil, M. Mallett, and M. Kruip, "A linearised *hp*–finite element framework for acousto-magneto-mechanical coupling in axisymmetric MRI scanners," *International Journal for Numerical Methods in Engineering*, vol. 112, no. 10, pp. 1323–1352, 2017.

[33] S. Bagwell, P. D. Ledger, A. J. Gil, and M. Mallett, "Transient solutions to nonlinear acousto-magneto-mechanical coupling for axisymmetric MRI scanner design," *International Journal for Numerical Methods in Engineering*, vol. 115, no. 2, pp. 209–237, 2018.

[34] M. Rausch, M. Gebhardt, M. Kaltenbacher, and H. Landes, "Magnetomechanical field computations of a clinical magnetic resonance imaging (MRI) scanner," *COMPEL-The International Journal for Computation and Mathematics in Electrical and Electronic Engineering*, vol. 22, no. 3, pp. 576–588, 2003.

[35] M. Rausch, M. Gebhardt, M. Kaltenbacher, and H. Landes, “Computer-aided design of clinical magnetic resonance imaging scanners by coupled magnetomechanical-acoustic modeling,” *IEEE Transactions on Magnetics*, vol. 41, no. 1, pp. 72–81, 2005.

[36] P. D. Ledger, A. J. Gil, R. Poya, M. Kruip, I. Wilkinson, and S. Bagwell, “Solution of an industrially relevant coupled magneto–mechanical problem set on an axisymmetric domain,” *Applied Mathematical Modelling*, vol. 40, no. 3, pp. 1959–1971, 2016.

[37] W. H. Schilders, H. A. Van der Vorst, and J. Rommes, *Model Order Reduction: Theory, Research Aspects and Applications*, vol. 13. Springer, Berlin, Germany, 2008.

[38] F. Chinesta and P. Ladevèze, “Separated Representations and PGD-Based Model Reduction,” *Fundamentals and Applications, International Centre for Mechanical Siences, Courses and Lectures*, vol. 554, 2014.

[39] B. Moore, “Principal component analysis in linear systems: Controllability, observability, and model reduction,” *IEEE Transactions on Automatic Control*, vol. 26, no. 1, pp. 17–32, 1981.

[40] K. Pearson, “On lines and planes of closest fit to systems of points in space,” *The London, Edinburgh, and Dublin Philosophical Magazine and Journal of Science*, vol. 2, no. 11, pp. 559–572, 1901.

[41] A. Quarteroni and A. Veneziani, “Analysis of a geometrical multiscale model based on the coupling of ODE and PDE for blood flow simulations,” *Multiscale Modeling & Simulation*, vol. 1, no. 2, pp. 173–195, 2003.

[42] D. Modesto, S. Zlotnik, and A. Huerta, “Proper Generalized Decomposition for parameterized Helmholtz problems in heterogeneous and unbounded domains: Application to harbor agitation,” *Computer Methods in Applied Mechanics and Engineering*, vol. 295, pp. 127–149, 2015.

[43] D. Ryckelynck, F. Chinesta, E. Cueto, and A. Ammar, “On thea priori model reduction: Overview and recent developments,” *Archives of Computational methods in Engineering*, vol. 13, no. 1, pp. 91–128, 2006.

[44] E. Cueto, D. González, and I. Alfaro, *Proper Generalized Decompositions: An Introduction to Computer Implementation with Matlab*. Springer, New York, United States, 2016.

[45] Y. Liang, H. Lee, S. Lim, W. Lin, K. Lee, and C. Wu, “Proper orthogonal decomposition and its applications. Part i: Theory,” *Journal of Sound and Vibration*, vol. 252, no. 3, pp. 527–544, 2002.

[46] V. Buljak, *Inverse Analyses with Model Reduction: Proper Orthogonal Decomposition in Structural Mechanics*. Springer Science & Business Media, Germany, 2011.

[47] L. Sirovich, “Turbulence and the dynamics of coherent structures. I - III,” *Quarterly of Applied Mathematics*, vol. 45, no. 3, pp. 561–590, 1987.

[48] P. Díez, S. Zlotnik, A. García-González, and A. Huerta, “Algebraic PGD for tensor separation and compression: An algorithmic approach,” *Comptes Rendus Mécanique*, vol. 346, no. 7, pp. 501–514, 2018.

[49] M. Seoane, P. D. Ledger, A. J. Gil, S. Zlotnik, and M. Mallett, “A combined reduced order-full order methodology for the solution of 3D magneto-mechanical problems with application to MRI scanners,” Submitted 2019.

[50] A. Chatterjee, “An introduction to the proper orthogonal decomposition,” *Current Science*, pp. 808–817, 2000.

[51] T. Bui-Thanh, M. Damodaran, and K. Willcox, “Proper orthogonal decomposition extensions for parametric applications in compressible aerodynamics,” in *21st AIAA Applied Aerodynamics Conference, Florida*, p. 4213, 2003.

[52] D. Nicola, T. Marco, G. Gianluca, L. Gianpiero, and G. Rozza, “Shape optimization by means of proper orthogonal decomposition and dynamic mode decomposition,” arXiv:1803.07368v2, 2018.

[53] N. N. Cuong, K. Veroy, and A. T. Patera, “Certified real-time solution of parametrized partial differential equations,” in *Handbook of Materials Modeling*, pp. 1529–1564, Springer, 2005.

[54] K. Veroy, C. Prud’Homme, and A. T. Patera, “Reduced-basis approximation of the viscous Burgers equation: rigorous a posteriori error bounds,” *Comptes Rendus Mathematique*, vol. 337, no. 9, pp. 619–624, 2003.

[55] J. S. Hesthaven, G. Rozza, B. Stamm, *et al.*, *Certified Reduced Basis Methods for Parametrized Partial Differential Equations*. Springer, New York, United States, 2016.

[56] R. Bialecki, A. Kassab, and A. Fic, “Proper orthogonal decomposition and modal analysis for acceleration of transient FEM thermal analysis,” *International Journal for Numerical Methods in Engineering*, vol. 62, no. 6, pp. 774–797, 2005.

[57] G. Berkooz, P. Holmes, and J. L. Lumley, “The proper orthogonal decomposition in the analysis of turbulent flows,” *Annual Review of Fluid Mechanics*, vol. 25, no. 1, pp. 539–575, 1993.

[58] G. Kerschen, F. Poncelet, and J.-C. Golinval, “Physical interpretation of independent component analysis in structural dynamics,” *Mechanical Systems and Signal Processing*, vol. 21, no. 4, pp. 1561–1575, 2007.

[59] H. V. Ly and H. T. Tran, “Modeling and control of physical processes using proper orthogonal decomposition,” *Mathematical and Computer Modelling*, vol. 33, no. 1-3, pp. 223–236, 2001.

[60] R. Ruotolo and C. Surace, "Using SVD to detect damage in structures with different operational conditions," *Journal of Sound and Vibration*, vol. 226, no. 3, pp. 425–439, 1999.

[61] L. Sirovich and M. Kirby, "Low-dimensional procedure for the characterization of human faces," *Josa A*, vol. 4, no. 3, pp. 519–524, 1987.

[62] D. Tang, D. Kholodar, J.-N. Juang, and E. H. Dowell, "System identification and proper orthogonal decomposition method applied to unsteady aerodynamics," *AIAA Journal*, vol. 39, no. 8, pp. 1569–1576, 2001.

[63] A. Ammar, D. Ryckelynck, F. Chinesta, and R. Keunings, "On the reduction of kinetic theory models related to finitely extensible dumbbells," *Journal of Non-Newtonian Fluid Mechanics*, vol. 134, no. 1-3, pp. 136–147, 2006.

[64] A. Ammar, B. Mokdad, F. Chinesta, and R. Keunings, "A new family of solvers for some classes of multidimensional partial differential equations encountered in kinetic theory modeling of complex fluids," *Journal of Non-Newtonian Fluid Mechanics*, vol. 139, no. 3, pp. 153–176, 2006.

[65] A. Ammar, B. Mokdad, F. Chinesta, and R. Keunings, "A new family of solvers for some classes of multidimensional partial differential equations encountered in kinetic theory modelling of complex fluids: Part II: Transient simulation using space-time separated representations," *Journal of Non-Newtonian Fluid Mechanics*, vol. 144, no. 2-3, pp. 98–121, 2007.

[66] M. Signorini, S. Zlotnik, and P. Diez, "Proper generalized decomposition solution of the parameterized helmholtz problem: Application to inverse geophysical problems," *International Journal for Numerical Methods in Engineering*, vol. 109, no. 8, pp. 1085–1102, 2017.

[67] J. M. de Almeida, "A basis for bounding the errors of proper generalised decomposition solutions in solid mechanics," *International Journal for Numerical Methods in Engineering*, vol. 94, no. 10, pp. 961–984, 2013.

[68] R. García-Blanco, D. Borzacchiello, F. Chinesta, and P. Diez, "Monitoring a PGD solver for parametric power flow problems with goal-oriented error assessment," *International Journal for Numerical Methods in Engineering*, vol. 111, no. 6, pp. 529–552, 2017.

[69] R. Ibáñez, E. Abisset-Chavanne, F. Chinesta, and A. Huerta, "Simulating squeeze flows in multiaxial laminates: Towards fully 3D mixed formulations," *International Journal of Material Forming*, vol. 10, no. 5, pp. 653–669, 2017.

[70] P. Díez, S. Zlotnik, and A. Huerta, "Generalized parametric solutions in Stokes flow," *Computer Methods in Applied Mechanics and Engineering*, vol. 326, pp. 223–240, 2017.

[71] V. Tsiolakis, M. Giacomini, R. Sevilla, C. Othmer, and A. Huerta, “Nonintrusive proper generalised decomposition for parametrised incompressible flow problems in OpenFOAM,” *arXiv preprint arXiv:1906.05403*, 2019.

[72] C. Ghnatios, F. Masson, A. Huerta, A. Leygue, E. Cueto, and F. Chinesta, “Proper generalized decomposition based dynamic data-driven control of thermal processes,” *Computer Methods in Applied Mechanics and Engineering*, vol. 213, pp. 29–41, 2012.

[73] J. V. Aguado, A. Huerta, F. Chinesta, and E. Cueto, “Real-time monitoring of thermal processes by reduced-order modeling,” *International Journal for Numerical Methods in Engineering*, vol. 102, no. 5, pp. 991–1017, 2015.

[74] B. Bognet, A. Leygue, and F. Chinesta, “On the fully 3D simulations of thermoelastic models defined in plate and shell geometries,” *European Journal of Computational Mechanics/Revue Européenne de Mécanique Numérique*, vol. 21, no. 1-2, pp. 40–51, 2012.

[75] S. Zlotnik, P. Díez, D. Modesto, and A. Huerta, “Proper generalized decomposition of a geometrically parametrized heat problem with geophysical applications,” *International Journal for Numerical Methods in Engineering*, vol. 103, no. 10, pp. 737–758, 2015.

[76] J. Li and W. Zhang, “The performance of proper orthogonal decomposition in discontinuous flows,” *Theoretical and Applied Mechanics Letters*, vol. 6, no. 5, pp. 236–243, 2016.

[77] M. Seoane, P. Ledger, A. Gil, and M. Mallett, “An accurate and efficient three-dimensional high-order finite element methodology for the simulation of magneto-mechanical coupling in MRI scanners,” *International Journal for Numerical Methods in Engineering*, vol. 119, no. 12, pp. 1185–1215, 2019.

[78] A. J. Gil, “Lagrangian and Eulerian formulation of magneto-mechanical coupled problems,” Technical report. Swansea University, 2019.

[79] S. Baek, R. Gleason, K. Rajagopal, and J. Humphrey, “Theory of small on large: potential utility in computations of fluid-solid interactions in arteries,” *Computer Methods in Applied Mechanics and Engineering*, vol. 196, no. 31-32, pp. 3070–3078, 2007.

[80] A. J. Gil and J. Bonet, “Finite element analysis of prestressed structural membranes,” *Finite Elements in Analysis and Design*, vol. 42, no. 8-9, pp. 683–697, 2006.

[81] A. J. Gil, “Structural analysis of prestressed Saint Venant-Kirchhoff hyperelastic membranes subjected to moderate strains,” *Computers & Structures*, vol. 84, no. 15-16, pp. 1012–1028, 2006.

[82] A. J. Gil and J. Bonet, “Finite element analysis of partly wrinkled reinforced prestressed membranes,” *Computational Mechanics*, vol. 40, no. 3, pp. 595–615, 2007.

[83] R. Poya, R. Sevilla, and A. J. Gil, “A unified approach for a posteriori high-order curved mesh generation using solid mechanics,” *Computational Mechanics*, vol. 58, no. 3, pp. 457–490, 2016.

[84] J. Bonet, A. J. Gil, and R. D. Wood, *Nonlinear Solid Mechanics for Finite Element Analysis: Statics.* Cambridge University Press, United Kingdom, 2016.

[85] J. Darong, *An hp-Finite Element Computational Framework for Nonlinear Magneto-Fluid Problems Including Magnetostriction.* PhD thesis, Swansea University, 2015.

[86] S. M. Nazeer, F. Bordeu, A. Leygue, and F. Chinesta, “Arlequin based PGD domain decomposition,” *Computational Mechanics*, vol. 54, no. 5, pp. 1175–1190, 2014.

[87] R. A. Horn, “The Hadamard product,” in *Proceedings of Symposia in Applied Mathematics*, vol. 40, pp. 87–169, 1990.

[88] G. Barroso, A. J. Gil, P. D. Ledger, M. Mallett, and A. Huerta, “A regularised-adaptive proper generalised decomposition implementation for coupled magneto-mechanical problems with application to MRI scanners,” *Computer Methods in Applied Mechanics and Engineering*, vol. 358, p. 112640, 2020.

[89] J. Schöberl and S. Zaglmayr, “High order Nédélec elements with local complete sequence properties,” *COMPEL-The International Journal for Computation and Mathematics in Electrical and Electronic Engineering*, vol. 24, no. 2, pp. 374–384, 2005.

[90] J. Donea and A. Huerta, *Finite Element Methods for Flow Problems.* John Wiley & Sons, New Jersey, United States, 2003.

[91] G. Barroso, M. Seoane, A. J. Gil, P. D. Ledger, M. Mallett, and A. Huerta, “A staggered high-dimensional proper generalised decomposition for coupled magneto-mechanical problems with application to MRI scanners. Submitted,” September 2019.

[92] A. Ammar, A. Huerta, F. Chinesta, E. Cueto, and A. Leygue, “Parametric solutions involving geometry: A step towards efficient shape optimization,” *Computer Methods in Applied Mechanics and Engineering*, vol. 268, pp. 178–193, 2014.

[93] F. Chinesta, A. Leygue, F. Bordeu, J. V. Aguado, E. Cueto, D. González, I. Alfaro, A. Ammar, and A. Huerta, “PGD-based computational vademecum for efficient design, optimization and control,” *Archives of Computational Methods in Engineering*, vol. 20, no. 1, pp. 31–59, 2013.

[94] R. Sevilla, S. Zlotnik, and A. Huerta, “Solution of geometrically parametrised problems within a CAD environment via model order reduction,” *Com-*

puter Methods in Applied Mechanics and Engineering, vol. 358, p. 112631, 2020.

[95] Z. Q. Xie, R. Sevilla, O. Hassan, and K. Morgan, "The generation of arbitrary order curved meshes for 3D finite element analysis," *Computational Mechanics*, vol. 51, no. 3, pp. 361–374, 2013.

[96] H. B. Demuth, M. H. Beale, O. De Jess, and M. T. Hagan, *Neural Network Design, 2nd Edition.* Martin Hagan, Idaho, United States, 2014.

[97] Q. Wang, R. R. Medeiros, C. E. Cesnik, K. Fidkowski, J. Brezillon, and H. M. Bleecke, "Techniques for improving neural network-based aerodynamics reduced-order models," in *AIAA Scitech 2019 Forum*, p. 1849, 2019.

[98] G. Sun and S. Wang, "A review of the artificial neural network surrogate modeling in aerodynamic design," *Proceedings of the Institution of Mechanical Engineers, Part G: Journal of Aerospace Engineering*, p. 0954410019864485, 2019.

[99] M. Mehnert, M. Hossain, and P. Steinmann, "Towards a thermo-magneto-mechanical coupling framework for magneto-rheological elastomers," *International Journal of Solids and Structures*, vol. 128, pp. 117–132, 2017.

[100] V. Pagonis, C. Ankjærgaard, A. Murray, M. Jain, R. Chen, J. Lawless, and S. Greilich, "Modelling the thermal quenching mechanism in quartz based on time-resolved optically stimulated luminescence," *Journal of Luminescence*, vol. 130, no. 5, pp. 902–909, 2010.

[101] D. Moens and D. Vandepitte, "A survey of non-probabilistic uncertainty treatment in finite element analysis," *Computer Methods in Applied Mechanics and Engineering*, vol. 194, no. 12-16, pp. 1527–1555, 2005.

[102] P. Ladevèze and L. Chamoin, "Toward guaranteed PGD-reduced models," *Bytes and Science. CIMNE: Barcelona*, pp. 143–154, 2013.

[103] A. Bjorck, *Numerical Methods for Least Squares Problems*, vol. 51. Siam, United States, 1996.

[104] P. C. Hansen, *Rank-Deficient and Discrete Ill-Posed Problems: Numerical Aspects of Linear Inversion*, vol. 4. Siam, United States, 2005.

[105] L. De Lathauwer, B. De Moor, and J. Vandewalle, "A multilinear singular value decomposition," *SIAM Journal on Matrix Analysis and Applications*, vol. 21, no. 4, pp. 1253–1278, 2000.

[106] R. Rama, *Proper Orthogonal Decomposition with Interpolation-Based Real-Time Modelling of the Heart.* PhD thesis, University of Cape Town, 2017.

[107] R. Rama, S. Skatulla, and C. Sansour, "Real-time modelling of the heart using the proper orthogonal decomposition with interpolation," in *VI International Conference on Computational Bioengineering (ICCB)*, pp. 1–12, 2015.

[108] N. Demo, N. Tezzele, G. Gustin, G. Lavini, and G. Rozza, "Shape optimisation by means of proper orthogonal decomposition and dynamic mode decomposition," *arXiv preprint arXiv:1803.07368*, 2018.

[109] S. Georgaka, G. Stabile, G. Rozza, and M. Bluck, "Parametric POD-Galerkin model order reduction for unsteady-state heat transfer problems," *arXiv preprint arXiv:1808.05175*, 2018.

[110] G. Stabile, S. Hijazi, A. Mola, S. Lorenzi, and G. Rozza, "POD-Galerkin reduced order methods for CFD using finite volume discretisation: Vortex shedding around a circular cylinder," *Communications in Applied and Industrial Mathematics*, vol. 8, no. 1, pp. 210–236, 2017.

[111] C. Hesch, A. J. Gil, A. A. Carreño, J. Bonet, and P. Betsch, "A mortar approach for fluid–structure interaction problems: Immersed strategies for deformable and rigid bodies," *Computer Methods in Applied Mechanics and Engineering*, vol. 278, pp. 853 – 882, 2014.

[112] T. McDevitt and T. Laursen, "A mortar-finite element formulation for frictional contact problems," *International Journal for Numerical Methods in Engineering*, vol. 48, no. 10, pp. 1525–1547, 2000.

[113] A. Popp, M. W. Gee, and W. A. Wall, "A finite deformation mortar contact formulation using a primal–dual active set strategy," *International Journal for Numerical Methods in Engineering*, vol. 79, no. 11, pp. 1354–1391, 2009.

[114] "Matlab," R2018a. The MathWorks, Natick, MA, USA.